Volume 70A
Number 2
Mar.–Apr. 1966

Physics and Chemistry

U.S. DEPARTMENT OF COMMERCE

SECTION A

JOURNAL OF RESEARCH

NATIONAL BUREAU OF STANDARDS

Journal of Research

of the

National Bureau of Standards

A. Physics and Chemistry

Mar.–Apr. • 1966

VOLUME • 70A

NUMBER • 2

Editor: C. W. Beckett

Associate Editors: D. D. Wagman
J. M. Richardson

Publication dates:
Feb. 1, Apr. 1, June 1, Aug. 1, Oct. 1, Dec. 1, 1966

JOURNAL OF RESEARCH

The National Bureau of Standards Journal of Research reports research and development in the fields of activity shown at right. Also included from time to time are survey articles on topics closely related to the Bureau's scientific and technical program.

The Journal is published in three separate sections as follows:

A. Physics and Chemistry

Contains papers of interest primarily to scientists working in these fields. Issued six times a year. Annual subscription: domestic, $5.00; foreign, $6.00. Single copy, $1.00.

B. Mathematics and Mathematical Physics

Presents studies and compilations designed mainly for the mathematician and the theoretical physicist. Issued quarterly. Annual subscription: domestic, $2.25; foreign, $2.75. Single copy, 75c.

C. Engineering and Instrumentation

Reports research and development results of interest chiefly to the engineer and the applied scientist. Issued quarterly. Annual subscription: domestic, $2.75; foreign, $3.50. Single copy, 75c.

The National Bureau of Standards is a principal focal point in the Federal Government for assuring maximum application of the physical and engineering sciences to the advancement of technology in industry and commerce. Its responsibilities include development and maintenance of the national standards of measurement, and the provision of means for making measurements consistent with those standards; determination of physical constants and properties of materials; development of methods for testing materials, mechanisms, and structures, and making such tests as may be necessary, particularly for government agencies; cooperation in the establishment of standard practices for incorporation in codes and specifications; advisory service to government agencies on scientific and technical problems; invention and development of devices to serve special needs of the Government; assistance to industry, business and consumers in the development and acceptance of commercial standards and simplified trade practice recommendations; administration of programs in cooperation with United States business groups and standards organizations for the development of international standards of practice; and maintenance of a clearinghouse for the collection and dissemination of scientific, technical and engineering information. The scope of the Bureau's activities is suggested in the following listing of its three Institutes and their organizational units.

Institute for Basic Standards. Applied Mathematics. Electricity. Metrology. Mechanics. Heat. Atomic Physics. Physical Chemistry. Laboratory Astrophysics.* Radiation Physics. Radio Standards Laboratory.* Radio Standards Physics & Radio Standards Engineering. Office of Standard Reference Data.

Institute for Materials Research. Analytical Chemistry. Polymers. Metallurgy. Inorganic Materials. Reactor Radiations. Cryogenics.* Materials Evaluation Laboratory. Office of Standard Reference Materials.

Institute for Applied Technology. Building Research. Information Technology. Performance Test Development. Electronic Instrumentation. Textile and Apparel Technology Center. Technical Analysis. Office of Weights and Measures. Office of Engineering Standards. Office of Invention and Innovation. Office of Technical Resources. Clearinghouse for Federal Scientific and Technical Information.**

*Located at Boulder, Colo., 80301.
**Located at 5285 Port Royal Road, Springfield, Va., 22171.

U.S. DEPARTMENT OF COMMERCE
John T. Connor, Secretary

NATIONAL BUREAU OF STANDARDS
A. V. Astin, Director

Order all publications from the Superintendent of Documents
U.S. Government Printing Office, Washington, D.C., 20402

Use of funds for printing this publication approved by the Director of the Bureau of the Budget (June 19, 1961).

JOURNAL OF RESEARCH of the National Bureau of Standards—A. Physics and Chemistry
Vol. 70A, No. 2, March–April 1966

The Mechanism of the Depolymerization of Polytetrafluoroethylene With Pyrolytic and Radiolytic Initiation*

Roland E. Florin, Midgett S. Parker,[1] and Leo A. Wall

Institute for Materials Research, National Bureau of Standards, Washington, D.C.

(December 22, 1965)

The rate of decomposition of polytetrafluoroethylene, exposed to gamma radiation in a flowing helium atmosphere, was studied in the range of temperatures 330 to 450 °C, dose rates 0.1 to 7.6 MR/h, and sample thicknesses 0.0006 to 0.01 cm. Rate measurements were made with a thermal conductivity cell in the exit stream, which recorded essentially the difference between the thermal and radiation-induced rate, in total molecules of volatiles per second. At temperatures below about 400 °C, the volatile products were a complex mixture. Above 400 °C, tetrafluoroethylene was the major product, and the radiation-induced rate had an activation energy* of 70 to 84 kJ/mol. The radiation-induced rate is proportional to square root of dose rate, after appropriate allowance for the thermal initiation is made. Analysis of the results suggests that the rate of the thermal initiation has a very high preexponential factor, 10^{28} to 10^{30} s^{-1}. The activation energy for termination is large, $E_4 > 155$ kJ/mol. Diffusion and reverse reaction appear to be minor factors above 400 °C, but a surface reaction may be important. The thermal decomposition mechanism seems clearly to consist of random initiation, termination by bimolecular recombination and a short kinetic chain (13 at 480 °C).

Key Words: Depolymerization, polytetrafluoroethylene, radiolysis, thermal decomposition, mechanisms of degradation, and gamma ray effects.

1. Introduction

It appears that the normal pyrolytic reactions of polymers can be much accelerated by the action of ultraviolet light and will then occur at measurable rates below the normal temperatures for pyrolysis. This has been demonstrated for polymethyl methacrylate [1].[2] The reason for this effect is that in the set of chain reactions

	Rate
$Q_n \xrightarrow{k_1} R_i + R_{n-i}$	$2k_1 n Q_n$
$R_n \xrightarrow{k_2} R_{n-1} + M$	$k_2 R_n$
$\left\{ \begin{array}{l} R_n + Q_m \xrightarrow{k_3} R'_m + Q_n \\ R'_{i+j} \xrightarrow{k_{3a}} R_i + Q_j \end{array} \right\}$	$k_3 Q_m R_n$
$R_i + R_j \left\{ \begin{array}{l} \xrightarrow{k_4} Q_{i+j} \\ \xrightarrow{k_{4a}} Q_i + Q_j \end{array} \right.$	$2k_4 R^2$ $2k_{4a} R^2$

for pyrolysis [2, 3, 4], the thermal initiation reaction of high activation energy is replaced by a photoinduced initiation reaction whose rate is proportional to the light intensity I and essentially independent of temperature.

$$Q_n \longrightarrow R_i + R_{n-i} \qquad 2\Phi n Q_n I.$$

In the above mechanism for polymer decomposition we have depicted only random initiation in anticipation of the conclusions made in this paper. The symbols are defined as: Q_n, concentration of polymer molecules with degree of polymerization n, R_i concentration of polymer radicals, M monomer, and Φ a factor including the quantum yield of radicals.

The same result can be anticipated from initiation by γ-rays and other forms of ionizing radiation. The effect is of some practical importance in limiting the service life of polymers exposed to ionizing radiation at relatively high temperatures, for example, in space applications or nuclear installations. It also can be applied to deduce more detailed information concerning the individual rate constants in pyrolysis, as illustrated by Cowley and Melville [1].

Initiation by gamma radiation is especially convenient in the study of polytetrafluoroethylene, which does not absorb ultraviolet very effectively at convenient wave lengths [5].

*Research based on work supported by the National Aeronautics and Space Administration.

[1] Present address: IBM Manufacturing Research Division, Endicott, New York.

[2] Figures in brackets indicate the literature references at the end of this paper.

The kinetics of the thermal decomposition of polytetrafluoroethylene have been reviewed in a recent experimental paper [6]. Investigators are in agreement that in vacuum between 360 and 510 °C, the product is nearly pure monomer and the rate is given rather closely by the eqs [7–10].

$$r_0 = \frac{1}{(1-C)}\frac{dC}{dt} = \frac{1}{\sum nQ_n(0)}\frac{dM}{dt} = 4.7 \times 10^{18} e^{-80{,}500/RT} s^{-1}, \quad (1)$$

where r_0 is the fractional rate of volatilization of the polymer. The conversion C, that is, the fraction of the original sample volatilized, is defined by

$$C = 1 - \frac{\sum nQ_n(t)}{\sum nQ_n(0)}. \quad (2)$$

In eq (1) and subsequent expressions, R takes the numerical value 1.98646 cal $°K^{-1}$ mol^{-1} and 1 cal = 1.4840 J.

The kinetic chain length has been estimated from molecular weight changes [6], but it and other parameters are still subject to large uncertainties.

Recent summaries of the radiation chemistry are available [11–13]. It is noteworthy that two radical species are formed, $-CF_2\cdot$ and $-CF_2CFCF_2-$, and that numerical G-values are low, for radical formation and other processes at room temperature [14, 15]. When polytetrafluoroethylene was exposed to radiation at a very high dose rate, the weight loss increased rapidly over a short temperature interval [16].

In the present work the decomposition of polytetrafluoroethylene has been studied in the range of temperatures 330 to 460 °C and dose rates 0.1 to 7.66 megaroentgens per hour (MR/h), and expressions have been deduced for the thermal initiation rate, the chain length under various circumstances, and the activation energies of elementary rate processes. Rate of monomer evolution was measured by changes in thermal conductivity of a flowing stream of helium.

2. Experimental Procedure

2.1. Apparatus

The polymer samples were usually polytetrafluoroethylene cast film, of thicknesses 0.0062, 0.0025, and 0.01 cm. In certain studies related to molecular weight, powdered samples were used, of molecular weights 1 to 2.5×10^5, 1 to 3×10^6, and 1×10^7, estimated by the standard specific gravity method of Sperati and Starkweather [12].

Tetrafluoroethylene for calibration was prepared by low-pressure pyrolysis of the polymer [17]. Helium was the commercial gas of 99.99 percent assay. Mass spectrometer analysis indicated no appreciable impurities, and specifically less than 0.07 percent of H_2. Attempts to concentrate CO_2 by trapping out from the stream at 77 °K led to inconsistent results, from less than 0.002 to 0.01 percent.

Helium was led from a cylinder through one side of a thermal conductivity cell, thence to a pyrolysis chamber containing the sample in the radiation source, and finally to the other side of the thermal conductivity cell and to a trap immersed in liquid nitrogen. The principle of the method has been applied before [18]. The pyrolysis chamber was constructed of stainless steel, in two pieces, joined at the top by a flange and an O-ring. The outer wall was 40 cm in length by 5 cm diam. The top member contained an extension, 35 cm length by 4.5 cm diam, which projected downward inside the chamber space, and carried at its lower end a helium inlet tube and a detachable, perforated hollow stalk bearing four aluminum trays 4.5 cm in diameter and 0.6 cm apart, upon which circular sheets of the sample were laid. An internal thermocouple was mounted near the middle of the stalk; its leads were brought out through the helium inlet tube and a picein seal. The helium outlet tube was connected to the top flange. A controlled furnace was wound about the outer wall covering the lower 15 cm of its length and extending 4 cm below the bottom. A control thermocouple was mounted in the furnace insulation. The furnace assembly was mounted in a cylindrical can at the end of a long tube which carried the electrical leads and the helium connections and served as a handle. Helium going from the tank to the furnace and from the furnace to the detector passed through 4 m of plastic tubing and 4.5 m of copper tubing in each line. The copper tubing was mounted in a thermostatted cabinet containing the detector. Helium flow and pressure were monitored by two flow meters and a manometer. Each side of the thermal conductivity cell contained a pair of tungsten filaments, in series, with a resistance of about 100 Ω, in each arm of the bridge. The bridge current was 250 mA, well above the recommended level, for increased sensitivity. Bridge unbalance was fed to a recorder. In the absence of the cabinet and copper heat exchange coils, the output of the bridge suffered considerable drift and a fluctuation of a large fraction of 1 mV, correlated with changes of room temperature. These fluctuations were reduced about 10-fold by the heat exchange coils and by controlling the room temperature to within 0.2 °C by a sensitive room thermostat.

Measurements were made by bringing the sample to temperature in the furnace at a chosen helium flow rate in a region of negligible radiation dose rate, establishing a recorder base line at this temperature, then placing the furnace in a position of known dose rate. A typical recorder curve is shown in figure 1. From the theory of vapor chromatography instrumentation [19], the height of the response will be nearly proportional to the mole fraction of nonhelium components in the gas passing the detector, minus the mole fraction of such components, if any, under base-line conditions. The shape of the experimental curve is roughly what is to be expected of a flow chamber with thorough mixing, in which product formation

at a constant rate begins and ceases sharply after the starting and cutoff times [20]. There is an additional delay, as shown in figure 1, for the time of travel through the tubing system. Most of the experiments were done at a helium flow rate of 0.217 cm^3/s, which involved a time delay of the order of 15 to 20 min to reach maximum response. This time delay obscures any short-lived transient phenomena in the kinetics of the decomposition. The weight loss was usually held to less than 20 percent during a series of experiments with a given sample. The apparatus was calibrated by bleeding pure tetrafluoroethylene into the helium line to the furnace, from a 30-ml bulb in which the pressure (1.1 to 2.0 atm) was accurately measured as a function of time by a mercury column and cathetometer. At low feed rates, precision was impaired by fluctuations of barometric pressure. Measurements at various flow rates are consistent with a sensitivity of 0.03 mol percent C_2F_4 per millivolt. The response was not noticeably influenced by variations of furnace temperature from 20 to 400 °C, nor by the presence or absence of radiation. It would presumably be the same within errors of measurement for most other gases of reasonably low thermal conductivity. A few attempts were made to measure changes with temperature of the purely thermal rate of decomposition by establishing a preliminary base line at about 250 °C. The results were in fair agreement with the thermal decomposition rates in the literature if a correction of about +27 °C is applied to the internal thermocouple reading, see table 1. However, factors other than the thermal decomposition rate could have contributed to the response of the instrument to changes of temperature, and it is probable that only rate differences at constant temperature are reliably detected.

TABLE 1. *Detector responses in the absence of radiation*

Temp., °C [a]	290	315.5	356.5	403.4	437.9
Response, mV	0	0.08, .24	0.24	0.88	2.33
Equivalent rate, $s^{-1} \times 10^{7}$ [b]	0	0.6, 1.9	1.9	7.2	19.0
Thermal rate, $\times 10^{7}$ [c]	< 0.001	< 0.001	0.002	0.52	11.0

[a] Corrected, see "Experimental Procedure."
[b] 0.0025 cm thickness, 0.35 g.
[c] Data of Madorsky, ref. 7.

The losses in weight measured after fixed long periods of time in the absence of radiation could be correlated with the thermal weight loss data of Madorsky [7] only if a correction of +27 °C was applied to the interior thermocouple temperature. The data of Madorsky on polytetrafluoroethylene appear to be nearly free from the usually encountered uncertainties of temperature in pyrolysis experiments. Since it was desired to correlate our results with these data, a temperature correction of +27 °C has been applied to all data except the temperature scale of figure 1. A nearly constant correction of this magnitude is not unreasonable for apparatus of the present shape, in which radiant heat transfer predominates [8].

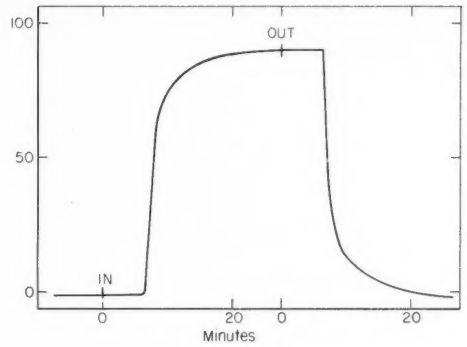

FIGURE 1. *Experimental detector response as a function of time.*
Time sample is placed in and taken out of γ-ray source is indicated.

2.2. Dosimetry

Dose rates were measured by cobalt glass dosimeters placed inside the furnace and exposed for measured times at several fixed sites. The ultimate calibration was referred to the Fricke ferrous sulfate dosimeter. The sources were a nominal 2000-Ci (curie) Co^{60} source and a 10,000-Ci source consisting of a cylindrical assembly of vertical pencil-shaped capsules, in a pool of water. Dose rates from somewhat idealized sources of this geometry are described mathematically in the literature [21]. At relatively small distances outside the source there appears to be little deviation from an inverse square relationship. Accordingly, the dose rate measurements were correlated by a plot of log (IX^2) against X_w, where I is the dose rate, X the distance from the center of the source, and X_w that part of the distance occupied by water. Such plots were nearly linear, with some downward curvature. The smooth-curve values were chosen as the dose rate at the given position.

Despite the considerable variation of distance within a circular sample, outside the source, the dose rate at its center can be shown to give good approximation to the dose rate averaged over sample area, and an excellent approximation if the square root of dose rate is averaged.

To estimate dose rate within the 10,000-Ci source, dosimeters were exposed at a variety of locations within the apparatus, and correlated with the aid of functions given in the literature [21], to obtain an average over the total sample. The measured values inside the source were about 20 percent lower than would be predicted from the values outside the source with the given mathematical description. The error may be in the dosimetry, as rather short exposure times were necessary, with large relative errors. Although the precision of individual measurements was never better than 5 percent, the relative values from the smoothed curve are presumably better.

The factor 0.526×10^{20} eV/g MR, derived from interpolated atomic absorption factors [22], was used to convert megaroentgens to eV/g in polytetrafluoroethylene.

Because the samples were quite thin, the dose rates in them may be subject to systematic errors associated with secondary electron equilibrium [22, 22a]. These errors may be nearly constant in a series of samples of the same thickness, but may vary with thickness. Considering the dimensions and materials, and neglecting the thickness of the helium atmosphere, 0.0002 to 0.0008 g/cm^3, the received dose will be higher than that computed from atomic absorption factors, and will be highest in the thinnest samples.

2.3. Product Analysis

In a number of instances the gases produced by the decomposition were collected in liquid nitrogen traps and analyzed by mass spectrometry and by vapor chromatography in a 60-cm column of silicone grease on Chromosorb at −80 °C.

A large excess of carbon dioxide was usually found, which was greatly reduced but not eliminated by the provision of a liquid nitrogen guard trap following the collection trap. The weight increase in the collection trap usually exceeded the weight loss of the polymer, presumably because of backward diffusion of atmospheric water and carbon dioxide. The chromatographic method employed produced relatively poor resolution: C_2F_4 was separated almost completely from CO_2 but not from air or CF_4: C_3F_6 coincided with CO_2: and the complex mixture from atmospheric pressure pyrolysis of Teflon [17] yielded five distinct but not totally resolved peaks.

Used polymer samples were adherent to the trays and apparently uniform in thickness. This was checked in a few instances by measuring the thickness of residue plus supporting tray with a micrometer thickness gage. The used film was discolored to a medium brownish gray, with nearly black lines extending outward from the helium flow orifices.

2.4. Chlorine Fixation

The radiation-induced fixation of chlorine was also measured by exposing sample tubes containing about 1 g polytetrafluoroethylene film and 30 cm^3 chlorine gas at 200 torr (measured at 25 °C), in a furnace at a dose rate of 7.6 MR/h, to a total dose of 20 to 30 MR. A large excess of chlorine remained. The product was then heated for 2 h at 270 °C under vacuum to remove volatile chlorine compounds, the resultant weight loss being a few percent, and the residue was analyzed for chlorine.

3. Results

3.1. Rate of Reaction

In general summary, the radiation-produced increments in gas evolution were small absolutely, always a fraction of the total weight loss, and exhibited a low temperature coefficient. In the volatile products, the monomer C_2F_4 was a principal component at the higher temperatures investigated, but rarely the only component.

The results of the rate experiments are shown in figure 2 as logarithmic plots of the rate-difference due to radiation, $r-r_0$, s^{-1}, versus the reciprocal of absolute temperature, for each of several dose rates and sample thicknesses. It is evident that these values are all rather low, and that their temperature coefficient is small. Supplementary results outside the range of the figure, and usually of lower precision, are listed in table 2. Since the detector response goes approximately as the number of moles of gas regardless of identity, the correct units for $r-r_0$ may be regarded as

$$\frac{\text{moles total gas}}{\text{(base mole polymer) (sec)}}.$$

TABLE 2. *Radiation-induced decomposition of polytetrafluoroethylene; supplement to figure 2* [a]

Temp °C [b]	354.6	417.0	369.9	386.6	401.2	405.2
Dose rate, MR/h	0.22	0.22	7.66	7.66	7.66	7.66
Rate, $r-r_0$, $s^{-1} \times 10^7$	2.9	3.4	19	19	20	15

[a] Thickness of film, 0.0025 cm.
[b] Corrected, see "Experimental Procedure."

The method of operation made it possible to obtain with fair precision only the difference between the actual rate r and the thermal rate in the absence of radiation, r_0. Under the most favorable conditions recorder fluctuations seldom exceeded ±0.03 mV for periods of 1 h. At the flow rate most used, this is equivalent to $0.03 \times \frac{2.82}{w} \times 10^{-7}$ mol/(base mol) (s) where w is the sample mass in grams. The resultant uncertainty is about 0.24×10^{-7} s^{-1} for the samples 0.0025 cm thick (mass 0.33 g), about 1×10^{-7} s^{-1} for the 0.00062-cm samples, and 0.06×10^{-7} s^{-1} for the 0.01-cm samples. For less favorable periods these estimates should be multiplied three-fold to allow for occasional unexplained drifts. An additional error of 5 to 10 percent of the reported value may be expected for experiments not near the beginning or end of a sequence, where the weight of the sample at the time of the experiment was uncertain. The curves of figure 2 would be activation energy plots for the γ-ray induced reaction if the thermal rate r_0 were negligible and the product composition constant over the temperature interval. Since these conditions did not usually prevail, the curves constitute merely a device for displaying and interpolating results. Figures 3 and 4 illustrate the variation of rate difference with dose rate in a carefully controlled sequence of experiments on 0.0025-cm film at 402.5 °C. It is evident that the rate-difference, $r-r_0$, is not linear in either dose rate I or square root of dose rate. This appears to be generally true for the 0.0025-cm and 0.01-cm films at all temperatures, as far as the much more limited data go, but not for the 0.0006-cm films, for which the variation seems nearly linear in dose rate, table 3. In this table, reduction to constant temperature has not been attempted; by reference to figure 2, the corrections cannot be much greater than the experimental error.

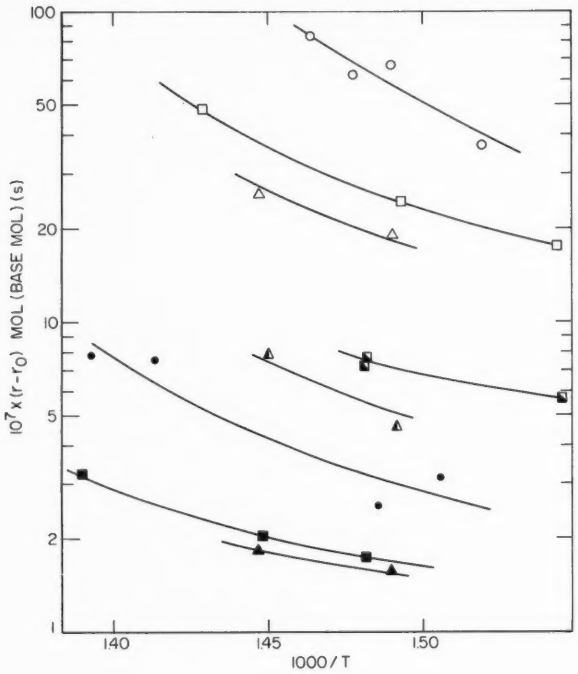

FIGURE 2. *Increments in gas evolution rate produced by radiation, $r - r_0$, as a function of temperature, dose rate and film thickness.*
Temperature uncorrected.

○ 7.66 MR/h, 0.0006 cm
□ 7.66 MR/h, 0.0025 cm
△ 7.66 MR/h, 0.01 cm
◪ 1.39 MR/h, 0.0025 cm
▲ 1.39 MR/h, 0.01 cm
● 0.22 MR/h, 0.0006 cm
■ 0.22 MR/h, 0.0025 cm
▲ 0.22 MR/h, 0.01 cm

TABLE 3. *Evolution of volatiles from 0.0006 cm film of polytetrafluoroethylene as a function of dose rate*

Temp, °C [a]	424.2	427.0	425.2	425.2	432	437
Dose rate, MR/h	0.144	0.22	0.337	0.644	2.2	7.66
$r - r_0$, s^{-1}, $\times 10^7$	1.6	2.5	3.9	5.3	12.9	88
$(r - r_0)/I$, $\times 10^7$	11	11	11	8	6	11

[a] Corrected, see "Experimental Procedure."

The thinnest samples are also exceptional with respect to $r - r_0$ considered as a function of sample thickness, figure 6.

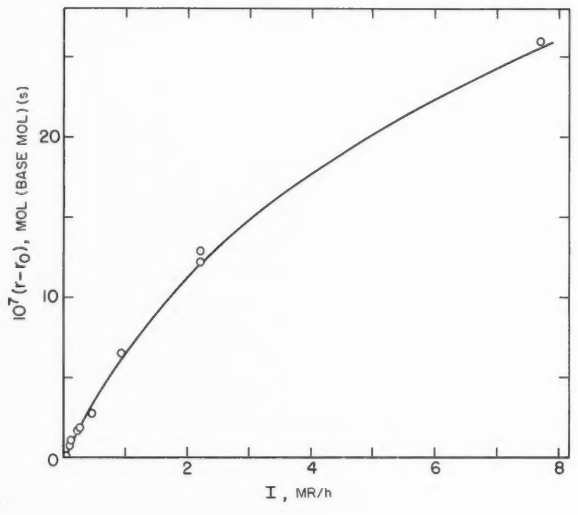

FIGURE 3. *Radiation increments in gas evolution rate from polytetrafluoroethylene, $r - r_0$ as a function of dose rate.*
Corrected temperature 429.5 °C: film thickness 0.0025 cm.

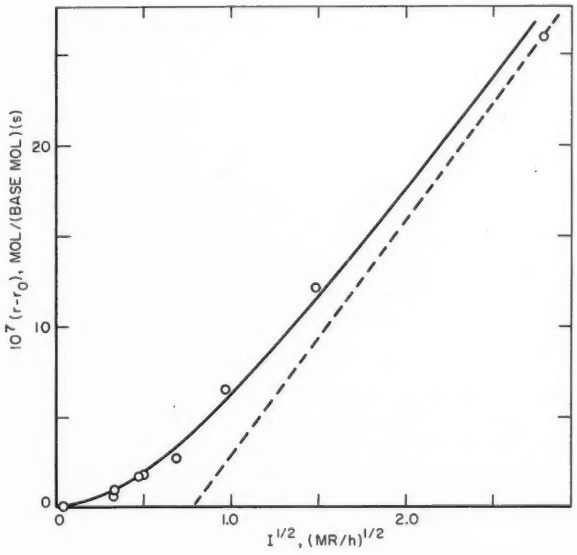

FIGURE 4. *Radiation increments in gas evolution rate from polytetrafluoroethylene, $r - r_0$, as a function of square root of dose rate.*
Corrected temperature 429.5 °C: film thickness 0.0025 cm. Theoretical hyperbola and asymptote, using parameters from figure 5. Equation of hyperbola is

$$\frac{(r - r_0 + 10.37 \times 10^{-7})^2}{(10.37 \times 10^{-7})^2} - \frac{(I^{1/2})^2}{(0.792)^2} = 1.$$

TABLE 4. *Weight loss and gas evolution rates* [a]

Temp, °C [b]	354.6	417	477.6	329	369.9	400	401	447	452
Dose rate, MR/h	0.22	0.22	0.22	7.66	7.66	7.66	7.66	7.66	7.66
Gas evolution, rate increment, mol/base mol · s, × 10^7	3.1	3.5	.....	15	21.7	20	21	30.4	37
Wt loss rate, s^{-1}, × 10^7 [c]	10±10 [d]	10±10 [d]	165±15 [d]	< 150	72	120	100	120	180
Units lost / mol gas	.....	.....	.....	< 10	3.3	6	4.8	4.0	4.9

[a] Sample thickness 0.0025 cm.
[b] Corrected, see "Experimental Procedure."
[c] Computed as $(1/t)\ln(w/w_0)$ for the period irradiated, exclusive of preheating.
[d] Limits estimated from assumed weighing error of 1 mg.

In table 4 the weight losses are compared with the rate-increment of gaseous product formation under various conditions. The weight loss is always several times the rate-increment measured by gaseous products. At the higher temperatures such large discrepancies can of course be explained by the existence of an appreciable thermal rate. At the lowest temperatures, the thermal rate is negligible and other factors are important. For example at 369.9 °C (corrected) and 7.66 MR/h the gaseous product rate increment was 21.7×10^{-7} s^{-1}, the observed weight loss rate 72×10^{-7} s^{-1} and the thermal weight loss rate, from the literature [7], should be 2×10^{-9} s^{-1}. Hence, the large ratio of weight loss to gas molecule production at this temperature must depend entirely upon the predominance in the product of unknown molecules much larger than monomer.

3.2. Products of Reaction

The mass spectra of collected volatile products were very complex, with mass peaks as high as 300 ($C_6F_{12}^+$), and defeated any attempts at full analysis. They also showed the presence of much carbon dioxide, 3 to 10 times as much as the maximum possible fraction of C_2F_4. Silicon tetrafluoride was absent except for a trace on one occasion. A large sample collected at 477.6 °C (corrected) and 0.22 MR/h was exceptional, consisting of C_2F_4 and 0.3 percent C_3F_6.

The large amount of CO_2 was probably a result of the trapping arrangements. This is supported by observations that the weight collected usually exceeded the polymer weight loss, and that the proportion of CO_2 was less in experiments with a second guard trap.

Other sources for some of the CO_2 require consideration. The analysis of the helium does not exclude 10^{-5} parts of O_2, and more could have diffused in through the 3 to 4 m of flexible tubing in the helium inlet line. From the quoted permeability of plasticized polyvinyl chloride [23] to oxygen, stated as 50 to 305 (cm^3) (mol)/(100 in^2) (24h) and the measured length (4m), diameter (0.75 cm), and wall thickness (0.19 cm), an amount equal to 1 to 10×10^{-10} mol/s^{-1} could have entered by diffusion, which if it reacts stoichiometrically, is equivalent to a rate of 0.3 to 3×10^{-7} s^{-1} in a 0.33 g sample. Golden [24] has reported and discussed a reaction of polytetrafluoroethylene with oxygen, forming COF_2 as a primary product, which can subsequently yield CO_2 and SiF_4 by reaction with glass or water. The failure to find SiF_4, as well as the low pressure at which any oxygen would be present, makes it unlikely that these reactions were important here. Possibly COF_2 could have been formed and reacted in the plastic part of the exit tube with small amounts of hydroxylic compounds or water, the resultant HF being totally absorbed in the plastic. It is assumed for the present that all the CO_2 found was of extraneous origin.

Another possible product from oxygen is the oxide $\overline{CF_2CF_2O}$, recently reported from the radiation-induced reaction of C_2F_4 and O_2 [25]; however, no trace of the corresponding fragment ions was found in mass spectra.

A few tentative conclusions may be drawn by considering the largest peaks of some of the mass spectra, table 5, in the light of the known cracking patterns of fluorocarbons [26]. The most important omissions in available cracking patterns are probably hexafluorocyclopropane, octafluorobutene-2 and the higher perfluoroolefins. The C_2F_3 peak is major for C_2F_4 and much smaller for other known fluorocarbons, the C_nF_{2n-1} and C_nF_{2n} peaks are large for a perfluoroolefin C_nF_{2n}, and the CF_3 peak is major in perfluoroparaffins and less important in perfluoroolefins.

Unless hexafluorocyclopropane and octafluorobutene-2 are present in large amounts and have large C_2F_3 sensitivities, the amount of C_2F_4 is probably not much lower than that computed from the sensitivity of C_2F_4 at this peak. The CF_3 peak height is

TABLE 5. *Relative intensities of mass spectra of volatiles produced from polytetrafluoroethylene (0.33 g) irradiated at the indicated temperatures* [a] *with 7.66 MR/h*

m/e, ion	Relative Intensities at		
	<360 °C	407 °C	462 °C
31 CF	1,550	300	390
44 CO_2	>10,000	2,190	2,610
50 CF_2	570	70	177
69 CF_3	2,310	234	198
81 C_2F_3	880	105	250
93 C_3H_3	132	45	36
100 C_2F_4	775	84	189
119 C_2F_5	280	29	22
131 C_3F_5	3,130	258	197
150 C_3F_6	184	13	14
181 C_4F_7	520	558	66
200 C_4F_8	126	7	7
231 C_5F_9	98		
250 C_5F_{10}	21		
281 C_6F_{11}	33		
300 C_6F_{12}	5		

[a] Corrected.

too small to accommodate any large proportion of perfluoroparaffins. Provisional constructions based on C_2, C_3, and C_4 olefins and perfluorocyclobutane are roughly compatible with the analyses suggested in table 6.

TABLE 6. *Decomposition products*

Temperature °C [a]	Mole percent in non-CO_2 portion				
	C_2F_4	C_3F_6	$i-C_4F_8$	$1-C_4F_8$	$cy-C_4F_8$
407 [b]	40	13	18	28	1
462 [b]	63	9	13	11	3
487 [c]	97	3			

[a] Corrected.
[b] Dose rate 7.66 MR/h, thickness 0.0025 cm.
[c] Dose rate 0.22 MR/h, thickness 0.01 cm.

Vapor chromatography was complicated by the large amounts of CO_2, which was not removed chemically. The overlap of CO_2 and C_3F_6 is almost complete, and because of the long tail region of CO_2 and great breadth of higher component peaks one can only say that no higher olefin amounted to as much as 10 percent of the CO_2, i.e., 100 percent of the C_2F_4. A clear separation of C_2F_4 and CO_2 was effected; however, any CF_4 would appear with C_2F_4. Air, which could also interfere, was removed by degassing at 77 °K. The principal utility of the chromatograms was to demonstrate that C_2F_4 was indeed present, and that its ratio to CO_2 was about that estimated from mass spectra.

The product composition showed no clear trend with dose rate or radiation history up to 100 MR, although such trends should exist. The only persistent correlation was with temperature; the mass spectral data suggest, for the non-CO_2 portion, about 40 percent C_2F_4 at 407 °C, 60 percent C_2F_4 at 462 °C, and nearly 100 percent C_2F_4 at 487 °C.

The product compositions and their trend with temperature introduce errors of the order of 50 percent into the rate data. Corrections for this appear futile, in view of the inexactness of the composition results, the slowness of the trend with temperature, and especially the lack of any demonstrable variation with dose rate. At temperatures below the range of figure 2, the complexity is too great for kinetic treatment. It is curious that despite this complexity, no waxlike deposits of high-molecular-weight products were ever found in the cooler regions of the decomposition chamber.

3.3. Chlorine Fixation

The *G*-value computed from fixation of chlorine in the polymer by radiation was 3.0 ± 0.1 atoms of chlorine fixed per 100 eV absorbed, at temperatures of 327, 340, and 380 °C. A thermal chlorination blank at 327 °C was negligible. The polymer strips were unchanged in appearance in the thermal blank, but melted in the radiation experiments. The *G*-value for chlorine absorption may be somewhere near that for creation of radicals escaping the primary cage.

4. Discussion

4.1. Kinetics

Assuming random initiation and moderate zip length and permitting monomer only to evaporate, one can derive the following rate expression for the process of decomposition

$$\frac{dM}{dt} = k_2 R_T \tag{3}$$

where dM/dt is the moles of monomer evaporated per second from a sample containing R_T moles of polymer radicals. Since this is an open system and the sample volume, which is decreasing, is proportional to weight, the formulation depends to some extent on the concentration units used in bimolecular steps. For our purpose we choose R as moles of radicals per cm³. Then the steady condition is written

$$k_1 \sum nQ_n = k_4 R^2 \tag{4}$$

where Q_n is now moles of polymer molecules per cm³. The $\sum nQ_n$ is simply ρ/m where ρ is the density and m the monomer molecular weight. The radical concentration is then

$$R = \left(\frac{k_1}{k_4}\frac{\rho}{m}\right)^{1/2}$$

and

$$\frac{dM}{dt} = k_2 RV = k_2 R \frac{W}{\rho} = k_2 R \frac{m \sum nQ_n(t)}{\rho}.$$

Since

$$\sum nQ_n(t) = [1-C] \sum nQ_n(0),$$

$$r_0 = (1-C)\frac{dC}{dt} = \frac{1}{(1-C)\sum nQ_n(0)}\frac{dM}{dt} = k_2 \left(\frac{k_1}{k_4}\frac{m}{\rho}\right)^{1/2} \text{s}^{-1}. \tag{5}$$

If conditions are such that initiation does not occur thermally but is induced photochemically or by ionizing radiation, and if the character of all species involved is unchanged, then the steady state condition, eq (4) is replaced by

$$\Phi I \sum nQ_n = k_4 R^2$$

where I is the intensity of radiation.

The resulting rate becomes

$$r_\gamma = k_2 \left(\frac{\Phi}{k_4}\frac{m}{\rho}\right)^{1/2} I^{1/2} \text{ s}^{-1}. \tag{6}$$

The ratio $r_\gamma I^{-1/2}$ should be independent of intensity. The constant Φ is derivable from the quantum yield or the radiation G-value for radical formation, and is normally almost independent of temperature.

From the comparison of r_0 and r_γ, the thermal and the radiation rates, a number of facts concerning the elementary reaction steps may be deduced. Thus the thermal initiation rate is given by the relation

$$\frac{r_0^2}{(r_\gamma I^{-1/2})^2} = \frac{k_1}{\Phi} \tag{7}$$

i.e.,

$$k_1 = \Phi \frac{r_0^2}{(r_\gamma I^{-1/2})^2} \tag{8}$$

and all the activation energies can be obtained with the aid of bond dissociation energies and thermochemical information.

In the present instance, at least two complications are present: (a) the initiation process is not the same for gamma-ray and thermal initiation, and (b) the thermal rate is appreciable.

4.2. Mechanism of Initiation and Termination

In thermal initiation, the C–F bond strength is great enough [27] so that only C–C splitting need be considered. Therefore, we write $Q \rightarrow 2R$, where R stands for $\sim CF_2CF_2\cdot$. Radiation seems to produce radicals by two reactions

$$Q \xrightarrow{\alpha I} 2R$$

$$Q \xrightarrow{\beta I} R_{II} + F$$

where R_{II} stands for the structure $\sim\dot{C}F_2CFCF_2\sim$ The evidence for R_{II} is old and direct [28] while that for R depends upon subtractions and upon identification of an oxygen reaction product $\sim CF_2CF_2O$. [29, 30]. Separation of the pairs R, generated thermally or by process α, may be strongly hindered by cage effects, whereas in process β separation of F from R_{II} could be much easier. Thus, although the bond scissions in the radiation processes α and β may be temperature independent, both the separation of radicals and the recombination reactions can be diffusion limited and thus in principle temperature dependent. For a diffusion-limited combination $A+B$. Smoluchowski [31] has shown that the second-order rate constant is proportional to $\frac{1}{2}(D_A+D_B)$, i.e., to the sum of diffusion constants. Since F is of small volume (cf. Ne, N) and highly mobile, not only the separation efficiency of F but the combination rate of F with large radicals will be very large, ($\propto \frac{1}{2}D_F$), while that for R + R will be much smaller. There is thus no necessary equivalence between the thermal and radiation processes, in either initiation or termination, and complete temperature independence of radiation initiation is doubtful. In special circumstances both the equivalence of species and the temperature independence of radiation initiation can be valid.

Two contributing circumstances can be noted. For termination, Siegle, Muus, Lin, and Larson [6] have postulated the reaction $R + R \xrightarrow{k_{4a}} S + U$ where S is a saturated molecule and U an olefinic molecule of polymer. The radical R_{II} should also decompose at a rate which is comparable with propagation

$$R_{II} \longrightarrow U + R$$

$\sim CF_2CF_2\dot{C}FCF_2CF_2CF_2\sim \longrightarrow \sim CF_2CF_2CF{=}CF_2 + \cdot CF_2CF_2\sim$, and is therefore rapid if there is a chain process at all. Therefore, the decomposition of R_{II} can produce as many olefinic groups as initiation process β produces F atoms. If the termination of Siegle et al., occurs to an appreciable extent, olefinic groups will accumulate more rapidly than F atoms. It is likely that the addition of F to a double bond occurs with near zero activation energy (cf cases involving Cl [32]) and at a rate roughly comparable to combination. Ultimately the large number of olefinic groups U will compete successfully with all radicals to consume nearly all F and produce further radicals R almost quantitatively. These processes with initiation β, in the presence of olefins, can produce 2R, not in a cage, and almost no F. Other processes which compete similarly with $R + F \longrightarrow S$ may be $F + \sim CF_2 - CF_2\sim \longrightarrow \sim CF_3 + \cdot CF_2$ [33]; $F + CF_2{=}CF_2 \longrightarrow CF_3CF_2\cdot$; and F (polymer melt) $\longrightarrow$ F (vapor). The combination F + F can be neglected, because of the low bond energy of F_2, 37 kcal [27], favoring dissociation at high temperature and low total concentration, and the low or zero activation energy for numerous reactions with F_2. If termination is by combination exclusively, but R_{II} decomposition is complete, more complex quadratic relations prevail among the several concentrations. Including the thermal rate of initiation $k_1(Q)$ and denoting the rates of processes α and β by $\alpha(Q)I$ and $\beta(Q)I$, it is probably safe to assert the inequality

$$\frac{[k_1+\alpha I][Q]}{k_4} < [R]^2 < \frac{[k_1+(\alpha+\beta)I][Q]}{k_4}.$$

To the extent that F atom reactions occur they may reduce the pair correlation, cage effect, and temperature dependence involved in the coefficient α.

4.3. Radiation Initiation Rate

Experimentally, the constant G-value of 3.0 for chlorine absorption suggests that in the temperature range 325 to 380 °C some sort of initiation process is temperature-independent.

This experimental G-value refers to some unknown composite of the reactions:

$$Q \longrightarrow > 2 \sim\sim CF_2\dot{C}F_2\cdot$$

$$Q \longrightarrow > \sim\sim CF_2CFCF_2 \sim\sim + F\cdot$$

$$\sim\sim CF_2\dot{C}FCF_2\sim\sim \longrightarrow > \sim\sim CF=CF_2 + \cdot CF_2\sim\sim$$

$$\sim\sim CF_2CF_2\cdot + Cl_2 \longrightarrow > \sim\sim CF_2CF_2Cl + Cl$$

$$\sim\sim CF_2\dot{C}FCF_2\sim\sim + Cl_2 \longrightarrow > \sim\sim CF_2CFClCF_2\sim\sim + Cl$$

$$\sim\sim CF=CF_2 + Cl_2 \longrightarrow > \sim\sim CFClCF_2Cl$$

Losses from scission of C–Cl bonds were presumably reversed by the excess chlorine present. An increased rate of scission at sites adjacent to C–Cl bonds could have raised the overall scission rate in the sample, but the published rates of pyrolysis of polychlorotrifluoroethylene [34, 35] suggest that this increase would be moderate for the temperatures and times used. At the low Cl_2 concentrations soluble in polytetrafluoroethylene at 300 to 400 °C, the uptake of Cl must be a measure only of radicals which have escaped the primary cage. Propagation reactions should not interfere with the measurement unless chains are completely consumed; the only requirement is that reaction with Cl_2 shall compete successfully with termination.

If radicals R_{II}, $\sim\sim CF_2\dot{C}FCF_2\sim\sim$ do not decompose to R, then G(Cl) measures $[2\alpha+\beta][Q]$ in the notation used earlier. If they decompose quantitatively according to

$$R_{II} \longrightarrow > R + U$$

$$\sim\sim CF_2CFCF_2\sim\sim \longrightarrow > \sim\sim CF=CF_2 + \cdot CF_2\sim\sim$$

and the products combine with chlorine to yield $\sim\sim CFClCF_2\,Cl + ClCF_2\sim\sim$, then G(Cl) measures $[2\alpha+3\beta][Q]$.

Other estimates of the G-value for radical formation in polytetrafluoroethylene, principally at room temperature, vary between 0.2 and 10 [14, 15, 36].

With reservations, the radiation initiation rate will be consolidated as $\Phi\frac{\rho}{m}I$ and it will be considered tentatively as temperature-independent and equal to the experimental chlorine absorption,

i.e., $$\left(\frac{d\,Cl}{dt}\right)_{\text{experimental}} = 2\Phi\frac{\rho}{m}I.$$

4.4. Reduction of Experimental Data for Mixed Thermal and Radiolytic Initiation

The data of figures 2 to 4 and table 1 are differences $r-r_0$ of the actual rate r and the thermal rate r_0. The composite initiation rate is represented by

$$k_1\sum nQ_n + \Phi I\sum nQ_n. \tag{9}$$

The total decomposition rate is

$$r=\frac{k_2(k_1+\Phi I)^{1/2}}{}\left[\frac{m}{k_4\rho}\right]^{1/2} \tag{10}$$

therefore,

$$r-r_0=r_0\left(1+\frac{\Phi}{k_1}I\right)^{1/2}-r_0.$$

The relation between the photo increment $r-r_0$ and $I^{1/2}$ describes a hyperbola which has an asymptote

$$r-r_0=r_0\left(\frac{\Phi}{k_1}\right)^{1/2}I^{1/2}-r_0. \tag{11}$$

The asymptote has the slope $r_0\left(\frac{\Phi}{k_1}\right)^{1/2}$ and intercepts at $I^{1/2}=\left(\frac{k_1}{\Phi}\right)^{1/2}$ and $(r-r_0)=-r_0$. Thus both the thermal rate and the ideal radiation rate parameter, eq (6) $r_\gamma I^{-1/2}=r_0\left(\frac{\Phi}{k_1}\right)^{1/2}$ can be isolated. In figure 4 a reasonable correspondence to the hyperbola

$$\frac{(r-r_0+10.37\times10^{-7})^2}{(10.37\times10^{-7})^2}-\frac{(I^{1/2})^2}{(0.792)^2}=1$$

is seen.

If the hyperbola of figure 4 does not include numerous points at high $I^{1/2}$, determination of the asymptote is unsatisfactory, and moreover the form is not well distinguished from a parabola. Since the initiation rates are to the half power in the rate expression it also follows that r_γ the pure γ-ray initiation fractional rate of monomer volatilization is related to the total and thermal rates by the expression

$$r_\gamma^2=r^2-r_0^2 \tag{12}$$

Using eqs (5) and (10)

$$r_\gamma^2=\frac{k_2^2}{k_4}\frac{m}{\rho}(k_1+\Phi I)-\frac{k_2^2}{k_4}\frac{m}{\rho}k_1$$

$$=\left[\frac{k_2^2 m}{k_4\rho}\right](\Phi I). \tag{13}$$

Factoring the right side of eq (12) permits the formulation

$$r-r_0=r_\gamma^2/(r+r_0) \tag{14}$$

$$r+r_0=r_\gamma^2/(r-r_0)$$

or

$$r-r_0=-2r_0+\frac{r_\gamma^2}{(r-r_0)}.$$

Rearranging and inserting the expression (eq (13)) for r_γ^2 we obtain

$$r-r_0=-2r_0+\frac{k_2^2}{k_4}\frac{m}{\rho}\frac{\Phi I}{(r-r_0)}. \qquad (15)$$

If $r-r_0$ is plotted against $\left(\frac{I}{r-r_0}\right)$, a straight line is obtained. The ideal radiation rate parameter $r_\gamma I^{-1/2}=r_0\left(\frac{\Phi}{k_1}\right)^{1/2}$ is given by the square root of the slope, and the thermal rate r_0 by one-half the negative intercept. The difficulty with this type of plot is that at low $r-r_0$ the error in the abscissa $I/r-r_0$ is very large. Within the large error figure 5 appears to constitute the required line. The value of the negative intercept is somewhat uncertain because of the long extrapolation: therefore, r_0 is not accurately determined. An algebraically equivalent value of r_0 can also be obtained as half the product of the slope and the intercept on the $(I/r-r_0)$ axis.

Plots similar to figure 5 were made for various temperatures and film thicknesses, utilizing the data of figure 2. They suggest a trend to upward curvature, difficult to establish because of the few points and large associated errors.

If the radiation process involves radical pairs which remain correlated throughout their lifetimes, r_γ and $r-r_0$ should be linear in I. Figure 3 shows that $r-r_0$ is not. Likewise figure 4 should be a parabola, which is more difficult to disprove, and figure 5 should be a vertical straight line. The possibility of some linear component, either from correlated pairs or molecular processes, is difficult to investigate. If the contributions are independent and the rate can be represented as

$$r=r_0\{(1+aI)^{1/2}+bI\} \qquad (16)$$

where $a=\Phi/k_1$ it is possible to develop $r-r_0$ and such ratios as $(r-r_0)/I$, $(r-r_0)I^{-1/2}$ as series in I or $I^{1/2}$, for low and high values of aI. In particular, a plot of $(r-r_0)I^{-1/2}$ versus $I^{1/2}$ has a limiting slope r_0b and a high dose asymptote with an intercept on the Y-axis equal to $r_0a^{1/2}$. The data of figure 4, treated in this fashion, did not indicate a large linear component.

The rate data for film 0.0006 cm thick (table 2) were anomalous and corresponded to linear variation with dose rate.

The radiation rate constant $r_\gamma I^{-1/2}$ was evaluated for the 0.0025-cm film by two methods—from the square root of slope of plots like figure 5, and from the highest available two points on plots like figure 4. These results are assembled in table 7. For 0.0025 cm film, these data fit the equations

$$r_\gamma I^{-1/2}=6.24\exp(-21{,}200/RT)\ \mathrm{s^{-1}MR^{-1/2}h^{1/2}} \qquad (17)$$
(slopes of fig. 5 plots, first line of table 7)

$$r_\gamma I^{-1/2}=0.28\exp(-16{,}900/RT)\ \mathrm{s^{-1}MR^{-1/2}h^{1/2}} \qquad (18)$$
(highest two points of fig. 4, plots, second line of table 7)

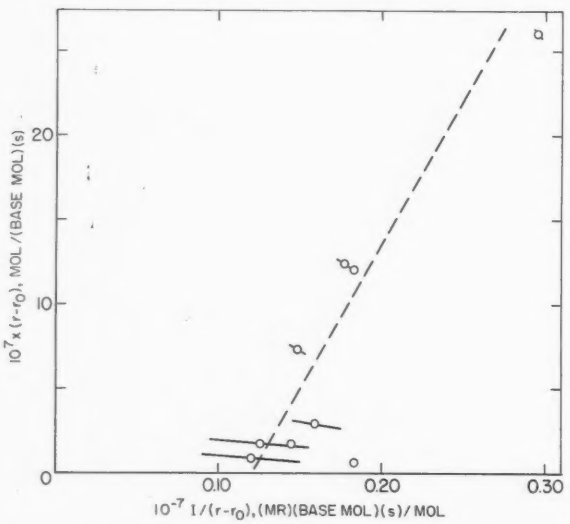

FIGURE 5. *Photo increment of rate of volatilization of polytetrafluoroethylene* $(r-r_0)$ *plotted as a function of* $I/(r-r_0)$, *see eq (15).*
Corrected temperature 429.5 °C.

TABLE 7. *Pure radiation rate constants for decomposition of polytetrafluoroethylene*

	Thickness, 0.0025 cm						
Temperature, °C [a]	403.2	420.5	429.5	429.5[d]	443.7	453.1	468.1
$10^7 r_\gamma I^{-1/2}$, $s^{-1}MR^{-1/2}h^{1/2}$ [b]	8.1	11.2	13.6	13.0	19.0	24.0	43.3
$10^7 r_\gamma I^{-1/2}$, $s^{-1}MR^{-1/2}h^{1/2}$ [c]	8.8	12.2	14.6	10.7	17.0	20.3	35.6

[a] Corrected, see "Experimental Procedure."
[b] From square root of slope, as in figure 5.
[c] From two points at high dose rate, as in figure 4.
[d] Data from figures 4 and 5; all others interpolated from figure 2.

4.5. Thermal Initiation

The rate of thermal initiation may be computed if the description outlined in eqs (6), (12), and (17) or (18) is valid. By eq (8)

$$k_1=\Phi r_0^2(r_\gamma I^{-1/2})^{-2}.$$

The rate parameter Φ for radiation initiation is estimated from the polymer density, the polymer segment molecular weight, and the experimental G-value for chlorine absorption. The refined representation de-

veloped by Siegle, Muus, Lin, and Larsen [6] can be rewritten with little loss of accuracy

$$\frac{\rho}{m}10^3 = 5.25 \exp(1393/RT) \text{ mol/liter } 750 > T\,^\circ\text{K} > 650.$$

For present purposes the value at 400 °C will be used, neglecting temperature variation, viz,

$$\frac{\rho}{m}10^3 = 14.38 \text{ mol/l.}$$

From the experimental $G(\text{Cl}) = 3.0$, and the estimated [22] relation for polytetrafluoroethylene, 1 MR $= 0.526 \times 10^{20}$ eV/g the value of Φ becomes

$$\Phi = 3.64 \times 10^{-8} \text{s}^{-1}\text{MR}^{-1}\text{hr.} \qquad (19)$$

By combining eqs (17) and (19) with Madorsky's [7] thermal rate,

$$r_0 = 4.7 \times 10^{18} \exp\{-80{,}500/RT\} \text{ s}^{-1} \qquad (5)$$

the resulting thermal initiation rate is,

$$k_1 = 2.07 \times 10^{28} \exp\{-118{,}600/RT\}\text{s}^{-1}. \qquad (20)$$

A similar estimate utilizing eq (18) in place of eq (17) yields

$$k_1 = 1.0 \times 10^{30} \exp\{-127{,}200/RT\}\text{s}^{-1}. \qquad (21)$$

Substitution of the thermal rate equation of Siegle, Muus, Lin, and Larsen [6] will yield nearly the same results. Both the activation energy and the preexponential factor are remarkably high, the preexponential factor being outside the range of usual experience.

4.6. Propagation

Activation energies of other steps can be computed from eqs (5), (17) or (18), (19) or (20), and the known bond dissociation energy [27] and equilibrium-pressure relationships [6]

$$E_0 = E_2 + \frac{1}{2}E_1 - \frac{1}{2}E_4$$

$$E_\gamma = E_2 - \frac{1}{2}E_4.$$

From Bryant's C–C bond dissociation energy [27]

$$D_{\text{C-C}} = E_1 - E_4 = 81.5 \text{ kcal}$$

$$E_2 = E_0 - \frac{1}{2}D_{\text{C-C}} = 80.5 - 40.75, \text{ or } 39.75 \text{ kcal,}$$

independent of the present radiation results.

$$E_4 = 2\left\{E_0 - \frac{1}{2}D_{\text{C-C}} - E_\gamma\right\}$$

$$= 2\{80.5 - 40.75 - 21.2\}$$

$$= 37.10 \text{ kcal,}$$

where $E_\gamma = 21.2$ kcal is derived from eq (17). Utilizing eq (18), the corresponding E_4 is 45.70 kcal. The value of $E_2 = 39.75$ kcal is in agreement with the equilibrium pressure relation [6] and heat of polymerization [27] and a reasonable allowance for the activation energy E_{-2} of the reverse propagation of 0 to 7 kcal.

$$E_2 = H_p + E_{-2}$$

$$= 37.57 + (0 \text{ to } 7) \text{ kcal.}$$

4.7. Termination

The value of $E_4 = 37.10$ kcal is in qualitative agreement with the concept that termination is diffusion-controlled and limited by the high melt viscosity. Melt viscosity measurements [37] have been variously interpreted to indicate that the activation energy for viscous flow is 36 kcal [37] or else [38] that below 365 °C it is about 25 kcal, and above this temperature it is 52 kcal, possibly with a chain-scission mechanism. It remains uncertain whether the apparent change near 365 or 380 °C is physical or chemical in nature, since a permanent degradation above 380 °C affects the measurements [39, 40].

More directly, the disappearance of radicals in irradiated polytetrafluoroethylene at temperatures up to 220 °C [41] appears to fit second-order rate expressions with relatively high activation energies

$$k = 6 \times 10^{13} \exp\{-30{,}000 \pm 3{,}000/RT\} \text{ liter/mol} \cdot \text{sec}$$
(amorphous phase, 46% crystalline sample) (22)

$$k = 6 \times 10^{17} \exp\{-40{,}000 \pm 4{,}000/RT\} \text{ liter/mol} \cdot \text{sec}$$
(crystalline phase, 46% crystalline sample) (23)

$$k = 6 \times 10^{26} \exp\{-65{,}000 \pm 5{,}000/RT\} \text{ liter/mol} \cdot \text{sec}$$
(crystalline phase, 74% crystalline sample). (24)

Although the radical species is presumably $\sim\!\!\sim\text{CF}_2\text{CFCF}_2\sim\!\!\sim$ rather than $\sim\!\!\sim\text{CF}_2\cdot$, the barriers to diffusion and recombination should be similar, especially in the amorphous phase.

By assuming one of these equations as a description of $2k_4$ a rough estimate of k_2 can be obtained by way of eq (8), which implies

$$k_2 = (r_\gamma I^{-1/2})\left[\frac{\rho}{m}10^3\right]^{1/2}\Phi^{-1/2}k_4^{1/2}. \qquad (25)$$

Substitution of

$$r_\gamma I^{-1/2} = 6.24 \exp\{-21{,}200/RT\} \quad (17)$$

$$2k_4 = 6 \times 10^{13} \exp\{-30{,}000/RT\} \quad (22)$$

and $\left[\frac{\rho}{m} 10^3\right] = 14.38$, $2\Phi = 7.29 \times 10^{-8}$, as previously used, gives

$$k_2 = 7 \times 10^{11} \exp\{-36{,}200/RT\} \text{ sec}^{-1} \quad (26)$$

which is close to the a priori estimate of Siegle, Muus, Lin, and Larsen [6]

$$k_2 = 10^{13} \exp\{-36{,}800/RT\}.$$

Comparisons involving the depolymerization equilibrium [6] and the measured propagation rate in polymerization [11] would require knowledge of monomer solubility in the polymer melt.

4.8. Kinetic Chain Length

The kinetic chain length, Y, propagations/initiations is given by

$$Y = \frac{k_2 R}{2\left(k_1 \sum nQ_n + \Phi \sum nQ_n I\right)} = \frac{r}{2(k_1 + \Phi I)}. \quad (27)$$

Table 8 lists a few values of Y computed from r_0 (eq (1)), $r - r_0$ (fig. 2 with corrected temperatures), k_1 (eq (20)) and Φ (eq (19)). Thermal kinetic chain length at high temperature are much less than the estimates of Siegle et al. [6], e.g., 13 instead of 720 at 480 °C. Approximate equations for the thermal kinetic chain length Y_0 and the fictitious radiation chain length neglecting thermal initiation Y_γ are,

$$\log_{10} Y_0 = -9.958 + 8320/T \quad (28)$$

$$\log_{10} Y_\gamma = 7.932 - 4640/T - \tfrac{1}{2} \log_{10} I. \quad (29)$$

In all the radiation experiments, the kinetic chain length is small. At low temperatures the chain length can be great only at extremely low dose rates, involving immeasurably low decomposition rates, while at high temperatures it is small because of extensive thermal initiation.

TABLE 8. *Kinetic chain lengths for polytetrafluoroethylene decomposition*

Temperature, °C	496	480	468	417	394
Y, 0 MR/h, thermal	8	13	18	132	350
Y, 0.22 MR/h	.....	13	20	19	10
Y, 7.66 MR/h	.....	13	16	4	3

4.9. Molecular Weight as a Function of Conversion

The molecular weight changes given by these authors then imply not that the chain length is long, but that termination occurs almost exclusively by combination. To show this, let $Q(t)$ = the total moles of polymer molecules in $W(t)$ g of sample. $\overline{M}_n(t) = m\overline{P}(t)$ = the number average molecular weight, where m is the monomer molecular weight and $\overline{P}(t)$ is the number average degree of polymerization. The sample volume is given by $V(t) = W(t)/\rho$: the conversion to volatiles by $C = 1 - W(t)/W(0)$.

The rate constants and kinetic parameters are k_1, k_2, k_3, k_4, k_{4a}, r, and Y, as used previously. Radical concentration, mol/cm³, is denoted by $[R]$, and r = fractional weight loss rate, s^{-1}, Y = kinetic chain length, $k_2[R]/k_{40}[R]^2$. Also let $k_{40} = k_4 + k_{4a}$, and $\sigma = \frac{k_3[R]\rho/m}{2k_{40}[R]^2}$, the chain transfer constant.

A constant steady-state radical concentration is maintained as in eq (4):

$$[R]^2 = \frac{k_1}{k_{40}} \frac{\rho}{m}.$$

By virtue of the constant fractional weight loss rate r

$$V(t) = \frac{W(t)}{\rho} = \frac{W(0)}{\rho} e^{-rt}$$

$$= \frac{W(0)}{\rho} e^{-2k_1 Yt}.$$

The total number of polymer molecules is left unchanged by initiation and combination, and increased by one by disproportionation and by chain transfer. Therefore,

$$Q(t) = Q(0) + \int_0^t \left(k_{4a}[R]^2 + k_3[R]\frac{\rho}{m}\right) V(t)dt.$$

Noting that

$$k_{4a}[R]^2 + k_3[R]\frac{\rho}{m} = k_{40}[R]^2 \left(\frac{k_{4a}}{k_{40}} + \frac{k_3[R]\frac{\rho}{m}}{k_{40}[R]^2}\right)$$

$$= \frac{k_1 \rho}{m}\left(\frac{k_{4a}}{k_{40}} + \sigma\right),$$

$$Q(t) - Q(0) = \frac{k_1 \rho}{m}\left(\frac{k_{4a}}{k_{40}} + \sigma\right) \int_0^t \frac{W(0)}{\rho} e^{-2k_1 Yt}\, dt$$

$$= \frac{k_1 W(0)}{m}\left(\frac{k_{4a}}{k_{40}} + \sigma\right) \frac{1}{2k_1 Y}\left(1 - e^{-2k_1 Yt}\right)$$

$$= \left(\frac{k_{4a}}{k_{40}} + \sigma\right) \frac{W(0)C}{2mY}.$$

Since

$$Q(t)=\frac{W(t)}{\bar{M}_n(t)}=\frac{W(0)\{1-C(t)\}}{m\bar{P}(t)},$$

$$\frac{1-C}{\bar{P}(t)}-\frac{1}{\bar{P}(0)}=\left(\frac{k_{4a}}{k_{40}}+\sigma\right)\frac{C}{2Y}.$$

A plot of $\frac{1-C}{\bar{P}(t)}$ versus C should be linear, with a slope $\frac{1}{2Y}\left(\frac{k_{4a}}{k_{40}}+\sigma\right)$. From the data of Siegle et al. [6], one estimates for the slope the value 6.4×10^{-4}. The equation utilized previously [6] is somewhat unnecessarily imprecise and was derived assuming all termination to be by disproportionation. By substituting the chain length $Y=13$, it can be concluded, with reservations due to the large experimental error, that neither k_{4a}/k_{40} nor σ is much larger than 3×10^{-3}. Alternatively, the molecular weight changes cited could be a consequence of reaction with impurities. If each molecule of impurity reacts to generate a chain break, the number of moles of impurities that have reacted at 16 percent conversion is given by

$$Q(0.16)=Q(0)+x$$

$$x=\frac{W(0)\,(1-0.16)}{1.2\times10^6}-\frac{W(0)}{9\times10^6}.$$

Thus, reaction of impurities to the extent $\frac{xm}{W_0}=5.9$ 10^{-5} of the number of moles of chain segments could also account for the observed molecular weight decrease at 16 percent conversion. Half of this reaction could have taken place before 4 percent conversion, as judged by the earliest experimental molecular weight. The present picture of low kinetic chain length and little, if any, disproportionation is consistent with many other observations in the literature, viz, the failure to observe disproportionation products in experiments with perfluoroalkyl radicals [43], and inhibition studies in which the polymer was decomposed in the presence of various gases and fluorine atoms [33]. The decomposition of polytetrafluoroethylene if carried out in the presence of a perfect inhibitor, i.e., a chemical species that reacted only with the radicals formed by random thermal initiation to produce a stable molecule, should exhibit a net random decomposition type of $\frac{dC}{dt}$ versus C curve [4], and the rate constant for the random decomposition should be identical to the thermal initiation constant for the thermal volatilization reaction studied here. Random decomposition can be shown to give a behavior characterized by a maximum in dC/dt at 26 percent conversion and in our case related to the rate constant by the expression

$$\left(\frac{dC}{dt}\right)_{max}\doteq k_1L/e,$$

where e is the base for the natural logarithm and L the critical size for evaporation [4]. Hydrogen appears to be the best inhibitor studied [33] showing a maximum in dC/dt, albeit not quite at $C=0.26$. Applying the above expression to the maxima of the earlier data [33] one obtains

$$k_1=10^{30.4}e^{-118{,}000/RT}$$

which is in very good agreement with the initiation constant deduced from the comparison of the thermal and γ-ray rates.

4.10. Diffusion Effect on Initiation and Termination

The large activation energy and pre-exponential factor for thermal initiation, A_1 and E_1, differ considerably from previous ad hoc speculations. The experimental values reported here are sensitive to experimental errors, as illustrated by the differences between eqs (20) and (21), and their validity depends upon the realization of the rather stringent conditions already discussed in connection with the initiation and termination in the presence of radiation. The high E_1 can be attributed to the need for diffusion of radicals out of the primary cage, comparable to the high-energy diffusion process governing E_4. The large preexponential factor, 4×10^{28}, is difficult to explain on the basis of diffusion out of the cage. For small molecules, the analysis of Rabinowitch [44], especially his eqs (8) and (3), leads to a fraction f escaping recombination

$$f=\frac{\dfrac{4D_0e^{-E_D/RT}}{a^2\gamma}}{\dfrac{4D_0e^{-E_D/RT}}{a^2\gamma}+\nu e^{\frac{\Delta S^*}{R}}e^{-E_C/RT}}. \tag{38}$$

Here $D_0e^{-E_D/RT}$ is the diffusion coefficient in obvious notation, a is the distance between lattice points in cm, γ is a ratio of total to ineffective lattice displacements, ν is a frequency close to the limiting Debye frequency $\cong5\times10^{12}$ sec^{-1} and E_C is the activation energy for combination within the cage, taken as zero. A factor $e^{\Delta S^*/R}$ has been inserted to allow for a possible entropy of activation for cage recombination.

If the fraction f is to be of Arrhenius form with the requisite preexponential factor,

$$f\approx\frac{10^{28}}{10^{14}}e^{-E_D/RT}$$

this requires

$$\frac{4D_0e^{-E_D/RT}}{a^2\gamma} \ll \nu e^{\Delta S^*/R}$$

and

$$\frac{4D_0}{a^2\gamma\nu e^{\Delta S^*/R}} \approx 10^{14}.$$

These conditions can be met only if $e^{-E_D/RT} \ll 10^{-14}$, which at 650 °K requires the excessively high $E_D > 83$ kcal. The second condition alone is impossible unless either D_0 is much greater than the ideal small-molecule value $D_0 = \frac{1}{2} a^2 n\nu$ given by Rabinowitch, or ΔS^* is large and negative.

Alternatively, the large A_1 could be explained by supposing that several bonds are loosened in the transition state. According to this view, the loosening effect contributes about 40 eu to the transition state for dissociation of ethane [45] and raises the pre-exponential factor to 10^{17}; in the present instance a contribution of about 80 eu is needed.

It is also conceivable that escape from the primary cage occurs mainly when dissociation is followed by one propagation step. Essentially this idea has been used to explain the transition from low-temperature radiolysis of petroleum products to a so-called radiation thermal cracking, the rate of which is proportional to dose rate but has a high activation energy [45]. Applied to thermal decomposition of polytetrafluoroethylene, the activation energy increment would be E_2 and the effective E_1 would be $D_{C-C} + E_2$, which is numerically not far from the E_1 deduced here. However, arguments similar to those for cage escape would require $A_{1C}A_2/A_{4C} \approx 10^{28}$, where the subscript C denotes cage reactions, and this cannot be met with "normal" preexponential factors. In general, the kinetics of these authors should not apply here, since, in polytetrafluoroethylene, decomposition to olefin, i.e., propagation, does not destroy a radical as in their system, but leaves it unchanged as a kinetic entity.

For related reasons, it is very difficult to devise kinetics of radiolysis involving "unzipping" for a kinetic chain length which is long but less than the degree of polymerization, which can result in decomposition linear in dose rate. The usual conclusion, that about half of the radical pairs escaping the primary cage will never recombine with their original partners [47, 48], implies that the steady-state concentration of all radicals, paired and unpaired, will be governed largely by bimolecular termination and thus go as the square root of dose rate. Perhaps a complex intermediate behavior could be observed in special situations.

4.11. Diffusion Effect on Propagation

The idea that the reverse propagation reaction

$$R_m + M \xrightarrow{k_{-2}} R_{m+1} \qquad (31)$$

could be a factor is suggested by the appreciable partial pressures of monomer existing in some of the present experimental work, and by the low values of the published thermodynamic equilibrium pressure [6]. The equilibrium pressures could be in error by a factor of ten. Preliminary arguments against reverse polymerization as a serious influence are

(1) At different helium flow rates, the partial pressure of monomer varied widely, but the observed rate of evolution remained approximately unchanged.

(2) The observed rates were nearly the same in 0.01- and 0.0025-cm sample thicknesses, despite the four-fold difference in monomer partial pressure.

(3) In the pyrolyses reported by Siegle et al. [6], the presence of excess monomer pressure, although it profoundly altered the product composition, reduced the rate of weight loss only by about 50 percent. At 380 °C, when polymerization should have been highly favored by thermodynamics, it proceeded only very slowly, although its reverse had measurable velocity in independent experiments in a vacuum. It is possible that the monomer concentration was actually maintained at a low level either by thermal dimerization (not favored at too low a pressure) [49] or by transfer to monomer

$$RCF_2CF_2\cdot + C_2F_4 \longrightarrow RCF{=}CF_2 + C_2F_5.$$

or

$$RCF_2CF_2\cdot + C_2F_4 \longrightarrow RCF_2CF_3 + C_2F_3.$$

which is only very slightly endothermic [27].

The problem of diffusion-limited monomer evolution in depolymerization has been treated by Cowley and Melville [1]. However, the possibility that reverse depolymerization occurs to an appreciable extent, arising from a buildup of the concentration of monomer in the bulk polymer, does not appear to have been treated explicitly.

The sample can be regarded as a slab of thickness l cm, with no flux of material through the bottom surface ($x=0$) and open at the top ($x=l$). This differs from the slab of Cowley and Melville [1] which corresponds to two such slabs assembled bottom to bottom. Monomer is generated within a volume element of 1 cm³ of the slab at a net rate

$$\frac{dM}{dt} = k_2[R] - k_{-2}[R][M],$$

where $[M]$ is monomer concentration, in units of mol/cm³, $[R]$ is radical concentration in the same units, the latter being constant throughout the slab, t is in seconds, k_2 is in s^{-1}, and k_{-2} is in $cm^3\ mol^{-1}\ s^{-1}$. Monomer at $x=l$ is in solubility equilibrium with monomer in the gas phase at a partial pressure p, with a Henry's Law constant S:

$$[M]_l = Sp.$$

The differential equation governing monomer concentration in the slab is then

$$\left(\frac{d[M]}{dt}\right)=D\left(\frac{\partial^2[M]}{\partial x^2}\right)+k_2[R]-k_{-2}[R][M] \qquad (32)$$

where D is the diffusion constant, cm²/s. The initial condition is $[M]=0$ everywhere and boundary conditions are

$$[M]=Sp \text{ at } x=l$$

$$\frac{[\partial M]}{\partial x}=0 \text{ at } x=0 \text{ (no flux).}$$

The steady-state solution, for $\frac{d[M]}{dt}=0$ is given by the usual methods for linear differential equations with constant coefficients.

$$[M]=\frac{k_2}{k_{-2}}+(Sp-k_2/k_{-2})\frac{\cosh\left\{x\left(\frac{k_{-2}[R]}{D}\right)^{1/2}\right\}}{\cosh\left\{l\left(\frac{k_{-2}[R]}{D}\right)^{1/2}\right\}}. \qquad (33)$$

The rate of monomer escape per unit area or flux out of the top surface is given, in mol/cm² s, by the usual condition applied at the surface $x=l$

$$F=\frac{ds}{dt}\Big)_{x=l}=-D\frac{\partial[M]}{\partial x}\Big)_{x=l}$$

where s refers to moles of monomer passing through a 1 cm² surface element in an imaginary plane at position x.

The rate per unit volume is given by AF/V, i.e., by F/l, and the rate per unit weight by $F/\rho l$, where A is the surface area, V the volume and ρ the density. Evaluation of the derivative amd multiplication give, as the rate in moles/(base mole)(sec)

$$\frac{D}{100\,\rho l}\left(\frac{k_2}{k_{-2}}-Sp\right)\left\{\frac{k_{-2}[R]}{D}\right\}^{1/2}\tanh l\left\{\frac{k_{-2}[R]}{D}\right\}^{1/2}. \qquad (34)$$

Utilizing the relationship between rate constants and equilibrium constants

$$k_{-2}/k_2=K_C=SK_p$$

and the composite parameter

$$Z=l(k_{-2}[R]D^{-1})^{1/2}=l(k_2[R]D^{-1}S^{-1}K_p^{-1})^{1/2}$$

the rate in moles/(base mole)(sec) is

$$\frac{k_2[R]}{100\,\rho}\left\{1-\frac{p}{K_p}\right\}\frac{\tanh Z}{Z}. \qquad (35)$$

Although p is related to the monomer evolution rate, gas flow rate and sample weight by an easily derived proportionally constant, the insensitivity of observed results to flow rate suggest that it is safe to neglect the term p/K_p.

For the case $p=0$, Carslaw and Jaeger [50] give a complete solution including the time-dependent behavior, which becomes identical with the equation of Cowley and Melville [7] upon proceeding to the limit of no reverse reaction.

The steady state in the limit of infinite thickness is easily derived from the general solution given above

$$[M]=SK_p\left\{1-\left(1-\frac{p}{K_p}\right)\exp\left(-x\left(\frac{k_2[R]}{DSK_p}\right)^{1/2}\right)\right\}. \qquad (36)$$

$$F=(k_2[R]DSK_p)^{1/2}\{1-Sp\} \qquad (37)$$

If p/K_p is negligible, the monomer concentration is within e^{-2} of its limiting value at a depth in cm

$$x=2\left(\frac{k_2[R]}{DSK_p}\right)^{-1/2} \qquad (38)$$

The corresponding time-dependent surface flux is

$$F=(k_2[R]DSK_p)^{1/2}\ \text{erf}\ (k_2[R]SK_p^{-1}t)^{1/2}$$

if $p=0$. This form may possibly apply at very low temperatures and great thicknesses, if monomer production alone is measured, but does not apply in the present experiments.

In the present work, the time-dependent region is masked by holdup of vapor in the reaction furnace, and the steady-state is reached before 20 min and perhaps long before this time. Thus the steady-state form eq (35) applies. The solid line in figure 6 shows a logarithmic plot of the ratio, rate/k_2R, as a function of Z, according to eq (35) with $p=0$. The experimental rate-differences, $r-r_0$, are shown on the same plot as a function of thickness at constant temperature and dose rate. A logarithmic plot of the rate r versus l should have the same shape as the curve, with coordinates shifted. It is seen that there is no correspondence with the curve. The use of the correct but somewhat uncertain r in place of $r-r_0$ would not appreciably alter the disagreement. Dose rate variations could be explored somewhat similarly if thermal initiation were negligible. The simplest explanation of the very high rate at a thickness of 0.0006 cm is a combination of uniform bulk rate b with a high surface rate a. A plot of rate versus thickness would be a hyperbola, $r=b+a/l$ which appears to be the variation encountered. The surface rate a could involve either the polymer-gas interface or the polymer-metal interface, as suggested by recent studies at much higher temperature [51].

It is conceivable that the observed surface rate is a result of a higher temperature in the thinner samples.

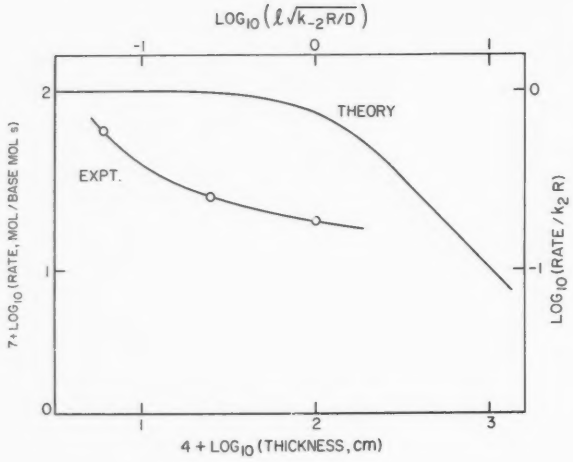

FIGURE 6. *Gas evolution rates as a function of sample thickness, eq (35).*

Upper curve, theoretical variation of r with thickness for rate limited by reverse reaction and diffusion. Lower curve experimental, $r - r_0$, for polytetrafluoroethylene at 429.5 °C, 7.60 MR/h.

Sample temperature is not easily controlled and measured with such thin films. The sample temperature is a function of many factors, heat of reaction, thermal conductivity of polymer, radiative heat transfer, heat capacity of the furnace, and others. Another reasonable mechanistic concept for the greater rate from the thin films is that the concentration of polymer radicals is greater as a result of a more rapid loss of small radicals whose only function would be in termination.

Although our rate studies indicate that diffusion and reverse reaction do not dominate the radiation-induced decomposition, it is very likely from the product compositions, table 6, that the process is appreciably perturbed by these influences and by side reactions not present in the usual thermal decomposition in a vacuum. At a low enough temperature these influences will be major. A rough estimate of these effects can be made with the aid of eq (38), which asserts that in a semi-infinite slab the monomer concentration is $1-e^{-2}$ of the equilibrium value at a depth $2K_c^{1/2}D^{1/2}(k_2[R])^{-1/2}$.

For temperatures low enough to avoid appreciable thermal initiation, $k_2[R] = r_\gamma \left[\frac{\rho}{m}\right]$ is taken from eq (17): in mol/cm³ s, this is approximately

$$9.0 \times 10^{-2} I^{1/2} \exp\{-21{,}200/RT\} \frac{\text{mol}}{\text{cm}^3\ \text{s}}. \qquad (40)$$

D is estimated from the room temperature value of Goldfarb et al. [42], and an activation energy in the range 8.4 to 14.6 kcal found for various gases in polytetrafluoroethylene [51]. Using the corrected value [42] of $D = 1.2 \times 10^{-8}$ cm²/s at 24 °C and taking $E_D =$ 9,000 cal, the estimate gives

$$D(T) = 5.2 \times 10^{-2} \exp(-9{,}000/RT). \qquad (41)$$

The solubility could be estimated similarly from the same sources.

A likely upper limit can be found by assuming ideal solubility in polymer segments and extrapolating the vapor pressure equation [53] far beyond the critical temperature [54]. On this basis the solubility S is

$$S = 5.2 \times 10^{-7} \exp(+3{,}965/RT)\text{mol/cm}^3\ ^{atm}. \qquad (42)$$

Combination with the thermodynamic equilibrium pressure data [6] yields

$$K_c = 4.37 \times 10^{1} \exp\{-31{,}735/RT\}\text{mol/cm}^3 \qquad (43)$$

over the range 390 to 480 °C. The depth for $C = K_c(1-e^{-2})$ is, by substitution in eq (38)

$$2.2\, I^{-1/4} \exp\{-9{,}700/RT\}\text{cm}. \qquad (44)$$

At a temperature of 340 °C and a dose rate of 1 MR/h, this is 8×10^{-4} cm, and films of this thickness would be approaching semi-infinite behavior, with a rate of monomer evolution dependent mainly upon surface area. Under these circumstances it is not surprising that the principal products observed at the lowest temperatures are complex mixtures, arising from termination and from side reactions.

5. Summary

The decomposition of polytetrafluoroethylene exposed to gamma radiation at dose rates of 0.1 to 7.6 MR/h appears to be a process with a relatively short chain length and a rate near 400 °C not many times greater than the thermal rate. The rate is essentially proportional to the square root of the dose rate and mutual termination occurs. The very low activation energy, 84kJ/mol for the γ-ray process indicates a very high activation energy for thermal initiation which is supported by earlier observations. It is unlikely that diffusion of the monomer through the polymer is hindered to such an extent that repolymerization is important. The deduced rate of thermal initiation has an abnormally high preexponential factor and a high activation energy, and the activation energy for termination is also high. The very short kinetic chain length and well-known independence of initial molecular weight together indicate that thermal initiation is random.

The short chain length and the previously observed molecular weight changes indicate that the termination step occurs nearly exclusively by radical combination. The observed decrease in DP over that anticipated for termination exclusively by combination can be the result of very small amounts of other processes such as disproportionation, transfer or impurities. At lower temperatures but above the melting transition, the γ-ray induced decomposition has little temperature dependence and the volatile

products are very complex and presumably the result of direct radiolysis. This complex low-temperature process is probably what was observed by Taubman and Ianova.

The authors thank Dr. C. A. Sperati and E. I. du Pont de Nemours & Co., for the molecular weight samples and data.

6. References

[1] P.R.E.J. Cowley and H. W. Melville, Proc. Roy. Soc. **A210,** 461 (1951): **A211,** 320 (1952).
[2] R. Simha, L. A. Wall, and P. J. Blatz, J. Polymer Sci. **5,** 615 (1950).
[3] R. Simha and L. A. Wall, J. Polymer Sci. **6,** 39 (1951).
[4] R. Simha and L. A. Wall, J. Phys. Chem. **56,** 707 (1952).
[5] H. B. Klevens and J. R. Platt, J. Am. Chem. Soc. **69,** 3056 (1947).
[6] J. C. Siegle, L. T. Muus, Tung-Po Lin, and H. A. Larsen, J. Polymer Sci. **A2,** 391 (1964).
[7] S. L. Madorsky, V. E. Hart, S. Straus, and V. A. Sedlak, J. Res. NBS **51,** 327 (1953) RP2461.
[8] S. L. Madorsky, J. Res. NBS **62,** 219 (1959) RP2957.
[9] S. L. Madorsky and S. Straus, J. Research NBS **64A** (Phys. and Chem.) No. 6, 513 (1960).
[10] S. L. Madorsky, Vacuum Microbalance Techniques, Vol. **2,** p. 56. (Plenum Press, Inc., 1962.)
[11] M. I. Bro, E. R. Lovejoy, and G. R. McKay, J. Appl. Polymer Sci. **7,** 2121 (1963).
[12] C. A. Sperati and H. W. Starkweather, Jr., Fortschritte der Hochpolymeren-Forschung **2,** 488 (1961): ibid, 472.
[13] J. A. Wethington, Jr., in Fluorine Chemistry, ed., Vol. 5, p. 282–294. J. H. Simons (Academic Press, New York, 1964).
[14] R. E. Florin and L. A. Wall, J. Res. NBS **65A** (Phys. and Chem.) No. 4, 384 (1961).
[15] R. E. Florin and L. A. Wall, SPE Trans. **3,** 293 (Oct. 1963).
[16] A. B. Taubman and L. P. Ianova, All Union Conference on Radiation Chemistry, Moscow 1957, p. 287, discussion 306: tr. Consultants Bureau Inc. pp. 271, 291.
[17] E. E. Lewis and M. A. Naylor, J. Am. Chem. Soc. **69,** 1968 (1947).
[18] A. Barlow, R. S. Lehrle, and J. C. Robb, Polymer **2,** 27 (1961).
[19] H. Purnell, Gas Chromatography, p. 278, Table 1 (Wiley & Sons, Inc., N. Y., 1962).
[20] H. H. Young, Jr. and L. P. Hammett, J. Am. Chem. Soc. **72,** 280, eq 2 (1950).
[21] J. G. Lewis, J. V. Nehemias, D. E. Harmer and J. J. Martin, Nucleonics **12,** [1], p. 40 (1954).
[22] Report of the International Commission on Radiological Units and Measurements (ICRU) 1956: NBS Handbook 62: pp. 10–17 (1956).
[22a] L. V. Spencer and F. H. Attix, Radiation Research **3,** 239 (1955).
[23] Modern Plastics Encyclopedia, 1963: Union Carbide Section, "Krene, cast, plasticized". (1963).
[24] J. H. Golden, J. Polymer Sci. **45,** 534 (1960).
[25] D. Cordischi, M. Lenzi, and A. Mele, Trans. Faraday Soc. **60,** 2047 (1964).
[26] F. L. Mohler, V. H. Dibeler, and R. M. Reese, J. Res. NBS **49,** 343 (1952) RP2370.
[27] W. M. D. Bryant, J. Polymer Sci. **56,** 277 (1962).
[28] H. N. Rexroad and W. Gordy, J. Chem. Phys. **30,** 399 (1959).
[29] T. Matsugashita and K. Shinohara, J. Chem. Phys. **35,** 1652 (1961).
[30] N. Tamura, J. Polymer Sci. **60,** 55 (1962).
[31] M. V. Smoluchowski, Z. Physik. Chem. (Leipzig) **92,** 102 (1917).
[32] E. W. R. Steacie, Atomic and Free Radical Reactions, 2d ed. ACS Monograph 125, Vol. **2** (Reinhold, New York, 1954), p. 670
[33] L. A. Wall and J. D. Michaelson, J. Res. NBS **56,** 27 (1956) RP2644: J. D. Michaelson and L. A. Wall, J. Res. NBS **58,** 327 (1957) RP2765.
[34] S. L. Madorsky and S. Straus, J. Research NBS **55,** 223 (1955) RP2624.
[35] L. A. Wall and S. Straus, J. Res. NBS **65A** (Phys. and Chem.) No. 3, 233 (1960).
[36] A. Nishioka, K. Matsumae, M. Watanabe, M. Tajima, and M. Owaki, J. Appl. Polymer Sci. **2,** 117 (1959).
[37] A. Nishioka and M. Watanabe, J. Polymer Sci. **24,** 298 (1957).
[38] L. C. Case, J. Appl. Polymer Sci. **3,** 254 (1960).
[39] A. V. Tobolsky, D. Katz, and A. Eisenberg, J. Polymer Sci. **A1,** 483 (1963).
[40] M. Takahashi and A. V. Tobolsky, Polymer Letters **2,** 129 (1964).
[41] Yu. D. Tsvetkov, Ya. C. Lebedev, and V. V. Voevodsky, Vysokomol. Soed. **3,** 887 (1961).
[42] I. J. Goldfarb, R. J. McHenry, and E. C. Penski, J. Polymer Sci. **58,** 1283 (1962): E. C. Penski, private communication: E. C. Penski and I. J. Goldfarb, Polymer Letters **2,** 55 (1964).
[43] G. O. Pritchard, G. H. Miller, and J. R. Dacey, Can. J. Chem. **39,** 1968 (1961).
[44] E. Rabinowitch, Trans. Faraday Soc. **33,** 1225 (1937).
[45] A. F. Trotman-Dickenson, Free Radicals, p. 38 (Methuen, London, 1959).
[46] A. M. Brodskii, K. P. Lavrovskii, and V. B. Titov, Kinetika i Kataliz **4,** 337 (1963).
[47] A. Kupperman, in The Chemical and Biological Action of Radiation, ed. M. Haissinsky (Academic Press, London, 1961), Vol. **5,** p. 123.
[48] R. M. Noyes, J. Am. Chem. Soc. **77,** 2042 (1955).
[49] B. Atkinson and A. B. Trenwith, J. Chem. Soc. **1953,** 2084 (1953).
[50] H. S. Carslaw and J. C. Jaeger, Conduction of Heat in Solids, 2d ed (Clarendon Press, Oxford, 1959), p. 404.
[51] H. H. G. Jellinek and H. Kachi, Am. Chem. Soc. Polymer Preprints **5,** [2], p. 375 (Sept. 1964).
[52] W. W. Brandt and G. A. Anysas, J. Appl. Polymer Sci. **7,** 1924 (1963).
[53] M. M. Renfrew and E. E. Lewis, Ind. Eng. Chem. **38,** 870 (1946).
[54] S. Glasstone, Textbook of Physical Chemistry, 2d ed., p. 702 (Van Nostrand, New York, 1946).

(Paper 70A2–387)

799-883 O-66—2

JOURNAL OF RESEARCH of the National Bureau of Standards—A. Physics and Chemistry
Vol. 70A, No. 2, March–April 1966

Effect of Some Halogenated Hydrocarbons on the Flame Speed of Methane

Carl Halpern

Institute for Applied Technology, National Bureau of Standards, Washington, D.C.

(November 17, 1965)

The effects of five halogenated hydrocarbons on the flame speed of methane have been studied. Bromides are more effective in reducing flame speeds than are chlorides and the reduction in flame speed is proportional to the amount of inhibitor added.

Key Words: Flame speed, combustion, inhibitor, halogenated hydrocarbon, bromide, chloride.

1. Introduction

Halogenated hydrocarbons have long been used to extinguish unwanted fires and a method of ranking the effectiveness of these compounds was wanted. In a previous paper [1],[1] the effect of a single inhibitor, methyl bromide (CH_3Br), on the flame speed of methane was studied. It was shown that the flame speed was very sensitive to the presence of methyl bromide and that the maximum flame speed for given experimental conditions decreased proportionally as the concentration of inhibitor increased. It appeared that the decrease in maximum flame speed could be used as a measure of the effectiveness of flame inhibitors.

In the present work, the effects of five additional inhibitors were studied. The inhibitors were bromotrifluoromethane, CF_3Br: dibromodifluoromethane, CF_2Br_2: methyl chloride, CH_3Cl: chlorotrifluoromethane, CF_3Cl; and dichlorofluoromethane, $CHFCl_2$.

2. Apparatus and Procedure

The apparatus and method of measuring flame speeds have been described in previous publications [1, 2]. Briefly, the apparatus consists of drying and metering sections for air and fuel and a nozzle, the exit of which is the port of the burner. Means are provided to measure and control the temperature of the combustible mixture. Flame speeds are determined by a total area method which is based on the measurement of the area of the schlieren image of the inner flame cone and on the measurement of the rates of flow of fuel and air.

Mixtures of inhibitor and dry air were prepared in a large steel tank and were metered by observing the pressure drop across a calibrated sharp-edged orifice. Some error is introduced since the orifice was calibrated for air, but in view of the small quantities of inhibitor used (maximum quantity was 0.5 percent, by volume, of the air), it was felt that the error would be tolerable.

Mixtures in air of 0.1, 0.2, 0.3, 0.4, and 0.5 percent, by volume, of each inhibitor were prepared. The variation of flame speed with mixture ratio[2] was determined for each mixture, the gas velocity at the nozzle remaining constant. Mixture ratio was varied from 0.054 to 0.072. (A stoichiometric mixture of methane and air is equivalent to mixture ratio 0.0583.)

Flame speeds of the 0.1 percent mixture of each inhibitor were determined at gas velocities measured at the port of the nozzle of 3, 4, 5 and 6 ft/s. This procedure was adopted to determine the variation of flame speed with gas velocity over an extended range. For all other mixtures, flame speeds were determined only at gas velocities of 4 and 5 ft/s.

[1] Figures in brackets indicate the literature references at the end of this paper.

[2] Mixture ratio is here defined as the weight of methane divided by the weight of air, or in the case of an inhibited mixture, as the weight of methane divided by the weight of air plus added inhibitor.

Variation of flame speed with initial temperature was determined for mixtures containing each inhibitor. Mixture ratio was 0.060; 0.2 percent of inhibitor was added to the air; and the gas velocity was 4 ft/s. The range of temperatures in these determinations was from 75 to 100 °F. Flame speed increased as the temperature increased and the change of flame speed with temperature was found to be linear. The results, together with values for methane and methane plus methyl bromide taken from previous work, are listed in table 1. These values were used to correct all flame speeds to 75 °F.

TABLE 1. *Variation of flame speed with initial mixture temperature*

Inhibitor	Feet per sec per °F
Methane [a]	0.00391
Methyl bromide [b]	.00328
Bromotrifluoromethane	.00329
Dibromdifluoromethane	.00200
Methyl chloride	.00322
Dichlorofluoromethane	.00199
Chlorotrifluoromethane	.00504

[a] Value for methane is taken from [2].
[b] Value for methyl bromide is taken from [7].

TABLE 2. *Maximum flame speeds*

Inhibitor	Flame speed	Inhibitor added	wt. CH_4 / wt. air + inhib.	Flame speed / Flame speed, CH_4 × 100	Gas velocity
	ft/s	%			*ft/s*
CF_3Br	1.208	0.1	0.0602	101.0	3
	1.196	.1	.0601	100.0	4
	1.171	.1	.0600	97.9	5
	1.166	.1	.0599	97.5	6
	1.068	.2	.0600	89.3	4
	1.061	.2	.0620	88.8	5
	1.012	.3	.0582	84.6	4
	1.016	.3	.0620	85.0	5
	0.932	.4	.0580	78.0	4
	[a].950	.4	.0620	79.4	5
	[b].857	.5	.0600	71.6	4
	[c].856	.5	.0640	71.6	5
CF_2Br_2	1.151	.1	.0580	96.2	3
	1.124	.1	.0581	94.0	4
	1.113	.1	.0621	93.0	5
	[d] 1.107	.1	.0601	92.6	6
	0.970	.2	.0581	81.1	4
	.977	.2	.0617	81.7	5
	[e].881	.3	.0600	73.6	4
	[f].844	.3	.0641	70.6	5
	[g].775	.4	.0620	64.8	4
	[h].638	.4	.0681	53.4	5
	[i].578	.5	.0661	48.3	4
	[j].500	.5	.0720	41.8	5
CH_3Cl	1.242	.1	.0600	103.9	4
	1.236	.1	.0601	103.4	5
	1.224	.3	.0601	102.4	4
	1.231	.3	.0581	103.0	5
	1.208	.5	.0601	101.0	4
	1.197	.5	.0581	100.1	5
CF_3Cl	1.320	.1	.0603	110.4	3
	1.274	.1	.0621	106.5	4
	1.208	.1	.0621	101.0	5
	1.238	.1	.0620	103.5	6
	1.271	.2	.0581	106.3	4
	1.195	.2	.0600	100.0	5
	1.248	.3	.0581	104.4	4
	1.143	.3	.0600	95.6	5
	1.122	.4	.0581	93.8	4
	1.127	.4	.0600	94.3	5
	1.139	.5	.0601	95.3	4
	1.105	.5	.0579	92.4	5
$CHCl_2F$	1.321	.1	.0579	110.5	3
	1.296	.1	.0600	108.3	4
	1.257	.1	.0578	105.1	5
	1.233	.1	.0600	103.1	6
	1.302	.2	.0580	108.8	4
	1.221	.2	.0600	102.1	5
	1.151	.3	.0600	96.3	4
	1.141	.3	.0580	95.4	5
	1.136	.4	.0601	95.2	4
	1.139	.4	.0600	95.3	5
	1.113	.5	.0599	93.1	4
	1.121	.5	.0600	93.8	5

[a] Blowoff occurred at 0.060.
[b] Blowoff occurred at 0.058.
[c] Blowoff occurred at 0.062.
[d] Blowoff occurred at 0.058.
[e] Blowoff occurred at 0.058.
[f] Blowoff occurred at 0.062.
[g] Blowoff occurred at 0.060.
[h] Blowoff occurred at 0.066.
[i] Blowoff occurred at 0.064.
[j] Blowoff occurred at 0.070.

3. Results

The outer mantle of flames to which bromine inhibitors were added was colored brown presumably by the formation of free bromine and the odor of bromine was noticeable. Hydrogen bromide is also thought to be present in the combustion products. Flames containing chlorine inhibitors were brighter than methane-air flames and the acid odor of hydrogen chloride was noticeable.

Water condensed on the surface of the nozzle during some experiments and this condensate was found to react acid; copper was also detected in the condensate. In other experiments, solid products of corrosion, most likely halides of copper and zinc, were formed around the port of the nozzle. In some instances, this deposit developed in quantities sufficient to interfere with the flow of gas and cause distorted flames. However, these deposits were soft and easily removed.

At the end of the experiments, the upper surface of the nozzle was found to be eaten away to a depth of 1/16 in. beginning about 0.02 in. from the lip and extending outward about 1/4 in., thus leaving a thin rim of untouched metal surrounding the port of the nozzle. This eroded area occupied a position which could not affect the flow of gas.

Maximum flame speed observed for each experimental condition is listed in table 2.

3.1. Bromotrifluoromethane, CF_3Br

The addition of CF_3Br generally resulted in a decrease in the flame speed of methane-air mixtures. However, at a few experimental conditions, an increase in flame speed was observed. At a gas velocity of 3 ft/s and with 0.1 percent of CF_3Br added to the combustion air, the maximum flame speed, which occurred at mixture ratio 0.062, was found to be greater than that of methane-air—1.208 ft/s as compared to 1.196 ft/s. At conditions leaner in fuel than mixture ratio 0.062, the flame speeds were also greater than those of methane-air. At conditions richer in fuel than mixture ratio 0.062, flame speeds were lower than those of methane-air. At a gas velocity of 4 ft/s and with 0.1 percent CF_3Br present in the combustion air, maximum flame speed was found at mixture ratio 0.060 and was equal to that of methane-air 1.196 ft/s. At conditions leaner in fuel than mixture ratio 0.060, flame speeds were increased by the presence of CF_3Br, but at conditions richer in fuel than mixture ratio 0.060, flame speeds were decreased. At gas velocities of 5 and 6 ft/s and with 0.1 percent CF_3Br added, flame speeds were always less than those of methane-air. Flame speeds of mixtures containing 0.2 percent of CF_3Br and more added to the air were always less than those for methane-air.

3.2. Dibromodifluoromethane, CF_2Br_2

At a gas velocity of 3 ft/s, the addition of 0.1 percent of CF_2Br_2 to the combustion air decreased the flame speed of methane-air except at two conditions, at mixture ratios of 0.054 and 0.056, where a slight increase in flame speed was noted. At all other experimental conditions of gas velocity, mixture ratio, and concentration of inhibitor, flame speed was decreased by the addition of CF_2Br_2. All maximum flame speeds at given conditions were lower than those of methan-air and are listed in table 2. Reduction in flame speed at given mixture ratio and gas velocity was found to be directly proportional to the amount of CF_2Br_2 added. The decrease in maximum flame speed for a given addition of CF_2Br_2 was also found to be directly proportional to the amount of inhibitor added and was found to be 0.1450 ft/s for each 0.1 percent addition, in the range of concentrations used in these experiments. Variation of flame speed with mixture ratio is presented in figures 4 and 5.

Why CF_3Br should be more effective as an inhibitor than CH_3Br is not apparent. Fluorine atoms seem to have little or no inhibiting power. If fluorine, as an inhibitor, were comparable to bromine, one would expect CF_3Br to be much more effective than CH_3Br which is not the case. If, as has been proposed [4], hydrogen halides are formed in the reaction zone and are the effective inhibitors, then hydrogen fluoride is either not present or is too stable to react with the chain-carrying radicals. The carbon to fluorine bond has a heat of formation of 107 kcal/mol while the carbon to bromine bond has a heat of formation of 54 kcal/mol. Likewise, the hydrogen to fluorine bond has a heat of formation much larger than the hydrogen to bromine bond: 147.5 kcal/mol as compared to 87.3 kcal/mol [3]. Since fluorine bonds are much stronger, it is less likely that they would rupture in the comparatively low temperature methane-air flames. The possibility exists that the hydrogen atoms of CH_3Br may act as centers of chain initiation and counterbalance the chain-breaking activities of the bromine atom. But if this process does occur, it must play a very minor role as the maximum flame speeds, produced by inhibition by CF_3Br and CH_3Br, are very close in magnitude.

CF_3Br and CF_2Br_2, under certain circumstances, actually increase the flame speed of methane. In our previous work with CH_3Br, some instances of increased flame speed were also found and the opinion was expressed that CH_3Br in an excess of air probably acted as a fuel [1].

CF_3Br and CF_2Br_2 increase flame speeds only when 0.1 percent is added to the combustion air and in lean mixtures, that is, in mixtures which contain an excess of air. The mixture ratio at which maximum flame speed occurs, as compared to methane, is shifted toward the lean side. This exactly parallels the behavior of CH_3Br and suggests that CF_3Br and CF_2Br_2 may also act as fuels in an excess of air.

3.3. Comparison of Bromine Inhibitors

A comparison of the maximum flame speeds of methane-air mixtures to which the bromine-containing inhibitors CH_3Br, CF_3Br, and CF_2Br_2 were added shows CF_2Br_2 to be the most effective in reducing flame speeds. For example, at a gas velocity of 4 ft/s, 0.3 percent CH_3Br added to air resulted in a maximum flame speed of 1.029 ft/s which is 86.0 percent of the maximum flame speed of methane-air. The same concentration of CF_3Br in the burning mixture yielded a maximum flame speed of 1.012 ft/s or 84.6 percent of the maximum flame speed of methane-air. The same concentration of CF_2Br_2 in the burning mixture resulted in a maximum flame speed of 0.881 ft/s or 73.6 percent of the maximum flame speed of methane-air. Maximum flame speeds of mixtures inhibited by CF_3Br and CF_2Br_2 are listed in table 2. Maximum flame speeds for mixtures containing CH_3Br are listed in [1]. The rate of decrease in maximum flame speed with the increase in concentration of inhibitor is also greatest for CF_2Br_2. These rates are listed in table 3. The fact that CF_2Br_2 contains two bromine atoms to one in both CH_3Br and CF_3Br suggests that increasing the number of bromine atoms in the molecule also increases its inhibiting powers.

Flame speeds of methane-air mixtures inhibited by CF_3Br are lower than those containing the same volume of CH_3Br except in two cases: at a gas velocity of 3 ft/s with 0.1 percent inhibitor present and at a gas velocity of 4 ft/s with 0.1 percent inhibitor present. Flame speeds of mixtures containing CF_3Br are about 98 percent of the flame speeds of the corresponding mixture containing CH_3Br. The rates of decrease of flame speed with increasing concentration of inhibitor are similar in magnitude and are listed in table 3.

TABLE 3. *Variation of maximum flame speeds with added inhibitor*

Inhibitor	Decrease in flame speed for each 0.1% added inhibitor
	ft/s
CH_3Br[a]	0.0828
CF_3Br	.0823
CF_2Br_2	.1450
CH_3Cl	.00922
CF_3Cl	.0313
$CHCl_2F$	.0398

[a] Value for CH_3Br is taken from [1].

Flame speeds at constant gas velocity and at constant mixture ratio were found to decrease as the amount of CF_3Br added to the air was increased and the decrease in flame speed was proportional to the amount of CF_3Br added. Maximum flame speeds were also found to decrease as the amount of CF_3Br was increased, and this decrease amounted to 0.0823 ft/s for each 0.1 percent added, over the range of addition here tested. Rates of decrease of flame speed are listed in table 3. Figure 1 presents the variation of flame speed with mixture ratio for methane, while in figures 2 and 3, the effect of addition of CF_3Br on the variation of flame speed with mixture ratio is presented.

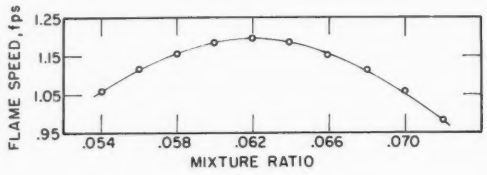

FIGURE 1. *Variation of flame speed of methane-air with mixture ratio.*
Gas velocity = 6 ft/s.

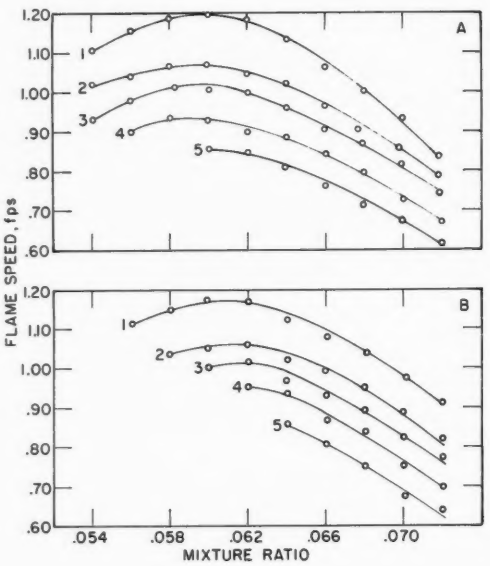

FIGURE 2. *Effect of* CF_3Br *on the flame speed of methane-air.*
CF_3Br added: 1 = 0.1%; 2 = 0.2%; 3 = 0.3%; 4 = 0.4%; and 5 = 0.5%.
Gas velocity: *A* = 4 ft/s and *B* = 5 ft/s.

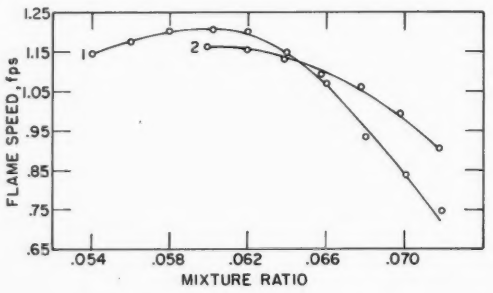

FIGURE 3. *Effect of* CF_3Br *on the flame speed of methane-air.*
0.1% CF_3Br added. Gas velocity: 1 = 3 ft/s and 2 = 6 ft/s.

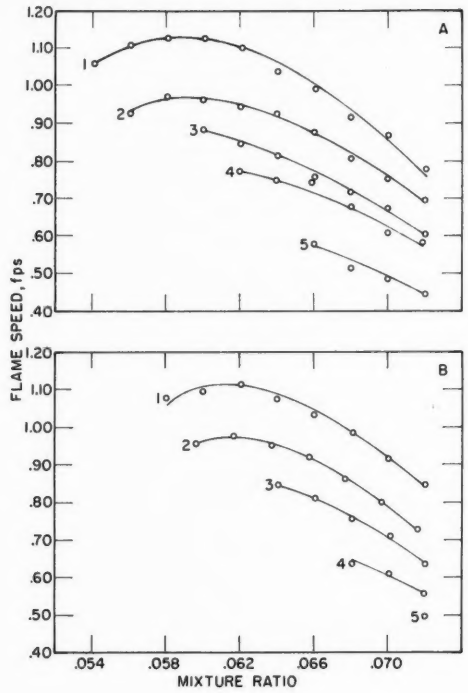

FIGURE 4. *Effect of* CF_2Br_2 *on the flame speed of methane-air.*
CF_2Br_2 added: 1 = 0.1%; 2 = 0.2%; 3 = 0.3%; 4 = 0.4%; and 5 = 0.5%.
Gas velocity: *A* = 4 ft/s and *B* = 5 ft/s.

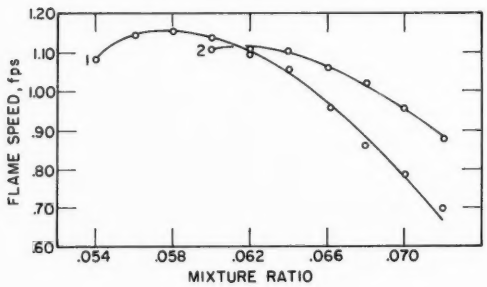

FIGURE 5. *Effect of* CF_2Br_2 *on the flame speed of methane-air.*
0.1% CF_2Br_2 added. Gas velocity: 1 = 3 ft/s and 2 = 6 ft/s.

Cullis, Fish, and Ward have reported on the effect of compounds of bromine on the slow, low-temperature oxidation of methane, among other fuels [5]. They find that these compounds, HBr and various bromomethanes, exert both a promoting and inhibiting effect on the rate of oxidation. They consider that HBr is formed from the bromomethanes and is the active agent. From a consideration of activation energies, it is deduced that HBr reacts easier with O_2 than does CH_4 and provides another mode of chain initiation. Thus, they account for the promoting action of HBr. In the later stages of the reaction of O_2 and CH_4, HBr reacts with the OH radical, retarding chain branching and so acts as an inhibitor.

It is questionable whether results obtained from the slow oxidation of CH_4 at low temperatures can be applied directly to the fast, high temperature combustion in a flame. However, the view that inhibitors may act as fuels in an excess of air is not incompatible with the view that inhibitors react easier with oxygen than does methane. Whatever the explanation, there is no doubt that low concentrations of bromine compounds can act as promotors in lean mixtures.

3.4. Inhibitors Containing Chlorine

Experimental results obtained with inhibitors containing chlorine were not as regular or as consistent as those obtained with bromine compounds. No conclusions could be drawn from the first set of experiments with CH_3Cl as the results were completely erratic. A second set of experiments was run with additions of 0.1, 0.3, and 0.5 percent, by volume, of CH_3Cl to the combustion air, at gas velocities of 4 and 5 ft/s. Results from these experiments were more regular and coherent. CF_3Cl and $CHCl_2F$ behaved alike: there was some scatter of the data and some inconsistencies, but a pattern of the effect of these compounds on flame speed could be made out.

Why chlorine compounds should behave erratically is not clear. Deficiencies in experimental techniques may be partly responsible, but the same techniques were used with bromine inhibitors which yielded much more coherent data. HCl which is formed in the flame from chlorine compounds is corrosive to the brass nozzle and copper chloride, which is one of the products of corrosion, is itself an inhibitor [6]. It is possible that deposits of copper chloride around the port of the burner could have affected the flame speed. On occasion, bright blue-green flashes caused by the entrance of copper chloride were observed. But then the flame was extinguished, the nozzle was cleaned and the flame was relit before photographs were taken. Nevertheless, the possibility of metallic halides influencing the flame speed must be borne in mind.

3.5. Methyl Chloride, CH_3Cl

Variation of flame speed with mixture ratio was determined at additions of 0.1, 0.3, and 0.5 percent of CH_3Cl at gas velocities of 4 and 5 ft/s. Results of these experiments are shown in figure 6. Maximum flame speeds for given experimental conditions are listed in table 2.

Methyl chloride did not prove to be an effective inhibitor of the combustion of methane. In fact, at most experimental conditions, it acted as a combustion promoter. Maximum flame speeds of methane-air mixtures containing up to 0.5 percent methyl chloride, added to the air, were larger than those of methane-air. Maximum flame speeds, at a gas velocity of

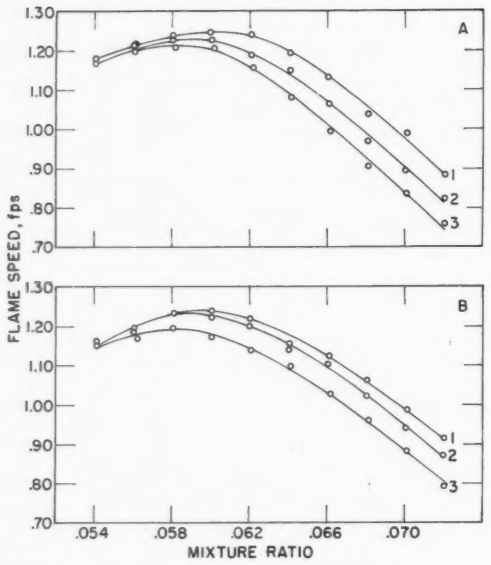

FIGURE 6. *Effect of* CH_3Cl *on the flame speed of methane-air.*
CH_3Cl added: 1 = 0.1%; 2 = 0.3%; and 3 = 0.5%.
Gas velocity: *A* = 4 ft/s and *B* = 5 ft/s.

4 ft/s were 1.242, 1.225, and 1.208 ft/s for 0.1, 0.3, and 0.5 percent addition, respectively, while the maximum flame speed of methane-air is 1.196 ft/s. Mixtures to which CH_3Cl was added and which contained less fuel than those which gave the maximum flame speeds always resulted in flame speeds that were larger than the corresponding flame speeds of methane-air. Mixtures to which CH_3Cl was added gave flame speeds which were smaller than the corresponding flame speed of methane-air only when the mixture contained less fuel than mixture ratio 0.062.

However, flame speeds of these mixtures did decrease as the amount of CH_3Cl was increased. The decrease in flame speed at a given mixture-ratio was proportional to the amount of CH_3Cl added. The decrease in maximum flame speeds was also proportional to the amount of CH_3Cl added and was 0.00922 ft/s for each 0.1 percent of CH_3Cl added.

3.6. Chlorotrifluoromethane, CF_3Cl

Maximum flame speeds determined at 4 ft/s for mixtures containing up to 0.3 percent of CF_3Cl added to the air, and maximum flame speeds determined at 5 ft/s for mixtures containing up to 0.2 percent CF_3Cl added to the air, were larger than the maximum flame speed of methane-air. Mixtures containing more than these amounts of CF_3Cl resulted in flame speeds which were less than those of methane-air. Thus, CF_3Cl can act both as a promotor and as an inhibitor of the combustion of methane. In fuel-rich mixtures CF_3Cl consistently acts as an inhibitor. At mixture ratio 0.072, flame speeds of all mixtures containing up to 0.5 percent CF_3Cl were always less than the corresponding flame speed of methane-air. In mixtures containing up to 0.3 percent CF_3Cl at a gas velocity of 4 ft/s, the flame speed becomes less than that of the corresponding methane-air mixture only at mixture ratio about 0.064; at leaner conditions, the flame speed is larger.

Variation of flame speed with mixture ratio is presented in figures 7 and 8. Maximum flame speeds for given conditions are listed in table 2.

Although CF_3Cl acts as a promotor of combustion up to 0.3 percent addition, for concentrations in excess of 0.1 percent flame speeds at given experimental conditions always decreased as the amount of CF_3Cl was increased. Likewise, the maximum flame speed for each addition of CF_3Cl decreased as the amount was increased and the rate of decrease was 0.0313 ft/s for each 0.1 percent of added CF_3Cl.

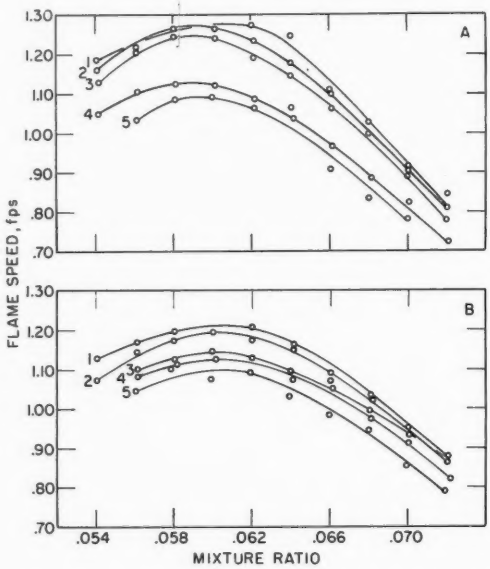

FIGURE 7. *Effect of* $CClF_3$ *on the flame speed of methane-air.*
CF_3Cl added: 1 = 0.1%; 2 = 0.2%; 3 = 0.3%; 4 = 0.4% and 5 = 0.5%.
Gas velocity: *A* = 4 ft/s and *B* = 5 ft/s.

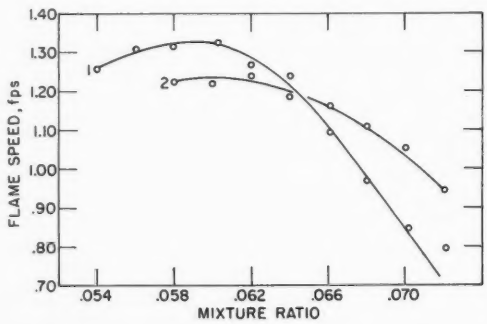

FIGURE 8. *Effect of* $CClF_3$ *on the flame speed of methane-air.*
0.1% CCl_3 added. Gas velocity: 1 = 3 ft/s and 2 = 6 ft/s.

3.7. Dichlorofluoromethane, $CHCl_2F$

At the addition of 0.1 and 0.2 percent $CHCl_2F$ to the combustion air, maximum flame speeds were larger than those observed for methane-air, while at additions of 0.3, 0.4, and 0.5 percent of $CHCl_2F$, maximum flame speeds were less than for methane-air. When 0.1 percent $CHCl_2F$ was added, up to mixture ratio 0.066, flame speed was larger than for methane-air. For mixtures richer in fuel than mixture ratio 0.066, the flame speeds of mixtures containing 0.1 percent of $CHCl_2F$ added to the air were less than the corresponding flame speed of methane-air. When 0.2 percent of $CHCl_2F$ was present in the combustion air, flame speeds, up to mixture ratio 0.064, were larger than the corresponding flame speed of methane-air. In mixtures richer than 0.064, the flame speeds were smaller than the corresponding flame speed of methane-air. At 0.3, 0.4, and 0.5 percent addition of $CHCl_2F$, only at mixture ratio of 0.054 was the flame speed larger than that of methane-air.

$CHCl_2F$ can act either as a promotor or as an inhibitor of the combustion of methane. Based on its effect on the maximum flame speed, $CHCl_2F$ becomes an inhibitor only when 0.3 percent or more is added to the air. However, even at 0.1 percent addition, $CHCl_2F$ acts as an inhibitor in fuel-rich mixtures.

Flame speeds became smaller as the amount of $CHCl_2F$ was increased. This was true both for the maximum flame speed and for the flame speed at a given mixture ratio. The rate of decrease of maximum flame was 0.0398 ft/s for each 0.1 percent of added $CHCl_2F$. Variation of flame speed with mixture ratio is presented in figures 9 and 10. Maximum flame speeds for given experimental conditions are listed in table 2.

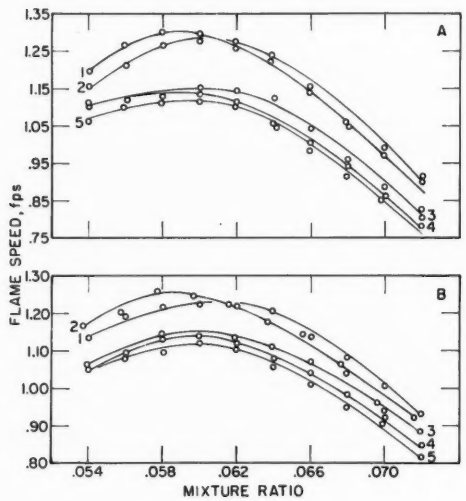

FIGURE 9. *Effect of* $CHCl_2F$ *on the flame speed of methane-air.* $CHCl_2F$ added: 1 = 0.1%; 2 = 0.2%; 3 = 0.3%; 4 = 0.4% and 5 = 0.5%. Gas velocity: *A* = 4 ft/s and *B* = 5 ft/s.

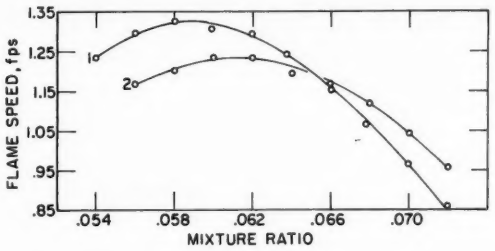

FIGURE 10. *Effect of* $CHCl_2F$ *on the flame speed of methane-air.* 0.1% $CHCl_2F$ added. Gas velocity: 1 = 3 ft/s and 2 = 6 ft/s.

3.8. Comparison of Bromine and Chlorine Compounds

None of the chlorinated compounds tested can be considered a good inhibitor of the flame speed of methane-air mixtures. CH_3Cl is the least effective and CF_3Cl and $CHCl_2F$ are about equal and only slightly better than CH_3Cl. The presence of two chlorine atoms in $CHCl_2F$ does not increase its powers of inhibition. Bromine compounds are much more effective in reducing the flame speed of methane-air. For example, at a gas velocity of 4 ft/s, 0.5 percent of CF_3Br added to the combustion air will reduce the maximum flame speed of methane-air from 1.196 to 0.856 ft/s which is 72 percent of the uninhibited value. The same percentage of CF_3Cl will reduce the flame speed to 1.139 ft/s or 95 percent of the flame speed of methane-air.

A comparison of the bond energies [3] of carbon to chlorine and carbon to bromine (66.5 kcal/mol versus 54.0 kcal/mol) and of hydrogen to chlorine and hydrogen to bromine (102.7 kcal/mol versus 87.3 kcal/mol) shows that chlorine bonds are considerable stronger than bromine bonds. Hence, chlorine compounds will be more stable in flames and less liable to react with the active chain-carrying particles than bromine compounds. This may explain why bromine compounds are more effective as inhibitors than are chlorine compounds.

3.9. Reaction Zone Thickness

The position of the schlieren image in a flame marks the region where gradients of density and temperature are steepest and is considered to be the beginning of the reaction zone [7], while the position of the visible image is taken to mark the region where reactions are complete [8]. Hence, the distance between the two images will be a measure of the thickness of the reaction zone. And the thicker the reaction zone, the slower will be the rate of reaction.

In the experimental procedure, the visible and schlieren images of a flame were photographed simultaneously on the same film. Measurements of the distance between images are made on photographic enlargements and the images are rather diffuse. The measurements cannot be considered precise or extremely accurate, but they do establish relative magnitudes and indicate trends.

Thickness of the reaction zone varies inversely as the flame speed and the minimum thickness, indicating the greatest reaction rate, occurs at or close to the mixture ratio for maximum flame speed. Reaction zone thickness at mixture ratio 0.072 is much larger than at mixture ratio 0.054. Addition of inhibitors to burning mixtures results in an increased reaction zone thickness and the thickness increases as the amount of inhibitor increases, indicating that the rate of reaction is decreased by the presence of inhibitors. Bromine compounds which are much more effective in reducing flame speeds of methane-air than are chlorine compounds also produce much thicker reaction zones.

Some representative measurements of reaction zone thickness at various experimental conditions are listed in table 4 together with some measurements for methane.

TABLE 4. *Reaction zone thicknesses*

Inhibitor	Percent inhibitor added to air	Reaction zone thickness, inches			
		At mixture ratio 0.054	Minimum	At mixture ratio 0.072	Gas velocity
					ft/s
CH_4[a]	.....	0.0159	0.0149	0.0196	6
CH_3Br	0.2	.0203	.0182	.0295	4
	.5	.0248	.0233	.0370	3
CF_3Br	.2	.0202	.0190	.0303	4
	.5	.....	.0259[b]	.0405	4
CF_2Br_2	.1	.0199	.0194	.0305	4
	.5	.....	.0377[c]	.0527	4
CH_3Cl	.1	.0195	.0173	.0263	5
	.5	.0184	.0174	.0303	4
CF_3Cl	.1	.0197	.0181	.0280	5
	.4	.0208	.0200	.0297	5
$CHFCl_2$	.2	.0196	.0170	.0258	4
	.5	.0185	.0178	.0298	4

[a] CH_4 flame containing no inhibitor.
[b] Leanest stable flame, at 0.060, blowoff occurred at 0.58.
[c] Leanest stable flame, at 0.066, blowoff occurred at 0.64.

3.10. Effect of Quenching

All the inhibitors tested were found to be much more effective in reducing flame speeds in rich mixtures than in lean. The maximum flame speed of a mixture containing 0.2 percent of CF_3Br added to the air is 1.068 ft/s or 89.3 percent of the maximum flame speed of methane-air, 1.196 ft/s. At mixture ratio 0.054, a lean mixture, the flame speed of the inhibited mixtures is 1.019 ft/s or 96.4 percent of the corresponding flame speed of methane-air, 1.057 ft/s. At mixture ratio 0.072, a rich mixture, the flame speed is 0.786 ft/s or 80.2 percent of the corresponding flame speed of methane-air, 0.980 ft/s. The flame speed of the inhibited mixture at 0.054 is 95.4 percent of its maximum, while at 0.072, it is only 73.6 percent of the maximum. The corresponding values for methane-air are 88.3 and 81.9 percent.

Even more striking is the behavior of CF_3Cl. The maximum flame speed at a gas velocity of 4 ft/s of a mixture of methane and air containing 0.2 percent of CF_3Cl added to the air is 1.271 ft/s which is 106.3 percent of the maximum flame speed of methane-air, 1.196 ft/s; an increase in flame speed has resulted. At mixture ratio 0.054, the flame speed of the "inhibited" mixture is 1.155 ft/s which is 109.2 percent of the corresponding flame speed of methane-air, 1.057 ft/s; here, again, an increase in flame speed has resulted. At mixture ratio 0.072, the flame speed of the inhibited mixture is 0.808 ft/s which is 82.4 percent of the corresponding flame speed of methane-air, 0.980; a noticeable decrease in flame speed has occurred. At 0.054, the flame speed of the inhibited mixture is 90.0 percent of its maximum, while at 0.072 it is 63.6 percent.

Previously, it had been found that the flame speed of methane-air mixtures, at constant mixture ratio, varies with the velocity of the gas in the nozzle [2]. The flame speed decreases as the gas velocity increases and the change in flame speed is about 2 percent when the gas velocity is doubled. The presence of inhibitors in flames alters this behavior. At a given addition of inhibitor and at constant mixture ratio, the flame speed decreases as the gas velocity increases only when the mixture ratio is 0.064 or less. When the mixture ratio is 0.066 or larger, the flame speed increases sharply as the gas velocity increases and this increase in flame speed may be as much as 20 percent when the gas velocity is increased from 3 to 6 ft/s.

The diameter of the base of the schlieren cone of a methane-air flame increases slightly as the burning mixture becomes richer in fuel [2], and the diameter of the base is larger than the diameter of the port of the nozzle except where conditions producing flashback prevail. Then the diameter of the base is less than the diameter of the port. Again, the addition of an inhibitor changes the behavior of the flame. The diameter of the base of the schlieren cone of an inhibited flame increases as the burning mixture becomes richer in fuel, but only up to mixture ratio 0.064 or 0.066. When the amount of fuel is increased beyond these values, a sharp decrease in the diameter is found. At the same time, the flame cone becomes extremely elongated. When the maximum amount of inhibitor used in these experiments is present, the diameter of the base of the schlieren cone may be less than the diameter of the port of the nozzle, but flashback does not take place. As the burning mixture becomes richer in fuel, the diameter of the base of the visible flame cone remains practically constant and is larger than the diameters of the schlieren cone and the port of the nozzle. The decrease in the diameter of the base of the schlieren cone and the increase in flame speed with gas velocity, both of which occur in rich mixtures, are related inasmuch as flame speeds are calculated by a total-area method based on the surface area of the schlieren cone and the surface area depends on the diameter of the base.

It is apparent that the position of the schlieren cone in inhibited flames is displaced toward the center relative to the visible cone in fuel-rich mixtures. The increased thickness of the reaction zone is an indication that the rate of reaction has decreased.

Quenching of reactions at the surface of the nozzle also takes place. The phenomena associated with

flame quenching (quenching distance, dead space, etc.) can be explained qualitatively either by a thermal theory or by a diffusion theory [9]. Probably a diffusion theory is more applicable to the present case. It has been pointed out [4] that small amounts of inhibitors do not lower flame temperatures. Hence, the rapid decrease in flame speeds in inhibited rich mixtures may be explained if active particles (atoms or free radicals) are lost at the surface of the nozzle as well as destroyed by the inhibitor.

4. Conclusions

Inhibitors containing bromine are more effective in reducing the flame speed of methane than are inhibitors containing chlorine. CF_2Br_2 is more effective as an inhibitor than either CH_3Br or CF_3Br. Over the range of inhibitor concentrations investigated, it is usually found that maximum flame speeds are reduced proprotionately to the amount of inhibitor added. And all inhibitors tested are more effective in rich mixtures than in lean.

5. References

[1] C. Halpern, J. Res. NBS **67A,** (Phys. and Chem.) No. 1, 71 (1963).
[2] C. Halpern, J. Res. NBS **60,** 535 (1958) RP2867.
[3] L. Pauling, Nature of the Chemical Bond, (Cornell Univ. Press, Ithaca, New York, 2d ed., 1940).
[4] W. A. Rosser, H. Wise, and J. Miller, Seventh Symposium (International) on Combustion, p. 175 (Butterworths Scientific Publications, London 1959).
[5] C. F. Cullis, A. Fish, and R. B. Ward, Proc. Roy. Soc. (London) **A276,** 527 (1963).
[6] W. A. Rosser, S. H. Inami, and H. Wise, Comb. Flame **7,** 107 (1963).
[7] J. J. Broeze, Third Symposium (International) on Combustion, p. 146 (Williams and Wilkins, Baltimore, Md., 1949).
[8] A. G. Gaydon and H. G. Wolfhard, Flames, Their Structure, Radiation, and Temperature, p. 96 (Chapman, and Hall, Ltd., London, 1960).
[9] R. Friedman, Third Symposium (International) on Combustion, p. 110 (Williams and Wilkins, Baltimore, Md., 1949).

(Paper 70A2–388)

JOURNAL OF RESEARCH of the National Bureau of Standards—A. Physics and Chemistry
Vol. 70A, No. 2, March–April 1966

Rupture-Disk Ampoule for Anhydrous Addition of Hydrogen Fluoride*

Augustus R. Glasgow, Jr.[1]

Institute for Materials Research, National Bureau of Standards, Washington, D.C.

(January 3, 1966)

The rapid increase in vapor pressure of liquid HF with temperature has been used in a rupture-disk-ampoule technique for mixing HF with materials under anhydrous conditions. At room temperature where HF has a vp near 1.4 atm, the disk with a rupture limit near 10 atm confines the acid. At higher temperatures, 100 and 150 °C, where the internal pressure of HF in the ampoule is 10 and 30 atm, respectively, the disk is ruptured and the acid is released. The construction of the ampoule from platinum and reuseable platinum-iridium parts; the details of the filling, sealing and weighing; and its use for anhydrous addition of HF to other materials in a closed vessel are described.

Key Words: Anhydrous filling, anhydrous mixing, ampoule, capsule, hydrogen fluoride, metal, rupture-disk.

1. Introduction

Glass ampoules with break-tips or thin walls have long been used for the two-fold purpose: one, sealing a volatile substance under its own vapor pressure for weighing, storage, protection of its purity, etc.; and two, providing for the transfer of the substance in the absence of air or moisture to other vessels and to other materials by breaking the tip or thin wall of the ampoule under controlled conditions. A metal, rupture-disk ampoule of platinum and platinum-iridium parts was designed to extend this technique to hydrogen fluoride, whereby: one, liquid HF is confined in the ampoule under its own vapor pressure by sealing the inlet tube of the ampoule; and two, HF is subsequently transferred to other vessels and to other materials under anhydrous conditions by rupturing the disk of the ampoule. Whereas breakage of the tip or thin wall of the glass ampoule is effected by the mechanical impact from a magnetic hammer of fused wire, the marked increase in the vapor pressure of liquid HF with temperature is used to rupture the disk of the metal ampoule. A disk of 0.025 mm platinum foil was selected, because disks of this thickness were found to rupture under a pressure near 10 atm in experiments in which nitrogen gas pressures from a cylinder were applied. This disk safely confines HF in the sealed ampoule at 25 °C where liquid HF has a vapor pressure of about 1.4 atm. Rupture of the disk for anhydrous addition of HF to other materials is effected by raising the temperature which causes the internal pressure of HF in the sealed ampoule to increase to a value exceeding the rupture limit of the disk; at 100 and 150 °C, liquid HF has a vapor pressure of 10 and 30 atm, respectively.

2. Construction

Whereas other types of designs of rupture-disk ampoules based on this principle may be used, the cross-sectional drawing of the ampoule, shown in figure 1, was designed to fit inside a Morey pressure bomb. The ampoule is composed of four parts: a platinum inlet tube, A; a platinum-iridium shell, B; a platinum-iridium protective ring, C; and a rupture-disk of platinum foil, D. The ring C is not gold soldered to the shell and serves only as a protective guard for the thin platinum disk, D. The shell B is reused to form a new ampoule by gold soldering a new section of platinum tubing, A, at 4 and a new disk, D,[2] at 5 as described in the legend to figure 1.

*Part of talk entitled "Rupture-disk ampoule for anhydrous addition of HF to a closed bomb" presented by A. R. Glasgow, Jr. at 19th Annual Calorimetry Conference, National Bureau of Standards, October 15, 1964.

[1] Present address: Pesticides Branch, Division of Food Standards and Additives, Food and Drug Administration, Washington, D.C.

[2] Note: In the sealing of the platinum disk, D, to the shell B at position 5, the protective ring C should not be on the shell portion because of possible alloying through the thin foil D to both parts B and C. The reason for this precaution is as follows: the gold soldering can form with the thin platinum foil an alloy of 90 percent Pt and 10 percent Au which has a melting range of 2950–3125 °F and therefore cannot be unsoldered by heating from the Pt-Ir alloy (parts B and C) which have a melting point of 3290 °F. In the case of unsoldering the platinum tube A of 0.025 mm thickness no difficulty was experienced and the unsoldering behaved as expected from the melting points of Au (1945 °F), Pt (3200 °F) and the alloy of 90 percent Pt-10 percent Ir (3290 °F).

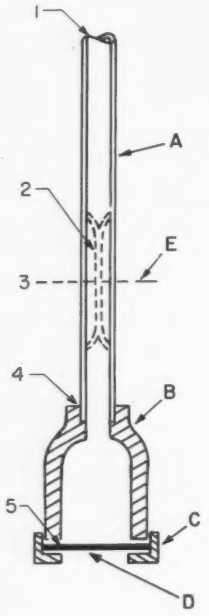

A. Platinum tube 1/3 inch o.d., 0.010 inch wall

B. Platinum-iridium shell (90% Pt-10% Ir alloy)

C. Platinum-iridium ring (90% Pt-10% Ir alloy)

D. Platinum disk, foil 0.025 mm thick soldered to B and C

E. Position where tube is cut off after filling with HF and closing tube with pliers.

FIGURE 1. *Rupture-disk ampoule.*

FIGURE 2. *Manifold and coolant device used in filling and sealing hydrogen fluoride in an ampoule under its own vapor pressure.*

3. Operation

For filling, the ampoule is attached at its position 1, figure 1, through a union fitting of Monel to a Monel manifold as shown in figure 2. This manifold is joined on one end to a cylinder of HF gas and on the other end to a high-vacuum system that contains a nickel-Monel trap. Before filling, the ampoule is first evacuated in this manifold to 10^{-6} mm Hg, tested for leaks with a helium-leak detector, filled with dry air to atmospheric pressure, disjoined from the manifold at the union coupling and weighed. After filling and sealing, the filled ampoule and inlet tube containing the attached union coupling are weighed. From this and the previous weighing, the amount of HF sealed in the ampoule is determined.

The sequence of operations that is usually performed in glass systems for sealing a volatile substance under its own vapor pressure in a glass break-off-tip ampoule was applied to the metal system of Monel and nickel parts which was used to seal HF under its own vapor pressure in a rupture-disk ampoule of platinum and platinum-iridium parts. These metals were selected because they offer good chemical resistance to HF whereas glass is attacked. Hydrogen fluoride lended itself well to these operations because of its following properties: boiling point near 19.4 °C; fp near −83 °C where its vapor pressure is about 5mm Hg; and a vapor pressure at the temperature (−196 °C) of a liquid-nitrogen bath near 10^{-6}mm Hg. By the same techniques used with glass systems, HF gas was transferred from a cylinder through the evacuated manifold of Monel, condensed in a Monel-nickel trap, alternately frozen and melted in a vacuum to remove dissolved gases, transferred under its own vapor pressure to the rupture-disk ampoule, and then cooled in the ampoule by refrigeration in a liquid-nitrogen bath before sealing the HF in the ampoule under its own vapor pressure. Since most of these operations do not differ from the conventional practice with glass systems only the final cooling and sealing, which is different, will be described.

For the cooling, the ampoule is placed in the cavity of a solid copper rod that is immersed in a liquid-nitrogen bath. This rod is shown in figure 2 in an up-raised position for photographing. A contact medium, such as CCl_4, that was added as a liquid and cooled as a solid to −196 °C, was used to fill the space between the cavity and the ampoule for the purpose of improving the heat transfer between the ampoule, rod, and bath. After cooling the filled ampoule in this manner, the inlet tube A was compressed by pliers with parallel jaws as shown at 2 in figure 1. This compressed section had been previously annealed to soften the platinum, gold coated on its inner surface, and partially compressed so that a small coil of gold wire fitted just above position 2 in figure 1. After the compression with the pliers, this gold wire is heated to fusion as a final precaution in the sealing. The ampoule after this sealing is allowed to warm to room temperature, tested through the manifold system for leaks, and then disconnected at the union fitting and weighed. After weighing, the ampoule is disjoined from the inlet tube by cutting at position 3 as shown in figure 1.

4. Results

In a filling of this ampoule with a 0.429 g amount of HF, the reweighing of the filled ampoule after a weekend was constant to 1 mg. This weight was also checked to within 1 mg from the reweighing of the empty ampoule after an experiment in which the ampoule was placed in a bomb and heated to about 125 °C to release the HF to the cavity of the closed bomb.

5. Conclusion

This technique for the anhydrous addition of a weighed amount of HF in a rupture-disk ampoule was perfected for use in the development of a new hydrofluorothermal process whereby crystal growth of BeF_2 in a platinum-lined bomb under HF pressure was to be performed by a method analogous to that used in the hydrothermal growth of quartz from SiO_2. In the hydrofluorothermal method, BeF_2 was to replace SiO_2, HF was to replace H_2O, and NH_4F was to be substituted for NaOH as the flux material. Whereas in the hydrothermal process water is a component and is therefore no problem, the mixing of HF, BeF_2 and NH_4F in the bomb under anhydrous conditions was a major problem solved by the rupture-disk ampoule technique.

Although the ampoule discussed was specifically designed for use in the above process, this technique is described because of its general utility in other applications where a weighed amount of HF is to be mixed with other materials or added to vessels under anhydrous conditions. The filled and sealed ampoule allows HF to be added at room temperature to vessels under anhydrous conditions along with nonvolatile solids; and after closure of the vessel to be mixed with the contents of the closed vessel.

In cases where heating the HF-filled and sealed ampoule is not desirable, the disk may be punctured by mechanical impact by techniques such as fusing a wire to release a weight for puncturing the disk.

This work was part of the research into methods for the preparation of high-purity, well-characterized, crystalline BeF_2 which was supported by the Advanced Research Projects Agency in the Light-Element Program at the National Bureau of Standards.

(Paper 70A2–389)

JOURNAL OF RESEARCH of the National Bureau of Standards—A. Physics and Chemistry
Vol. 70A, No. 2, March–April 1966

Further Studies in the Annealing of a Borosilicate Glass

Sam Spinner and Albert Napolitano

Institute for Materials Research, National Bureau of Standards, Washington, D.C.

(December 22, 1965)

Time-index of refraction isotherms for a borosilicate glass in the transformation region have been established. By comparing two quenched glasses of the same index, one quenched after attaining equilibrium at a given temperature and the other quenched from a temperature at which the specimen was approaching a higher value of index, curves similar to the one obtained by Ritland in comparing rate cooled and quenched specimens are developed.

Key Words: Annealing, borosilicate glass, glass, time-index of refraction isotherms, transformation range, index of refraction.

1. Introduction

Ritland [1][1] has demonstrated that glasses of the same composition and refractive index can nevertheless be quite different in other respects, such as expansivity, electrical resistivity, etc, depending upon whether the index was achieved by cooling the glass at some (relatively slow) constant rate through the transformation range ("rate cooled"), or by cooling the glass rapidly from some holding temperature within the transformation range, this temperature being maintained for a time sufficient for the glass to stabilize at that temperature ("soaked"). This demonstrated the inadequacy of certain aspects of the fictive temperature concept which assumes that the structural state of a glass can be completely described by a single ordering parameter. Ritland also pointed out that Tool [14], who originated the fictive temperature concept, was not guilty of this over-simplification, recognizing that although every temperature in the transformation range corresponds to a certain equilibrium[2] state, "it does not necessarily follow that every nonequilibrium state is identical with one of these."

One of the several ways by which Ritland demonstrated the difference between rate cooled and soaked specimens (and the one which forms the starting point of the present investigation) is shown in figure 1, which is taken from his paper (fig. 3, of ref. 1). When a rate cooled specimen is placed in a furnace held at the temperature required to maintain the same index as for a soaked specimen, the index of the rate cooled specimen is seen to dip rather quickly before returning more slowly to its initial value. Clearly, had the rate cooled specimen been initially in the same structural state as the soaked specimen of the same index, then this dip in index before returning to its initial value would not have taken place; instead, the rate cooled specimen would follow the same flat line as the soaked specimen.

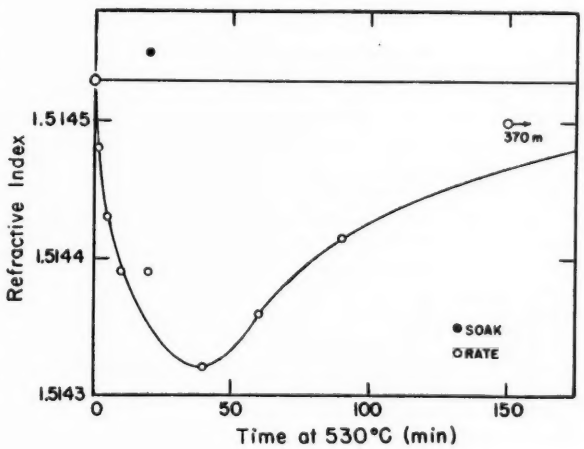

FIGURE 1. *Room temperature refractive index as a function of treatment time at 530 °C.*
Figure 3 from Ritland [1].

[1] Figures in brackets indicate literature references at end of this paper.

[2] The word "equilibrium" as used in this paper is, of course, not to be interpreted in the fullest thermodynamic sense, but rather, in the more limited sense of the condition of a glass at which the structure in the transformation range has stabilized, so that its properties no longer change within reasonable time [2].

799-883 O-66—3

In an attempt to shed further light on this problem of the relation between the condition of a glass and its thermal history, the present investigation takes the following line of approach. It is known that the lower the temperature at which a glass is held in the annealing region, the higher the room-temperature equilibrium value of refractive index that will be reached. Then, the same room temperature value of index for two glasses can be obtained not only by soaking and appropriate rate cooling, but also using only suddenly cooled (quenched) glasses; one glass being quenched from an equilibrium index at some given temperature (corresponding to Ritland's soak specimen) and the other glass being quenched from some lower temperature, but at that instant in its approach to its equilibrium, when its index equaled that of the specimen already at equilibrium. We, then, propose to compare two such quenched specimens in a manner similar to that used by Ritland, as described above in comparing soaked and rate cooled specimens. Such an experimental approach should be revealing since, figuratively speaking, one freezes the structure of the glass in its approach to equilibrium; and the nature of this approach to equilibrium is recognized to be of fundamental importance in understanding the processes taking place in the glass transformation range.

Kovacs [3] has already performed an experiment which, though quite different in detail, is similar in principle to the one proposed here. His test material was an organic polymer having a transformation range from about 10 to 40 °C and the property measured was the change in volume. It will be shown that the results obtained in this investigation, using an oxide glass, having a transformation range from about 490 to 605 °C, with refractive index as the indicating property, are in qualitative agreement with those of Kovacs.

2. Experimental Procedure

2.1. Specimens

The glass used in this study was a borosilicate crown, BSC 517. This is the same type of glass used in a previous study on annealing and is also very similar in composition to the one used by Ritland. All the specimens were cut from the same large block, to about 1 cm × 1 cm × 0.1 cm.

There are several advantages in the use of such small specimens. First, no appreciable strain is introduced into the specimens when they are subjected to the sudden temperature changes which the experimental procedure requires, so that this possibly disturbing factor does not affect the measurement of index nor the pattern of the data to be shown. Second, and related to this, the danger of breakage of specimens in the course of the experiment is lessened. Actually, some of the specimens did break after repeated heating and cooling, but, if necessary, these were replaced by other specimens without loss in the continuity of the data. Also, as long as one square corner remained, it was still possible to measure the index of a broken specimen on the refractometer (described in the next section). Third, the times required for a specimen to come to thermal equilibrium, when suddenly introduced into, or removed from the furnace are quite short. Using relations developed by Brandt [4], the time taken for the central layer of a specimen of the size used here to come to within one degree of the surface temperature when subjected to such sudden temperature changes (of about 500 °C) is computed to be less than 5 sec. These relations assume that the ambient temperature does not change in the vicinity of the specimen. Since this condition was not fully realized for the quenched specimens, the time for the specimens to reach room temperature is somewhat longer than this. However, this is unimportant since the time for cooling of the specimens through the transformation region is well within this figure.

2.2. Apparatus

a. Refractometer

All measurements of index, using the sodium D line, were made on the Grauer refractometer previously described [5]. It will only be recalled here that if reasonable care is taken in cutting the corners of the specimens square (no grinding or polishing of the specimens is necessary), then absolute values of index can be measured to ±2 in the fifth decimal place; and differencies in values of index, which this study mainly utilized, can be determined to better than ±1 in the fifth decimal place.

b. Furnace

A sketch of the furnace used is shown in figure 2. Its main feature is a cylindrical metal slab, shown in the upper right-hand corner of the figure, containing ten radially placed slots which serve as receptacles for the specimens. Phosphor bronze metal is used to prevent scaling and serves to reduce thermal gradients between specimens in the slots. The slab can be rotated in the furnace by means of a ceramic rod attached to its center and extending vertically outside the furnace. When a specimen in a slot in the rotary slab lines up with the exit slot, appropriately cut in a stationary metal plate on which the rotary slab rests, the specimen drops from the furnace. [The expression "drops from the furnace" thus refers to the sudden drop in temperature which the specimen undergoes when it is air-quenched as well as the physical dropping from the furnace.] A detent mechanism permits any of the ten slots in the rotary slab to line up exactly with the exit slot. The specimens can be introduced into any of the slots in the rotary slab in a similar manner by being dropped from above the furnace, through a long entry slot cut in a ceramic cylinder which rests on the rotary slab. This cylinder can also be rotated so that the entry slot lines up with any of the slots in the rotary slab. The advantage in time saving and flexibility of being able to heat nine specimens simultaneously, if desired, is obvious.

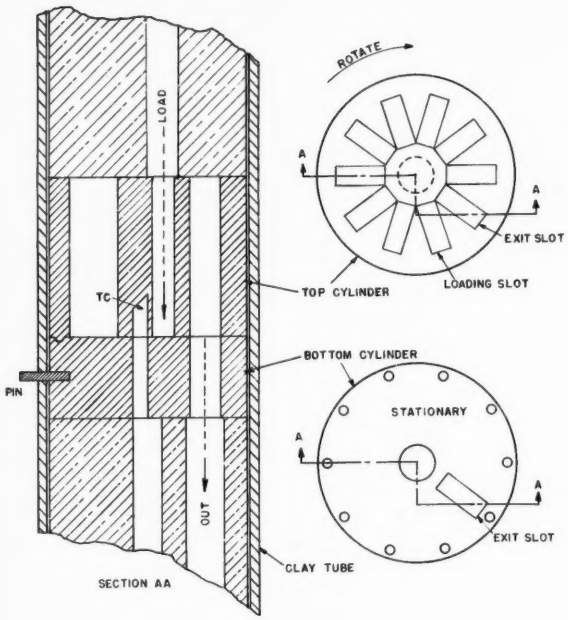

FIGURE 2. *Cross-sectional sketch of rotary furnace.*

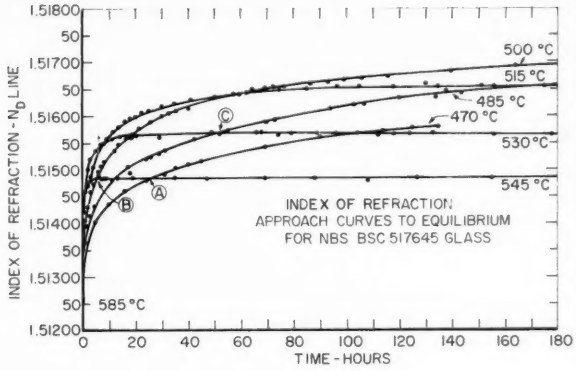

FIGURE 3. *Time, index isotherms for BSC 517.*
Indices measured at room temperature.

The furnace as well as the refractometer were designed by O. W. Grauer [5], to be used in conjunction with each other in annealing studies with specimens of the dimensions used here.

2.3. Procedure

The first step in the experimental procedure consisted in holding all the specimens at 585 °C for 1 h before quenching from the furnace to room temperature. This determined the starting value of index at 1.51250 for all the specimens, shown in the lower left hand corner of figure 3. The furnace is then set at some lower temperature in the transformation range, the specimens are inserted into the furnace, held for a given time, one specimen is dropped out, and its index measured. Then, the specimen is reinserted into the furnace, another specimen is removed at a later time, and the process is repeated until a complete time-index curve for each temperature has been established. Since all index measurements are made at room temperature, they are lower [6] than the corresponding values at the elevated temperatures.

The time for a specimen to come to thermal equilibrium is so small in comparison with even the shortest times a specimen is in the furnace (about 6 min) that it may be safely neglected in establishing the time base. The experimental justification for neglecting the time for a specimen to come to thermal equilibrium may be seen from figure 3. The points forming these curves are based both on repeated short time-in-furnace measurements on some specimens, interspersed with others based on much longer time intervals in the furnace between index measurements; yet the curves are quite smooth. Had the time for establishing thermal equilibrium been significant, then the scatter between points based on these different time intervals in the furnace between index measurements would have been greater than actually was the case.

3. Results

The time-index isotherms for various temperatures in the transformation range of the glass used here are shown in figure 3. Similar curves have been obtained by other investigators [7, 8, 9, 10]. Roughly similar curves can also be established in which the equilibrium values are reached from above rather than below. Daragon, [10] for instance, has obtained curves in which equilibrium is approached from higher as well as lower values, using density as the indicating parameter. It is experimentally more convenient, mainly because of the shorter times involved, to go from lower to higher values of index, as was done here.

Figure 4 shows the equilibrium index as a function of the equilibrium temperature in the transformation range, based on the data in figure 3. The linear relationship is the usual one for multicomponent oxide glasses, and enables one to readily select the annealing temperature required to obtain a given index.

The general characteristic of the curves in figure 3 is seen to be that the higher the temperatures used the more rapid the rise to a lower equilibrium index. At the lowest temperatures (below 500 °C) equilibrium was not achieved, the index continuing to rise slightly but significantly after seven weeks. We now designate the flat portion of each curve as the "equilibrium line" and the preceding portion of each line as the "approach curve." It is seen from the figure that the pattern of these curves leads to a series of crossover points at which an approach curve to a higher

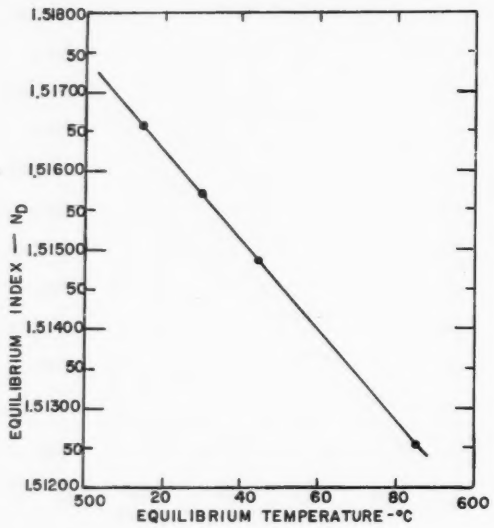

FIGURE 4. *Equilibrium index as a function of temperature for BSC 517.*

equilibrium index (at a lower temperature) intersects either an equilibrium line at a lower index (higher temperature) or another faster approach curve, also at a higher temperature. Following now, the approach already indicated, we select certain of these crossover points, and interrupt the approach curve at the moment when the index of the specimen reaches the value of the equilibrium line. The temperature of the furnace is then reset as closely as practicable to the original value for the equilibrium line and the specimen is reinserted at this new temperature. Successive index readings are then taken after short intervals in the furnace so that slight effects will not be overlooked. The crossovers selected for this are shown as A, B, and C in figure 3. Figure 5 shows the index-time changes following this procedure for crossover points A and B, in which two different approach curves (470 and 500 °C) cross the same equilibrium line (545 °C) and figure 6 shows the results of the 477 °C approach curve meeting the 527 °C equilibrium line.

In figure 5, in order to check the reproducibility of the data, three specimens from the approach curve were selected, one at an index slightly below, one above, and one as close as possible to the index at equilibrium. The three resulting curves are seen to be similar to each other. The curves are seen to approach the equilibrium line at a slightly higher value than the original one, due to the fact that the resetting of the temperature controller resulted in a slightly lower temperature and, hence, a slightly higher value of index. This is demonstrated by the control specimen shown at the left retained at the original equilibrium index, also coming to the new value of index. The lines are drawn (mainly) through the experimental points primarily to distinguish these three sets of points.

Once the similarity of the three sets of points was demonstrated in figure 5, only one set was used to show the data in figure 6. In this figure also, the temperatures (approach temperature, 477 °C; equilibrium temperature, 527 °C) are seen to be somewhat different

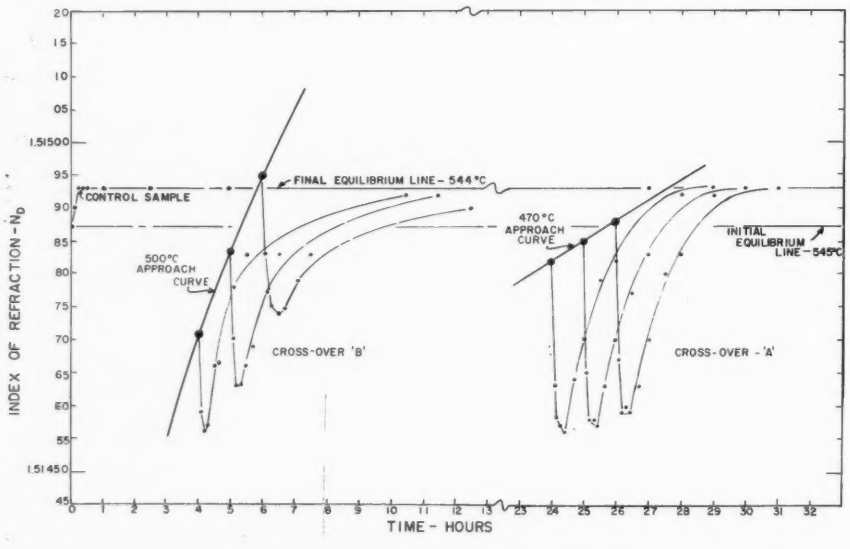

FIGURE 5. *Index versus time at crossovers A and B.*
Equilibrium temperature for both crossovers is 545 °C. Approach temperature for crossover A is 470 °C, for crossover B, 500 °C.

from the corresponding ones in figure 3, as the original temperatures were not duplicated exactly to establish the data for this crossover. The similarity of the data in figures 5 and 6 for the specimens from the approach curve to Ritland's results for the rate cooled specimens is quite clear.

An additional experiment was designed to compare a specimen held for a relatively long time at equilibrium, with one held for a considerably shorter time at equilibrium. The test for this comparison was the characteristic of the curve of the descent to a lower equilibrium index. A third specimen at the same index, but on an approach curve to a higher index (an approach specimen) was included in the comparison. The two curves from the equilibrium line agreed within experimental error, indicating no difference in specimens held for longer or shorter times at equilibrium; however, the approach specimen descended more rapidly than the other two to the new value of index. The similarity in the characteristics of the two equilibrium specimens indicates that in comparing an approach specimen with an equilibrium specimen of the same index, it is not necessary to choose an equilibrium specimen at that instant when it is intersected by the approach specimen. An equilibrium specimen may be selected from any point along its time base. Furthermore, in those cases where no intersection is observed at all (this occurs more often

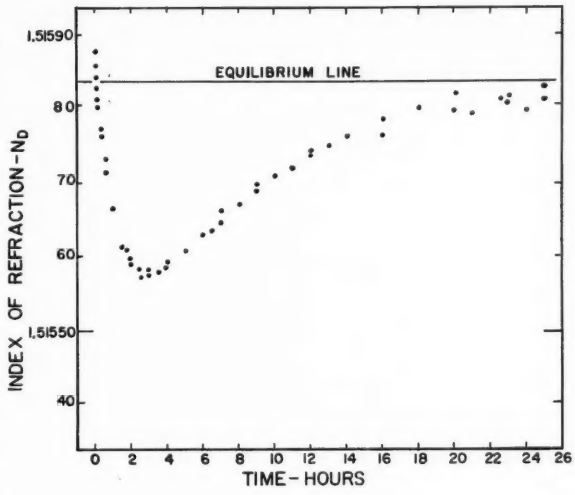

FIGURE 6. *Index versus time for crossover C.*
Equilibrium temperature, 527 °C, approach temperature 477 °C.

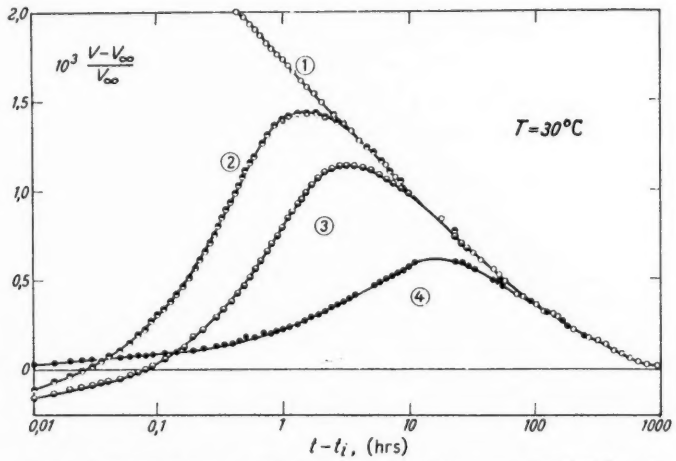

Fig. 24. Evolution isotherme du PVA II après trempe et réchauffement à 30° C (Tableau 8)

Tableau 8. *Paramètres expérimentaux de la Fig. 24*

Courbe n°	T_0 (°C)	T_1 (°C)	t_1 (hrs)	$10^3 \cdot (\delta_i - \delta_1)_{T_1}$	t^* (hrs)
1	40	—	—	0	—
2	40	10,0	160	3,2	1,4
3	40	15,0	140	3,2	3,2
4	40	25,0	90	3,1	18,0

FIGURE 7. *Figure 24 from Kovacs* [3].

when equilibrium is approached by going from higher to lower indices or densities), the method of this investigation is still applicable. Although in this study the crossover experiment actually involved an intersection between the approach curve and the equilibrium line, all that is actually required is for an approach specimen to be compared with an equilibrium specimen of the same index whether an intersection between the approach curve and equilibrium line takes place or not.

It is interesting to compare the results obtained here with those of Kovacs [3], previously mentioned. The results from his paper are reproduced in figure 7. First, his data involve no crossover. The three curves following the transfer of the specimens from the three different approach temperatures he used, to the equilibrium temperature selected (30 °C) have been superposed by him at "zero" time for comparison. The rise before returning to equilibrium, instead of a dip, as obtained here, comes from the fact that Kovacs was measuring a reciprocal property from the one used here. (Index and density vary concomitantly with annealing [11, 12, 13].) The sudden rise at the start corresponding to the sudden dip obtained here is not observed because Kovacs plots the logarithm of the time as his abscissa. Kovacs' times before the approach specimen returns to equilibrium are much longer than the ones obtained here. This is to be expected for an organic polymer. Also, the maximum in his rise is a greater proportion of the entire approach curve than the corresponding dip obtained here.

Kovacs concluded from his results that a distribution of relaxation times must be present in the approach curves to equilibrium. If this holds for the material used by him it must also hold for the glass used here; although the shorter times involved before equilibrium is attained by the approach specimens at the crossover indicates that this distribution is considerably narrower for the inorganic glass used here.

4. References

[1] H. N. Ritland, Limitations of the fictive temperature concept, J. Am. Ceram. Soc. **39** [12] 403–406 (1956).

[2] S. Spinner and A. Napolitano, Relation between refractive index and elastic moduli of a borosilicate glass after heat treatment, J. Am. Ceram. Soc. **39** [11] 390–94 (1956).

[3] A. J. Kovacs, Glass transition in amorphous polymers. A phenomenological study, Fortschr, Hochpolym-Forsch, **3,** 394–507 (1963).

[4] N. M. Brandt, Annealing of 517:645 borosilicate optical glass: I, Refractive index, J. Am. Ceram. Soc. **34** [11] 332–38 (1951).

[5] O. W. Grauer, An improved refractometer, NBS Tech. News Bull. **37** (9) 135 (1953); **38** (4) 63 (1954).

[6] Fred A. Molby, Index of refraction and coefficients of expansion of optical glass at low temperature, J. Opt. Soc. Am. **39** [7] 600–11 (1949).

[7] Anuita Winter, Transformation region of glass, J. Am. Ceram. Soc. **26** [6] 189–200 (1943).

[8] H. A. McMaster, Variation of refraction index with time and temperature in annealing region, J. Am. Ceram. Soc. **28** [1] 1–4 (1945).

[9] P. W. Collyer, Study of time and temperature effects on glass in annealing range, J. Am. Ceram. Soc. **30** [11] 338–44 (1947).

[10] (a) B. Daragon, The annealing of flat glass, The Glass Industry **33** [2] 69–74 (1952).
(b) B. Daragon, Annealing curves based on changes in glass structure, Verres et Réfractaires **7** [3] 157–66 (1953).

[11] A. Q. Tool, L. W. Tilton, and J. B. Saunders, Changes caused in refractivity and density of glass by annealing, J. Res. NBS **38** [5] 519–26 (1947); RP1793; Ceram. Abstr., 1951, September, p. 153i.

[12] N. J. Kreidl and R. A. Weidel, Annealing of 517:645 borosilicate optical glass: II, Density, J. Am. Ceram. Soc. **35** [8] 198–203 (1952).

[13] H. N. Ritland, Relation between refractive index and density of a glass at constant temperature, J. Am. Ceram. Soc. **38** [2] 86–88 (1955).

[14] (a) A. Q. Tool, Viscosity and the extraordinary heat effects in glass, J. Res. NBS **37,** 73–90 (1946) RP1730; Ceram. Abstr. 1947, January, p. 7.
(b) A. Q. Tool, Relation between inelastic deformability and thermal expansion of glass in its annealing range, J. Am. Ceram. Soc. **29,** 240–53 (1946).
(c) A. Q. Tool, Effect of heat-treatment on density and constitution of high-silica glasses of the borosilicate type, ibid **31**, 177–86 (1948).

(Paper 70A2–390)

JOURNAL OF RESEARCH of the National Bureau of Standards—A. Physics and Chemistry
Vol. 70A. No. 2. March–April 1966

Infrared Spectra of the Hydrated Borates

C. E. Weir

Institute for Materials Research, National Bureau of Standards, Washington, D.C.

(November 4, 1965)

Infrared absorption spectra of 42 different hydrated borates were obtained in the 2000–300 cm^{-1} range. A few spectra were obtained between 4000 and 2000 cm^{-1}. Most spectra are complex and cannot be interpreted satisfactorily except in the case of the simplest anions. Many correlations between spectra are possible, however, and possible anion types have been deduced. Differentiation between triangular and tetrahedral boron is possible on the basis of the spectra but is less certain than in the case of the anhydrous borates.

Key Words: Hydrated borates, infrared spectra, absorption spectra, borates, boron coordination, borate anions

1. Introduction

A comprehensive survey of the infrared spectra of the crystalline anhydrous inorganic borates was reported recently [1].[1] The spectra were correlated with known structures and predictions of unknown structures were made on the basis of the observed spectra. Two of the predicted anion structures have been verified by subsequent x-ray crystallographic studies [2, 3]. The obvious extension of the studies to include the hydrated borates is the subject of this report.

The hydrated borates have been subjected to a more systematic study than the anhydrous materials, largely as a consequence of their mineralogical occurrence. Miller and Wilkins [4] reported data on eight hydrated borates obtained by the mull technique. Several years later, Takeuchi [5] studied the spectra of 17 borates of which 12 were hydrated. Takeuchi also used the mull technique of sample preparation. Moenke and his coworkers, in a series of papers, [6–13] have presented spectra obtained on approximately 17 hydrated borates using the KBr pellet technique. Akhamanova [14] has reported on seven hydrated borates and Plyusnina and Kharitonov [15] have studied six, with spectra in both cases being obtained using films deposited from isopropyl alcohol on alkali halide plates. The early work by Miller and Wilkins [4] and that of Takeuchi [5] had a lower frequency limit of about 600 cm^{-1} which is too high to obtain some of the known fundamental vibrations of the borate anion. All the more recent studies, however, extend as far as 400 cm^{-1}.

In the present study, infrared spectra were obtained for 42 different hydrated borates. Most specimens were natural minerals but in many instances synthetic materials were also available. Approximately 63 different specimens were studied so that it was possible to determine the reproducibility of the spectra for materials of different origin—a question of importance for natural minerals which may contain infrared active impurities.

2. Experimental Method and Apparatus

Experimental techniques and equipment were similar to those described previously for the anhydrous borates [1]. A double-beam grating spectrometer was used to cover the range 4000–200 cm^{-1}. This range was covered in two steps, 4000–400 cm^{-1} and 2000–200 cm^{-1}. In each case the lower frequency limit imposed by the available energy was higher than the limits given. Most spectra were obtained only in the range 2000–300 cm^{-1} because the fundamentals of the borate anions were known to occur in this range. For these studies powdered films deposited on CsBr plates from a volatile liquid were used. A few spectra in the higher frequency range were obtained to locate the OH fundamental stretching modes. For these studies the spectra were obtained using a mull with perfluorokerosene as the suspending medium. In both cases a blank cell was placed in the reference beam of the spectrometer. The possibility of dehydrating the specimens precluded using dry air in the instrument and considerable care was exercised in the 500–300 cm^{-1} region. In this range only those bands were considered to originate in the specimen which were not obtained on a comparison spectrum run with no specimen in the beam.

[1] Figures in brackets indicate the literature references at the end of this paper.

TABLE 1. *Description of samples studied*

Material	Empirical formula	Origin of specimen [a]
Hambergite	$4BeO \cdot B_2O_3 \cdot H_2O$	C 4744
Bandylite	$CuO \cdot CuCl_2 \cdot B_2O_3 \cdot 4H_2O$	103459.
Teepleite	$Na_2O \cdot 2NaCl \cdot B_2O_3 \cdot 4H_2O$	102798.
Pinnoite	$MgO \cdot B_2O_3 \cdot 3H_2O$	C 4488; synthetic $Mgo \cdot B_2O_3 \cdot 3H_2O$ (R. C. Erd).
Inyoite	$2CaO \cdot 3B_2O_3 \cdot 13H_2O$	114260; Pacific Coast Borax open pit, Boron, Calif.
Meyerhofferite	$2CaO \cdot 3B_2O_3 \cdot 7H_2O$	96072; Gower Gulch, Death Valley Nat. Monument.
Colemanite	$2CaO \cdot 3B_2O_3 \cdot 5H_2O$	96445; Pacific Coast Borax open pit, Boron, Calif.
Inderite	$2MgO \cdot 3B_2O_3 \cdot 15H_2O$	11462; Pacific Coast Borax open pit, Boron, Calif.
Kurnakovite	$2MgO \cdot 3B_2O_3 \cdot 15H_2O$	R 11023; Pacific Coast Borax open pit, Boron, Calif.
Inderborite	$MgO \cdot CaO \cdot 3B_2O_3 \cdot 11H_2O$	Inder region, USSR.
Hydroboracite	$MgO \cdot CaO \cdot 3B_2O_3 \cdot 6H_2O$	Inder region, USSR (R. C. Erd via H. B. Mason).
Synthetic	$2SrO \cdot 3B_2O_3 \cdot 5H_2O$	Synthetic strontium colemanite (R. C. Erd via C. R. Parkerson).
Tunellite	$SrO \cdot 3B_2O_3 \cdot 4H_2O$	Pacific Coast Borax open pit, Boron, Calif.; synthetic tunellite (R. C. Erd).
Nobleite	$CaO \cdot 3B_2O_3 \cdot 4H_2O$	115278; N. of DeBely mine, Death Valley Nat. Monument; synthetic nobleite (R. C. Erd).
Gowerite	$CaO \cdot 3B_2O_3 \cdot 5H_2O$	115277; Hard Scramble Claim, Death Valley Nat. Monument; synthetic gowerite (R. C. Erd).
Veatchite	$SrO \cdot 3B_2O_3 \cdot 2H_2O$	117214; synthetic veatchite (C. R. Parkerson via R. C. Erd).
Synthetic	$CaO \cdot 3B_2O_3 \cdot 2H_2O$	Synthetic calcium veatchite (C. R. Parkerson via R. C. Erd).
Synthetic	$MgO \cdot 3B_2O_3 \cdot 7\frac{1}{2}H_2O$	Synthetic macallisterite (R. C. Erd).
Synthetic	$MgO \cdot 3B_2O_3 \cdot 5H_2O$	Synthetic aksaite (H. A. Lehmann via R. C. Erd).
Synthetic	$SrO \cdot 3B_2O_3 \cdot 4H_2O$?	Synthetic (C. R. Parkerson via R. C. Erd), possibly a dimorph of tunellite but degree of hydration uncertain.
Ginorite	$2CaO \cdot 7B_2O_3 \cdot 8H_2O$	112966; synthetic ginorite (R. C. Erd).
Strontian Ginorite	$2SrO \cdot 7B_2O_3 \cdot 8H_2O$	Natural mineral via R. C. Erd.
Synthetic	$2SrO \cdot 7B_2O_3 \cdot 8H_2O$	Synthetic volkovite [?] (R. C. Erd).
Priceite	$4CaO \cdot 5B_2O_3 \cdot 7H_2O$	Death Valley Nat. Monument (J. F. McAllister via R. C. Erd).
Pandermite	$4CaO \cdot 5B_2O_3 \cdot 7H_2O$	Panderma, Asia Minor (W. T. Schaller via R. C. Erd).
Tertschite	$4CaO \cdot 5B_2O_3 \cdot 20H_2O$[?]	Kurtpinari mine, Bigadic district, Turkey (H. Meixner via R. C. Erd).
Preobrazhenskite	$3MgO \cdot 5B_2O_3 \cdot 4\frac{1}{2}H_2O$[?]	Inder region, USSR (M. E. Mrose via R. C. Erd).
Ulexite	$Na_2O \cdot 2CaO \cdot 5B_2O_3 \cdot 16H_2O$	96994; Pacific Coast Borax open pit, Boron, Calif.; Muddmine, Boron, Calif.
Probertite	$Na_2O \cdot 2CaO \cdot 5B_2O_3 \cdot 10H_2O$	96077; Mudd mine, Boron, Calif.; Harmony Borax Works, Death Valley Nat. Monument.
Kaliborite	$K_2O \cdot 4MgO \cdot 11B_2O_3 \cdot 9H_2O$	R 5844.
Parahilgardite	$6CaO \cdot 2CaCl_2 \cdot 9B_2O_3 \cdot 4H_2O$	105822.
Kernite	$Na_2O \cdot 2B_2O_3 \cdot 4H_2O$	95737; Mudd mine, Boron, Cal.
Tincalconite	$Na_2O \cdot 2B_2O_3 \cdot 5H_2O$	107397.
Synthetic	$Na_2O \cdot 2B_2O_3 \cdot 10H_2O$	Synthetic borax, reagent grade.
Synthetic	$K_2O \cdot 2B_2O_3 \cdot 4H_2O$	Reagent grade.
Synthetic	$Na_2O \cdot 5B_2O_3 \cdot 10H_2O$	Synthetic (V. Morgan via R. C. Erd).
Larderellite	$NH_4 \cdot 5B_2O_3 \cdot 4H_2O$	C 4481.
Ammonioborite	$NH_4 \cdot 5B_2O_3 \cdot 5\frac{1}{2}H_2O$	R 6167.
Ezcurrite	$2Na_2O \cdot 5B_2O_3 \cdot 7H_2O$	Tincalayu, Argentina.
Synthetic	$2Na_2O \cdot 5B_2O_3 \cdot 7H_2O$	N. P. Nies via R. C. Erd.
Synthetic	$2Na_2O \cdot 5B_2O_3 \cdot 5H_2O$	N. P. Nies via R. C. Erd.
Synthetic	$2Na_2O \cdot 5B_2O_3 \cdot 4H_2O$	C. Cipriani via R. C. Erd.
Szaibelyite	$2MgO \cdot B_2O_3 \cdot H_2O$	95111.
Sussexite	$2MnO \cdot B_2O_3 \cdot H_2O$	C 4456.
Synthetic	$NaBO_3 \cdot 4H_2O$	Sodium perborate.

[a] Number of specimens studied is equal to the number of listings for each material separated by semicolons. Numerals represent catalog numbers in the mineral collection of the Smithsonian Institution.

3. Samples

The samples studied are listed in table 1. Column 1 of this table lists the mineral or chemical name, column 2, the empirical formula, and column 3, the source of the material. Throughout this paper, samples will be referred to by the mineral names and synthetic samples will be designated by their composition unless it is known that the synthetic and natural minerals are equivalent. In the latter case the mineral name will be used. Samples were obtained generally from two sources, the mineralogical collection of the Smithsonian Institution and the U.S. Geological Survey. In column 3, designations denoted by numbers correspond to catalog numbers in the Smithsonian collection. Origins of specimens obtained from the U.S. Geological Survey are listed in column 3. The total number of samples of each mineral type studied is indicated by the number of listings in column 3 separated by semicolons. The order in which the samples are listed in table 1 corresponds to the order followed in the discussion.

4. Results and Discussion

4.1. Presentation of Data

Data will be presented here as in the previous report [1]. Compounds are grouped according to the anion type expected based on the ideas presented by Christ [16]. For each compound, observed bands are tabulated with the type of band designated by the usual abbreviations.[2] Typical spectra are shown only for a few of the materials and only for the range 1800 cm^{-1} to approximately 300 cm^{-1}.

4.2. Borates With Simple Anions

In order to assess the extent to which analyses of the spectra of the hydrated borates can be pursued, it is instructive to consider first the spectra of hambergite, bandylite, teepleite, and pinnoite. These materials have known structures with relatively simple anions. Hambergite contains unhydrated planar BO_3^{-3} groups [17, 18] and the formula $Be_2(OH)BO_3$ represents the structure. Both bandylite and teepleite contain isolated $B(OH)_4^{-1}$ groups and their structures may be represented by the formulas $CuB(OH)_4Cl$ and $Na_2B(OH)_4Cl$ respectively [19, 20, 21]. Pinnoite contains anions of the form $[B(OH)_3OB(OH)_3]^{-2}$ which can be considered as resulting from condensing two $B(OH)_4^{-1}$ groups with the elimination of H_2O [22]. It is of interest to compare the spectra of these substances with those obtained in previous studies of the anhydrous borates [1] where it was found that boron in

[2] s—strong, v—very, b—broad, m—medium, w—weak, sh—shoulder.

three-fold coordination could be differentiated by the strong absorption derived from ν_3 of the isolated ions which generally persisted in the complex anion. It was found that triangular boron even in complex anions exhibited broad strong absorption in the region 1100–1300 cm^{-1} and tetrahedral boron in the region 800–1100 cm^{-1}. The ν_2 and ν_4 region (600–800 cm^{-1}) of the isolated ions also was found useful for differentiating these anion types provided isotope substitution was possible (see ref. 1; figs. 1, 2, 19, and p. 486).

The validity of these conclusions with respect to the hydrated borates can be evaluated by considering the spectra of the hydrates with simple anions shown in figure 1 and the absorption bands listed in table 2. In hambergite the strong band at 1300 cm^{-1} can be ascribed to ν_3 and the strong broad band centered at 750 cm^{-1} probably arises from Be–O vibrations. The 600 and 650 cm^{-1} bands superimposed on the Be–O band are probably the two components of ν_4, and ν_2 is probably obscured by the Be–O band. The 1155 cm^{-1} band is unexpected. It does not seem strong enough for a ν_3 band and it is tentatively considered to be a bending mode involving BeOH.

In teepleite and bandylite the ν_3 bands are ascribed to the strong bands between 900 and 950 cm^{-1}. The somewhat weaker band at 845 cm^{-1} in teepleite may arise from a second component of ν_3 or from ν_1. In both materials the strong bands at lower frequencies may be due to ν_4 or to an OH torsional mode. In teepleite the bands at 1170 and 1302 cm^{-1} are quite strong and might be erroneously considered to be ν_3 fundamentals of triangular borate ions. In this spectrum they are weaker than the ν_3 for the tetrahedral borate group and there is no danger of misinterpretation. These bands may represent either combinations or B–OH bending modes. In bandylite the 1255 cm^{-1} band is no weaker than the ν_3 band and misinterpretation is possible. From spectral studies on orthoboric acid, however, it seems that this band most probably arises from an OH distortion vibration [23].

In the pinnoite spectrum the strong broad bands in the 800–1000 cm^{-1} range are the most prominent features of the spectrum and presumably are derived from the antisymmetrical vibration, ν_3, of the tetrahedral units. The complex series of bands below 800 cm^{-1} are probably derived from the original ν_2 and ν_4 vibrations. The region above 1100 cm^{-1} contains three broad strong bands which are somewhat weaker than the antisymmetrical bands and are probably the result of B–OH distortion modes. These bands might easily be assumed to arise from triangular boron in a material with an unknown anion and show that interpretations must be made with great caution.

On the basis of these spectra it must be concluded that hydration of the borate anions produces spectra which cannot be interpreted readily from a knowledge of the spectra of the corresponding anhydrous anion. Hydration appears to produce absorption bands, some of which are very strong, throughout the spectra range studied. Bands apparently derived from ν_3 modes of the anhydrous BO_3^{-3} and BO_4^{-5} groups still appear in the spectra of the hydrated anions. These bands are very strong and occur in the expected positions, i.e., 800–1100 cm^{-1} for tetrahedral boron and above 1100 cm^{-1} for triangular boron. However, strong bands apparently originating from B–OH distortion modes complicate the spectra, particularly in the region 1100–1400 cm^{-1}.

Data on teepleite have been obtained by Plyusnina and Kharitonov [15]. In gross features the spectra agree reasonably well but there are significant differences. For example, they do not report the 1450 or 430 cm^{-1} bands at all and band positions vary up to 21 cm^{-1} for the 845 cm^{-1} band which they found

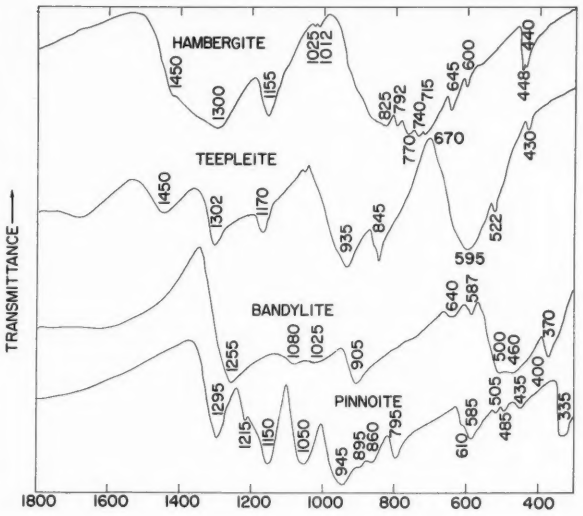

FIGURE 1. *Infrared absorption spectra of hydrated borates containing simple anions.*

TABLE 2. *Infrared absorption spectra of borates with simple anions*

Hambergite	Pinnoite	Teepleite	Bandylite
	3560 s	3530 s	3480 s
	3400 sb	3400–2500 sb	3440 sbsh
	3140 svb	1450 mvb	2400 sb
1450 ssh	2930 vb	1302 sb	1255 svb
1300 vsvl.	1295 sb	1170 s	1080 mvb
	1215 mb	935 vsb	1025 mvb
1155 s	1150 sb	845 vs	905 svb
1025 w	1050 svb	670 sh	640 w
1012 w	945 svb	595 svb	587 w
	895 msh		
825 sb	860 sb	522 w	500 svb
792 s	795 sb	430 w	460 svb
770 s			370 m
740 s			300 w
715 s	610 wsh		
645 m	585 mb		
600 m	505 w		
448 m	485 m		
440 m	435 mb		
	400 m		
	335 m		
	310 m		

at 866 cm^{-1}. The spectrum of pinnoite has been reported by Takeuchi [5] with considerable disagreement in the data. Comparison of the various spectra shows that there are considerable discrepancies in numbers of bands, band locations, and band contours.

5. Divalent Metal Borates

5.1. The $MeO \cdot 3B_2O_3 \cdot xH_2O$ Compounds

The family of divalent metal borates of general formula $2MeO \cdot 3B_2O_3 \cdot xH_2O$ comprise the minerals inyoite, meyerhofferite, colemanite, fabianite, inderite, kurnakovite, inderborite, and hydroboracite. Except for fabianite ($2 \cdot 3 \cdot 1$) all of these minerals, as well as a synthetic strontium ($2 \cdot 3 \cdot 5$) analog of colemanite were examined during the present study. The infrared spectrum for fabianite has been reported by Kuhn and Moenke [13]. Among the other $2 \cdot 3 \cdot x$ compounds crystal structures have been determined for the following: Inyoite [25], meyerhofferite [26], colemanite [27], inderite [28, 29], and hydroboracite [30]. These borates all contain similar anions built up from six-membered rings formed from alternate boron and oxygen atoms by corner sharing among two BO_4 tetrahedra and one BO_3 triangle. The oxygen atoms not shared by two boron atoms attach a hydrogen to form hydroxyl groups [16]. Isolated anions, $[B_3O_3 \cdot (OH)_5]^{-2}$ are found in inyoite, meyerhofferite and inderite. In colemanite and hydroboracite, similar anions polymerize into chains having the formula $[B_3O_4(OH)_3]_n^{-2n}$.

Typical spectra for some of these materials are shown in figure 2 and the observed absorption bands are listed in table 3. As seen in figure 2, the spectra are very complex and more than a cursory interpretation is not possible. The spectra of inyoite and meyerhofferite are very similar with the predominant features being a strong complex absorption band near 1400 cm^{-1} and a similar band below 1200 cm^{-1}. The former band probably is the counterpart of the antisymmetric mode for the triangular boron atoms and the latter band for the tetrahedral boron groups.

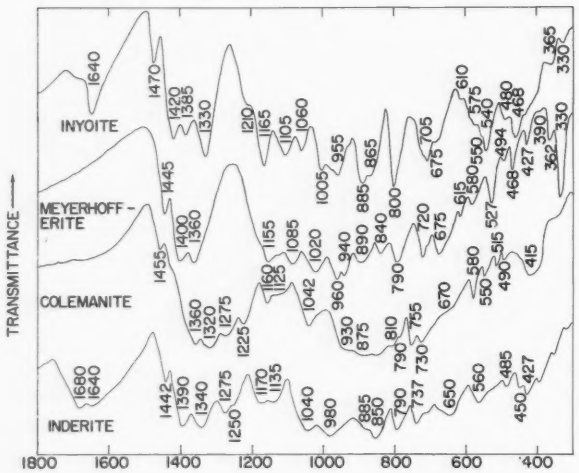

FIGURE 2. *Infrared absorption spectra of* $2MeO \cdot 3B_2O_3 \cdot XH_2O$ *compounds.*

TABLE 3. *Infrared absorption spectra of* $2MeO \cdot 3B_2O_3 \cdot XH_2O$ *compounds*

Inyoite	Kurnakovite	Inderite	Inderborite
3530 s	3550 m		
3440 s	3450 s		
3200 vsvb	3200 vsvb		
		1680 mb	
1640 mb	1650 mvb	1640 mb	1660 mvb
1470 msh	1450 msh	1442 msh	1460 msh
1420 s	1400 sb		1410 sb
1385 s	1390 s	1390 sb	1390 msh
1330 s	1347 sb	1340 sb	1340 sb
	1257 s	1275 s	1290 msh
1210 msh	1215 s	1250 msh	1200 sb
1165 s	1160 m	1170 mb	1150 wsh
1105 sb	1080 msh	1135 mb	1065 s
1060 s	1045 msh	1040 s	1020 msh
1005 s	1010 sb		
955 sb	987 sb	980 svb	960 sb
885 sb	860 svb	885 msh	
865 sb		850 sb	860 sb
800 s	807 s	790 m	810 m
	735 m	737 m	755 m
705 sb	710 m		715 mvb
675 msh	650 mb	650 mvb	650 mbsh
610 w			
575 msh		560 m	
550 w	520 mb		530 mvb
540 m			
480 msh		485 m	
468 s	460 s	450 m	435 m
365 m		427 s	
330 w		325 mb	

TABLE 3. *Infrared absorption spectra of* $2MeO \cdot 3B_2O_3 \cdot XH_2O$ *compounds*—Continued

Colemanite	Sr Colemanite	Hydroboracite	Meyerhofferite
3590 s			3600 s
3510 b			3470 s
			3420 sb
			3000 sb
3130 svb			3020 svb
1455 msh	1450 msh		1445 msh
1360 sb	1350 sb	1365 sb	1400 sb
1320 sb	1300 sb	1300 s	1360 sb
1275 sb	1260 sb	1280 s	
1225 s	1190 mb	1188 s	
1160 mb	1150 mb	1130 mb	1155 sb
1125 mvb	1060 msh	1080 sb	1085 sb
1042 s	1030 mb	1050 mb	1020 sb
		985 mbsh	960 sb
930 svb	925 b	950 sb	940 sb
875 svb	865 sb	882 s	890 mb
810 msh		835 s	840 mb
790 msh	790 msh	800 msh	790 sb
755 s	750 s	760 s	720 s
730 s	730 m		675 m
670 w	710 msh		615 w
580 m	575 m	580 m	580 m
550 m	545 w	550 w	
515 m	510 w	530 w	527 m
490 w	490 w	505 w	494 w
		470 m	468 s
	435 w	435 w	427 m
415 sb		425 w	
		410 w	390 w
			362 m
	330 sb	310 sb	330 s

Aside from the gross similarity it is not possible to correlate the spectra band for band because there appear to be noticeable shifts of bands between the two spectra. These shifts are probably to be attributed to differences in hydrogen bonding largely produced by water molecules in the two structures, the formula of inyoite having $4H_2O$ whereas that of meyerhofferite has only one H_2O (table 1). The noticeable effects throughout the spectral range produced by this water are the main deterrent to a more detailed analysis of these spectra. The effect of polymerization on the isolated anions to form the chains in colemanite and hydroboracite can be determined by comparing their spectra with those of inyoite and meyerhofferite. The bands in colemanite and hydroboracite are broader and apparently more complex. In addition, there is a considerable apparent shifting of bands as might be expected from loss of hydrogen bonding water and coupling of the anions. The spectrum of colemanite gives a clear indication that the stretching vibrations involving the triangular boron atoms are represented by the band complex near 1300 cm^{-1}. In the spectra of inyoite and meyerhofferite the strong bands, just below 1200 cm^{-1} might have been considered part of the antisymmetric stretch of the triangular borons. The fact that these bands become much weaker in colemanite which contains fewer B—OH bonds implies that these bands may arise from B—OH bending modes which might be expected in this frequency range [23]. It should be noted, however, that the spectrum of fabianite reported by Kühn and Moenke [13] appears to contradict the present conclusions, because it exhibits a strong band near 1142 cm^{-1}.

Inderite and kurnakovite are polymorphs and their spectra correspond very closely as shown by the tabulated bands. Inderborite, a mixed calcium-magnesium compound, also shows a spectrum similar to both the magnesium and the calcium compounds. The gross features of the spectra of the various magnesium and calcium compounds are also similar, but there are many differences in band positions and intensities.

Data on all of these materials, except the synthetic compound, have been reported by one or more of the earlier workers [5, 7, 8, 9, 14, 15]. In place of comparing the previous data for each material, it is useful to consider reported results on colemanite which has been studied by all these investigators. The frequency range considered is from 650 to 1350 cm^{-1} since this was the range used by Takeuchi [5]. In general appearance, of all five spectra for colemanite are very similar, but the similarity holds only for the gross features. Between 650 and 1350 cm^{-1} Takeuchi [5] and Moenke [7] report twelve absorption bands; Plyusnina and Kharitonov [15], fourteen; Akhamanova [14], nine; and the present work, thirteen. Thus the most probable number of bands would seem to be between twelve and fourteen. However, the totals are obtained quite differently by the several workers. Consider, for example, the 1042 cm^{-1} band of figure 2 which appears to be distinct and well separated from neighboring bands. Akhamanova [14] reports a band at 1050 cm^{-1}, Plyusnina and Kharitonov [15] a strong band at 1048 cm^{-1} plus two additional bands at 1002 and 1062 cm^{-1}, Moenke [7] a strong band at 1046 cm^{-1} and Takeuchi's [5] spectra indicate a band at about 1030 cm^{-1}. In addition to these uncertainties in band numbers and locations there are considerable differences in relative intensities and band contours for many of the bands throughout the spectrum. The same considerations apply to comparisons between the present and previous data on the other members of the 2:3:x borates. Possible explanations and implications of these facts will be discussed later.

5.2. The $MeO \cdot 3B_2O_3 \cdot XH_2O$ Compounds

Compounds studied with the empirical formula $MeO \cdot 3B_2O_3 \cdot XH_2O$ are tunellite, nobleite, gowerite, synthetic aksaite, veatchite, synthetic calcium-veatchite [32], synthetic macallisterite [33], and a synthetic 1:3:4? strontium borate. Of these materials, the structure is known only for nobleite and tunellite [34] which are isomorphous. The anion consists of three six-membered rings forming a $[B_6O_9(OH)_2]^{-2}$ unit. The six-membered rings are the same as those found in the $2MeO \cdot 3B_2O_3 \cdot XH_2O$ compounds and each contains two tetrahedral and one triangular boron. The $[B_6O_9(OH)_2]^{-2}$ ion contains three triangular and three tetrahedral boron groups and is unique in that one oxygen atom is common to all three rings. The ions are linked in sheets through certain of the off-ring oxygen atoms. The structures of the anions in the other members of this series are not yet known, but it might be expected to be similar, probably linked with differing degrees of hydration and/or polymerization [16].

Data obtained on these materials are given in table 4 and typical spectra are shown in figure 3. It would be expected that these spectra should show some similarities with those of figure 2, since the anions are built of similar units and indeed there are many similarities in band positions in the two sets of spectra. However, it was surmised that the coupling between rings in tunellite would be strong enough to produce considerable broadening and band overlap. The reverse situation actually occurs, many bands being clearly resolved and relatively sharp. From the similarities of the spectra (see data of table 4), it is clear that nobleite, tunellite, and the synthetic 1:3:4? synthetic strontium borate have similar anions. Examination of figure 3, shows that it is probable that gowerite has the same anion on the basis of the similarity of the spectra. In gowerite the bands are sharper and appear to be resolved better, a result to be expected if depolymerization of the anion occurs with increased water content. It also appears that veatchite possesses the same anion as tunellite with band broadening and loss of resolution accompanying

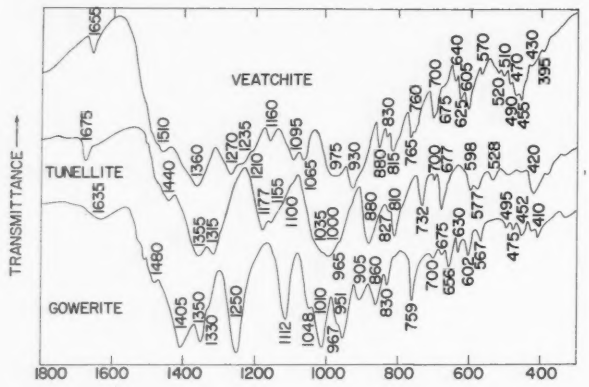

FIGURE 3. *Infrared absorption spectra of* $MeO \cdot 3B_2O_3 \cdot XH_2O$ *compounds.*

the dehydration and polymerization. From the tabular data (table 4), it is clear that the spectra of veatchite and synthetic calcium-veatchite are very similar and the materials probably contain the same anion. The conclusions with respect to the two magnesium compounds, synthetic aksaite, and synthetic macallisterite, are made with much less certainty; but again it seems probable that these materials also may contain the same anion with differing degrees of hydration and polymeriztion. On the basis of the infrared spectra alone, therefore, it is concluded that all the $MeO \cdot 3B_2O_3 \cdot XH_2O$ compounds probably contain similar anions. These spectra do not appear to have been reported previously.

TABLE 4. *Infrared absorption spectra of* $MeO \cdot 3B_2O_3 \cdot XH_2O$ *compounds*

Nobleite	Tunellite	Synthetic $SrO \cdot 3B_2O_3 \cdot 4H_2O$?
3540 mb		
3380 svb		
3200 svb		
2400 svb		
1675 mvb	1675 mb	
	1440 msh	1460 mb
1385 sbsh	1355 sb	1375 svb
1322 sb	1315 sb	1325 svb
1300 msh		
1180 mb	1177 mb	1180 sb
1160 mb	1155 mb	
1125 mb		1125 sb
1107 m	1100 w	1100 w
1033 msh	1035 msh	1010 sb
965 sb	1000 sb	962 svb
930 msh	965 msh	927 mb
880 sb	880 sb	875 sb
827 m	827 msh	
805 sb	810 s	810 sb
737 m	732 m	735 m
705 m	700 w	
670 mb	677 m	670 mb
602 m	598 m	
570 w	577 m	
	528 w	
460 wb		
425 w	420 m	

TABLE 4. *Infrared absorption spectra of* $MeO \cdot 3B_2O_3 \cdot XH_2O$ *compounds*—Continued

Veatchite	Synthetic Ca-Veatchite
3420–2900 b	
1655 w	1665 w
1510 ssh	
1360 sb	1390 sb
1270 sb	1265 wsh
1235 msh	1240 sb
1210 wsh	
1160 m	1180 msh
1095 mb	1130 m
1065 mb	1075 mb
975 sb	975 sb
930 sb	910 sb
880 m	870 m
830 w	832 m
815 m	810 m
765 m	755 m
760 m	745 wsh
700 m	700 w
675 msh	
640 w	650 w
625 m	610 m
605 m	600 wsh
570 w	572 wsh
520 w	535 wb
510 w	
490 w	495 w
470 m	
455 m	
430 msh	
395 mb	

TABLE 4. *Infrared absorption spectra of* $MeO \cdot 3B_2O_3 \cdot XH_2O$ *compounds*—Continued

Gowerite	Synthetic Aksaite	Synthetic MacAllisterite
	3600 s	
	3450–2400 sb	
1635 wb	1652 mb	
1480 msh	1485 msh	1470 msh
1405 s	1425 sb	1410 sb
1350 s	1385 sb	1358 sb
1330 msh	1325 sb	
1250 s	1245 sb	1240 s
	1210 sb	
1112 s	1155 mb	1158 mb
	1095 sb	1122 sb
1048 ssh		1060 sb
1010 s	1020 sb	1005 msh
		980 m
967 msh		965 m
951 s	950 sb	880 msh
905 mb	898 mb	
860 mb	850 mb	855 s
830 m		812 s
759 m	800 sb	
700 w	725 w	698 wb
675 w	675 mb	670 m
656 m	655 w	
630 w		
602 w		
567 w	525 w	580 wb
495 w	455 w	
475 w		
452 w		
410 w	410 w	440 w

5.3. The $2MeO \cdot 7B_2O_3 \cdot 8H_2O$ Compounds

Three members of this series were studied, the data are given in table 5 and spectra are shown in figure 4. The marked similarity of the spectra and the compounds makes it almost certain that the anions are identical. The structures of the anions are not known and the spectra are too complex to attempt to predict the anion on this basis alone. There is no doubt that the anion contains both three-fold and four-fold coordinated boron as shown by the strong bands

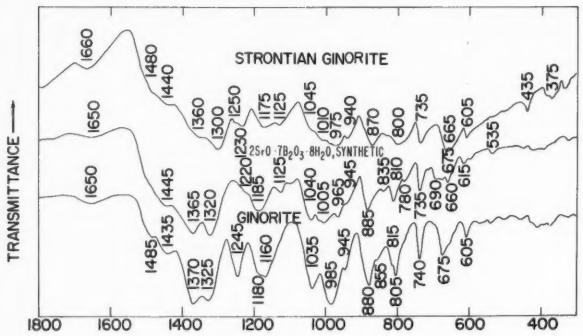

FIGURE 4. *Infrared absorption spectra of* $2MeO \cdot 7B_2O_3 \cdot 8H_2O$ *compounds.*

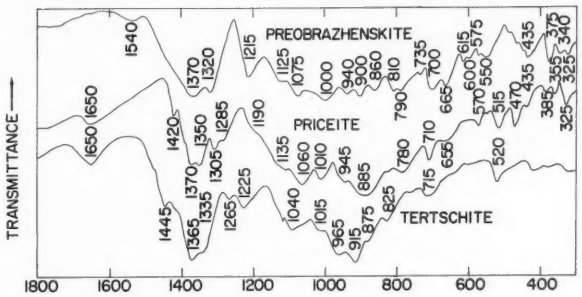

FIGURE 5. *Infrared absorption spectra of miscellaneous hydrated divalent metal borates.*

TABLE 5. *Infrared absorption spectra of* $2MeO \cdot 7B_2O_3 \cdot 8H_2O$ *compounds*

Ginorite	Strontian Ginorite	$2SrO \cdot 7B_2O_3 \cdot 8H_2O$ Synthetic
3250 vsvb		
1650 wvb	1660 mvb	1650 wvb
1485 msh	1480 mbsh	
1435 msh	1440 mbsh	1445 mbsh
1370 s	1360 svb	1365 s
1325 s	1300 sb	1320 s
1245 s	1250 m	
	1230 mb	1220 mb
1180 s	1175 svb	1185 s
1160 s	1125 mvb	1125 m
1035 m	1045 m	1040 s
985 sb	1010 sb	1005 sb
945 m	975 svb	965 m
880 s	940 sb	945 msh
855 msh	870 s	885 s
815 msh		835 m
805 s	800 sb	810 s
		780 msh
740 s	735 s	735 s
675 sb	655 sb	690 m
605 m	605 m	675 m
		660 m
	435 m	615 w
	375 mvb	535 w

TABLE 6. *Infrared absorption spectra of miscellaneous divalent metal borate compounds*

Priceite	Tertschite	Preobrazhenskite
1650 mvb	1650 mb	1540 mvb
1420 m	1445 m	
1370 s	1365 s	1370 sb
1350 s	1335 ssh	1320 s
1305 s		
1285 msh	1265 w	
1190 msh	1225 m	1215 sb
1135 msh		1125 msh
1060 sb	1040 sb	1075 sb
1010 sb	1015 msh	1000 svb
945 ssh	965 sb	940 mb
885 svb	915 sb	900 m
	875 msh	
780 sb	825 m	860 mvb
710 m	715 m	810 m
655 mb		790 m
		735 w
570 m		700 sb
515 m	520 m	665 mb
470 m		615 m
		600 w
435 w		575 w
		550 mb
385 m		435 mvb
355 w		375 m
325 m		340 m
		325 m

near 1400 and 1000 cm^{-1} respectively. In addition the spectra show a strong resemblance to the previous spectra for compounds containing six-membered rings of alternate boron and oxygen atoms, with one triangular and two tetrahedral boron atoms. Consequently, it appears likely that these rings may exist in the anions. The relative weakness of lower frequency vibrations (i.e., below 600 cm^{-1}) in these spectra, however, is an indication that the anions are not coupled six-membered rings and it is very unlikely that the anions are so small that no low frequency vibrations exist. It is probable that the symmetry of the anions is sufficiently high that lower frequency modes are much weaker than in the previous compounds. Again there do not appear to be any previous reports of spectra of these materials.

5.4. Miscellaneous Divalent Metal Borates

Data on the $4CaO \cdot 5B_2O_3 \cdot XH_2O$ compounds are given in table 6 together with those for preobrazhenskite $-3MgO \cdot 5B_2O_3 \cdot 4\frac{1}{2}H_2O$[?] [35]. The spectra are shown in figure 5. The three materials show evidence of both triangular and tetrahedral boron in the strong bands in the 1300–1400 cm^{-1} and 800–1000 cm^{-1} region respectively. The spectra of priceite and tertschite are very similar and these materials may contain similar anions. The spectrum of preobrazhenskite is indicative of a large anion with considerable interaction between the anion structural units.

From the data obtained here the spectra of pandermite and priceite are considered to be identical. The sample of priceite yielded much the better spectrum of the two specimens, that for pandermite being less well resolved. However, for each band found in the spectrum of pandermite a corresponding band is observed in the priceite with frequencies differing at most by ± 1 cm^{-1}. In addition, the same relative intensity relationships are shown by the bands in the two materials. It seems possible to conclude that these materials are most probably identical [36].

The spectrum of priceite (pandermite) has been reported by other workers [5, 7, 14, 15] and that of tertschite by Meixner and Moenke [12]. Comparison of the present and previous results leads to the same conclusions mentioned earlier. The spectra for a given material are in superficial agreement. There are many discrepancies when details are examined.

Data obtained on other divalent metal borates are given in table 7 with spectra for ulexite and kaliborite shown in figure 6. The anions of probertite and ulexite are known to be a ring structure containing three tetrahedra and two triangles with one tetrahedron being common to both rings [37, 38]. From the tabulated data it is clear that the infrared spectra corroborate the similarity of the anions in these materials probertite and ulexite. The spectrum of kaliborite is very poorly resolved in the ν_3 region for tetrahedral borate groups, but is otherwise similar to the spectra of ulexite. The parahilgardite yielded a very poor spectrum and it is suspected that this material was contaminated with $CaCO_3$ as the 875 and 725 cm^{-1} bands strongly resemble the ν_2 and ν_4 bands of calcite.

6. Monovalent Metal Borates

6.1. The $Me_2O \cdot 2B_2O_3 \cdot XH_2O$ Compounds

Several borates of the type $Me_2O \cdot 2B_2O_3 \cdot XH_2O$ were studied and the data are tabulated in table 8. Typical spectra for tincalconite and potassium tetraborate tetrahydrate are shown in figure 7. Morimoto [39] has determined the structure of borax and found that the anion consists of isolated $[B_4O_5(OH)_4]^{-2}$ rings. Marezio et al., [40] have found the same anion in potassium tetraborate tetrahydrate. The rings contain two triangular and two tetrahedral borate groups joined at common oxygen atoms. The two tetrahedral groups are further linked by means of an oxygen bridge across the ring. All off-ring oxygen atoms are hydrated in borax.

As noted in the previous study the alkali borates yield very poorly resolved spectra under the conditions used here. From the tabulated absorption bands it is noted that all the materials show similar spectra and probably all contain the basic $[B_4O_5(OH)_4]^{-2}$ anion

TABLE 7. *Infrared absorption spectra of miscellaneous borate compounds*

Ulexite	Probertite	Kaliborite	Parahilgardite
3562 s	3620 s		
3400 sb	3550 s		
3000 vsvb	3350 vsvb		
1650 mb	1650 mvb		
1620 mb			
1470 m	1470 m		
1415 sb			
1390 s	1425 msh	1410 msh	1425 vsvb
1355 s	1375 s	1350 sb	1350–1000 vsvb
1315 s	1325 sb		
1205 s	1210 m	1185 svb	
1090 ssh	1130 ssh		
1050 sb	1080 sb	1080 sb	
995 s	1040 m	1000–750 svb	
975 s	985 msh		
950 ssh	955 s		
925 msh	930 s		
855 s	900 s		875 s ($CeCO_3$?)
825 ssh	830 s		790 s
740 m	750 m		775
710 m	675 m	705 s	725 s ($CaCO_3$?)
640 m	555 w	655 s	
530 m	515 m	625	
		570 w	
430 mb	440 m	445 vsb	
350 m	380 m		355 vbvs

TABLE 8. *Infrared absorption spectra of* $Me_2O \cdot 2B_2O_3 \cdot XH_2O$ *compounds*

Kernite	Tincalconite	Borax	$K_2O \cdot 2B_2O_3 \cdot 4H_2O$ synthetic
	3500 sb	3500–	
	3340 vsb	3000 vsvb	
	3000 svb		
	2400 svb	2000 svb	
1700 mvb	1630 mvb	1620 mvb	1625 mvb
1460 m	1455 msh	1450 msh	
1425 msh	1405 svb	1390 svb	1395 svb
1340 vsvb	1340 vsvb	1330 vsvb	1320 vsvb
	1190 msh	1275 mvb	
1160 m	1155 sb	1155 mb	1220 s
	1125 svb	1123 mvb	1160 m
1075 mb	1075 svb	1070 mb	1080 sb
1010 svb	1025 svb		1060 msh
	985 sb	980 sb	970 sb
950 vsvb	940 sb	935 sb	905 sb
865 svb			
820 svb	805 sb	800 svb	805 svb
	750 mvb	750 svb	745 w
			710 m
685 mvb	665 mvb	665 mvb	665 mb
			600
	600 mvb	595 wb	560 mvb
550 s	520 mvb	505 mshvb	490 m
495 mb	425 mvb	420 sb	450 mb
455 mb		395 s	422 mvb
425 mvb			390 m

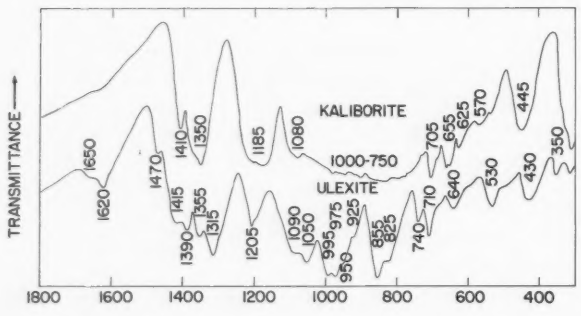

FIGURE 6. *Infrared absorption spectra of hydrated borates containing both mono- and divalent metal ions.*

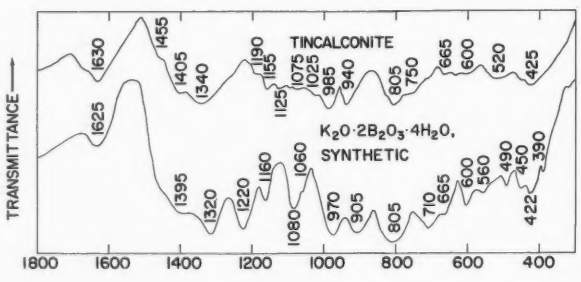

FIGURE 7. *Infrared absorption spectra of* $Me_2O \cdot 2B_2O_3 \cdot XH_2O$ *compounds.*

in some state of hydration or polymerization. The specimen of $K_2B_4O_7 \cdot 4H_2O$ used was obtained from a commercially available reagent labeled $K_2B_4O_7 \cdot 5H_2O$. The x-ray diffraction pattern of this compound can be indexed readily from the unit cell data of Marezio et al., [40] and it has been tabulated as the tetrahydrate.

The previous data obtained on this group of materials together with the present data exhibit a confusing pattern. The spectra for borax of Miller and Wilkins [4] and of Moenke [7] agree with each other but differ considerably from that of Akhamanova [14] and the present results. Miller and Wilkins [4] reported the spectrum of $K_2B_4O_7 \cdot 5H_2O$ which closely resembles their spectrum of borax but differs considerably from the spectrum of $K_2B_4O_7 \cdot 4H_2O$ obtained here. Takeuchi's [5] results for kernite agree well with the present data but both disagree in many respects with the results of Moenke [7]. The overall lack of agreement between the spectra obtained by different workers appears to be greatest for these materials. This question will be discussed later.

6.2. The $Me_2O \cdot 5B_2O_3 \cdot XH_2O$ Compounds

Data for the minerals ammonium larderellite and ammonioborite [41] and the synthetic 1:5:10 sodium borate are given in table 9. Representative spectra are not shown because there is strong absorption and poor resolution throughout the entire spectral range. The strong absorption is to be expected in the two ammonium compounds because they contain the infrared active NH_4^+ ion in addition to water of hydration and a complex borate anion. Christ [16] has predicted that sborgite, larderellite, and ammonioborite have the same anion and the data of table 9 confirm this prediction for the ammonium compounds with little question. The spectrum of the 1:5:10 synthetic sodium borate differs from those of the ammonium borates in many details but not in gross features. Because of the unknown effect of the NH_4^+ ion on the spectra, it is possible that all three compounds contains similar anions.

TABLE 9. *Infrared absorption spectra of* $Me_2O \cdot 5B_2O_3 \cdot XH_2O$ *compounds*

$Na_2O \cdot 5B_2O_3$: $10H_2O$ synthetic	Ammonioborite	Larderellite
1670 mb	1650 mvb	
	1425 vsvb	1425 vsvb
1375 vsvb	1350 vsvb	1350 vsvb
1300 vsvb	1235 vsvb	1225 mvb
1195 m	1190 sb	1185 s
1145 svb	1160 mb	1165 m
1075 sb	1085 sb	1085 mvb
1045 m	1055 sb	1055 mb
1010 sb	1015 svb	1015 mvb
950 m	940 svb	940 mb
925 s	915 sb	920 mvb
910 s	880 w	880 w
780 s	820 mvb	810 mb
765 s	775 sb	775 s
675 vsvb	740 m	
470 mb	675 sb	675 mvb
440 mb	545 s	545 s
375 mvb	510 mb	455 m
	460 mb	425 mvb

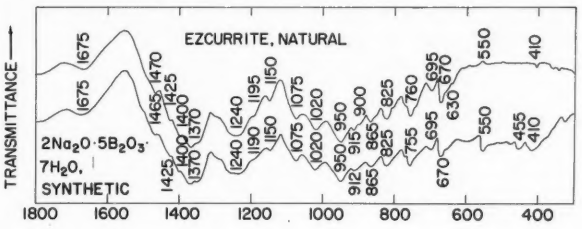

FIGURE 8. *Infrared absorption spectra of* $2Na_2O \cdot 5B_2O_3 \cdot 7H_2O$ *compounds.*

6.3. The $2Me_2O \cdot 5B_2O_3 \cdot XH_2O$ Compounds

Ezcurrite and the $2:5:X$ synthetic sodium borates show rather poor spectra characterized by strong absorption throughout the spectral range studied. The absorption bands observed are listed in table 10 and figure 8 shows the spectra for a synthetic and a natural ezcurrite. It is obvious from figure 8 that despite the rather poor resolution that these materials are almost certainly the same insofar as the anions are concerned. In addition, the fact that, band for band the frequencies are the same within experimental error may be interpreted to mean that the materials are chemically and structurally identical. This conclusion is based on previous studies which showed that change of anion or crystal structure generally produces shifting of some bands in the infrared spectrum [42]. The close similarity in the spectra of all three minerals listed in table 10 indicates that the anions are similar.

TABLE 10. *Infrared absorption spectra of* $2Me_2O\ 5B_2O_3\ XH_2O$ *compounds*

Ezcurrite	$2Na_2O \cdot 5B_2O_3 \cdot 5H_2O$ Synthetic	$2Na_2O \cdot 5B_2O_3 \cdot 4H_2O$ Synthetic
1675 mvb	1625 mvb	1650 mvb
1470 mb	1465 mb	1440 mvb
1425 m		
1400 mbsh	1400 mb	1360 svb
1370 vsb	1350 vsvb	1325 svb
1240 sb	1245 svb	1250 mvb
1195 msh		1230 svb
1150 m		1150 m
1075 mb	1045 mvb	1070 sb
1020 mb	1015 svb	1030 svb
950 sb	945 svb	925 sb
915 m		
900 w		
865 m	870 m	880 svb
825 m	825 mvb	830 mvb
760 m	740 mvb	740 mvb
695 m	695 mb	695 mvb
670 s	670 mvb	650 mb
	630 w	600 mvb
550 w	550 mvb	550 m
455 w	455 mvb	440 mb
410 mb	410 mvb	

6.4. Miscellaneous Borates

Data for three borates not readily classified with the previous groups are given in table 11 and the spectra are shown in figure 9. The data for szaibelyite and

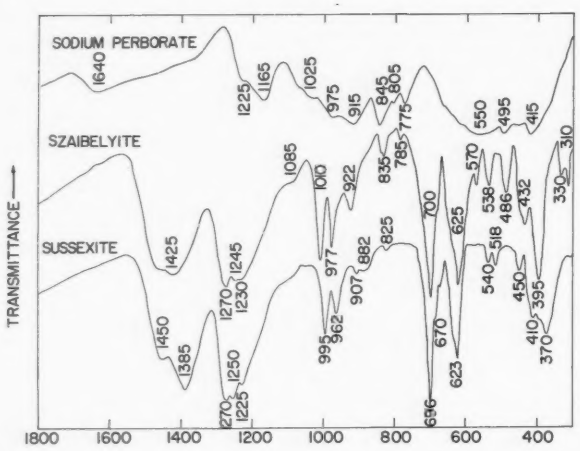

FIGURE 9. *Infrared absorption spectra of miscellaneous hydrated borates.*

TABLE 11. *Infrared absorption spectra of miscellaneous borate compounds*

$NaBO_3 \cdot 4H_2O$ sodium perborate	Szaibelyite	Sussexite
3590 s	3555 s sharp	
3500–3000 svb	1425 vs	1450 sb
1640 wvb	1270 s	1385 s
1225 msh	1245 s	1270 s
1165 mvb	1230 s	1250 s
1025 mb	1085 msh	1225 m
975 sb	1010 s	995 m
915 svb	977 s	962 m
845 sb	922 m	907 m
805 m	835 m	882 mb
775 mb		825 w
550 svsb	785 w	696 s
495 sb	700 vs	670 msh
415 sb	625 s	623 s
	570 m	540 m
	538 m	518 m
	486 m	450 m
	432 m	410 m
	395 s	370 sb
	330 m	
	310 m	

sussexite agree reasonably well with the results obtained by Takeuchi [5] for camsellite (szaibelyite) and sussexite and with the results of Plyusnina and Kharitonov [15] for ascharite (szaibelyite). From his spectra, Takeuchi [5] concluded that the anion in these compounds was the pyroborate ion while Plyusnina and Kharitonov, apparently being unaware of Takeuchi's earlier work, noted that the spectrum of ascharite was similar to that of $LaBO_3$ which contains a triangular borate anion. However, the latter workers concluded tentatively that the complexity of the spectrum indicated a more complex ion than the simple triangular ion [15]. Akhamanova independently arrived at the same conclusion [14].

The structure of this anion has been reported to be a singly hydrated pyroborate group, with some uncertainty as to the exact structure [43] caused by translation. It is not clear that both borons are coordinated with three oxygen atoms. However, the spectrum clearly indicates that there is no tetrahedral boron present in the structure. From the earlier work on the pyroborates [1] it appears that the spectrum of anhydrous magnesium pyroborate becomes considerably less complex in the ν_2 region on hydration but more complicated in the ν_1 region. Tentative assignments are possible for many of the bands in the spectrum of szaibelyite on the basis of the spectrum of anhydrous magnesium pyroborate and the known spectrum of triangular borate groups. These are obvious and need not be specified here.

In sodium perborate the anion has been reported [44] to consist of two partly hydrated tetrahedral borate groups connected through peroxide linkages and to have the structure 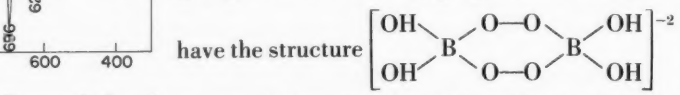 The structural formula of sodium perborate may be written $Na_2[BO_2(OH)_2]_2 \cdot 6H_2O$. This anion is unlike any previously encountered here and its spectrum is likewise unique as shown in figure 9. In this spectrum the 3590 cm^{-1} band indicates some nonhydrogen bonded OH and the broad strong band between 3500 and 3000 cm^{-1} shows that much of the OH is hydrogen bonded. The weak 1640 cm^{-1} band is attributed to the bending mode of H–O–H, and the medium broad bands at 1225 and 1165 cm^{-1} to the B–OH bending modes plus overtones and combinations. The strong absorptions at 915 and 845 cm^{-1} are derived from the ν_3 tetrahedral modes and the doublet is indicative of tetrahedral coupling as noted earlier. The strong broad band at low frequencies probably contains modes derived from ν_2 and ν_4 of tetrahedral units plus OH torsional modes. The complexity of the band indicates the presence of several overlapping bands. The spectrum for this material has been reported by Miller and Wilkins [4] with reasonably good agreement between the data.

7. Reliability of Infrared Spectra of Hydrated Borates

In comparing the spectra of different workers it has been noted that the agreement was not satisfactory. It is to be expected that on a given material, the same infrared bands having similar relative intensities should be obtained. Some latitude in the exact frequencies reported (i.e., a few cm^{-1}) and perhaps in the detection of weak bands might be expected. For the hydrated borates it is clear that data do not agree to this extent and it is desirable to examine possible reasons for the discrepancies.

The discordance in the data must be traced to one or more of three sources; first, the materials themselves; second, the preparation techniques used to prepare the materials for study; and third, the actual measurements. Of these three sources the third can probably be dismissed as a real source of error. There is no

evidence that any appreciable errors in band positions exist between the results obtained on different spectrometers. In fact the evidence is that the spectrometers agree within experimental error because many strong bands can be identified in spectra of various workers which agree within the frequency limits expected. It is believed, therefore, that the real causes for the discrepancies are to be attributed to variation in the materials or differences arising from techniques of preparation.

Insofar as the identity of the materials investigated is concerned, the previous reports give little information. Miller and Wilkins used chemical reagents in their studies [4]. Takeuchi [5] reports that his substances were carefully selected and were well-developed crystals of highest purity. Plyusnina and Kharitonov [15] used single crystals, but Akhamanova [14] and Moenke [7] give no details of the method used for selection of their specimens. In the present study most of the materials were of the highest purity presently available as judged by microscopic examination and x-ray powder diffraction. It must be noted, however, that neither these methods nor that of selecting natural single crystals ensures that the specimens are free of contaminants. If the contaminants should consist of other borates (all of which are strongly active in the infrared) even in small quantity, it is clear that some differences in the spectra may result. In addition to the question of purity, there remains a problem associated with the degree of crystallinity of the specimen. Most of the borates yield complex spectra containing many broad, obviously complex bands, containing unresolved structural details. Experience in this laboratory has indicated that two specimens of identical composition but differing either in degree of crystallinity or perhaps in perfection of crystallites can yield spectra which are very similar in gross appearance but remarkably different in detail. Broad featureless bands frequently show many resolvable details when the degree of crystallinity of the specimen is apparently improved. It appears most probable that discrepancies in the spectra of various workers consisting of differences in numbers of bands reported is to be attributed either to actual contamination of the specimens by other borates (or other spectrally active chemical species) or to differences in the crystallinity of the specimens.

Insofar as the specimen preparation techniques are concerned, the problem of purity is also involved but in a different manner. Here the concern is with the actual identity of the materials studied because of changes in degree of hydration or of interaction with the alkali halide windows used. The various workers used the following techniques of sample study: Miller and Wilkins and Takeuchi—mulls with hydrocarbon or fluorocarbon liquids using salt (NaCl?) plates [4, 5]; Moenke—pressed pellet technique using vacuum formation of KBr pellets [7]; Akhamanova—film deposited on KBr plates by evaporation of isobutyl alcohol dispersing medium [14]; Plyusnina and Kharitonov—films deposited on KCl or NaCl plates by evaporation of isopropyl alcohol [15]; present work—films deposited on CsBr plates by evaporation of CCl_4. It is well known that solids (and in particular hydrates) interact with the alkali halides and that the interaction produces changes in the spectra. Of the methods used, it would appear that the mull technique is the most preferable from the viewpoint of lessening such interactions, the film method next, and the KBr pellet the most objectionable. In addition to the increased probability of interaction in KBr pellets must be added the undesirable procedure of subjecting the hydrated borates to vacuum in the pellet forming process. Reduction in pressure might affect the state of hydration of the small quantity of hydrate present. It seems very probable that differences in positions of bands observed by different workers may be caused by shifts due to interaction with the alkali halide windows used.

In addition to the question of interaction with the alkali halide there is some uncertainty introduced by the mechanical and thermal effects of the fine grinding required to produce particles sufficiently small for infrared study. As noted earlier, the spectra for borax, a chemically pure reagent, obtained by different workers differ radically. C. J. Bowser [45] has obtained evidence showing that in KBr pellets, borax produces the spectrum of tincalconite, a lower hydrate. Thus the spectra for borax of Miller and Wilkins [4] and Moenke [7] which agree very well actually appear to represent tincalconite. Dehydration of borax can be understood in the KBr pelleting process but is hard to visualize in the mull technique, unless it occurs during grinding. Therefore, it is necessary to include the fine grinding technique among the details which might produce differences in the spectra.

It is concluded that the infrared spectra of the hydrated borates, at present, are not of acceptable reliability. The lack of reproducibility is most probably to be attributed to differences in chemical composition and degree of crystallinity and to varying interactions between the hydrated borates and the alkali halide windows. Production of definitive spectra will require systematic study of the effect of these disturbances.

8. Identification of Borate Minerals by Infrared Spectroscopy

H. Moenke has studied the infrared spectra of several hydrated borate minerals in a series of papers generally oriented toward differentiating among various borates [6–13]. As a result of his study he concluded that the spectral method could be used to identify hydrated borate minerals and has pointed out identifying features in the spectra of various minerals.

It is clear from the immediately preceding discussion and the comparisons between spectra made throughout this report that the present conclusions must disagree with the idea of identification by infrared methods. The fact that there is a disturbing amount of disagree-

799-883 O-66—4

ment between the spectra of various workers at the present time would appear to invalidate the use of spectroscopy as a method of identification. Moreover, the spectra of most borates are so complex that it seems imperative to obtain at least a degree of understanding of the origin of the spectral bands before identification of minerals of this type is attempted on the basis of their spectra. In the case of the simpler spectra, i.e., sussexite, hambergite, etc., identification by means of infrared spectroscopy is believed to be possible. However, if such minerals were contaminated with other borates (as for example sussexite contaminated with szaibelyite) identification would be almost impossible.

9. Conclusions

The infrared spectra of the hydrated borates are considerably more complex than the spectra of the anhydrous analogues. The increased complexity arises from the effects of the hydration of the borate anions and hydrogen bonding between anions. The effect of the hydrogen bonding appears to produce noticeable changes in most of the borate anion fundamentals and results in complicating the spectrum throughout the frequency range 400–4000 cm^{-1} studied here. Thus the effects are by no means restricted to the region commonly considered to be diagnostic for OH.

As a result of the increased number of bands the spectra are frequently poorly resolved and detailed interpretation appears to be remote. It is unlikely that any hydrated borate anion can be identified solely from its infrared spectrum. However, the previous conclusions concerning identification of three-fold and four-fold coordinated boron appear to be equally valid in the hydrated and anhydrous borates. For the hydrated compounds the conclusions are more uncertain because strong bands near 1200 cm^{-1} apparently arising from B—OH bending modes fall into the region previously considered as indicative of trigonal borate groups. Any serious attempt to understand the spectra of the hydrated borates will probably require deuteration as well as boron isotope substitution.

At the present time agreement between spectra obtained by different investigators is not considered to be satisfactory. The probable causes of the disagreement are believed to originate in differences in the materials themselves or from varying degrees of interaction with the alkali halide cells used. As a result of the lack of agreement between various workers as well as the inherent complexity of the spectra it is considered that borate minerals cannot be identified at this time on the basis of their infrared spectra alone.

The author is indebted to E. R. Lippincott and R. A. Schroeder for many discussions concerning the infrared data and to G. Switzer of the Smithsonian Institution and R. C. Erd of the U.S. Geological Survey who furnished the samples which made this study possible. The very helpful comments of J. R. Clark and R. C. Erd of the U.S. Geological Survey on the structure and properties of the borate minerals were invaluable.

10. References

[1] C. E. Weir and R. A. Schroeder, J. Res. NBS **68A** (Phys. and Chem.) No. 465 (1964).
[2] A. Perloff and S. Block, submitted to Acta Cryst.
[3] A. Mighell, A. Perloff, and S. Block, submitted to Acta Cryst.
[4] F. A. Miller and C. H. Wilkins, Anal. Chem. **24,** 1253 (1952).
[5] Y. Takeuchi, Min. J. (Japan) **2,** 245 (1958).
[6] H. Moenke, Jenaer Jahrbuch 1959 (II) 361.
[7] H. Moenke, Jenaer Jahrbuch 1960 (I) 191.
[8] H. Moenke, Jenaer Jahrbuch 1961 (I) 239.
[9] H. Moenke, Naturwiss. **49,** 7 (1962).
[10] H. Moenke, Spectralanalyse von Mineralien und Gesteinen (Geest and Portig, Leipzig, 1962).
[11] H. Moenke, Fortschr. Min. **40,** 76 (1962).
[12] H. Meixner and H. Moenke, Kali u. Steinsalz **3,** 228 (1961).
[13] R. Kühn and H. Moenke, Kali u. Steinsalz **12,** 399 (1963).
[14] M. V. Akhamanova, Zh. Strukt. Khim. **3,** 24 (1962).
[15] I. I. Plyusnina and Yu A. Kharitonov, Zh. Strukt. Khim. **4,** 506 (1963).
[16] C. L. Christ, Am. Min. **45,** 334 (1960).
[17] W. H. Zachariasen, Z. Krist. **76,** 289 (1931).
[18] W. H. Zachariasen, H. A. Plettinger, and M. Marezio, Acta Cryst. **16,** 1144 (1963).
[19] M. Fornaseri, Period. Min. (Rome) **18,** 103 (1949): **19,** 159 (1950).
[20] R. L. Collin, Acta Cryst. **4,** 204 (1951).
[21] V. Ross and J. O. Edwards, Am. Min. **44,** 875 (1959).
[22] F. Paton and S. G. McDonald, Acta Cryst. **10,** 653 (1957).
[23] D. F. Hornig and R. C. Plumb, J. Chem. Phys. **26,** 637 (1957).
[24] C. R. Parkerson, Naval Ordnance Laboratory, Corona, Rept. 585 (1963b).
[25] J. R. Clark, Acta Cryst. **12,** 162 (1959).
[26] C. L. Christ and J. R. Clark, Z. Krist. **114,** 21 (1960).
[27] C. L. Christ, J. R. Clark, and H. T. Evans, Acta Cryst. **11,** 761 (1958).
[28] A. Ashirov, I. M. Rumanova, and N. V. Belov, Dokl. Akad. Nauk SSR **143,** 331 (1962).
[29] I. M. Rumanova and A. Ashirov, Kristallografiya, **8,** 517 (1963).
[30] I. M. Rumanova and A. Ashirov, Kristallografiya, **8,** 828 (1963).
[31] J. R. Clark, D. E. Appleman, and C. L. Christ, J. Inorg. Nucl. Chem. **26,** 73 (1964).
[32] C. R. Parkerson, Naval Ordnance Laboratory, Corona, Rept. 583 (1963a).
[33] W. T. Schaller, A. C. Vlisidis, and M. E. Mrose, Am. Min. **50,** 629 (1965).
[34] J. R. Clark, Am. Min. **49,** 1549 (1964).
[35] V. V. Kondrat'eva, Zap. Vses. Min. Obshch. **88,** 330 (1959).
[36] See Dana's System of Mineralogy, C. Palache, H. Berman, and C. Frondel, Vol. II, p. 343 (John Wiley & Sons, Inc., New York, N.Y. 1951).
[37] H. M. Kurbanov, I. M. Rumanova, and N. V. Belov, Dokl. Akad. Nauk. SSR **152,** 1100 (1963).
[38] J. R. Clark and D. E. Appleman, Sci. **145,** 1295 (1964).
[39] N. Morimoto, Min. J. (Japan) **2,** 1 (1956).
[40] M. Marezio, A. A. Plettinger, and W. H. Zachariasen, Acta Cryst. **16,** 975 (1963).
[41] J. R. Clark, Am. Min. **45,** 1087 (1960); J. R. Clark and C. L. Christ, Am. Min. **44,** 1150 (1959).
[42] C. E. Weir and E. R. Lippincott, J. Res. NBS **65A** (Phys. and Chem.) No. 3, 173 (1961).
[43] C. P'eng, C. Y. Su, and P. H. Chang, Sci. Sinica (Peking) **12,** 1761 (1963).
[44] A. Hansson, Acta. Chem. Scan. **15,** 934 (1961).
[45] C. J. Bowser, submitted to Am. Min.

(Paper 70A2–391)

JOURNAL OF RESEARCH of the National Bureau of Standards—A. Physics and Chemistry
Vol. 70A, No. 2, March–April 1966

Interpretation of the Solution Absorption Spectra of the $(PuO_2)^{++}$ and $(NpO_2)^{+}$ Ions

J. C. Eisenstein

Institute for Basic Standards, National Bureau of Standards, Washington, D.C.

and

M. H. L. Pryce

Physics Department, University of Southern California, Los Angeles, Calif.

(November 15, 1965)

Eleven years ago we proposed a model for the electronic configuration of ions of the uranyl type. The solution absorption spectra of the $(PuO_2)^{++}$ and $(NpO_2)^{+}$ ions are here interpreted on the basis of this model. The interpretation is based on exact calculations, and on plausible arguments about the strengths and widths of the absorption peaks. If suitable values are chosen for the Coulomb integrals, the spin-orbit coupling constant, and the ligand field parameters then the calculated energy levels agree well with the observed positions of the absorption peaks.

Key Words: $(NpO_2)^{+}$ ion, plutonyl ion, absorption spectrum.

1. Introduction

Eleven years ago we published a paper [1][1] on the magnetic and spectroscopic properties of the plutonyl ion. We now know [2] that the parameters which we used in calculating the energy levels were assigned the wrong values. Despite this unhappy circumstance the correct interpretation was given to the dominant peaks in the absorption spectrum and, since the ground state of the ion was correctly identified, the calculated magnetic properties agreed with the meager available experimental data.

Our purpose in this paper is partly to present revised values of the parameters and new calculations of the energy levels. Our primary purpose is to discuss in detail the absorption spectra of the isoelectronic $(PuO_2)^{++}$ and $(NpO_2)^{+}$ ions, both of which have two electrons outside what we might call the uranyl core. We have been curious to see the extent to which plausible, semiquantitative arguments about strengths and widths of absorption lines could be used in identifying the rather complex solution absorption spectra of these ions.

In analyzing the $(NpO_2)^{+}$ and $(PuO_2)^{++}$ spectra the first important question which one has to decide is whether the ligand field strengths for these ions are the same as those for the neptunyl ion. Information bearing indirectly on this point comes from the infrared measurements of Jones and Penneman [3] on uranyl and transuranium (V) and (VI) ions in aqueous solutions. Table 1 gives the asymmetric stretching frequencies of these ions as determined by Jones and Penneman. The similarity of the stretching frequencies for the first four ions in the table indicates that the ligand fields are similar for all four. On the other hand, since for $(NpO_2)^{+}$ and $(AmO_2)^{+}$ the vibration energies are lower, the bond length is probably greater and the ligand field weaker.

TABLE 1. *Asymmetric stretching frequencies of uranyl-type ions in aqueous perchloric acid solution*

Ion	Frequency/c
	cm^{-1}
$(UO_2)^{++}$	965
$(NpO_2)^{++}$	969
$(PuO_2)^{++}$	962
$(AmO_2)^{++}$	939
$(NpO_2)^{+}$	824
$(AmO_2)^{+}$	832

Indirect information on the variation of the ligand field strengths in the uranyl type ions can also be obtained by studying the variation of the crystal field parameters in any series of structurally similar compounds. For example, for several rare earth trichlorides [4] the variation from one rare earth ion to the next is probably 10 or 20 percent.

Data on the absorption spectrum of the $(UO_2)^{+}$ ion would yield important information on the strength of the ligand field in $(NpO_2)^{+}$ if it is really the case that

[1] Figures in brackets indicate the literature references and notes at the end of this paper.

similar ions have similar fields. The only experiments on the $(UO_2)^+$ absorption have been done by Kraus, Nelson, and Johnson [5]. They found no absorption peak with a molar extinction coefficient as high as 1.5 in the region between 10,000 and 27,800 cm^{-1}. The peaks corresponding to the transitions to $|1->$ and $|1+>$ should fall in this region. In neptunyl they have extinction coefficients of approximately 6. The more intense absorption peaks, which the $(UO_2)^+$ spectrum should have, occur below 10,000 cm^{-1}.

To begin the calculations we assumed that the ligand field strengths were the same for $(PuO_2)^{++}$ as for $(NpO_2)^{++}$ and were about 15 percent smaller for $(NpO_2)^+$. This assumption proved to be a reasonable starting point.

One expects the value of ζ to be larger for the plutonyl ion than for the neptunyl ion because the spin-orbit coupling constant generally increases with increasing atomic number. ζ may not have quite the same value for $(NpO_2)^+$ as for $(NpO_2)^{++}$ because the overlap of the wave functions on the surrounding ions may be slightly different.

The important additional complication in the two-electron spectra is the Coulomb repulsion of the electrons. The calculation of the matrix elements is considerably facilitated by use of table 1 of Condon and Shortley's [6] book. All the matrix elements of the Coulomb interaction depend on numerical factors, which can be obtained from the table, and on the four radial integrals $F^{(0)}$, $F^{(2)}$, $F^{(4)}$, and $F^{(6)}$ or, more conveniently, the parameters $F_0=F^{(0)}$, $F_2=F^{(2)}/225$, $F_4=F^{(4)}/1089$ and $F_6=25\ F^{(6)}/(429)^2$. In practice, we have followed Racah by using the linear combinations:

$$L=5F_2+6F_4-91\ F_6$$

$$A=924\ F_6$$

$$B=14\ F_4-84\ F_6.$$

We used a Fermi-Thomas model to calculate a $5f$ radial wave function appropriate to Pu^{5+} from which Basu calculated $F^{(2)}=79{,}000$ cm^{-1}. We then used an approximate wave function to calculate the relative values of the $F^{(2n)}$. We found, for example, that $L=1577$ cm^{-1}. A further useful guide comes from the wave functions calculated by Ridley [7] for U^{6+} by a Hartree method. For the $5f$ electrons she found $F_0=137{,}340$ cm^{-1}, $F_2=297.9$ cm^{-1}, $F_4=39.68$ cm^{-1} and $F_6=4.281$ cm^{-1}; therefore $L=1338$ cm^{-1}. These calculations give one only a rough idea of the values of L, A, and B. The actual values of these parameters in $(PuO_2)^{++}$ and $(NpO_2)^+$ must be determined by analyzing the absorption spectra.

2. Procedure

In our analysis of the $(NpO_2)^{++}$ data in III we had ten parameters at our disposal when covalent effects and ligand fields of threefold and sixfold symmetry were considered. For $(NpO_2)^+$ and $(PuO_2)^{++}$ six additional parameters are required to characterize the Coulomb interaction (covalent effects included). The total of 16 parameters is inconveniently large. We have therefore simplified the problem by leaving out of consideration covalent effects and ligand fields with threefold symmetry. We hoped that by varying the eight remaining parameters we would be able to obtain agreement with at least the gross features of the observed spectra, and this hope has been fulfilled. It is not difficult to include the neglected effects in the calculations, and this should probably be done when low-temperature absorption spectra of crystalline uranyl-type compounds become available.

In II we excluded from consideration the σ-states—i.e., states in which m_l for one or both electrons is zero. However, we have included these states here. When the Coulomb and the spin-orbit interactions are taken into account, and the ligand fields of axial and sixfold symmetry, one obtains secular equations of order 12, 5, 14, 16, 7, and 7. These numbers correspond, respectively, to crystal field quantum numbers 0, 0, 1, 2, 3, and 3. The secular equations can readily be solved, for particular values of the parameters, by using an electronic computer.

Our procedure in analyzing each spectrum was to select values for all the eight parameters and then to calculate eigenvalues and eigenvectors. The calculated eigenvalues were studied in relation to the known absorption spectrum and an attempt was made to find improved values of the parameters. These improved values were then used for another calculation of the energy levels. The procedure was repeated until we had what we felt was the most satisfactory possible interpretation of the spectrum.

3. The Plutonyl Spectrum

For both the $(NpO_2)^+$ and the $(PuO_2)^{++}$ ions the principal component of the ground state is the $^3H_4$ $|3-, 2->$ state [8, 9]. In the absence of the "crystalline" field Hund's rules place this state lowest. In all the calculations we have done, with widely varying values of the parameters, $^3H_4$ has been found to be lowest. Finally, and most important, the paramagnetic resonance data on crystalline plutonyl rubidium nitrate [10] and plutonyl sodium acetate [11] indicate unambiguously that the ground state is $^3H_4$. Therefore in discussing the absorption spectra we shall assume, without further comment, that all transitions take place from a ground state which is predominantly $^3H_4$.

The absorption spectra of the $(PuO_2)^{++}$ and $(NpO_2)^+$ ions are shown in figures 1 and 2. It will be seen that the two spectra have certain similarities particularly in their low frequency regions. The spectrum of $(PuO_2)^{++}$ is shifted towards higher frequencies relative to that of $(NpO_2)^+$.

The most prominent peak in the plutonyl spectrum is the one at 12,037 cm^{-1} for which the molar extinction

coefficient is 300, the width at half maximum is 34 cm^{-1} and the strength [12] is about 31. We regard the identification of this peak as predominantly $^3\Pi_2$ $|2-, -3->$ as certain. The transition which takes place is $|3-, 2-> \rightarrow |-3-, 2->$. We have already argued in III that the $3 \rightarrow -3$ transitions should give rise to narrow absorption peaks. The fact that they are strong as well was of crucial importance in the interpretation of the neptunyl spectrum. By suitably choosing the values of the Coulomb integrals and the spin-orbit coupling constant other levels, rather than the $|2-, -3->$ level, can be made to fall at 12,037 cm^{-1}. However, if such a choice is made one is left without a plausible identification for the next most prominent peaks at 10,185 and 10,500 cm^{-1}.

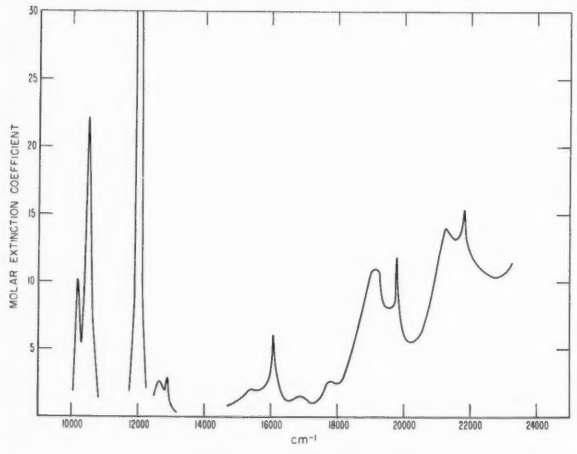

FIGURE 2. *Absorption spectrum of* Np (V) *in 1.0* M $DClO_4$–D_2O.
The curve has been replotted from data given by W. C. Waggener in J. Phys. Chem. **62**, 382 (1958).

We identify these peaks, in part, as due to the transitions $2 \rightarrow -2$ to a split $^3\Pi_0$ level. The apparent degeneracy of the states $|3-, -2->$ and $|2+, -3+>$ is removed by the spin-orbit coupling in a second order perturbation calculation [13]. The symmetric combinations

$$|3-, -2-> + |2+, -3+>$$

etc., are coupled by $\zeta\ \mathbf{L} \cdot \mathbf{S}$ to the Σ_0 states. The antisymmetric combinations, however, are not coupled to any other states by $\zeta\ \mathbf{L} \cdot \mathbf{S}$. They are coupled to one another by the Coulomb interaction, and to $^1I_6$ by the ligand field component which has sixfold symmetry. We shall refer to these antisymmetric combinations as $^3\Pi_0'$ states, and to the symmetric combinations as $^3\Pi_0$ states although this notation is the reverse of that used in our previous paper on the plutonyl ion (II). One finds, as a result of calculation, that the $^3\Pi_0'$ $|3-, -2->$ state lies below the corresponding $^3\Pi_0$ state. Since $^3\Pi_0'$ $|3-, -2-->$ interacts weakly with the other $^3\Pi_0'$ states, and since it can be reached from the $^3H_4$ ground state by a $2 \rightarrow -2$ transition which leaves the charge distribution nearly unaffected, we conclude that the $^3\Pi_0'$ peak should be narrow. If we adjust the parameters of our theory so that $^3\Pi_2$ is located near 12,000 cm^{-1} then we find that $^3\Pi_0'$ lies near 10,000 cm^{-1}. Its position is rather insensitive to all parameters except ζ and $\mathbf{L}$. We therefore identify the peak at 10,185 cm^{-1} as due to transitions to $^3\Pi_0'$, and we regard this identification as virtually certain.

The experimental peak at 10,500 cm^{-1} probably consists of two unresolved peaks since the absorption curve has a well developed shoulder [14] at about 10,700 cm^{-1}. One of these unresolved peaks is due to transitions to $^3\Pi_0$ $|3-, -2->$. The peak should be wider and also less intense than the $^3\Pi_0'$ peak because of the extensive coupling of $^3\Pi_0$ to other states.

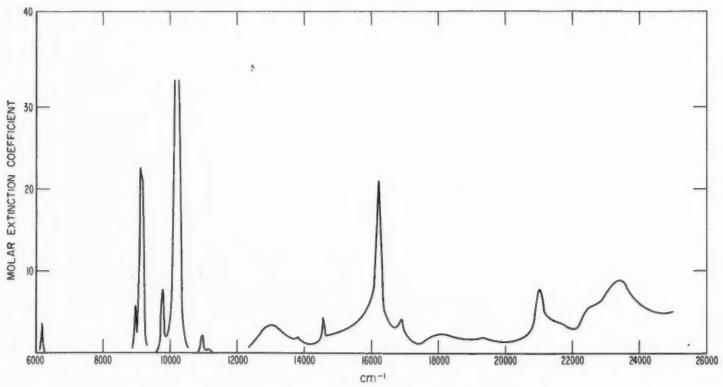

FIGURE 1. *Absorption spectrum of* Pu (VI) *in 0.5* M HCl.
The curve has been replotted from data given by R. E. Connick, M. Kasha, W. H. McVey and G. E. Sheline in The Transuranium Elements, National Nuclear Energy Series, IV, 14b, McGraw-Hill Book Co., New York, 1949. (Paper 4.20, figs. 12–15.)

The calculations place $^3\Pi_0$ in the vicinity of 10,700 cm^{-1}, and since the shoulder has less strength than the peak we have identified with $^3\Pi_0'$, we ascribe the unresolved 10,700 cm^{-1} peak to $^3\Pi_0$.

The other component of the unresolved doublet is probably a Σ_1 state. The transitions that give rise to this absorption peak are $|3-, 2-> \rightarrow |-2-, 2->$ and $|3-, 2-> \rightarrow |3-, -3->$; that is, they are $3 \rightarrow -2$ and $2 \rightarrow -3$ transitions. For the neptunyl ion the $3 \rightarrow -2$ transitions are almost as narrow as the $3 \rightarrow -3$ transitions, so one can expect the same to be true for the plutonyl ion. They are, however, less probable [15]. It therefore seems likely that the experimental peak at 10,500 cm^{-1} should be identified with transitions to Σ_1. The principal difficulty with this assignment is that the peak has at least twice the strength we would expect from our study of the neptunyl spectrum. We regard the identification of the unresolved structure between 10,300 and 10,800 cm^{-1} as partly Σ_1 and partly $^3\Pi_0$ as pretty certain, but it is difficult to say precisely where the two peaks should lie.

The two small peaks at 12,660 and 12,890 cm^{-1} may be due either to the $^3H_6$ and $^3H_6'$ states or to the vibrational fine structure of the 12,037 cm^{-1} peak. The charge distribution in the $^3H_6$ states is such that the corresponding absorption peaks should be narrow. They should also be weak since the absorption is due principally to the contamination of the $^3H_6$ states by $^3\Pi_0$ states. We consider it unlikely that the two peaks are due to transitions to the $^3H_6$ and $^3H_6'$ states because the separation of these states is less than 100 cm^{-1} in almost all of our calculations.

If the peaks are to be ascribed to vibrations the vibrational energy would have to be 620 or 850 cm^{-1}. The energies of the symmetric and antisymmetric stretching vibrations in the ground state of solid sodium plutonyl acetate are 818 and 930 cm^{-1} respectively [16]. Therefore we consider it reasonable to assign the peak at 12,890 cm^{-1} to the symmetric stretching vibration. Since the charge distribution in the excited $^3\Pi_2$ state is nearly the same as in the ground state the vibrational energies should be nearly the same in the excited state as in the ground state. Despite the fact that the $3 \rightarrow -3$ transitions do not excite many vibrations the peak at 12,890 cm^{-1} shows up because of the very great strength of the 12,037 cm^{-1} peak.

The $^3H_6$ doublet is probably not resolved, both components being concealed in the single hump at 12,660 cm^{-1}. One can perhaps understand in this way why the 12,660 cm^{-1} peak is broader than one would expect for $^3H_6$.

There now follows a discussion of the identification of the remaining peaks of the experimental absorption spectrum of the plutonyl ion. These identifications rest on arguments about intensities and breadths and on detailed calculations of the positions of the energy levels. In contrast to the peaks just discussed we do not regard the identification of any of the remaining peaks as certain. The difficulty we have encountered can be stated in the following way. Depending on the choice of parameters either there are too few calculated levels in the region from 15,000 to 25,000 cm^{-1}, or else there are calculated levels with no corresponding observed levels.

This circumstance makes it necessary for us to concentrate our attention on what we think are the principal transitions, and on the dominant features of the experimental spectrum. Consider the possible "allowed" transitions from the $^3H_4$ $|3-, 2->$ ground state. They are $3 \rightarrow -3$, -2, -1, 0, or 1 and $2 \rightarrow -3, -2, -1, 0$, or 1. We have already located the $3 \rightarrow -3$ and the $2 \rightarrow -2$ transitions. The $3 \rightarrow 0$ and $2 \rightarrow 0$ transitions are almost certainly well above 25,000 cm^{-1} since an electron in an $m_l = 0$ state is strongly repelled by the axial charge distribution. Due to the extensive mixing of the Π_1 and Σ_1 states it is unlikely that the $3 \rightarrow -2$ and $2 \rightarrow -3$ transitions will give rise to any peaks that are stronger than the peak at 10,500 cm^{-1} which we have associated with a Σ_1 state. The remaining possible transitions are $3 \rightarrow -1$ or 1 and $2 \rightarrow -1$ or 1. The calculations place the excited states in the following order of ascending energy: $^3\Gamma_3$ and $^3\Gamma_3'$ $(2 \rightarrow 1)$ [17], $^3\Phi_2$ $(3 \rightarrow 1)$, $^3\Delta_1$ $(2 \rightarrow -1)$, $^3\Pi_0'$ and $^3\Pi_0$ $(3 \rightarrow -1)$.

For the neptunyl ion the $3 \rightarrow 2$ transition is relatively narrow, probably because the change in the charge distribution is mainly in the equatorial region and does not excite vibrations of the ion, or even of its surroundings, to any large extent. However the $3 \rightarrow 1$ and $3 \rightarrow -1$ transitions are broad because vibrations are excited. It follows that the redistribution of charge which accompanies a $2 \rightarrow 1$ transition also ought to excite vibrations. Therefore the absorption peaks corresponding to transitions to the $^3\Gamma_3$, $^3\Gamma_3'$, $^3\Phi_2$, $^3\Delta_1$, $^3\Pi_0'$, and $^3\Pi_0$ states of the plutonyl ion should all be broad. By analogy with the neptunyl ion the widths at half maximum should be about 1000 cm^{-1} [18].

The first prominent feature of the absorption spectrum above 14,000 cm^{-1} is the sharp peak at 16,075 cm^{-1}. Because of its sharpness this peak cannot be associated with any of the states listed in the previous paragraph. It is a moot question, but one which is crucial for our analysis, whether or not the 16,075 cm^{-1} peak rests on a broad base. If so, the strength of the underlying peak may be as large as 5. It would then be reasonable to associate this broad peak with transitions to $^3\Gamma_3$ and $^3\Gamma_3'$.

A serious difficulty then arises: It becomes necessary to associate the strong, broad peaks at 19,100 and 21,200 cm^{-1} with transitions to $^3\Phi_2$ and $^3\Delta_1$, respectively. The observed separation of the peaks is 2100 cm^{-1} but the calculated separation is about 4000 cm^{-1} and cannot be significantly reduced by any reasonable adjustment of the parameters.

Because of this difficulty [19] we consider it more likely that the nearly degenerate $^3\Gamma_3$ and $^3\Gamma_3'$ states should be identified with the broad peak at 19,000 cm^{-1}. The principal difficulty now is that there are only three calculated levels in the region between 14,000 and 19,000 cm^{-1} but the absorption curve indicates the presence of transitions to at least four states.

TABLE 2. *Observed and calculated absorption spectrum of the* $(PuO_2)^{++}$ *ion*

Level	Purity[a]	Position in cm^{-1}		$\epsilon_{max.}$	Width at half max. in cm^{-1}	Strength[b]	Composition of wave function by $\lvert m_l \rvert$ value				Calculated strength[c]
		Calc.	Exptl.				3	2	1	0	
$^3H_4$	0.9249	0	0				0.9526	1.0180	0.0295	0.0000	
Σ_0	.7331	2445									
Π_1	.5929	4258									
$^3H_5$	.9825	7133									
$^3\Pi_0'$ (3, −2)	.9580	10157	10185	10.2	150	~ 5.7	.9617	0.9993	.0385	.0005	0.8860 (2 → − 2) + 0.0350 (3 → − 1)
Σ_1	.5966	10489	10500	22.2	195	16.	.6953	1.2645	.0395	.0008	.4091 (3 → − 2) + .1499 (2 → − 3) + .0216 (2 → − 1)
$^3\Pi_0$ (3, −2)	.6281	10640	10700	~ 4.4	~ 160	~ 2.5	.6518	1.3295	.0143	.0043	.5916 (2 → − 2)
$^3\Pi_2$ (3, −2)	.9204	11892	12037	300.	34	31.	.9579	0.9623	.0788	.0009	.8517 (3 → − 3)
$^3H_6$	.9278	12862	12660	2.7	400	3.	1.0680	.9318	.0000	.0000	< 0.01
$^3H_6'$	.9580	12866					1.0686	.9312	.0002	.0000	< 0.01
$^1\Gamma_4$ (2, 2)	.8068	15469	15420	0.6	~ 200?	~ 0.3?	0.1130	1.7539	.1330	.0000	.0931 (gnd)
Σ_0	.9720	15980	16075	~ 5.	~ 135	~ 1.6	1.1555	0.7877	.0564	.0004	.0229 (3 → − 1)
Σ_1	.6328	17877	17800	2.7	~ 600	~ 3.	1.2731	.6989	.0267	.0012	.1540 (3 → − 2) + .4301 (2 → − 3)
$^3\Gamma_3'$	.8828	19080	19100	11.	~ 1100	~ 24.	0.8978	.1022	.9840	.0159	.8170 (2 → 1)
$^3\Gamma_3$	.8838	19086					.8981	.1018	.9842	.0157	.8179 (2 → 1)
Σ_0	.8102	19780	19810	~ 7.	~ 80	~ 1.	.8681	1.0141	.1136	.0042	.0901 (3 → − 1) + .0999 (2 → − 2)
$^3\Phi_2$ (2, 1)	.8584	21253	21200	14.	~ 1200	~ 30.	.0959	0.8874	.9957	.0209	.7938 (3 → 1)
$^1H_5$	.8935	21885	21840	~ 7. ?	~ 300	~ 4.	1.0028	.8986	.0985	.0000	.0120 (1 → 2) + .0407 (2 → 3)
Π_1	.6660	23063					1.1679	.7183	.1125	.0011	.0227 (3 → − 2) + .2926 (2 → − 3)
Δ_2	.7349	23153					0.7780	.2504	.9580	.0136	.1037 (3 → 1) + .0380 (3 → − 3)
$^3\Gamma_4$	.8381	24527					.8745	.1750	.9453	.0052	.0229 (gnd)
$^1I_6$	.9301	24780					1.9294	.0704	.0001	.0000	.0125 (1 → 3)
$^1I_6'$	.9310	24781					1.9310	.0689	.0000	.0000	.0125 (→ 3)
$^3\Delta_1$ (3, −1)	.8506	24917					0.9302	.1416	.9233	.0048	.7870 (2 → − 1)

[a] By "purity" we mean the extent to which the level can be characterized by the designation in column 1.
[b] The formula used in computing the strength is given in footnote 12.
[c] See the appendix.

When the $^3\Gamma_3$ states are placed at 19,000 cm^{-1} the broad peak at 21,200 cm^{-1} can readily be identified with transitions to the $^3\Phi_2|2-, 1-\rangle$ state.

With the dominant peaks in the spectrum at least tentatively identified we can refine out estimates of the various parameters, repeat the calculations, and then try to identify the remaining absorption peaks.

It appears that the narrow peaks at 16,075 and 19,810 cm^{-1} should be associated with transitions to states that are predominantly Σ_0. This assignment is reasonable in view of the positions, widths and strengths of the two peaks.

We associate the peaks at 15,420, 17,800, and 21,840 cm^{-1} with transitions to $^1\Gamma_4$, Π_1, and $^1H_5$ states, respectively. These assignments are all dubious and are made only because there are no alternatives. $^1\Gamma_4$ is in the right position but it appears fairly broad in figure 1 whereas the calculations indicate it should be narrow. Also its calculated strength would be negligible were it not for the fact that its wave function contains some of the same zero-order states as the ground state wave function.

The Σ_1 state whose calculated position is 17,877 cm^{-1} should be narrow and perhaps half as strong as Σ_1 at 10,500 cm^{-1}. It is possible that the Π_1 state is an unresolved part of the large absorption peak at 19,100 cm^{-1}.

The difficulty with the $^1H_5$ assignment is that the calculated strength seems to be too small.

We have now discussed all calculated levels from 10,000 to 23,000 cm^{-1}. There is however one more observed peak at 16,950 cm^{-1}. We are not entirely convinced that this peak exists since it seems to be located by a single point on the most detailed figure in the paper of Connick et al. [20], and disappears when the HCl concentration is increased.

It is possible that both the 16,950 (if real) and the 17,800 cm^{-1} peaks are associated with the major peak at 19,100 cm^{-1} in the same way as the ripples on the low energy side of the neptunyl absorption peaks are associated with the strong 19,100 and 21,100 cm^{-1} peaks.

The observations and the calculations on the plutonyl ion are summarized in table 2. See the appendix for an explanation of the right hand side of the table.

4. The $(NpO_2)^+$ Spectrum

The $(NpO_2)^+$ ion, like the $(NpO_2)^{++}$ ion, is believed to be linear. The optical absorption spectrum of the $(NpO_2)^+$ ion in aqueous solution has striking similarities to that of the $(PuO_2)^{++}$ ion so we shall assume that $(NpO_2)^+$ is an ion of the uranyl type and attempt to interpret its properties on this basis. It has already been mentioned that the asymmetric stretching frequency for the $(NpO_2)^+$ ion is lower than for the neptunyl or plutonyl ions. Also, the $(NpO_2)^+$ spectrum, as compared with the plutonyl spectrum, is shifted toward the red. We attribute these shifts to a weakening of the molecular field, to a lower value of the spin-orbit coupling constant, and to lower values of the Coulomb integrals for the $(NpO_2)^+$ ion.

The solution absorption spectrum of the $(NpO_2)^+$ ion is shown in figure 2. We regard the identification of the following absorption peaks as nearly certain:

8953 cm^{-1}	$^3\Pi_0'$
9146	Σ_1
9780	$^3\Pi_0$
10208	$^3\Pi_2$

TABLE 3. *Observed and calculated absorption spectrum of the* $(NpO_2)^+$ *ion*

Level	Purity[a]	Position in cm^{-1}		$\epsilon_{max.}$	Width at half max. in cm^{-1}	Strength[b]	Composition of wave function by $\lvert m_l \rvert$ value				Calculated strength[c]
		Calc.	Exptl.				3	2	1	0	
$^3H_4$	0.9216	0	0				0.9626	0.9991	0.0382	0.0000	
Σ_0	.6920	2475									
Π_1	.6181	3893									
$^3H_5$	.9115	6148	6173	3.5	47	1.2	.9692	1.0093	.0215	.0000	0 .0333 (3→−2) + 0.0186 (1→2) + 0.8400 (+→−)
$^3\Pi_0'$ (3, −2)	.8380	8725	8953	5.8	55	1.3	.9483	.9943	.0570	.0003	.7723 (2→−2) + .0523 (3→−1)
$^3\Sigma_1$	.6492	9450	9146	22.4	137	13.	.8301	1.1163	.0530	.0006	.3704 (3→−2) + .2332 (2→−3) + .0350 (2→−1)
$^3\Pi_0$ (3, −2)	.4804	9862	9780	7.7	83	2.5	.7417	1.2427	.0129	.0027	.4486 (2→−2)
$^3\Pi_2$ (3, −2)	.8503	10294	10208	> 82	< 139	45?	.9250	.9311	.1427	.0011	.7851 (3→−3)
vib			10970	2.1	93	0.7					
$^3H_6'$	.8225	11171	11160	0.5	~ 150	~ 0.3	1.0627	.9274	.0098	.0000	.0876 (2→−2)
$^3H_6$	.7076	11199					1.0213	.9753	.0028	.0006	.1352 (2→−2)
$^3\Gamma_3'$	.9122	12949	13020	2.1	~ 900	~ 9.	.9301	.0700	.9901	.0099	.8410 (2→1)
$^3\Gamma_3$	.9162	12969					.9315	.0685	.9908	.0091	.8447 (2→1)
Σ_0	.9006	13894	13824	< 0.5	~ 200	< 0.3	1.1547	.6680	.1754	.0020	.0739 (3→−1) + .0103 (1→−3)
$^1\Gamma_4$ (2, 2)	.6550	14345	14577	2.4	80	0.5	.1897	1.5267	.2835	.0001	.0814 (gnd)
$^2\Sigma_1$	.5931	15911	16220	~ 9	160	> 5.5	1.0743	.8651	.0592	.0014	.2132 (3→−2) + .3155 (2→−3)
$^3\Phi_2$ (2, 1)	.6598	16045	16100	< 7.6	~ 700	~ 11.	.2906	.7095	.9838	.0159	.6081 (3→1) + .0232 (3→−3)
Δ_2 (3, −1)	.4482	16907	16906	~ 1.6	~ 150	~ 0.5	.6535	.4065	.9355	.0047	.2733 (3→1) + .0451 (3→−3)
Σ_0	.7912	17169					.7888	1.0511	.1570	.0030	.1288 (3→−1) + .0524 (2→−2)
$^3\Delta_1$	.5633	18085	18116	2.3	~ 1000	~ 5.	.9953	.2706	.7339	.0003	.0318 (2→−3) + .5202 (2→−1)
$^3\Gamma_4$	.6659	18149					.8568	.2518	.8866	.0047	.0229 (gnd) + .0125 (3→−3) + .0135 (3→1)
$^1H_5$	.3654	18589					.9410	.5942	.4620	.0029	.0585 (2→−3) + .2540 (2→−1) + .0128 (2→3)
Π_1	.5895	19452	19360?	≥ 0.3	~ 500	~ 0.3	.7486	.7760	.4707	.0047	.0902 (2→−3) + .0271 (2→−1)
$^3\Phi_3$ (2, 1)	.8810	20337					.0993	.9008	.9937	.0064	.0394 (2→1) + .0182 (3→2)
$^3\Phi_3'$ (2, 1)	.9240	20425					.0554	.9446	.9961	.0039	.0509 (2→1) + .0191 (3→2)
$^1I_7'$	.9216	20532					1.9205	.0785	.0012	.0000	.0140 (1→3)
$^1I_6$	.8782	20578	21008	6.4	320	3.7	1.8369	.1580	.0049	.0003	.0133 (1→3)
Π_1	.7665	21359					.5242	.8574	.6020	.0164	.1465 (2→−3) + .0498 (3→−2)
$^3\Delta_2'$ (2, 1)	.9811	21841					.9976	.0024	.9907	.0093	< 01
$^3\Delta_2$ (2, 1)	.9289	21912	21700?	3.5?	~ 800	~ 5.	.9525	.0475	.9925	.0075	.0155 (2→1)
$^3\Pi_0''$ (2, −1)	.9220	22380	22600	5.6	~ 700	~ 7.	.0664	.9872	.9342	.0122	.8497 (3→−1) + .0595 (2→−2)
$^3\Pi_0$ (2, −1)	.6347	23397	23400	8.7	~ 800	~ 11.	.2989	.9586	.7327	.0098	.5858 (3→−1) + .0582 (2→−2)
$^3\Gamma_5$	.7056	24292					.9954	.2835	.7212	.0000	.0102 (2→−1)
$^3\Pi_2$ (2, −1)	.7623	24399					.2109	.7964	.9779	.0149	.0191 (3→−3)

[a] By "purity" we mean the extent to which the level can be characterized by the designation in column 1.
[b] The formula used in computing the strength is given in footnote 12.
[c] See the appendix.

The reasons for these assignments are the same as those for the corresponding assignments for the plutonyl ion. There are two small difficulties here which keep us from being completely certain about the assignments. (1) The peak at 9146 cm^{-1} has a curious top [2] which makes it look as though it might be two unresolved peaks. (2) The $^3\Pi_0$ peak is stronger than the $^3\Pi_0'$ peak. Since $^3\Pi_0'$ is more nearly a pure state the reverse should be true, as is the case for the plutonyl ion. However, it is difficult (impossible ?) to find an interpretation of the peak which is alternative to the one given above.

The peak at 6173 cm^{-1} is due primarily to the magnetic dipole transition from $^3H_4$ to $^3H_5$. The strength of this peak, calculated according to the formula given in III is 1.2; for a pure magnetic dipole transition the strength should be 1.0. It is rather unusual to find a line in a solution absorption spectrum that can be identified as due to a magnetic dipole transition. The calculated position of the $^3H_5$ peak is very near the observed position so we regard the identification of this peak as certain.

There are two small peaks at 10,970 and 11,160 cm^{-1} in the $(NpO_2)^+$ spectrum. If one of them is assigned to the $^3H_6$ states and the other to excitation of a vibrational mode the energy associated with the vibration would have to be 760 or 950 cm^{-1}. We do not have any direct information on the symmetric stretching frequency for the $(NpO_2)^+$ ion in aqueous solution. However we note that according to the data of Jones [16], and of Jones and Penneman [3], the ratio of the asymmetrical stretching frequencies for $(NpO_2)^+$ and $(NpO_2)^{++}$ in solution is 824/969 while the ratio of the asymmetrical stretching frequencies in solution and in a crystalline solid is 969/934. Therefore we estimate that the energy of the stretching vibration should be (824/969) × (969/934) × (energy of symmetric stretching vibration in a crystalline solid). The latter number [16] is 844 cm^{-1} so our estimate for the energy of the symmetric stretching vibration of the $(NpO_2)^+$ ion in aqueous solution is 745 cm^{-1}. We therefore associate the peak at 10,970 cm^{-1} with a combined electronic and vibrational transition and the peak at 11,160 cm^{-1} with the transitions to the $^3H_6$ and $^3H_6'$ states.

As in the case of the plutonyl ion we do not regard our identification of any of the remaining peaks in the $(NpO_2)^+$ spectrum as certain. Generally speaking, our procedure in this case was the same as before: we interpreted the relatively strong, broad peaks as due to the "allowed" transitions to the $^3\Gamma_3$, $^3\Phi_2$, $^3\Delta_1$, and $^3\Pi_0$ (2,−1) states. We found that parameters could be chosen so that the calculated positions of these states agreed with the observed positions of strong, broad peaks insofar as they could be determined.

We believe one of these peaks definitely exists and is centered at 13,020 cm^{-1}. We ascribe it to transitions to the $^3\Gamma_3$ and $^3\Gamma_3'$ states. We place the next broad peak somewhat arbitrarily at 16,100 cm^{-1}. It

lies under the fairly sharp, strong peak at 16,220 cm^{-1}. We associate the broad peak with the $^3\Phi_2$ state. The plots we have made with expanded abscissa reveal the structure much more clearly than figure 2 does.

The third broad peak is at about 18,120 cm^{-1}. We identify it as being due to transitions to the $^3\Delta_1$ state.

The peak at 21,010 cm^{-1} is too narrow to be associated with a major redistribution of charge. It appears to rest on the low energy side of a broad peak centered at about 21,700 cm^{-1}. There are two more broad peaks at about 22,600 and 23,400 cm^{-1}. We identify two of these three peaks with transitions to the $^3\Pi_0'$ (2, −1) and $^3\Pi_0$ (2, −1) states. The most plausible identification of the remaining peak is achieved if the $^3\Pi_0'$ and $^3\Pi_0$ states correspond to the peaks at 22,600 and 23,400 cm^{-1}, respectively. The remaining peak at 21,700 cm^{-1} must then be ascribed to transitions to $^3\Delta_3$ and $^3\Delta_3'$ states. The principal objection to these assignments is that the experimental strength of the 21,700 cm^{-1} peak is greater than the calculated strength for transitions to $^3\Delta_3$ states.

Another possibility is that some of the structure observed above 20,000 cm^{-1} is due to excitation of the vibrational modes of the $(NpO_2)^+$ ion.

With all the broad peaks now identified plausibly but not certainly we consider the remaining features of the $(NpO_2)^+$ absorption spectrum. We ascribe the moderately strong 16,220 cm^{-1} peak to transitions to a Σ_1 state and the 21,010 cm^{-1} peak to transitions to a Π_1 state. These assignments are reasonable in terms of calculated position, strength and charge distribution, and in relation to the width and strength of the $^3\Sigma_1$ peak at 9146 cm^{-1}.

We identify the peak at 14,577 cm^{-1} with the $^1\Gamma_4$ (2, 2) state. The corresponding transition has a calculated strength different from zero only because the $^1\Gamma_4$ state contains the same zero order wave functions as the ground state. The 14,577 cm^{-1} peak is narrower than we expect for $^1\Gamma_4$ on the basis of the calculated charge distribution. The identification is therefore rather unsatisfactory. However, the only other state in the vicinity is a Σ_0. It is difficult to adjust the parameters so that Σ_0 lies in the correct position.

We ascribe the two small peaks at 13,824 and 16,906 cm^{-1} to transitions to Σ_0 and Δ_2 states, respectively. Again, the assignments are reasonable in terms of calculated position, strength and charge distribution.

The very small peak at 19,360 cm^{-1} may be due to transitions to the $^1H_5$ state or a Π_1 state.

5. Values of the Parameters

The values of the parameters used in the final calculations on $(NpO_2)^+$ and $(PuO_2)^{++}$ are given in table 4. It is gratifying that X, Y, Z, and V_6 have values that are consistent with expectations based on our analysis of the $(NpO_2)^{++}$ spectrum in III. Also, the Coulomb integrals are larger for the $(PuO_2)^{++}$ than for the $(NpO_2)^+$ ion. This behavior is what one would expect since the higher nuclear charge for $(PuO_2)^{++}$ pulls the electrons in toward the center more and therefore increases their Coulomb repulsion.

The parameters ζ and L are probably determined to within 5 percent. The levels below 13,000 cm^{-1} that we regard as almost certainly identified depend principally on ζ and L and enable us to fix their values fairly closely. A is probably determined to within 10 percent by minimizing the mean square deviation for as many levels as we can reasonably identify.

TABLE 4. *Values of the Parameters*

	$(NpO_2)^+$	$(PuO_2)^{++}$
	cm^{-1}	cm^{-1}
X	253	−1183
Y	12034	16793
Z	48555	49650
V_6	807	168
ζ	2090	2467
L	919	934
A	4322	5926
B	184	36
F_2	219.5	254.2
F_4	41.21	41.05
F_6	4.677	6.413

The value of B is determined largely by the position of the $^1\Gamma_4$ (2,2) level. As indicated above we are not at all sure we have located this level. We therefore estimate that B is known only within a factor of 2.

We started the calculations with $V_6 \sim 1000$ cm^{-1}. For both $(NpO_2)^+$ and $(PuO_2)^{++}$ we were forced to reduce this value substantially in order to minimize the rms deviations. It is difficult to estimate the accuracy of the determination of V_6 because the assumption of sixfold symmetry about the axis may be a drastic simplification.

Similarly we started the calculation with $Z \sim 35{,}000$ cm^{-1} and were forced to raise it to mimimize the rms deviations. Of all the levels below 25,000 cm^{-1} $^3\Phi_2$ (2,1) depends most sensitively on Z. However $\Delta E\ (^3\Phi_2) \sim 0.03\ \Delta Z$ so one sees that Z is probably not very closely determined by the positions of these low levels.

The values given for X and Y depend on whether we have correctly located and identified the broad, strong peaks in the absorption spectra. If we assume that both the locations and the identifications are correct then the accuracy of determination of X and Y is probably ± 300 cm^{-1}.

For the $(PuO_2)^{++}$ ion the rms deviation between the calculated and the observed positions of 12 peaks is 150 cm^{-1}. The deviation was calculated from the formula:

$$\Delta^2 = \sum_i (\Delta E_i)^2/(n-8)$$

n is the number of observed levels and 8 is the number of parameters. Actually this formula may exaggerate the deviation because physical requirements limit one's freedom in adjusting the parameters. Also,

a more refined variational calculation than we used would undoubtedly enable one to choose parameters that would decrease the rms deviation somewhat. The 150 cm^{-1} deviation is comparable with the deviation of 125 cm^{-1} that Sugar [22] gives for the levels of the free Pr^{3+} ion.

For the $(NpO_2)^+$ ion the rms deviation between the calculated and the observed positions of the 14 peaks used to fix the parameters is 272 cm^{-1}. If we include also the $^3\Delta_3$, $^3\Pi_0'$ (2, −1) and $^3\Pi_0$ (2, −1) peaks the rms deviation is 241 cm^{-1}.

6. Conclusion

We have shown how the solution absorption spectra of the $(NpO_2)^+$ and $(PuO_2)^{++}$ ions can be interpreted on the basis of exact calculations and plausible arguments concerning the strength and width of the absorption peaks. To confirm the interpretation it would be of some value to locate experimentally the two peaks for $(NpO_2)^+$ that lie below 6,000 cm^{-1} and the three peaks for $(PuO_2)^{++}$ that lie below 9,000 cm^{-1}. Further to check the theory developed here it is highly desirable to obtain the low temperature absorption spectra of a crystalline plutonyl compound and of a Np (V) compound. A study of the Zeeman effect would be helpful.

We think the parameters and their variations among the ions $(NpO_2)^{++}$, $(NpO_2)^+$ and $(PuO_2)^{++}$ are now sufficiently well known so that a theoretical investigation of the absorption spectrum of the $(AmO_2)^{++}$ ion could be undertaken. Also, by combining the information gained from studying NpF_6 and the $(PuO_2)^{++}$ ion, it should be possible to interpret the spectrum of PuF_6.

We are indebted to Mr. Walter Lipton who coded the matrices for the machine calculations, and to Dr. W. C. Waggener who sent us a large scale plot of his neptunium data.

7. Appendix

In analyzing the spectra it is useful to have some quantitative ideas, however crude they may be, concerning the relative breadths and strengths of the absorption peaks that correspond to the various calculated energy levels. One then has some basis for judging whether or not it is reasonable to associate a calculated level with an observed absorption peak. We have developed a method which gives us some insight into this problem.

In the ground state the electrons are predominantly in states with $m_l = \pm 3$ and ± 2. If in the excited state the electrons are still predominantly in the ± 3 and ± 2 states we assume that the absorption peak will be narrow. On the other hand, if in the excited state there is an appreciable probability that the $m_l = \pm 1, 0$ orbitals are occupied, then we assume the absorption peak will be broad. We can calculate from the eigenvectors the distribution of charge over the various orbital states. These calculations have been made and the results are given in table 2 for the $(PuO_2)^{++}$ ion and in table 3 for the $(NpO_2)^+$ ion.

Now suppose we have two states Ψ and Φ between which a transition can take place. Due to the various interactions each one of these states will be a complicated mixture of the zero order states. Let us therefore write

$$\Psi = a\psi_a + b\psi_b + c\psi_c + \ldots .$$

$$\Phi = \alpha\psi_\alpha + \beta\psi_\beta + \gamma\psi_\gamma + \ldots .$$

Here the $\psi_a, \ldots, \psi_\alpha, \ldots$ denote the zero order states and $a, \ldots, \alpha, \ldots$ are appropriate numerical coefficients. Suppose the transition from ψ_a to ψ_α is "allowed"; that is, suppose ψ_a and ψ_α differ in, at most, the value of m_l for one electron. For example, ψ_a might be $^3H_4|3-, 2->$ and ψ_α might be $^3\Pi_2|-3, 2->$. Similarly, suppose the transition from ψ_b to ψ_β is "allowed," etc. We then take as a quantitative estimate of the strength of the peak corresponding to the Ψ to Φ transition

$$a^2\alpha^2\,(\psi_a \rightarrow \psi_\alpha) + b^2\beta^2\,(\psi_b \rightarrow \psi_\beta) + \ldots .$$

The bracketed quantities denote the probabilities for the indicated transitions.

This device is useful in estimating the relative strengths of transitions that would be forbidden if the states were pure, but which are somewhat "allowed" because of the complicated mixing of the states which actually occurs. The numbers $a^2\alpha^2$, $b^2\beta^2$, etc., have been calculated and are given in tables 2 and 3 when they exceed 0.01.

The estimates of relative strengths obtained in this way can conceivably be improved by using empirical information which may be available. For example, the strengths of the observed neptunyl lines at 6752 and 8168 cm^{-1}, calculated according to the formula in the appendix to III, are about 7.7 and 39, respectively. The former corresponds principally to a $3 \rightarrow -2$ transition: the latter to a $3 \rightarrow -3$ transition. The ratios of the strengths of these two transitions should therefore be about 1:5. We would expect the relative strengths of the $3 \rightarrow -2$ and $3 \rightarrow -3$ transitions for the $(NpO_2)^+$ and $(PuO_2)^{++}$ ions also to be in the approximate ratio 1:5. The ratio seems to be closer to 1:3 but the difference is perhaps not surprising in view of the crudeness of the assumptions made. Also there may be real differences between the one- and the two-electron cases.

8. References and Notes

[1] J. C. Eisenstein and M. H. L. Pryce, Proc. Roy. Soc. **A229**, 20 (1955). This paper (to be referred to here as II) contains a brief reference to the $(NpO_2)^+$ ion which, like $(PuO_2)^{++}$, is believed to be of the uranyl type.

[2] J. C. Eisenstein and M. H. L. Pryce, J. Res. NBS **69A** (Phys. and Chem.) No. 3, 217 (1965). This paper will be referred to as III.

[3] L. H. Jones and R. A. Penneman, J. Chem. Phys. **21,** 542 (1953).
[4] See J. C. Eisenstein, J. Chem. Phys. **39,** 2128 (1963), table IV. It must be conceded that there are peculiar variations from ion to ion but they may be due to differences in the approximations made in the calculations.
[5] K. A. Kraus, F. Nelson, and G. J. Johnson, J. Am. Chem. Soc. **71,** 2510 (1951).
[6] E. U. Condon and G. H. Shortley, Theory of Atomic Spectra, Cambridge University Press (1935).
[7] E. C. Ridley, Proc. Roy. Soc. **A243,** 422 (1958).
[8] Here, and in what follows, we shall designate the states by their principal components. We use the normal spectroscopic notation for linear molecules in Russell-Saunders coupling in so far as possible. Since there is no Greek letter corresponding to H we denote states with $\Lambda = 5$ by the Roman letter H. These states should not be confused with the H-states of atomic spectroscopy. The zero-order states are sometimes so extensively mixed that no spin assignment can be made.
[9] Actually the $|3-, 2->$ and the $|-2+, -3+>$ states are degenerate. All states for which $\Sigma m_j = 1$ or 2 (mod 6) have a twofold degeneracy. We shall not make any further explicit reference to this degeneracy.
[10] B. Bleaney, P. M. Llewellyn, M. H. L. Pryce and G. R. Hall, Phil. Mag. **45,** 991 (1954).
[11] C. A. Hutchison and W. B. Lewis, Phys. Rev. **95,** 1096 (1954).
[12] The method of calculating strengths is described in the appendix of III. We assume that the formula

$$\text{strength} = 37.9\ \epsilon_{max} \Delta\nu / \nu_0$$

which is appropriate to peaks with a Gaussian shape can be used.
[13] The same is true for the pairs of $^3\Pi_0$ states:

$|2-, -1->$, $|1+, -2+>$ and $|1-, 0->$, $|0+, -1+>$.

[14] This shoulder is barely discernible in figure 1. However it shows up clearly when the data are plotted on a scale with expanded abscissa.
[15] The mixing of the zero-order states for the neptunyl ion by the spin orbit interaction and the part of the ligand field with sixfold symmetry makes it impossible to determine the relative probabilities for the $3 \rightarrow -3$ and the $3 \rightarrow -2$ transitions. The $(NpO_2)^{++}$ absorption peak at 6752 cm^{-1} which is due mostly to the $3 \rightarrow -2$ transition has strength 7.7. The absorption peak at 8168 cm^{-1} which is due mostly to the $3 \rightarrow -3$ transition has strength 39.
[16] L. H. Jones, J. Chem. Phys. **23,** 2105 (1955).
[17] The apparent degeneracy of the states $^3\Gamma_3|3-, 1->$ and $^3\Gamma_{-3}|-1+, -3+>$ is removed by the component of the ligand field which has sixfold symmetry. Contrary to the situation for $^3\Pi_0$ and $^3\Pi_0'$ no significant distinction can be made between $^3\Gamma_3$ and $^3\Gamma_3'$.
[18] We say 1000 rather than 1600 cm^{-1} because the $3 \rightarrow -3$ and $3 \rightarrow -2$ transitions are narrower for the plutonyl than for the neptunyl ion.
[19] Difficulties in identifying the less prominent peaks also arise if we place $^3\Gamma_3$ at 16,000 cm^{-1}.
[20] R. E. Connick, M. Kasha, W. H. McVey, and G. E. Sheline, The Transuranium Elements, National Nuclear Energy Series, IV, 14b, paper 4.20 (McGraw-Hill Book Co., New York, 1949).
[21] We have located this peak at 9146 cm^{-1}. Actually the extinction coefficient has its maximum value at 9124 cm^{-1}. The structure at the top of this peak is hardly noticeable in figure 1 but becomes apparent when the scale for the abscissa is expanded.
[22] J. Sugar, Phys. Rev. Letters **14,** 731 (1965).

(Paper 70A2-392)

JOURNAL OF RESEARCH of the National Bureau of Standards—A. Physics and Chemistry
Vol. 70A, No. 2, March–April 1966

Vapor Pressure and Heat of Sublimation of Rhenium[1]

E. R. Plante and R. Szwarc[2]

Institute for Materials Research, National Bureau of Standards, Washington, D.C.

(October 27, 1965)

The vapor pressure of rhenium was measured by the Langmuir method in the temperature range 2350–3050 °K using a vacuum microbalance. The least squares line through the four series of data points is $4.5756 \log P(\text{atm}) = 32.26 - 180700/T$. Least squares lines for each of the four series yield heats and entropies of sublimation higher than the corresponding third law values. The vapor pressure equation based on the average heat and entropy is, $4.5756 \log P(\text{atm}) = 33.36 - 183500/T$.

The selected third law heat of sublimation, ΔH_S° (298) is 185.9 kcal mol^{-1}. Our recommended equation for the vapor pressure is $4.5756 \log P(\text{atm}) = 31.86 - 180200/T$ based on our mean third law heat and tabulated values for the entropies and enthalpies.

Key Words: Heat of sublimation, Langmuir vaporization, rate of vaporization, rhenium, vapor pressure.

1. Introduction

The only published experimental data on the rate of sublimation of rhenium is due to Sherwood et al., [1].[3] Their data were obtained by the Langmuir method using a modification of the hot wire technique and utilizing an emissivity correction to obtain absolute temperatures.[4] Although there is no special reason to question the accuracy of their results, past experience has shown that large systematic errors often occur and are difficult to detect in high temperature vaporization measurements. Hence, in view of this and the interest in rhenium as a useful material for particular high temperature applications, it was considered worthwhile to undertake additional measurements.

2. Experimental Method

The specimen used in this work came from a sample of zone refined rod supplied by MRC Corporation, Orangeburg, New York and was fabricated by arc erosion at NBS into a right circular cylinder about 1.5 cm long and 0.25 cm in diameter. A hole 0.1 cm in diameter and 1.0 cm long, assumed to represent blackbody conditions, was drilled along the cylinder axis and a suspension hole 0.025 cm in diameter was drilled along a diameter near the other end of the sample.

A "typical" analysis according to the supplier showed the principal metallic impurities to be Fe, Mo, and Si with impurity contents of < 10, 40, and 10 PPM, respectively, while the principal nonmetallic impurity was 12 PPM O_2.

A semiquantitative spectrochemical analysis performed at NBS indicated the presence of Cu and Si in the range of 10–100 PPM and Ca, Fe, and Mg in the range of 1–10 PPM.

The density of a piece of the rhenium stock was determined by weighing in water and was 20.95 g cm^{-3}, close to the theoretical x-ray density of 21.04 g cm^{-3} [2].

The measurements were made using the vacuum microbalance apparatus previously described [3]. Samples were heated directly by rf induction at 450 kHz. Vacuum in the ultra-high vacuum range (10^{-7} to 10^{-9} torr) was maintained by a 90 liter per second ion pump. Weight losses in the microgram range were determined by measuring balance beam displacement with a cathetometer.

The sample was suspended from one arm of an equal-arm quartz beam microbalance at the end of a chain of 0.025 cm diam fused silica and sapphire rods by a loop of 0.0075 cm diam tungsten wire which passed through the suspension hole in the sample and over a hook on the lowest rod. The chain of sapphire and fused silica rods was connected at each end by V-shaped hooks made by heating and bending the rods.

The arm of the vacuum chamber in which the sample hung was a 16 mm O.D. fused silica tube with a graded seal and Pyrex window at the bottom for temperature measurement. The window was protected from vapor deposition during the sublimation experiments by a magnetically operated shutter.

[1] This work was supported in part by the National Aeronautics and Space Administration.
[2] Present Address: Department of Materials Science, University of Cincinnati, Cincinnati, Ohio.
[3] Figures in brackets indicate the literature references at the end of this paper.
[4] All temperatures in this paper are based on the 1948 IPTS.

A Vycor sleeve of 13 mm O.D. fitted snugly inside the 16 mm O.D. fused silica tube of the vacuum system. A thin platinum coating deposited on the inner surface of this sleeve helped prevent static charge buildup in the vicinity of the sample from interfering with the weighing but did not heat inductively.

An NBS-calibrated optical pyrometer with a magnifying objective lens was used to measure temperatures by sighting on the blackbody hole through the calibrated window and mirror. Calibration corrections for the mirror and window were determined in situ, before and after a series of experiments, by sighting the pyrometer on a band lamp located above the vacuum apparatus on a rotatable mount. With the pyrometer and band lamp in one position, readings on the band lamp filament could be made using the same optical path as was used during the vapor pressure measurements except that the source was further away. By rotating the band lamp 90 degrees and raising the pyrometer, temperature readings could be made directly on the band lamp filament. The calibration correction was obtained from the difference between reciprocal absolute temperatures with and without the window and mirror in the optical path.

In obtaining each datum point the following sequence of operations was performed: (1) The rest point of the microbalance was determined, (2) the sample was slowly heated to a temperature several hundred degrees below the temperature of the experiment, (3) the sample was rapidly heated to the operating temperature and maintained as nearly constant as possible, (4) the sample was rapidly cooled to a temperature well below the experimental temperature, the power slowly reduced, and the oscillator then turned off, and (5) the rest point of the balance was redetermined. The slow heating and cooling portions of the cycle were necessary to avoid lateral motion of the specimen caused by the rf field while the rapid heating and cooling portions of the cycle made the measurement of the duration of the experiment more accurate. The duration of the experiment was measured from the time the oscillator was set at a predetermined power setting to the time the power was decreased. Hence, the deficiency in vaporized material resulting from the fact that the sample is not yet at temperature at zero time is compensated for by the excess of material vaporized after the experiment has been terminated. The mass change of the sample was determined from the displacement of the beam of the microbalance and the previously determined sensitivity of the balance which was about 0.5 micrograms/micron.

The change in sensitivity with load was sufficiently small so that the weight change of the sample during a series of experiments had negligible effect. As in our previous studies [4, 5] duplicate rest points usually agreed to within $\pm 2\ \mu$: however, on several occasions during the present experiments, long term drifts of 20 to 30 μ were noted, indicating that errors due to the weight loss measurement could become important for the experiments with the smaller weight losses.

3. Data and Thermodynamic Treatment

Vapor pressures were calculated using the equation:[5]

$$P = \frac{m}{\alpha\, at}\left(\frac{2\pi RT}{M}\right)^{1/2} \tag{1}$$

where m is the mass of material sublimed, t is the duration of the experiment, a is the projected surface area of the sample, T is the absolute temperature, R is the gas constant, M is the atomic weight of the vaporizing species, monatomic rhenium, and α is the vaporization coefficient, which was assumed equal to unity. The value of the sample area a, at temperature T was calculated from the area measured at room temperature a_0, by assuming that the equation $a = a_0[1 + 2\beta(T - 300)]$ was valid in the temperature range where vapor pressure measurements were carried out. In this equation β is the coefficient of linear thermal expansion which was assumed to be 7.2×10^{-6} $°K^{-1}$ based on the work of Sims et al., [2]. The sample area at room temperature a_0, is calculated from the measured length and diameter of the cylindrical specimen.

In general, the heat of sublimation can be computed from vapor pressure data in two ways. In the second law method, one can make use of the experimental data to evaluate both constants in the equation

$$\log P(\text{atm}) = -\frac{\Delta H°}{R'T} + \frac{\Delta S°}{R'} \tag{2}$$

where $\Delta H°$ is the heat of sublimation at the average temperature, $\Delta S°$ is the entropy change at the same temperature and R' is equal to $R\ln 10$. It should be noted that this equation is only approximate since it ignores the temperature dependence of $\Delta H°$ and $\Delta S°$. Although a more exact second law treatment can be made by inclusion of the temperature dependence of $\Delta H°$ and $\Delta S°$, the error introduced into the second law heat and entropy of sublimation by use of eq (2) in the present case is small in comparison with the error in these quantities resulting from scatter in the vapor pressure data. As a matter of interest, a correct second law treatment for each series of data in the present work was carried out and the values for $\Delta H°$ and $\Delta S°$ at the average temperatures agreed within 0.1 kcal mol^{-1} and 0.05 cal mol^{-1} $°K^{-1}$ with those obtained from the simpler treatment.

In the third law method, one makes use of absolute entropies, usually obtained from heat content and spectroscopic data, to calculate the entropy change for the assumed sublimation process at each temperature. These values and the experimental pressures can then be substituted in eq (2) to obtain the experimental values of $\Delta H°$ at the specified temperatures. In practice, use is generally made of free energy functions which allow one to calculate a value for the

[5] Values of constants used in the calculations were: $R = 1.98717$ cal mol^{-1} $°K^{-1}$, or 8.3143 J $°K^{-1}$ mol^{-1}; atomic weight of rhenium 186.2; one standard atmosphere = 101,325 N/m^2.

heat of sublimation at a reference temperature, usually 298.15 °K (or 0 °K) according to the equation,

$$\Delta H_s^\circ = T\left[\left(\frac{G_T^\circ - H_{298}^\circ}{T}\right)_c - \left(\frac{G_T^\circ - H_{298}^\circ}{T}\right)_g - R\ln P(\text{atm})\right] \quad (3)$$

where $\left(\frac{G_T^\circ - H_{298}^\circ}{T}\right)$ is the free energy function. Differences between $\Delta H_s^\circ(298)$ obtained by the second law and the third law methods can give information concerning the consistency of the vapor pressure data obtained, the free energy function data used, the sublimation reaction assumed, or the existence of a vaporization coefficient other than unity. Frequently, a lack of trend in the heat of sublimation calculated as a function of the experimental temperature is taken as an indication that no important systematic errors are present in the data. Actually, because of random error in the data points and limited temperature ranges, it is usually easier to find a discrepancy by comparing second and third law heats of sublimation or the experimental entropy change with that found from heat content and spectroscopic data.

4. Results

The basic data from four series of sublimation experiments are listed in table 1. The major differences between the first two series and the last two series of measurements are that different pyrometers were used for temperature measurements and different observers made the temperature and weight loss measurements. In addition to these differences, determinations of the window and prism factors ("*A*" values) before and after each of the first three series of measurements indicated that substantial increases in these quantities had taken place. It did not prove possible to determine what was responsible for the increase in *A* values. It is believed that a sufficient temperature gradient exists in the sample region of the vacuum system during measurements so that any Re_2O_7 in the sample region would evaporate and be able to migrate past the shutter to the sight window. An Re_2O_7 contaminant could have been introduced into the sample region of the vacuum system from the sample itself, by oxidation of Re metal during glass-blowing when the window was replaced after the series I measurements, or by oxidation of Re metal by H_2O_2 which was used after the series I and II measurements to remove small amounts of rhenium not collected by the Vycor insert tube. Another possibility is that Re reacted with the Vycor insert tube to form ReO_2(g) and a stable rhenium silicide. Calculation indicates that rhenium disilicide is sufficiently stable so that ReO_2(g) might be formed in appreciable quantities assuming its standard free energy of formation is zero, if the temperature of the rhenium-Vycor interface were 1400 °K or higher. An x-ray diffractogram of material scraped from the side of the Vycor insert tube at the conclusion of the series III data indicated the presence of a phase other than Re which, however, could not be identified as either $ReSi_2$, ReSi, SiO_2, or a Pt-Re alloy.

TABLE 1. *Vapor pressures and heats of sublimation of Rhenium* [a]

Temp.	Duration of run	Wt. loss [b]	Vapor pressure	$\Delta H_s^\circ(298)$
		Series I		
°K	*sec*	*μg*	*atm* × 10⁹	*Kcal mol*⁻¹
3058	240	5563	1280	185.5
2624	900	166	9.46	185.6
2707	540	248	23.9	186.3
2794	300	398	70.1	186.2
2837	245	584	127	185.6
		Series II		
2541	1800	141	3.97	184.3
2491	2400	92.5	1.94	184.3
2627	600	156	13.4	184.0
2712	300	241	42.0	183.6
2812	240	638	141	183.4
2686	300	181	31.4	183.5
2633	600	179	15.4	183.7
2405	240	26.7	0.550	184.2
2348	10800	51.8	.235	183.9
		Series III		
2435	5400	56.8	0.524	186.6
2559	1800	140	3.96	185.6
2645	1200	292	12.6	185.6
2550	1800	121	3.42	185.7
2674	720	252	18.2	185.6
2942	300	2663	482	184.4
2782	360	483	71.0	185.3
2492	3600	108	1.51	185.7
2462	4800	100	1.04	185.3
2351	10800	40.1	0.182	185.3
2401	5400	36.8	.337	186.3
2857	270	906	180	184.8
		Series IV		
2620	1200	189	8.13	186.1
2636	1200	238	10.3	186.0
2664	1200	362	15.7	185.7
2661	1200	320	13.9	186.1
2646	1200	270	11.7	186.0
2650	1200	268	11.6	186.3
2659	1200	285	12.3	186.6
2543	2400	128	2.71	186.4
2585	1200	132	5.64	185.6
2647	1200	260	11.2	186.3
2509	3600	113	1.59	186.7
2687	720	284	20.6	185.8
2442	7200	102	0.707	185.7
2729	420	332	41.6	184.8
2580	1500	177	6.04	184.9

[a] Listed in experimental sequence.
[b] Room temperature sample surface areas were 1.597, 1.591, 1.590, and 1.587 cm² for series I through IV, respectively.

Evidence that the observed increase in *A* value was not simply due to deposition of Re on the window was obtained from the series IV data in which about 3450 *μg* of Re was vaporized with no measurable change in the *A* value of the window and during a series of experiments performed between series III and IV during which 2000 *μg* of Re were vaporized without the shutter interposed between the sample and the window with no resulting change in *A* value. Likewise, the fact that the increase in *A* values for

the series I, II, and III data was all about the same while the total amount of Re vaporized was about 7000, 1150, and 6000 μg, respectively, is inconsistent with this hypothesis. Initially, it was thought that the change in A value had taken place during preliminary outgassing by volatilization of a rhenium oxide contaminant and that the A value measured at the end of the series was the appropriate one to use. However, analysis of the least squares residuals for the series II and series III data show a trend suggesting that at least part of the shift took place during the series. Therefore, for each of the first three series of measurements, the average of the A values determined before and after the series was used to correct the observed temperature to absolute temperature.

It should be noted that the adoption of any constant A value will have practically no effect on the heat of sublimation calculated by the second law method while the third law heat will be changed if the A value is changed as will the second law entropy. Also, if the temperatures are varied randomly during the series, a systematically changing A value will have little effect on the second law heat.

Table 2 summarizes the second law heats and entropies of sublimation calculated by least squares for each series of data in the present work and adjusted to temperatures of 298 and 2600 °K, respectively, using Stull and Sinke's tables [6]; similarly adjusted values based on those reported by Sherwood et al. [1]; mean third law heats of sublimation based on the free energy functions listed by Stull and Sinke; and the standard errors computed for each of these quantities as well as the estimated overall uncertainty in the third law heats of sublimation.

The final heat and entropy of sublimation based on the second law method were obtained by averaging the individual results obtained in the four series of experiments. These values lead to the equation $4.5756 \log P(\text{atm}) = 33.36 - 183500/T$ which can be used to represent the vapor pressure of rhenium in the temperature range (2350–3050 °K).

The final heat of sublimation is the mean third law value obtained from the series IV data. This heat and the tabulated entropy at 2600 °K lead to the equation $4.5756 \log P(\text{atm}) = 31.86 - 180200/T$. These two equations yield the same pressure at 2267 °K and gradually divergent pressures as the temperature increases or decreases. At 3000 °K the equation based on the second law values predicts a pressure of Re(g) about 20 percent higher than the equation based on the third law values.

All of the second law heats of sublimation tabulated in table 2 are higher than the mean third law heats reflecting the fact that the second law entropy changes are greater than the value based on the tables. Among the possibilities which could account for this fact is that the vapor above Re(c) contains vapor species other than Re(g), the tabulated entropy and free energy functions for Re(c) are too high, or a systematic error occurred in temperature measurements due to nonblackbody conditions in the "blackbody hole" of the sample. However, the difference between the second law entropies and third law entropy are not very large and it is questionable as to whether or not the differences are significant. For example, two or three standard errors are frequently accepted as a reasonable measure of the uncertainty in a value and within these limits, agreement of the second and third law heats and entropies of sublimation is satisfactory. The least squares line through all four series of data is $4.5756 \log P(\text{atm}) = 32.26 - 180700/T$, which yields values of the heat and entropy of sublimation in excellent agreement with the tabulated entropy and the third law heat based on the tabulated entropy. The only reason for not recommending these values is that serious biases can be introduced into second law treatments when sets of data points having slight systematic differences are treated as a single set. This is particularly true when the data involved cover different temperature ranges. Since we would not recommend the second law heat and entropy derived in this way if it led to poorer agreement between the second and third law values, it would be rather arbitrary to recommend them because they are in better agreement.

The standard errors (standard deviations in the mean) listed in table 2 are computed from the scatter of the individual determinations about the mean or fitted line. The overall uncertainties for the third law heats of sublimation are the square root of the sum of the squares of the uncertainties arising from random scatter in the data points, uncertainty due to pyrometer calibration and uncertainty in the A value.

The uncertainties due to random scatter are taken as three times the standard error while that in the pyrometer calibration is based on the overall uncertainty listed on the NBS calibration certificate. For the first three series of data the overall uncertainty in the A values were assumed to be equal to one-half of the increase in the A value that took place during

TABLE 2. *Heat and entropies of sublimation of rhenium*

Determination	Second law values				Third law values		
	$\Delta H^\circ_1(298)$ kcal mol^{-1} (kJmol^{-1})	Standard error kcal mol^{-1} (kJmol^{-1})	$\Delta S^\circ_1(2600)$ [a] cal mol^{-1} °K^{-1} (Jmol^{-1} °K^{-1})	Standard error cal mol^{-1} °K^{-1} (Jmol^{-1} °K^{-1})	$\Delta H^\circ_3(298)$ kcal mol^{-1} (kJmol^{-1})	Standard error kcal mol^{-1} (kJmol^{-1})	Overall uncertainty kcal mol^{-1} (kJmol^{-1})
Series I	188.4 (788.1)	3.4 (14.2)	32.76 (137.1)	1.22 (5.1)	185.8 (777.5)	0.2 (0.7)	1.7 (6.9)
Series II	188.2 (787.5)	1.6 (6.6)	33.53 (140.3)	0.61 (2.5)	183.9 (769.4)	0.1 (0.5)	1.4 (5.9)
Series III	190.9 (798.9)	1.9 (7.9)	33.94 (142.0)	0.73 (3.1)	185.5 (776.2)	0.2 (0.7)	1.3 (5.4)
Series IV	189.4 (792.6)	5.1 (21.4)	33.20 (138.9)	1.96 (8.2)	185.9 (778.0)	0.1 (0.6)	0.6 (2.7)
Sherwood et al., [1]	193.0 (807.6)	[b]6.0 [b](24.9)	34.56 (144.6)	[b]2.21 [b](9.2)	185.7 (776.8)	[b]0.4 [b](1.6)	[c]1.2 [c](4.8)
All points this work	186.6 (780.6)	2.6 (11.0)	32.32 (135.2)	1.00 (4.2)	185.3 (775.5)	0.2 (0.6)	[c]0.5 [c](1.9)
Final	189.2 (791.7)	[c]1.9 [c](7.8)	33.36 (139.6)	[c]0.64 [c](2.7)	185.9 (778.0)	0.1 (0.6)	0.6 (2.7)

[a] Calculated from Stull and Sinke [6]. $\Delta S^\circ_{2600} = 31.86$ cal mol^{-1} °K^{-1}.
[b] These standard errors were calculated from the data given in [1].
[c] These error estimates are 3 × standard error.

each series. For the series IV data the uncertainty in the A value was three times the standard error.

The uncertainties due to pyrometer calibration and A value were converted to equivalent uncertainties in the third law heat using the mean value of ΔH_s° (298) and the mean temperature for the series. These were then combined with the random uncertainty to yield the overall uncertainty listed in the last column of table 2.

In terms of uncertainties in temperature, the uncertainties in the pyrometer calibration, A value, random scatter and the overall temperature uncertainty were: series I—7, 22, 9, 25 °K; series II—6, 19, 4, 20 °K; series III—6, 16, 6, 18 °K; and series IV—6, 2, 6, 9 °K.

5. Summary and Conclusions

The mean third law heat of sublimation selected from the data in the present study as the most reliable is in excellent agreement with the mean value derived from the data of Sherwood et al. [1], while the agreement between the second and third law heats of sublimation is somewhat improved.

The question as to whether the second or third law heat of sublimation is the more reliable in the present case appears to be worthy of comment.

For metallic rhenium, heat content data obtained by conventional methods is available only to 1474 °K. Low temperature calorimetric data reported by Smith, Oliver, and Cobble [7] agrees within about one-half percent with the high-temperature data of Jaeger and Rosenbohm [8] in the range 0–20 °C. High temperature heat capacity data obtained by Taylor and Finch [9] in the range 300 to 2200 °K by the pulse heating method is systematically lower than the data of Jaeger and Rosenbohm; however, the estimated uncertainty of the former data is ±4 percent while that of the latter is ±0.5 percent and the data are in satisfactory agreement within these error limits. Between 1500 and 2600 °K, the contribution of the extrapolated heat capacity data to the free energy function and entropy of Re(c) is 3.34 and 4.53 cal mol^{-1} $°K^{-1}$, respectively, or about 20 percent. Hence, an extremely pessimistic view of the errors involved in the heat capacity of Re(c) would be necessary in order to justify the preference of the second law results. Because of this, the vapor pressure equation based on the third law heat of sublimation and tabulated entropies is recommended.

6. References

[1] E. M. Sherwood, D. M. Rosenbaum, J. M. Blocher, Jr., and I. E. Campbell, J. Electrochem. Soc. **102,** 650 (1955).

[2] C. T. Sims, C. M. Craighead, and R. I. Jaffee, J. Metals (AIME Trans. 203) **7,** 168 (1955).

[3] N. J. Carrera, R. F. Walker, W. Nalley, and C. Steggerda, Vacuum Microbalance Techniques, Vol. **3,** p. 153, K. Behrndt, ed., (Plenum Press, New York, N.Y., 1963).

[4] N. J. Carrera, R. F. Walker, and E. R. Plante, J. Res. NBS **68A** (Phys. and Chem.) No. 3, 325 (1964).

[5] R. Szwarc, E. R. Plante, and J. J. Diamond, J. Res. NBS **69A** (Phys. and Chem.) No. 5, 407 (1965).

[6] D. R. Stull and G. C. Sinke, Thermodynamic Properties of the Elements, American Chemical Society, Washington, D.C. (1956).

[7] W. T. Smith, Jr., G. D. Oliver, and J. W. Cobble, J. Am. Chem. Soc. **75,** 5785 (1953).

[8] F. M. Jaeger and E. Rosenbohm, Koninkl. Akad. Wetenschap. Amsterdam, Proc. Sect. Sci. **36,** 786 (1933).

[9] R. E. Taylor and R. A. Finch, J. Less-Common Metals **6,** 283 (1964).

(Paper 70A2–393)

799-883 O–66—5

JOURNAL OF RESEARCH of the National Bureau of Standards—A. Physics and Chemistry
Vol. 70A, No. 2, March–April 1966

Steady-State Response of Silicon Radiation Detectors of the Diffused P–N Junction Type to X rays. II: Photodiode Mode of Operation[1]

Karl Scharf and Julian H. Sparrow

Institute for Basic Standards, National Bureau of Standards, Washington, D.C.

(December 22, 1965)

The response to x rays of silicon radiation detectors of the *p-n* junction type was investigated with special consideration of their dependence on the applied voltage. In agreement with theory, the photocurrent, I_g, was found to consist of a voltage-independent part mainly determined by the average diffusion length of minority carriers in the base layer, and a voltage-dependent part which is proportional to the width of the depletion region, w. Due to the voltage dependence of w, I_g increases with increasing voltage applied, but its relative change produced by different voltages is independent of exposure rate and quality of radiation. Exposure rate and energy dependence of I_g expressed in relative values are thus independent of applied voltage. Silicon radiation detectors, used as photodiodes can therefore be useful for monitoring of radiations at exposure rates larger than 1 R/min, taking advantage of the possibility to increase current sensitivity by increasing the voltage V and to increase the voltage signal by increasing the load resistance R_L. There are however limitations in increasing V and R_L because of the increasing noise with increasing dark current and some dependence of measured current signals on R_L. The temperature coefficient of I_g is positive and independent of R_L, but shows some small voltage dependence. In the temperature range between 25 and 50 °C, the average temperature coefficient is approximately 0.35 percent per degree centigrade. A value of the average diffusion length of minority carriers in the base layer has been derived from the measured voltage dependence of I_g.

Key Words: X rays, dosimetry, silicon, silicon junctions, diodes, semiconducting devices, photodiodes, radiation detectors.

1. Introduction

In a previous paper [1][2] (hereafter referred to as part 1) an investigation was reported of the steady-state response of silicon radiation detectors of the diffused $p-n$ junction type to x rays when operated as photovoltaic cells. This paper reports an investigation of the steady-state response of such cells to x rays when operated as photodiodes. Both investigations were carried out in order to examine the suitability of such cells for exposure rate measurements of x rays and to obtain information leading to the establishment of optimum conditions for design and operation of such cells when used for x- and gamma-ray dosimetry.

Under the photodiode mode of operation, as well as in the case where the detector is operated as a photovoltaic cell, a photocurrent is generated by irradiation in the reverse direction of the detector which, for a given quality of radiation determined by its spectral energy distribution, is proportional to the exposure rate. Under the photovoltaic mode of operation, no external voltage is applied to the detector. But under irradiation, the detector becomes biased in the forward direction, causing part of the generated photocurrent to leak back through the detector in the forward direction. The current measured in the external circuit is equal to the difference of the generated photocurrent and the leakage current, and is thus strongly dependent on the current-voltage characteristic of the detector and the external load resistance.

Under the photodiode mode of operation, the detector is biased in the reverse direction by an externally applied voltage. The total current measured under irradiation is equal to the sum of the dark current produced by the bias voltage without irradiation and the generated photocurrent. The full value of the generated photocurrent can thus be determined by measuring the increase in reverse current produced by irradiation. This is usually done by measuring the change in voltage drop over a known load resistance, and this voltage signal can be increased over a wide range by increasing the load resistance, thereby increasing the sensitivity of measurements. The photocurrent measured under the photodiode mode of operation is not determined by the junction leakage current, as is the case under the photovoltaic mode of operation. Its value and temperature dependence should therefore be independent of the size

[1] Work supported in part by the U.S. Atomic Energy Commission.

[2] Figures in brackets indicate the literature references at the end of this paper.

of load resistance used. How far this ideal performance is obtained with silicon detectors will be discussed below. Special consideration is given in this paper to the voltage dependence of the generated photocurrent, which increases with increasing bias voltage, thereby increasing the radiation sensitivity of the detector.

Measurements were made of (a) the performance characteristics of silicon radiation detectors operated as photodiodes when irradiated with x rays, and of (b) the voltage dependence of the generated photocurrent at different values of exposure rate, detector temperature, and photon energy.

2. Theoretical Considerations

If a reverse voltage is applied to a *p-n* junction type silicon detector, the main part of the voltage drop inside the silicon wafer appears across the width of the depletion region. That means that, also under the photodiode mode of operation, the electric field in the base and surface layer outside the depletion region may be assumed to be negligibly small. Current carriers produced outside the depletion region are collected by the electric junction field by diffusion only and form, together with carriers produced by radiation inside the depletion region, the generated photocurrent I_g. One can, therefore, apply the relation for I_g (eq (1)), which was derived in part 1 for the photovoltaic mode of operation, considering a one-dimensional model of a *p-n* junction detector with a *p*-type base layer and an *n*-type surface layer (fig. 1):

$$I_g = \frac{qA_R g_s}{\mu} \exp(-\mu d_s)[1-(1-\mu L_n')\exp(-\mu w)+\mu L_p'] \text{ ampere} \quad (1)$$

where g_s is the carrier generation rate or the number of carriers produced per cm^3 per second at the irradiated silicon surface, and is given by the relation (eq (A16) in part 1):

$$g_s = \frac{86.9\mu_{en}}{\epsilon(\mu_{en}/\rho)_{air}}(\Delta X/\Delta t). \quad (2)$$

In eqs (1) and (2), q is the electronic charge in coulomb, A_R the irradiated silicon surface area in cm^2, μ and μ_{en} the linear attenuation and energy absorption coefficients respectively of x rays in silicon in cm^{-1}, $(\mu_{en}/\rho)_{air}$ the mass energy absorption coefficient of x rays in air in $g^{-1}cm^2$, d_s the thickness of the surface layer, and w the width of the depletion region in cm, ϵ the average electron-hole pair production energy in ergs, and $\Delta X/\Delta t$ the exposure rate in R/sec. The quantities L_n' and L_p' are the effective diffusion lengths defined in part 1 [1], which are functions of the attenuation coefficient μ, and of the electrical properties and geometrical dimensions of the silicon wafer used in the detector.

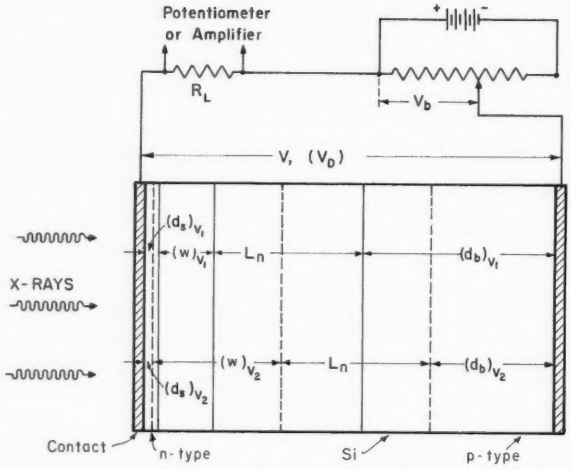

FIGURE 1 *Photodiode measuring circuit and geometry of* p-n *junction detector showing widths of surface layer* (d_s), *base layer* (d_b), *and depletion region* (w) *at two different voltages* V_1 *and* V_2 *applied at the detector.*

For the detectors investigated, it may be assumed that $d_b/L_n \gg 1$, and $d_s/L_p \ll 1$, if d_b and d_b are the widths of the base and surface layers respectively (fig. 1) and L_n and L_p the average diffusion lengths of the minority carriers determined by their lifetime τ and diffusion constant D ($L=\sqrt{D\tau}$). Assuming further negligible surface recombination on the base contact, one can substitute in eq (2)

$$L_n' = \frac{L_n}{\mu L_n + 1}; \; L_p' = \frac{d_s}{1+(s_p d_s)/D_p} \quad (3)$$

and obtain [1]

$$I_g = \frac{qA_R g_s}{\mu}\exp(-\mu d_s)\left[1-\frac{\exp(-\mu w)}{\mu L_n+1}+\frac{\mu d_s}{1+(s_p d_s)/D_P}\right] \quad (4)$$

if s_p and D_p are the surface recombination velocity and the diffusion constant of holes in the *n*-type surface layers respectively and L_n the average diffusion length of electrons in the *p*-type base layer.

A characteristic feature to be considered under the photodiode mode of operation is the voltage dependence of I_g. Under the photovoltaic mode of operation [1], the voltage dependence of I_g was neglected because radiation-produced forward voltages were of the order of a few millivolts only. However, when operating the detector as photodiode, bias voltages of several volts are applied. With increasing voltage, the width w of the depletion region is increased, while the effective diffusion lengths of the minority carriers remain unchanged, provided the previously made assumption of field-free diffusion regions is valid.

The charge collecting volume is thus increased and extended deeper into the silicon crystal (fig. 1), and according to eq (4), I_g is increased as well.

The voltage dependence of the width of the depletion region is given by the relation [2]

$$w_V = w_1 (V + V_0)^m \tag{5}$$

if w_V is the width of the depletion region at the voltage V applied at the detector during irradiation, V_0 the potential difference (barrier height) at the p-n junction at $V = 0$, and w_1 the width of the depletion region at $(V + V_0) = 1$ V. The power exponent m is dependent on the distribution of impurities in the transition region and has values between 1/3 and 1/2.

In diffused p-n junction detectors of the type investigated, w_1 is of the order of 10^{-3} cm. Therefore for x rays, except for very low photon energies and high bias voltages, one can assume $\mu w \ll 1$ and substitute in eq (4) as an approximation $\exp(-\mu w) = 1 - \mu w$. Furthermore, it may be considered that the surface layer thickness d_s is of the order of 1 to 2 μ, and is negligibly small compared with the diffusion length L_n of electrons in the p-type base layer, which is of the order of a few hundred microns. One can therefore neglect the absorption of radiation in the surface layer and the current contribution by carriers produced in this layer, which is further reduced by the strong surface recombination of minority carriers at the surface contact.

Under these assumptions one obtains from eq (4) and (5):

$$(I_g)_V = a + b(V + V_0)^m \tag{6}$$

if $(I_g)_V$ is the generated current at the applied voltage V and

$$a = (qA_R g_s L_n)/(\mu L_n + 1); \qquad b = (qA_R g_s w_1)/(\mu L_n + 1). \tag{7}$$

Equation (6) gives a simple interpretation of the voltage dependence of I_g, showing that I_g consists of a voltage-independent part a formed by carriers collected by diffusion, and of a voltage-dependent part $b(V + V_0)^m$ due to carriers produced inside the depletion region.

Both constants a and b are dependent on exposure rate and quality of radiation due to their dependence on g_s and μ, and are proportional to the irradiated surface area A_R. However their ratio

$$b/a = w_1/L_n$$

is independent of these parameters and only determined by the electronic properties of the silicon wafer. Equation (6) can therefore be written as

$$(I_g)_V = a k_V \tag{8}$$

if k_V is called the voltage factor at the voltage V given as

$$k_V = 1 + (b/a)(V + V_0)^m = 1 + (w_1/L_n)(V + V_0)^m. \tag{9}$$

For the detectors investigated one can assume $m = 0.5$ [3] and obtains for the voltage dependence of I_g

$$\frac{dI_g}{dV} = \frac{qA_R g_s w_1}{2(\mu L_n + 1)} (V + V_0)^{-1/2}. \tag{10}$$

For a given radiation, the voltage dependence of I_g decreases with increasing voltage V.

The diffusion part a of the generated photocurrent may also show a voltage dependence if high bias voltages are applied, for the following reasons: By increasing V, the depletion region is extended, pushing the diffusion region deeper into the silicon wafer. The width d_b of the base layer remaining outside the depletion region is thereby reduced, and the ratio d_b/L_n is decreased (fig. 1). For values smaller than approximately $d_b/L_n = 3$, the effective diffusion length L_n' will markedly decrease with decreasing values of d_b/L_n [1]. L_n' will become smaller than the value given by eq (3), and consequently I_g and dI_g/dV will be different from values obtained from eq (8) and (10). This effect, however, need not be considered in this investigation, because of the dimensions and electric properties of the detectors investigated and the moderate bias voltages applied.

3. Experimental Procedure

The silicon radiation detectors investigated were of the same type as those used in the measurements reported in part 1. They were commercially available encapsulated detectors of the diffused p-n junction type made of 1000 Ω-cm p-type silicon with an n-type surface layer on the irradiated side. The surface was protected by a one-micron-thick aluminum layer and was covered with additional aluminum sheets of a total thickness of approximately 325 μ, in order to approach electron-equilibrium conditions in the charge-collecting volume for the types of radiations used.

The x-ray sources were a 250-kV tube and a 50-kV beryllium-window-type tube with an inherent filtration of approximately 4.0 mm Al and 0.25 mm Be, respectively. The x-ray tubes were tungsten target tubes operated by stabilized constant voltage supplies. Different filtration was used as described in part 1 for obtaining different qualities of radiations. Exposure rates of x-rays were measured with calibrated R-meters, except in the case of low-energy radiations obtained from the 50-kV x-ray tube, which were measured with an NBS free-air chamber. If not otherwise stated, the x-ray beam was collimated as described in part 1, so that only the free sensitive surface of the detector was hit by the radiation.

Dark current and total current under irradiation were determined by measuring the voltage drop over a known load resistance (fig. 1) by a null method using

a potentiometer. For measurements of small voltage signals obtained with small load resistances, a d-c amplifying microvolt-ammeter of known amplifying ratio was used in measuring the amplified voltage output by a null method. The photocurrent or current signal was determined from the difference of voltages measured with and without irradiation. Only moderate bias voltages were applied to the detectors in order to avoid the increased noise and instability of the dark current observed at higher bias voltages.

Capacity measurements were carried out with a standard-type capacity bridge.

4. Results and Discussion of Measurements

4.1. Performance Characteristics

The performance characteristics of a silicon *p-n* junction radiation detector when operated as a photodiode is shown in figure 2. The detector had a free surface area of approximately 5 mm² and was fully irradiated with 30-kV x-rays of 0.09 mm Al half-value layer (HVL) at different exposure rates.

When the detector is being irradiated, the generated photocurrent I_g is added to the reverse current I_D produced by the applied bias voltage V_b without irradiation, also called the dark current. The current-voltage characteristic is raised and the vertical distance between the current-voltage characteristic obtained with and without irradiation is equal to I_g, which is proportional to the exposure rate. The detector can therefore be used for exposure rate measurements by determining I_g or any other quantity linearly related to it. How far this can be achieved will be discussed first.

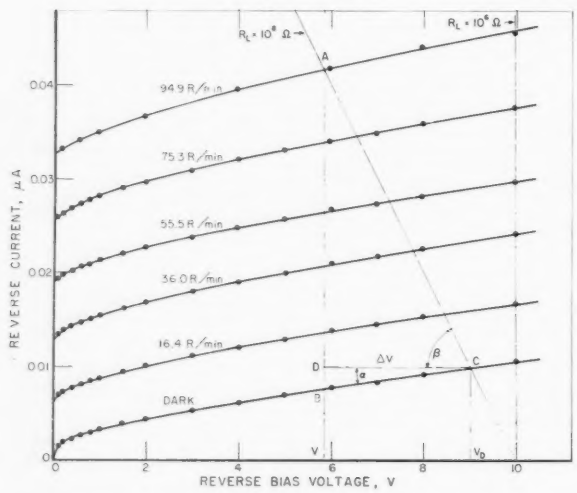

FIGURE 2. *Reverse current-voltage characteristics of a silicon radiation detector of the diffused* p-n *junction type measured without irradiation and when fully irradiated with 30 kV x rays of 0.09 mm Al HVL at different exposure rates with load lines indicated for two different load resistances.*

Irradiated cell surface area $A_E = 5.0$ mm².

At a certain bias voltage V_b, the voltage V applied at the detector is dependent on the load resistance and is, as indicated by the load lines in figure 2, at a certain current I

$$V = V_b - IR_L.$$

By irradiation, the reverse current is increased and V decreases by the additional voltage drop in the load resistance. This means that currents obtained with and without irradiation, are measured at different detector voltages.

For an ideal photodiode, it is assumed that the dark current reaches a voltage-independent saturation value at a voltage of a few volts and that I_g is voltage-independent. In this case, the current and voltage signals produced by irradiation are

$$\Delta I = I_g; \qquad \Delta V = I_g R_L. \tag{11}$$

By increasing the load resistance R_L, the voltage signal ΔV can be increased, theoretically without a limit, and this simple way of signal-amplifying is the main advantage in the use of photodiodes.

However, the assumptions made for an ideal photodiode cannot be applied to silicon *p-n* junction detectors. The dark current in a silicon detector does not reach a saturation value, but increases monotonously with increasing voltage, and the generated photocurrent shows a small voltage dependence. If $(I_R)_V$ is the total current measured under irradiation at the voltage V, and $(I_D)_{V_D}$ the dark current at the voltage V_D, then the current and voltage signals are

$$\Delta I = (I_R)_V - (I_D)_{V_D}; \qquad \Delta V = R_L \Delta I \tag{12}$$

but ΔI is now different from I_g, as seen from figure 2.

The relation between I_g and ΔI can be derived from figure 2. Assuming, for instance, $R_L = 10^8\Omega$, and an exposure rate of 96 R/min, the values of V and V_D were obtained from the intersections of the loadline for $10^8\Omega$ with the respective characteristics measured with and without irradiation. Assuming further a linear voltage dependence of the dark current within the range of ΔV, a triangle ABC can be constructed (fig. 2) where $\overline{AB} = (I_g)_V$, $\overline{AD} = (\Delta I)_V$, $\overline{CD} = \Delta V$, $|\tan \alpha| = (\Delta I_D / \Delta V)_{V_D}$, and $|\tan \beta| = (R_L)^{-1}$. By trigonometrical analysis one obtains from the triangle

$$(I_g)_V = k_c (\Delta I)_V \tag{13}$$

if the factor k_c, which will be called the curve factor, is

$$k_c = [1 + R_L (\Delta I_D / \Delta V)_{V_D}].$$

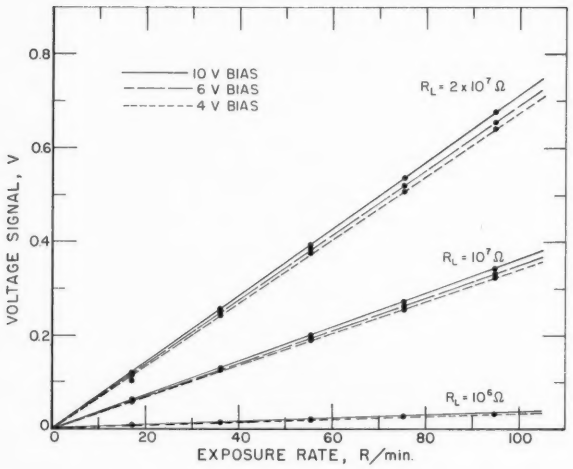

FIGURE 3. *Exposure rate dependence of voltage signals measured at different bias voltages and load resistances as derived from measurements shown in figure 2.*

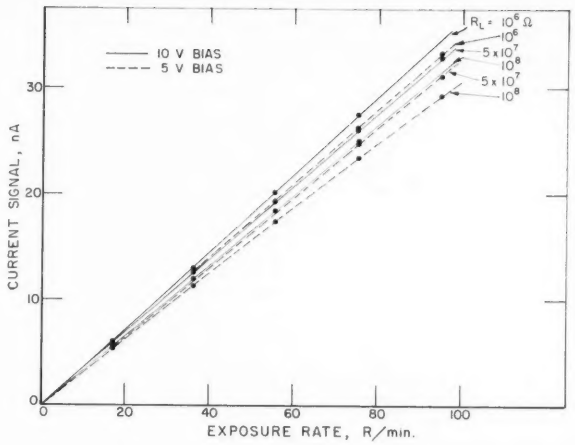

FIGURE 4. *Exposure rate dependence of current signals measured at different bias voltages and load resistances as derived from measurements shown in figure 2.*

At constant exposure rate and constant voltage V, i.e., at constant I_g, ΔI will be the smaller the larger R_L and the larger the slope of the current-voltage characteristic at the voltage V_D. Introducing the dynamic diode resistance $r_V = (dV/dI)_V$, eq (14) can also be written as

$$k_c = [1 + R_L/(r)_{V_D}] \tag{14a}$$

provided that the slope of the dark current-voltage characteristic is constant within the voltage range ΔV. This condition will obviously be fulfilled if the bias voltage is not too low and the voltage signal is kept small by reducing the load resistance. Because of the voltage dependence of r_V, which increases with increasing V_D, the curve factor will show some voltage dependence.

Figure 3 shows the exposure rate dependence of voltage signals at different bias voltages and load resistances, as derived from the performance characteristics shown in figure 2. Voltage signals are proportional to exposure rate and, at constant values of load resistance, increase with increasing V_b. Current signals derived from these voltage signals ($\Delta I = \Delta V/R_L$) show obviously the same dependence on exposure rate and bias voltage as ΔV (fig. 4), but decrease with increasing load resistance. This indicates that voltage signals increase with increasing load resistance at a smaller rate than R_L (eq (12)).

The dependence of ΔI and correspondingly of ΔV on circuit parameters like V_b and R_L can be explained by the dependence of the curve factor (eq (14)) on those parameters and by the voltage dependence of $(I_g)_V$. The larger R_L, the larger is k_c and, at constant V, the smaller is ΔI. For smaller bias voltages and very large R_L, e.g., $R_L = 10^8\Omega$ at $V_b = 5$ V (fig. 4), the slope $(\Delta I_D/\Delta V)_{V_D}$ does not remain constant within ΔV. Equation (14) cannot be applied and the exposure rate dependence of ΔI and ΔV becomes nonlinear. In particular, a nonlinear exposure rate dependence may also be observed at moderate values of R_L, if the voltage applied during irradiation at the detector is in the low-voltage region where the dynamic resistance r_V is strongly voltage dependent. The increase of ΔI with increasing bias voltage is due to the increase of I_g with increasing V according to eq (8).

4.2. Voltage Dependence of I_g

In order to measure the actual voltage dependence of I_g, the influence of the curve factor was reduced as much as possible by using small load resistances. In this way the curve factor could be kept approximately at unity value, thus allowing the assumption $\Delta I = I_g$.

The voltage dependence of the current signal measured on a silicon radiation detector is shown in figure 5. The detector had a sensitive surface area of approximately 2.5 cm², and was fully irradiated with heavily filtered 100-kv x rays of 11.2 mm Al HVL at an exposure rate of approximately 2 R/min. The voltage dependence of the dark current of the detector was of the order of 10^{-8} A/V and the load resistance $10^4\Omega$. The curve factor was therefore approximately 1.0001. The current signal shows a small nonlinear increase with increasing bias voltage, increasing only by about 11 percent when changing the bias voltage from 1 to 15 V.

In order to test the relation given by eq (6), the unknown quantities m and V_0 had to be determined by capacity measurements. By considering eq (5), one obtains the voltage dependence of the junction capacitance

$$C = \frac{\epsilon_{Si}\epsilon_0 A_c}{w} = \frac{\epsilon_{Si}\epsilon_0 A_c}{w_1}(V + V_0)^{-m} \tag{15}$$

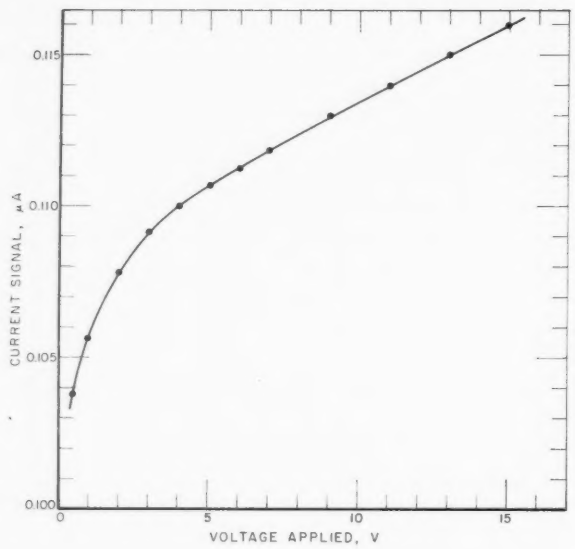

FIGURE 5. *Voltage dependence of current signals produced by heavily filtered 100 kV x rays of 11.2 mm Al HVL at an exposure rate of approximately 2 R/min.*
Surface area of detector is approximately 2.5 cm². $R_L = 10^6\Omega$.

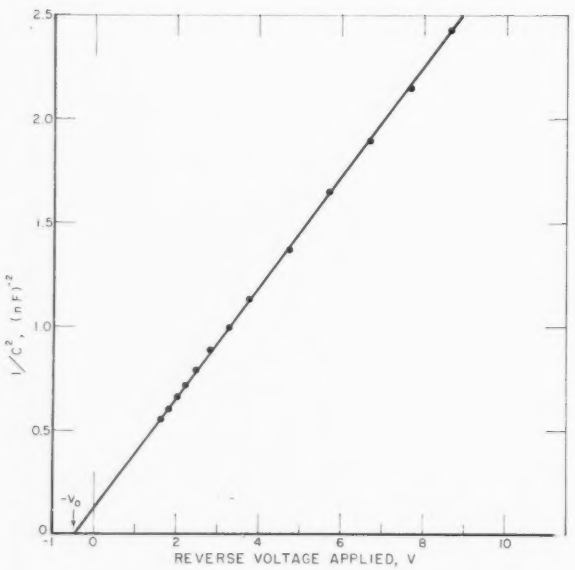

FIGURE 6. *Determination of zero-voltage junction barrier height* V_0 *and width* w_1 *of depletion region at* $(V + V_0) = 1$ V *from intercept at voltage axis and slope of graph* $1/C^2$ *versus V derived from measurement of voltage dependence of capacity C of* p-n *junction type silicon radiation detector.*

if ϵ_{Si} is the dielectric constant of silicon ($\epsilon_{Si} = 12$), ϵ_0 the permittivity of free space ($\epsilon_0 = 8.85 \times 10^{-12}$ F/m), and A_c the area of the surface contacts of the detector. From measurements of the voltage dependence of C, a value of m between 0.4 and 0.5 was obtained from a double logarithmic graph of C versus $(V + V_0)$ assuming tentatively $V_0 = 0.5$ V. Choosing the theoretical value of $m = 0.5$ for an abrupt junction [2], one can derive from eq (15) the relation:

$$\frac{1}{C^2} = \left(\frac{w_1}{\epsilon_{Si}\epsilon_0 A_c}\right)^2 (V + V_0) \tag{16}$$

from which V_0 and w_1 can be determined. By plotting measured values of $(1/C^2)$ versus V, a straight line was obtained (fig. 6) confirming the value chosen for m. The value of V_0 is given by the intercept on the voltage axis and w_1 could be determined from the slope of this graph. Values of V_0 and w_1 evaluated by the method of least squares were for the detector investigated $V_0 = 0.477$ V and $w_1 = 14.5 \times 10^{-4}$ cm, $(\text{volt})^{-1/2}$.

These values were used in the evaluation of measurements given in the following sections.

a. Exposure Rate Dependence

The voltage dependence of current signals at different exposure rates, as derived from measurements shown in figure 2, is given in figure 7. The current signals were measured over a load resistance of $10^6\Omega$, but due to the small dark current of the detector, the curve factor differed only by approximately 0.1 percent from unity. The current signals ΔI can

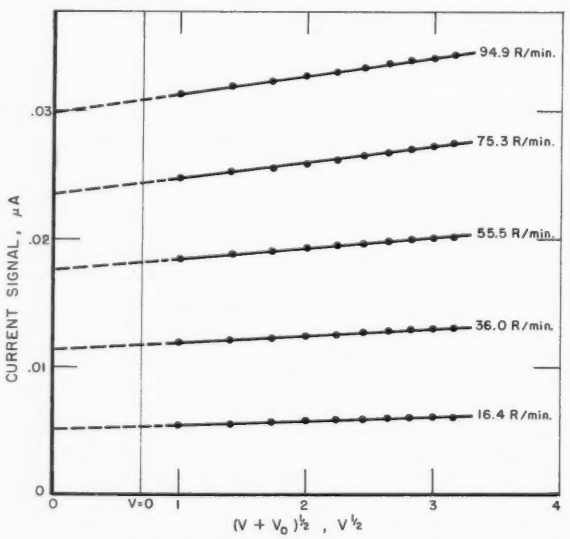

FIGURE 7. *Current signals measured at different exposure rates as function of* $(V + V_0)^{1/2}$.
Intercepts on current axis obtained by linear extrapolation of measured values, as indicated by dashed lines, are the voltage-independent diffusion parts of the current signals.

therefore be assumed to be equal to the values of the generated photocurrents I_g.

In agreement with eq (6), the current signal is at constant exposure rate a linear function of $(V+V_0)^{1/2}$ and increases with increasing voltage V, the slope b increasing with increasing exposure rate. By linear extrapolation of ΔI to $(V+V_0)^{1/2}=0$, one can separate the voltage-dependent and voltage-independent parts of the current signals, both parts showing proportionality with exposure rate. Or in other words, the current sensitivity of the detector, expressed in amperes per unit exposure rate, increases with increasing voltage, but the current signal measured at any voltage increases at the same rate with increasing exposure rate. This is indicated in table 1, showing that at different voltages ΔI increases at the same rate as the exposure rate. This means that the voltage factor (eq (8)) is independent of exposure rate and was in particular obtained from these measurements as $k_V=[1+0.05\,(V+V_0)^{1/2}]$.

TABLE 1. *Exposure rate dependence (fig. 7).*
Relative values of current signals measured at different voltages.

Exposure rate		Current signal (rel. value)		
R/min	Relative value	3V	6V	10V
16.4	0.173	0.175	0.176	0.175
36.0	.379	.378	.379	.379
55.5	.585	.582	.588	.584
75.3	.793	.788	.794	.795
94.9	1.000	1.000	1.000	1.000

b. Temperature Dependence

For measuring the voltage dependence of the current signal at different temperatures, the detector was placed inside a thermostatically controlled oven, and fully irradiated with 100-kV x rays filtered by 2 mm Al, and the nonmetallic oven wall at an exposure rate of approximately 50 R/min. The load resistance was $10^4\Omega$.

Figure 8 shows the current signals measured at different temperatures as function of $(V+V_0)^{1/2}$. The temperature dependence of V_0 was taken into account in determining the abcissa values. A reduction in V_0 of 2.8 mV per degree centigrade was assumed in accordance with calculations made by Baldinger et al., [4] for silicon detectors of a type similar to those used in this investigation. The values of V are the voltages applied at the detector as measured at different bias voltages and temperatures.

The current signal increases with increasing temperature and remains for voltages above approximately 1 V, proportional to $(V+V_0)^{1/2}$. The diffusion part a obtained by extrapolation of the linear part of the graph to $(V+V_0)^{1/2}=0$, increases with increasing temperature, while the slope b of the voltage dependent part decreases. By increasing the temperature from 23.4 to 51.1 °C, a increases by about 11 percent and b decreases by about 24 percent, thus reducing the ratio b/a. This means that the voltage factor (eq 9) is slightly temperature dependent, showing at 5 V a decrease from 1.06 to 1.04 when increasing the temperature from 23.4 to 51.1 °C. The voltage-dependent part is only a small fraction of the total current signal, and the temperature dependence of the current signal is mainly determined by the diffusion part, which increases with increasing temperature.

The temperature dependence of ΔI at constant applied voltages, as derived from these measurements is shown in figure 9. The curve factor was for the detector investigated for a load resistance of $10^4\Omega$ approximately 1.01 at 23.4 °C and $V=1.5$ V, slightly decreasing with increasing voltage and increasing with increasing temperature. These changes were of the order of 1 percent, so that the temperature

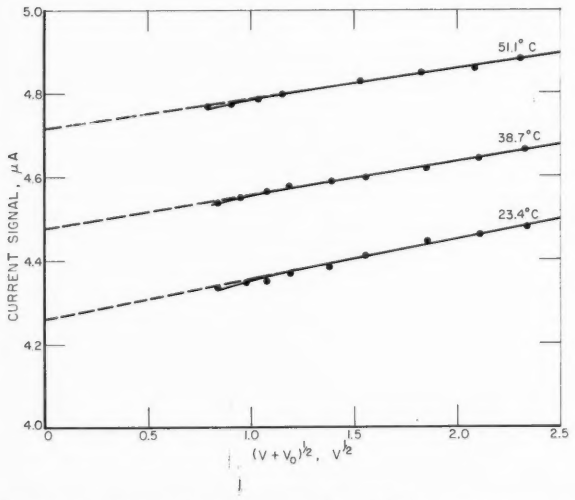

FIGURE 8. *Current signals measured at different temperatures as function of* $(V+V_0)^{1/2}$.
Linear extrapolation of measured values to $(V+V_0)^{1/2}=0$ is indicated by dashed lines.

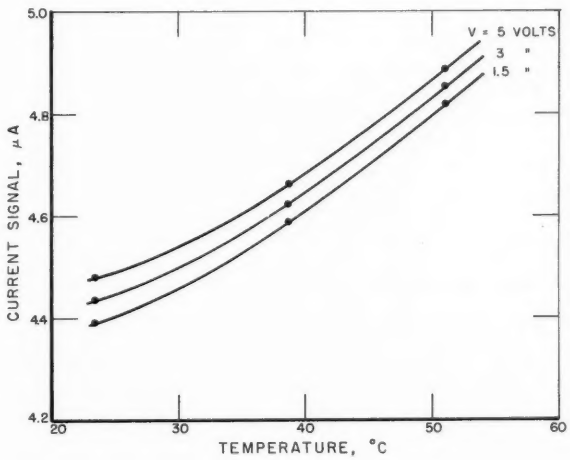

FIGURE 9. *Temperature dependence of current signals measured with different voltages applied at the detector.*

dependence given for the current signal may be assumed to be qualitatively the same for I_g. The temperature coefficient given as $\frac{1}{I_g}\left(\frac{dI_g}{dT}\right)$ increases with increasing temperature and decreases slightly with increasing voltage. At 51.1 °C the temperature coefficient has approximately the same value of 0.4 percent per degree centigrade for different voltages, but changes at 23.4 °C from 0.20 percent per °C at 1.5 V to 0.17 percent per °C at 5 V. Assuming linear temperature dependence between 25 and 50 °C

$$(I_g)_T = (I_g)_{T_0}(1+\gamma\Delta T) = (I_g)_{T_0}k_T \qquad (17)$$

where k_T is called the temperature factor, the average temperature coefficient γ expressed in percent is 0.36 percent per °C at 1.5 V and 0.33 percent per °C at 5 V. These values are in good agreement with the value of 0.32 percent per °C, given in part I for the temperature coefficient of the short circuit current measured in silicon *p-n* junction radiation detectors operated as photovoltaic cells [1].

As previously stated [1], no definite explanation can be given for the positive temperature coefficient of the generated photocurrent I_g. However, the measurements given here support the assumption made [1] that the positive temperature coefficient of I_g is due to an increase with increasing temperature of the average diffusion length L_n of electrons in the base layer, which determines the size of the voltage-independent part collected by diffusion. A decrease in the pair-production energy ϵ could have only a small effect because a larger decrease in ϵ would cause an increase rather than a decrease in the temperature dependence of the voltage-dependent part of I_g (eq 2) that is not observed. A reduction in the internal series resistance with increasing temperature, sometimes assumed to be responsible for the positive temperature coefficient of I_g [5], would only have an effect on the dark current characteristic, because I_g is independent of the total load resistance. At a constant applied voltage V, a decreasing series resistance may cause an increase of the voltage applied at the junction (barrier height). But this increase would be very small because of the small series-to-diode resistance ratio. A decrease in series resistances may affect the curve-factor, due to a change of the slope of the dark current characteristic. However, considering the values of voltage- and curve-factors and their temperature dependence given above, changes of these factors cannot account for the increase of approximately 11 percent in the measured current signal.

The decrease in the slope of the graphs in figure 8 with increasing temperature may be due to a decrease of w and an increase of L_n (eq (9)). A negative temperature coefficient of the width w of the depletion region has been indicated by measurements of the temperature dependence of the capacitance of silicon diodes, which is inversely proportional to w. Baldinger et al. [4], and Antula [6] found in silicon diodes an increase of junction capacitance with increasing temperature and a decrease of the temperature coefficient of the capacitance with increasing bias voltage, that is in qualitative agreement with measurements discussed here.

c. Energy Dependence

The energy dependence of radiation-produced current signals measured at different applied voltages, including zero voltage (photovoltaic current) is shown in figure 10 for moderately and lightly filtered x rays, and in figure 11 for heavily filtered x rays. Load

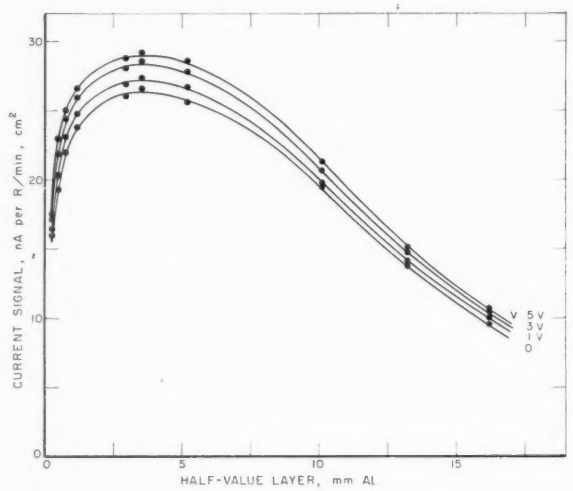

FIGURE 10. *Dependence of current sensitivity (current signal at an exposure rate of 1 R/min and 1 cm² irradiated surface) on quality of moderately and lightly filtered x rays as measured with different voltages applied at the detector.*

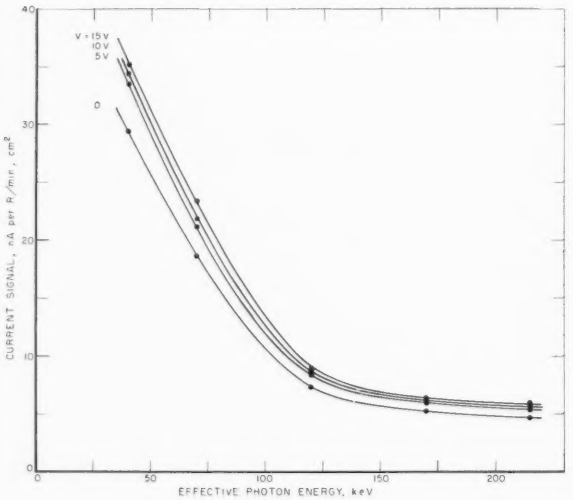

FIGURE 11. *Dependence of current sensitivity (current signal at an exposure rate of 1 R/min and 1 cm² irradiated surface) on effective photon energy of heavily filtered x rays (see table 1 in part I) as measured with different voltages applied at the detector.*

resistances used were of such size that curve factors were approximately of unity value and current signals may be assumed to be approximately equal to generated photocurrents.

The current sensitivity, expressed here by the radiation-produced current signal measured at 1 R/min and 1 cm² irradiated surface area, increases with increasing voltage V, but the shape of its energy dependence remains similar at different applied voltages. For a certain increase of V, the increment in current signal shows an energy dependence similar to that of the total current signal. It first increases with decreasing HVL, reaches a maximum at a HVL of approximately 3.5 mm Al and then decreases with further decreasing HVL.

The voltage dependence of ΔI can better be analyzed by plotting ΔI as a function of $(V+V_0)^{1/2}$ as shown in figure 12. The linear dependence of ΔI on $(V+V_0)^{1/2}$ is maintained for different types of radiation, but the slope b on the voltage-dependent part of ΔI, increases and decreases in the same way as the total signal ΔI changes with quality of radiation. This behavior is in agreement with eq (7) showing that the slope b and the voltage independent part a of the current signal are both proportional to $g_s/(\mu L_n+1)$. With decreasing photon energy, a and b are first increasing because of the increase of g_s. But due to the energy dependence of the attenuation coefficient μ, which increases with decreasing photon energy at a greater rate than g_s, both a and b reach a maximum and then decrease at lower energies.

If at different radiation qualities a and b increase and decrease at the same rate, then the ratio b/a, and consequently the voltage factor k_V (eq (9)), must be independent of radiation quality. The voltage factor

$$k_V = I_g/a \tag{18}$$

was evaluated by assuming $\Delta I = I_g$ and determining a by linear extrapolation of the measured current signals to $(V+V_0)^{1/2}=0$. Voltage factors obtained from measurement with heavily filtered x rays at exposure rates of the order of 1 R/min are shown in figure 13. For x rays of different HVL, values of k_V are proportional to $(V+V_0)^{1/2}$, but show at constant voltage a certain spread without indicating any definite trend in energy dependence. At $V=15$ V, the highest voltage applied, the deviation of k_V from an average value is approximately ±2 percent that is within the experimental error of these measurements. The error in k_V is dependent on the error in measuring I_g, which was at the small exposure rates obtained with heavily filtered x rays about 10 to 15 times smaller than the dark current, and by the error in determining the value a by the extrapolation method. One may therefore conclude from these measurements that k_V is independent of radiation quality, and photocurrents increase with increasing voltage at the same rate at different qualities of radiation. If $(I_g)_1$ and $(I_g)_2$ are the photocurrents measured at photon energies $h\nu_1$ and $h\nu_2$, then their ratio at constant V

$$\frac{(I_g)_1}{(I_g)_2}=\frac{a_1(k_V)_1}{a_2(k_V)_2}=\frac{a_1\left[1+\frac{w_1}{L_n}(V+V_0)^{1/2}\right]}{a_2\left[1+\frac{w_1}{L_n}(V+V_0)^{1/2}\right]}=\frac{a_1}{a_2} \tag{19}$$

is independent of V, which means that the energy dependence of I_g given in relative values is the same

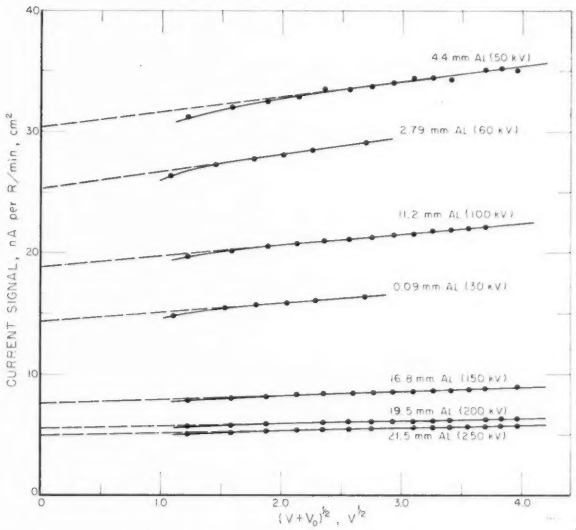
4.4 mm Al (50 kV)
2.79 mm Al (60 kV)
11.2 mm Al (100 kV)
0.09 mm Al (30 kV)
16.8 mm Al (150 kV)
19.5 mm Al (200 kV)
21.5 mm Al (250 kV)
CURRENT SIGNAL, nA per R/min, cm²
(V+V0)½, V½

FIGURE 12. *Current sensitivity measured with x rays of different qualities as function of* $(V+V_0)^{1/2}$.

Qualities of x rays are specified by HVL in Al and operating voltage of x ray tube as indicated.

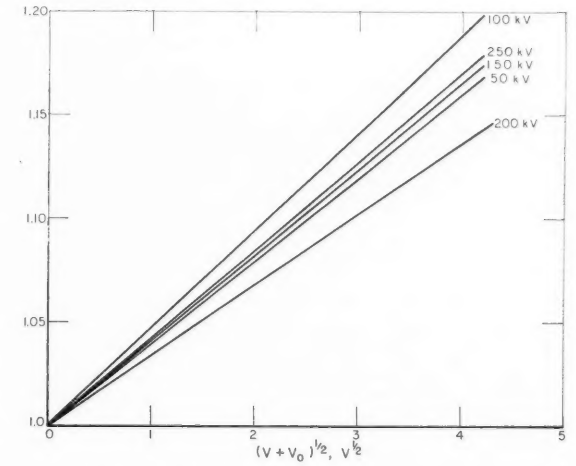

FIGURE 13. *Voltage factor as function of* $(V+V_0)^{1/2}$ *as derived from measurement of voltage dependence of current signals produced by heavily filtered x rays obtained at operating voltages as indicated (see table 2).*

for different applied voltages. This is shown in table 2 giving relative values of I_g at different applied voltages as measured with heavily, moderately, and lightly filtered x rays. The relative values at different voltages differ by about ±1 percent from their average values. Somewhat larger deviations are obtained for photovoltaic short-circuit currents at $V=0$, which were, however, not directly measured, but determined by extrapolation to $V=0$.

TABLE 2. *Energy dependence (figs. 10 and 11)*

Relative values of current sensitivities measured at different voltages. (Sensitive detector surface was covered with 325 micron thick Al-layer.)

X rays		Current signal per R/min, cm² (rel. value)			
kVcp	Approx. HVL mm Al	V=0	5V	10V	15V
		Heavily filtered x rays [a]			
50	4.4	1.576	1.590	1.577	1.578
100	11.2	1.000	1.000	1.000	1.000
150	16.8	0.392	0.397	0.397	0.399
200	19.5	.281	.285	.282	.282
250	21.5	.252	.256	.257	.257
X rays		Current signal per R/min, cm² (rel. value)			
kVcp	Approx. HVL mm Al	V=0	1V	3V	5V
		Lightly and moderately filtered x rays [a, b]			
30	0.30	0.601	0.600	0.600	0.600
30	.55	.728	.730	.736	.738
50	1.20	.880	.909	.910	.912
60	2.97	.980	.982	.981	.984
75	3.53	1.000	1.000	1.000	1.000
100	5.20	0.987	0.977	0.975	0.980
150	10.1	.730	.725	.724	.730
200	13.2	.519	.518	.516	.517
250	16.2	.370	.367	.366	.368

[a] For filter combination used see table 1 in part 1 [1].
[b] The additional filtration by the 325 μ thick Al cover was taken into account.

The slope of the straight lines in figure 13 should, in accordance with eq (9), be equal to (w_1/L_n). If w_1 is determined by capacity measurements as shown above, then L_n can be obtained from measurements of the voltage factor of I_g. Using the average value of (w_1/L_n) obtained from these measurements (fig. 13) of $(w_1/L_n)=0.041$, and assuming a value $w_1=14.5$ μ as given above, the average diffusion length L_n is obtained as $L_n=354\pm43$ μ. This value is of the right order of magnitude, but approximately 25 percent smaller than that obtained by solving eq (4) for L_n for a certain voltage. However, for solving this equation, one has to make assumptions about the quality of radiation, and exposure rate inside the charge collecting volume, and the effective irradiated surface area must be known, whereas the evaluation of L_n from the voltage factor is independent of these parameters. How far these values of L_n are correct, could not be decided, because lifetimes and diffusion lengths of minority carriers in the silicon wafer of the detector were not known.

5. Summary and Conclusions

It has been shown that if the detectors are operated as photodiodes the photocurrent produced by x rays in silicon radiation detectors of the *p-n* junction type may be considered to consist of two parts, a voltage-independent part which is determined by the average diffusion length of minority carriers in the base layer, and a voltage-dependent part which is proportional to the width of the depletion region, both parts being proportional to exposure rate. The voltage dependence of the generated photocurrent I_g was expressed by a voltage factor k_V (eq (8)), which for the detectors investigated, was a linear function of $(V+V_0)^{1/2}$, if V is the voltage applied at the detector during irradiation and V_0 is the zero-voltage barrier height of the junction. Due to the nonsaturating current-voltage characteristic of silicon radiation detectors, the measured current signal, or the radiation-produced change in reverse current, is different from the generated photocurrent by a factor k_c which was called the curve factor. The curve factor as defined by eq (13) is a linear function of the ratio of the load resistance and the dynamic resistance at the voltage applied under "dark" condition. Due to its dependence on the dynamic resistance, k_c is voltage and temperature dependent. Thus, assuming constant temperature, one obtains from eqs (8) and (13) for the photocurrent generated at the voltage V

$$(I_g)_V = ak_V = (k_c)_V(\Delta I)_V \tag{20}$$

or for the current signal

$$(\Delta I)_V = \frac{(I_g)_V}{(k_c)_V} = a\,\frac{k_V}{(k_c)_V} \tag{21}$$

if a is the voltage-independent diffusion part of I_g which cannot be measured directly, but is obtained by extrapolation of the current signals to $(V+V_0)^{1/2}=0$. It may sometimes be preferable to relate $(\Delta I)_V$ to a current signal $(\Delta I)_{V_1}$ obtained at a reference voltage V_1. In this case

$$(\Delta I)_V = (\Delta I)_{V_1}\,\frac{k_V(k_c)_{V_1}}{k_{V_1}(k_c)_V}. \tag{22}$$

By proper choice of R_L, the curve factors may be kept approximately at unity value, so that the ratio (k_V/k_{V_1}) can experimentally be determined by measuring the ratio $(\Delta I)_V/(\Delta I)_{V_1}$, as function of V at constant exposure rate of x rays of any quality.

The generated photocurrent I_g and correspondingly ΔI increase with increasing temperature, but while a increases, k_V decreases slightly with increasing temperature. The temperature dependence is nonlinear, and due to the temperature dependence of k_V, slightly voltage-dependent. However, within a temperature range between 25 and 50 °C, one may assume from these measurements, as an approximation, a voltage-independent linear temperature dependence determined by a positive temperature coefficient of approxi-

mately 0.35 percent per °C. The temperature dependence of I_g cannot satisfactorily be explained and further investigation will be required to establish the temperature dependence of different parameters as width of the depletion region, and lifetime and diffusion lengths of minority carriers.

In particular, the following conclusions can be drawn from this investigation with regard to the use of silicon radiation detectors as photodiodes for exposure rate measurements of x rays:

The photocurrent $(I_g)_V$ produced under the photodiode mode of operation shows qualitatively the same exposure rate and energy dependence as the short-circuit current produced under the photovoltaic mode of operation [1]. The increase of $(I_g)_V$ with applied voltage is rather small due to the small ratio of width of depletion region to diffusion length of minority carriers in diffused *p-n* junction type detectors. The advantage of increasing $(I_g)_V$ by increasing V, is offset by the accompanying increase in dark current, which becomes noisy and unstable at higher voltages. Large bias voltages should therefore be avoided.

Load resistance and applied voltage should be chosen in such a way that within the range of exposure rates considered, the curve factor k_c remains constant and approximately at unity value. If the dynamic resistance of the detector cannot be considered as being constant within the voltage signal measured across the load resistance, eq (14a) for k_c will not be applicable any more. The current signal will in a different way be related to $(I_g)_V$, resulting in a nonlinear exposure rate dependence. This situation may arise at low bias voltages or large voltage signals obtained with large load resistances and high exposure rates. The requirement of constant curve factor k_c, imposes a limitation on the size of the load resistance which can be used for amplification of the voltage signal.

The voltage factor has been shown to be independent of exposure rate or quality of radiation. This means that though current sensitivity will be different at different voltages, the ratio of two signals measured at different exposure rates or with x rays of different quality, but at constant voltage, will be the same independent of the voltage applied. Silicon radiation detectors operated as photodiodes may therefore specially be useful for monitoring of radiations, when only relative values of exposure rates are of interest. For measuring exposure rates in roentgens per unit time, detectors will have to be calibrated for the respective type of radiation with the same voltage and load resistance as used for the exposure rate measurements.

Compared with the photovoltaic mode of operation, the use of silicon radiation detectors as photodiodes has the advantages that their exposure rate and temperature dependence is, through the curve factor, only slightly dependent on the load resistance, and that it is possible, though within certain limits, to amplify voltage signals by increasing the load resistance. However, more elaborate circuitry is necessary for the operation of detectors as photodiodes, and the dark current, which shows some instability and strong temperature dependence, has to be measured or balanced out for each signal reading. For small exposure rates, the current signal may become much smaller than the dark current, limiting the measuring range to exposure rates larger than approximately 1 R/min. In this investigation, current signals produced at an exposure rate of 1 R/min were determined with a precision of ±1 percent by measuring the amplified voltage drop over a known load resistance of moderate size with a potentiometer.

Finally, it should be pointed out that the discussion of measurements reported here was based on eq (6) which was derived under certain simplifying assumptions. If these assumptions are not fulfilled, deviations from the voltage dependence of $(I_g)_V$ reported here may be observed.

6. References

[1] K. Scharf and J. H. Sparrow, J. Res. NBS **68A** (Phys. and Chem.) No. 6, 683 (1964).
[2] W. Shockley, Bell System Tech. J. **28,** 435 (1949).
[3] P. P. Webb, R. L. Williams, and R. W. Jackson, IRE Trans. Nuclear Sci. **NS-7,** 199 (1960).
[4] E. Baldinger, W. Czaja, and J. Gutman, Proc. Symp. Nuclear Instr, Harwell (ed. J. B. Birks), 98 (Sept. 1961).
[5] A. C. Muller, F. X. Rizzo, and L. Galanter, Nuclear Sci. Eng. **19,** 400 (1964).
[6] J. Antula, phys. stat. sol. **3,** 1840 (1963).

(Paper 70A2-394)

JOURNAL OF RESEARCH of the National Bureau of Standards—A. Physics and Chemistry
Vol. 70A, No. 2, March–April 1966

Absolute Isotopic Abundance Ratios and the Atomic Weight of a Reference Sample of Chromium

William R. Shields, Thomas J. Murphy, Edward J. Catanzaro, and Ernest L. Garner

Institute for Materials Research, National Bureau of Standards, Washington, D.C.

(December 28, 1965)

Absolute values have been obtained for the isotopic abundance ratios of a reference sample of chromium, using surface emission mass spectrometry. Samples of known isotopic composition, prepared from nearly pure separated chromium isotopes, were used to calibrate the mass spectrometers. The resulting absolute values are $Cr^{50}/Cr^{52} = 0.051859 \pm 0.000100$, $Cr^{53}/Cr^{52} = 0.113386 \pm 0.000145$, $Cr^{54}/Cr^{52} = 0.028222 \pm 0.000059$, yielding an atomic weight ($C^{12} = 12$) of 51.99612 ± 0.00033. The indicated uncertainties are overall limits of error based on 95 percent confidence limits for the mean and allowances for effects of known sources of possible systematic error.

Key Words: Chromium, atomic weight, isotopic abundances, absolute ratios.

1. Introduction

The NBS is conducting a long term program of physical atomic weight determinations, using solid-source mass spectrometry. Previous determinations include silver [1], chlorine [2], copper [3], and bromine [4]. The present work extends the study to chromium.

Recently Flesch et al., [5], published what were purported to be absolute measurements of the chromium isotope ratios. Because of analytical problems they were unable to calibrate their mass spectrometer directly with mixtures of separated chromium isotopes and resorted to indirect calibration, using mixtures of separated nitrogen isotopes. Unfortunately this procedure makes the assignment of the word "absolute" to their results highly questionable.

In the present study, both mass spectrometers used were calibrated for bias by the use of samples of known isotopic composition, prepared from nearly pure separated chromium isotopes. The measured biases were then used to obtain the absolute chromium isotope ratios of a reference sample of commercial chromium. The atomic weight was then calculated, using masses from Mattauch et al., [6].

In this laboratory considerable effort has been expended in the design of collectors and the modification of recorder systems to insure that any biases from these components are constant. The only "random" bias is due to the mass-dependent fractionation of the isotopes during ionization, and this bias is independent of the isotopic composition of the samples. Thus, for each instrumental system used in this study, a single mass-dependent bias correction factor is determined and is valid over the entire range of isotopic compositions measured.

The calibration samples were prepared by mixing aliquots of Cr^{50} and Cr^{54} separated isotope solutions. The use of the two extreme-mass isotopes gives the maximum sensitivity for determining the bias in the source region of a mass spectrometer. Had synthetic mixtures approximating natural chromium isotope composition been used for the calibrations, it would not have been necessary to make corrections for amplifier attenuators, but the propagation of isotopic composition uncertainty involved in mixing all four separated chromium isotope solutions and the fact that the two extreme-mass isotopes are both minor in natural chromium, would have made the bias determinations less accurate.

The fact that each instrument used requires a single correction factor for source discrimination has been demonstrated by numerous analyses of many different uranium isotope standards. However, the assumption was retested in this study by applying the correction factors determined by the unnatural mixes to the analyses of two "natural" synthetic mixes and comparing the experimental results with the theoretical values.

2. Experimental Procedure

2.1. Mass Spectrometry

The isotopic measurements were made with two different, single-focusing solid-source mass spectrometers. One instrument (MS–2) has a 6-in. radius of curvature 60° analyzer tube and 48° sector magnet; the other has a 12-in. radius of curvature 68° analyzer tube and 60° sector magnet. The electronic components and source and collector design are basically the same in both instruments. Surface ionization from single-filament platinum-ribbon sources was used. Triple filament sources (thermal ionization)

could not be used because they had large Cr^+ background signals which would have made it impossible to analyze accurately the separated isotopes. Ion currents were measured by means of a vibrating reed electrometer with an expanded-scale recorder. Ratios were measured by varying the magnetic field at constant ion-accelerating voltage.

The chromium was deposited on the sample filament in the form of dilute nitric acid (1 + 99) solutions of chromium nitrate. One drop of solution, containing approximately 0.06 mg Cr (3 mg Cr/ml), was deposited on the filament and dried with a heat lamp and an electrical current which was slowly increased to ~2.2 A. After this procedure the heat lamp and current were turned off and one drop 10 percent HNO_3 or distilled water was placed over the dried sample on the filament. The solution was then redried in the same manner as above. The drop of acid or water served to spread the sample more evenly over the filament surface. No difference was noted between the efficiency of the two reagents: the acid was used in the analyses performed on one mass spectrometer (MS–2) and the water on the other (MS–4).

In the mass spectrometer a strict pattern of filament heating was followed and all data were taken on stable or growing signals ($3–4 \times 10^{-12}$ A, Cr^{52}) between 37 and 60 min after the filament was turned on. Since the observed ratios varied with time, all analyses which did not follow the normal signal-growth pattern were discarded.

Before being used, all filaments were prebaked in a vacuum and under a potential field, to reduce the possibility of significant chromium background signals from the filament material. Small chromium signals were visible when unbaked filaments were heated to just below their melting point, but no signals were seen for prebaked filaments at the temperatures used in the analyses.

2.2. Preparation and Chromium Concentration of the Separated Isotope Solutions

Approximately 2 g each of electromagnetically separated Cr^{50}, Cr^{52}, Cr^{53}, and Cr^{54} isotopes, in the form of Cr_2O_3, were obtained from the Isotopes Division, Oak Ridge National Laboratory of the Union Carbide Nuclear Company. The $Cr_2^{50}O_3$ was designated series LZ, sample 1449A; the $Cr_2^{52}O_3$ was designated series LZ, sample 1450A; the $Cr_2^{53}O_3$ was designated series LZ, sample 1451A; and the $Cr_2^{54}O_3$ was designated series LZ, sample 1452A. The certificate of analysis accompanying each sample indicated a high degree of chemical impurity. The samples were further analyzed by the Spectrochemical Analysis Section of the NBS and the results of these analyses showed the following elements detected at a concentration level of less than 0.01 percent: Al, B, Ca, Cu, Fe, Mg, Mn, Mo, Ni, Pb, Si, and V. No impurities were detected at a higher concentration level. Since the chromium concentrations of the solutions to be prepared were to be determined by reduction of hexavalent chromium with ferrous iron, only vanadium and manganese would interfere in the analyses by being reduced from a higher to a lower oxidation state. These elements were determined quantitatively by emission spectrography. The results showed that the manganese concentration was less than 0.002 percent for each isotope sample and the vanadium concentration was less than 0.005 percent for each sample except the Cr^{50} sample which contained 0.008 percent V. These concentrations were too low to cause significant error in the chromium determinations, so it was not necessary to further purify the isotope samples.

A 1.3 to 1.5 g sample of each separated isotope was transferred to a 100 ml beaker and covered with 15 ml of redistilled perchloric acid. The beakers were heated overnight at 140 to 150 °C to dissolve the chromic oxide and oxidize the Cr^{+3} to Cr^{+6}. Tests showed that, if the temperature was kept between 140 and 150 °C, only a small amount of chromium would be lost as chromyl chloride and almost all of the chromium would be oxidized to the hexavalent state. The solutions were cooled, diluted with 15 ml of water, and heated on a steam bath until starch iodide paper gave a negative test for chlorine.

The solutions were filtered through sintered glass and transferred to 100 ml volumetric flasks whose necks had been cut off so that only about 1 cm remained. Enough water was added to bring the final volumes to about 65 ml and the solutions were thoroughly mixed by swirling for several minutes. Each flask was then sealed with a rubber serum septum and allowed to stand overnight in the case of a semimicrobalance to insure thermal equilibrium.

The flasks and contents were weighed on the balance to ±0.02 mg. Samples were withdrawn from each flask by inserting a platinum needle, attached to a glass hypodermic syringe with a Kel-F hub, through the rubber septum and withdrawing the desired amount of solution. A second needle which just punctured the septum served as a vent. The weight of the sample withdrawn was determined from the weight of the flask before and after withdrawal of solution.

Four samples each, weighing from 9 to 11 g and containing 7 to 10 meq (milliequivalent) of chromium, were withdrawn from each solution. Each sample was transferred to a 50 ml Erlenmeyer flask and the syringe and needle were washed with distilled water, the washings also being added to the flask. The volume was adjusted to 10 ml by evaporation. The solution was made alkaline with 10*N* NaOH solution and 1 ml of 3 percent hydrogen peroxide solution was added to insure complete oxidation to hexavalent chromium. The solution was then heated on a steam bath to destroy the excess hydrogen peroxide.

The chromium concentration of each solution was determined by constant-current coulometric titration with ferrous ions generated at a platinum cathode by electroreduction of ferric ion. The end point was de-

termined amperometrically. Details of this method are given in Marinenko and Taylor [7].

The accuracy and precision of the chromium concentration measurements were determined by applying the analytical procedure to NBS standard reference material 136b, potassium dichromate, which is known to be 99.977 ±0.003 percent $K_2Cr_2O_7$ [7] based on oxidizing power. Four solutions of this material, in the approximate concentration of the separated isotope solutions, were prepared on a weight basis and the concentration of each solution was calculated as milliequivalents of chromium per gram of solution. Four to six samples were withdrawn from each solution and the chromium in each sample was partially reduced by adding hydrogen peroxide or sulfurous acid. The chromium in each sample was determined by the method described above and the results were compared to the amounts known to be present.

Data resulting from these analyses showed that (a) the average concentration of chromium for each set, as determined by this method, agreed with the calculated concentration to within 0.002 percent, and (b) the standard deviation of an individual determination (17 degrees of freedom) is 0.010 percent for a solution containing 1.0 meq Cr/g solution.

The excellent agreement between the analytical and calculated amounts of chromium also prove that the oxidation of trivalent chromium to hexavalent chromium by hydrogen peroxide in alkaline solution is quantitative and that excess hydrogen peroxide is completely destroyed.

TABLE 1. *Concentration of chromium isotope solutions*

Soln	Sample No.	Wt. soln	Cr	Conc Cr meq/g soln
		g	*meq*	
Cr^{50}	A	10.72803	8.085459	0.753676
	B	10.98061	8.276915	.753776
	C	10.72370	8.082169	.753674
	D	10.69936	8.064068	.753698
				mean 0.753706 [a]
Cr^{52}	A	9.90713	8.214555	0.829156
	B	9.44785	7.830172	.828778
	C	9.82398	8.142790	.828869
	D	9.50548	7.921486	.829045
	E	9.06433	7.513026	.828856
				mean 0.828941 [a]
Cr^{53}	A	10.59417	8.202406	0.774238
	B	10.47034	8.106043	.774191
	C	10.83262	8.368052	.774148
	D	9.81393	7.608591	.774284
				mean 0.774215 [a]
Cr^{54}	A	10.27683	9.216768	0.896849
	B	9.51223	8.531343	.896881
	C	9.36201	8.398022	.897032
	D	9.15697	8.214576	.897085
				mean 0.896962 [a]

[a] The uncertainty of the mean at the 95 percent confidence level is $\pm 1.02 \times 10^{-4}$ meq Cr/g soln.

The results of the chromium analyses of the separated isotope solutions are given in table 1. Pooling the results of these four sets of analyses with those of the four sets on the standard material yields a value of 1.05×10^{-4} meq Cr/g solution as the standard deviation for an individual determination. The standard error of the mean of four determinations is therefore 0.50×10^{-4} meq/g solution and that of five determinations is 0.47×10^{-4} meq/g solution. At the 95 percent confidence level, the uncertainty in the chromium concentrations of the separated isotope solutions is $\pm(2.04 \times 0.50 \times 10^{-4}) = \pm 1.02 \times 10^{-4}$ meq/g solution.

2.3. Isotopic Analysis of the Separated Isotope Solutions

Each of the four separated isotope solutions was analyzed four times on each instrument. Sources were dismantled, cleaned and reassembled between the analysis of each solution, as a protection against the possibility of cross contamination from the source parts. Except for the sake of complete security this procedure appears to have been unnecessary. Tests showed that there were no significant differences between the results of an analyses of the Cr^{54} solution performed on the same source which was previously used for four consecutive analyses of the Cr^{50} solution and the four Cr^{54} solution analyses made on a newly cleaned source. No memory effects were visible even in this extreme procedure.

The isotopic compositions of the separated isotopes are given in table 2. They have been corrected for mass spectrometric bias, with changes being negligible after two rounds of iteration. The isotopic compositions reported by ORNL are "Cr^{50}", 95.9 ±0.1 atom percent Cr^{50}, 3.76 ±0.05 atom percent Cr^{52}, 0.26 ±0.05 atom percent Cr^{53} and 0.05 atom percent Cr^{54}; "Cr^{52}", 0.01 atom percent Cr^{50}, 99.87 ±0.02 atom percent Cr^{52}, 0.12 ±0.02 atom percent Cr^{53} and 0.01 atom percent Cr^{54}; "Cr^{53}", < 0.05 atom percent Cr^{50}, 3.44 ±0.05 atom percent Cr^{52}, 96.4 ±0.1 atom percent Cr^{53} and 0.18 ±0.02 atom percent Cr^{54}; "Cr^{54}", 0.11 atom percent Cr^{50}, 4.01 ±0.05 atom percent Cr^{52}, 1.79 ±0.05 atom percent Cr^{53} and 94.1 ±0.1 atom percent Cr^{54}. The ORNL limits quoted express the precision of the measurements. From known sources of systematic error, the absolute error is estimated by ORNL to be less than 1 percent.

TABLE 2. *Isotopic composition of separated chromium isotopes used in calibration samples*

Isotope	Isotopic composition[a] (atom percent)	
Cr^{50}	Cr^{50}	95.9118 ±0.0101
	Cr^{52}	3.7812 ±0.0106
	Cr^{53}	0.2582 ±0.0014
	Cr^{54}	.0487 ±0.0017
Cr^{52}	Cr^{50}	.0120 ±0.0009
	Cr^{52}	99.8664 ±0.0032
	Cr^{53}	0.1138 ±0.0028
	Cr^{54}	.0078 ±0.0012
Cr^{53}	Cr^{50}	.0425 ±0.0012
	Cr^{52}	3.4658 ±0.0088
	Cr^{53}	96.3266 ±0.0084
	Cr^{54}	0.1651 ±0.0020
Cr^{54}	Cr^{50}	.1163 ±0.0010
	Cr^{52}	4.1066 ±0.0123
	Cr^{53}	1.8078 ±0.0037
	Cr^{54}	93.9692 ±0.0114

[a] The uncertainties are the 95 percent confidence limits on the ratio determinations.

799-883 O-66—6

2.4. Preparation of the Calibration Samples and Synthetic Mixtures

Two calibration samples and two synthetic "natural" mixtures were prepared by mixing weighed portions of the separated isotope solutions. The calibration samples (I and II) were prepared from the Cr^{50} and Cr^{54} solutions in the approximate ratios 1:1 and 2:1, respectively. The synthetic mixtures (III and IV) were prepared by mixing weighed portions of all four of the separated isotope solutions to approximate the isotopic composition of natural chromium.

Each sample was thoroughly mixed and 1 ml of sulfurous acid was added to reduce Cr^{+6} to Cr^{+3}. Ammonium hydroxide was added to precipitate chromic hydroxide and the solution was filtered. The chromic hydroxide was dissolved in hot dilute HNO_3 and the solution was evaporated to near dryness on a steam bath. The residue was taken into solution with 1 percent HNO_3 and the volume adjusted so that the chromium concentration was 3 mg/ml. The compositions of the calibration samples (I and II) and the synthetic mixtures (III and IV) are given in table 3.

TABLE 3. *Composition of chromium calibration samples and synthetic mixtures*

Mixture no.	Isotope Cr	Wt. soln	Conc soln meq/g soln	Cr
		g		*meq*
I	50	1.00671	0.753706	0.758763
	54	0.97680	.896962	.876152
II	50	1.03063	.753706	.776792
	54	0.48383	.896962	.433977
III	50	.25443	.753706	.191765
	52	3.97721	.828941	3.296872
	53	0.49711	.774215	0.384870
	54	.11805	.896962	.105886
IV	50	.18903	.753706	.142473
	52	3.52945	.828941	2.925706
	53	0.47447	.774215	0.367350
	54	.09084	.896962	.081480

2.5. Isotopic Analyses of the Calibration Samples and Synthetic Mixtures

Two complete sets of analyses of the calibration samples and synthetic mixtures were made on each instrument. Each set consisted of the following sequence of analyses: Ref., Cal. I; Ref., Cal. II; Syn. III, Syn. IV, Ref., Cal. I; Ref., Cal. II. All ratios were measured for the reference and synthetic mixtures but only the Cr^{50}/Cr^{54} ratio of the calibration samples was measured.

The sources were dismantled, cleaned, and reassembled between each set of analyses but not during any set. The results of the memory tests made during the analyses of the separated isotope solutions showed that the latter precaution was not necessary.

3. Results and Discussion

Table 4 summarizes the results for the two calibration samples prepared from the Cr^{50} and Cr^{54} separated isotope solutions. The purpose of these samples and analyses was to measure the mass discrimination which resulted from the mode of ionization. The observed ratios have been corrected for the systematic biases of the amplifier attenuators.

Table 5 summarizes the results for the two synthetic mixtures prepared from all four separated isotope solutions. The purpose of these samples and analyses was to demonstrate that the corrections applied to the observed data do, in fact, correct the observed data to absolute. The experimental results (not directly shown in the table) were arrived at by correcting the observed results for attenuator bias, measured by impressing a calibrated voltage on the feedback loop of the amplifier, and mass discrimination, evaluated by the analyses of the calibration samples (table 4).

TABLE 5. *Comparison of theoretical and experimental values of "natural" synthetic mixtures*

Isotope	Synthetic mix III		Synthetic mix IV	
	Theoretical	Ratio: $\frac{\text{Theor.}}{\text{Exp.}}$	Theoretical	Ratio: $\frac{\text{Theor.}}{\text{Exp.}}$
50	4.639	0.9996	3.902	0.9990
52	83.365	.9999	83.686	1.0000
53	9.471	1.0010	10.208	1.0003
54	2.525	0.9995	2.203	0.9995

These are the only two instrumental corrections necessary. Collector efficiency and linear ohmic

TABLE 4. *Determination of mass discrimination in ionization*

Mass spectrometer	Determination number	Calibration mix I		Calibration mix II		Average correction factor for each determination (4 mass units)
		Theor. $Cr^{50}/Cr^{54} = 0.88476$		Theor. $Cr^{50}/Cr^{54} = 1.82648$		
		Obs. Cr^{50}/Cr^{54}	Ratio: $\frac{\text{Theor.}}{\text{Obs.}}$	Obs. Cr^{50}/Cr^{54}	Ratio: $\frac{\text{Theor}}{\text{Obs.}}$	
MS-2	1	0.91043	0.97180	1.87682	0.97318	0.97249
	2	.91168	.97047	1.87544	.97390	.97218
MS-4	3	.90922	.97310	1.87806	.97254	.97282
	4	.91088	.97133	1.87555	.97384	.97258

response of the high resistance input resistors were shown to be constant over a much larger range of ion currents by the analyses of many different uranium isotope standards. The ½ percent limit of error for "random" (ratio dependent) bias associated with strip-chart recorders was eliminated by the use of expanded scale recorders.

TABLE 6. *Corrected isotopic ratios for the reference sample*

Mass spectrometer	Determination number	Cr^{50}/Cr^{52} [b]	Cr^{53}/Cr^{52} [b]	Cr^{54}/Cr^{52} [b]
MS–2	1	0.051880	0.113416	0.028218
	2	.051898	.113415	.028209
MS–4	3	.051828	.113319	.028239
	4	.051830	.113393	.028220
Mean		0.051859	0.113386	0.028222
Overall limit of error [a]		±0.000100	±0.000145	±0.000059
Uncertainty components:				
95 percent confidence limits on ratio determination		± 0.000029	± 0.000032	± 0.000019
Bounds due to possible systematic error in correction factor		± 0.000039	± 0.000043	± 0.000022
Bounds due to possible systematic error in chemical analysis		± 0.000007	± 0.000015	± 0.000004
Bounds due to possible systematic error in attenuation calibration		± 0.000025	± 0.000055	± 0.000014

[a] The overall limit of error is the sum of the 95 percent confidence limits for the ratio determinations and the terms covering effects of known sources of possible systematic error.
[b] Each of these ratios is the average of 4 ratios from different runs.

Table 6 gives the corrected chromium isotope ratios as calculated in the four separate determinations, and the average values, with uncertainty components. Using the nuclidic masses given by Mattauch et al. [6], the results yield an atomic weight of 51.99612 ±0.00033 on the unified scale ($C^{12}=12$). These calculations are summarized in table 7.

Flesch et al., [5] report no variations in the isotopic composition of 18 chromite samples from various localities which are the major sources of commercial chromium, so the atomic weight of laboratory chromium should be constant. Svec et al. [8], measured the chromium isotope ratios of a number of secondary chrom-bearing minerals and two meteorite samples but their results left unresolved the question of possible variations in these samples. A further study of natural chromium samples is in progress at this laboratory.

The authors are indebted to Mrs. Martha Darr for the quantitative spectrochemical analyses of the Mn and V in the chromium isotope samples and to Hsien H. Ku for the statistical analysis of the experimental data.

TABLE 7. *Summary calculations of the atomic weight of chromium in the reference sample*

	Value	Overall limit of error [a]	Uncertainty components			
			95 percent confidence limits on ratio determination	Possible systematic error in calibration factor	Possible systematic error in chemical analyses	Possible systematic error in attenuation calibration
Atomic weight	51.99612	± 0.00033	± 0.000063	± 0.000135	± 0.000025	± 0.000108
Nuclidic masses [6] ($C^{12}=12$)						
Cr^{50}	49.9460545	± 0.0000037				
Cr^{52}	51.9405131	± .0000032				
Cr^{53}	52.9406527	± .0000032				
Cr^{54}	53.9388815	± .0000040				
Atom percent:						
Cr^{50}	4.3452	± 0.0085	± 0.00233	± 0.00350	± 0.00061	± 0.0021
Cr^{52}	83.7895	± .0117	± .00310	± .00172	± .00030	± .0066
Cr^{53}	9.5006	± .0110	± .00244	± .00334	± .00058	± .0046
Cr^{54}	2.3647	± .0048	± .00154	± .00173	± .00030	± .0012
Isotopic ratios [b]						
50/52	0.051859	± 0.000100	± 0.000029	± 0.000039	± 0.000007	± 0.000025
53/52	.113386	± .000145	± .000032	± .000043	± .000015	± .000055
54/52	.028222	± .000059	± .000019	± .000022	± .000004	± .000014

[a] The overall limit of error is the sum of the 95 percent confidence limits for the ratio determinations and the terms covering effects of known sources of possible systematic error.
[b] From table 6.

4. References

[1] W. R. Shields, E. L. Garner, and V. H. Dibeler, J. Res. NBS **66A** (Phys. and Chem.) No. 1, (1962).
[2] W. R. Shields, T. J. Murphy, E. L. Garner, and V. H. Dibeler, J. Am. Chem. Soc. **84,** 1519 (1962).
[3] W. R. Shields, T. J. Murphy, and E. L. Garner, J. Res. NBS **68A** (Phys. and Chem.), No. 6, 589 (1964).
[4] E. J. Catanzaro, T. J. Murphy, E. L. Garner, and W. R. Shields, J. Res. NBS **68A** (Phys. and Chem.), No. 6, 593 (1964).
[5] G. D. Flesch, H. J. Svec, and H. G. Staley, Geochim. et Cosmochim. Acta **20,** 300 (1960).
[6] J. H. E. Mattauch, W. Thiele, and A. H. Wapstra, Nuclear Physics **67,** 1 (1965).
[7] G. Marinenko and J. K. Taylor, J. Res. NBS **67A** (Phys. and Chem.), No. 5, 453 (1963).
[8] H. J. Svec, G. D. Flesch, and J. Capellen, Geochim. et Cosmochim. Acta **26,** 1351 (1962).

(Paper 70A2–395)

JOURNAL OF RESEARCH of the National Bureau of Standards—A. Physics and Chemistry
Vol. 70A, No. 2, March–April 1966

Publications of the National Bureau of Standards*

Selected Abstracts

Coulometric calibration of microvolumetric apparatus, G. Marinenko and J. K. Taylor, *J. Res. NBS* **70C** (*Engr. and Instr.*), *No. 1, 1–3 (Jan.–Mar. 1966).*
Coulometric titration provides a simple and accurate means to calibrate microvolumetric apparatus such as burets, micropipets, and syringes. The apparatus to be calibrated is caused to deliver a solution of known concentration into an electrolysis cell where it is analyzed coulometrically. By the method described, volumes ranging from 300 μl to 1 μl have been calibrated with relative standard deviation of 0.03 to 3 percent, respectively.

Measurement standards for low and medium peak pulse voltages, A. R. Ondrejka and P. A. Hudson, *J. Res.* **70C** (*Engr. and Instr.*), *No. 1, 13–8 (Jan.–Mar. 1966).*
Two systems for the measurement and standardization of peak pulse voltage have recently been developed in the Radio Standards Engineering Division of the National Bureau of Standards. Designed for use with pulses having durations as short as 10 nanoseconds, the systems represent the initial effort by NBS for establishment of standards in this field and it is expected that they will serve as the basis for a calibration service.
One of the systems is a refined, slideback voltmeter employing a solid state diode. The rise time is less than 10 nanoseconds and the instrument is useful for measurements in the range 5V to 100V as presently constructed.
The second system standardizes the output peak voltage level of pulse generators by means of cascaded zener diodes. The clipping level of the diodes is determined first by d-c voltage measurements and the system is subsequently used to generate pulses of known peak amplitudes. The rise time of the diodes is approximately 30 nanoseconds.
The accuracy of both systems is within 0.25 percent and comparison measurements have been made between the two, and with other NBS a-c and rf (CW) voltage standards.

Standard Reference Materials: Catalog and price list of standard materials issued by the National Bureau of Standards, *NBS Misc. Publ. 260 (Oct. 1, 1965), 45 cents. Supersedes NBS Misc. Publ. 241.*
A descriptive listing is given of the many different Standard Reference Materials issued by the National Bureau of Standards to calibrate a measurement system, or to produce scientific data that can be referred to a common base. A schedule of prices and amounts, as well as directions for ordering, is included. For composition standards summary tables of analyses are presented, to indicate the type of standards presently available. Announcements of new standard reference materials will be made in the Federal Register, in scientific and trade journals, and in the Technical News Bulletin of the National Bureau of Standards. The current status of the various standards will be indicated by an *insert sheet* available quarterly from the Bureau.

Standard Reference Materials: Methods for the chemical analysis of NBS copper-base spectrochemical standards, R. K. Bell, *NBS Misc. Publ. 260–7 (Oct. 25, 1965), 60 cents.*
The methods for chemical analysis described in this publication are those used in the laboratories of the National Bureau of Standards for the determination of the various constituents of 21 NBS copper-base spectrochemical standards. The methods cover procedures for the analysis of 7 principal standard alloys known as cartridge brass, free-cutting brass, naval brass, red brass, gilding metal, commercial bronze, and aluminum brass of nominal, high, and low composition. The methods are selected or designed primarily for accuracy rather than for speed. References are listed for additional information on chemical analysis of copper-base alloys.

Standard Reference Materials: Half lives of materials used in the preparation of standard reference materials of nineteen radioactive nuclides issued by the National Bureau of Standards, S. C. Anspach, L. M. Cavallo, S. B. Garfinkel, J. M. R. Hutchinson, and C. N. Smith, *NBS Misc. Publ. 260–9 (Nov. 15, 1965), 15 cents.*
Values are given for the half lives of materials used in the preparation of standard samples of Na^{22}, Ca^{45}, Sc^{46}, Mn^{54}, Co^{57}, Co^{60}, Zn^{65}, Kr^{85}, Sr^{85}, Sr^{89}, Sr^{90}, Y^{88}, Nb^{95}, I^{125}, Ce^{139}, Ce^{141}, Pm^{147}, Hg^{203}, Tl^{204}, issued by the National Bureau of Standards. Instrumentation, source preparation, and the determination of impurities are also discussed.

HAYSTAQ. A mechanized system for searching chemical information, E. C. Marden, *NBS Tech. Note 264 (Sept. 27, 1965), 50 cents.*
HAYSTAQ is a comprehensive computer system for searching chemical information and is particularly directed toward the stringent requirements of the U.S. Patent Office. The greatest activity to date has been in the design of a satisfactory method to search for chemical structures. A structure diagram is considered as a network, where the atoms or functional groups are the nodes and the bonds between them the links. The search algorithm consists of attempting to match, via a topological tracing, a question network (structure) against each structure in the file of chemical compounds stored on magnetic tape. The structure search includes provision for Markush structures and other generic concepts. Each of 385 questions was matched against a file of 2,400 entries containing (because of the Markush feature) effectively 162,000 compounds. The continuation of this work includes the use of the Hayward linear notation as input and extension of the search routines to other kinds of information associated with chemical structures.

Selected values of chemical thermodynamic properties. Part 1. Tables for the first twenty-three elements in the standard order of arrangement, D. D. Wagman, W. H. Evans, I. Halow, V. B. Parker, S. M. Bailey, and R. H. Schumm, *NBS Tech. Note 270–1 (Oct. 1, 1965), 65 cents. Supersedes NBS Cir. 500.*
The tables contain values where known of the enthalpy and Gibbs energy of formation, enthalpy, entropy and heat capacity at 298.15 °K (25 °C), and the enthalpy of formation at 0 °K, for all inorganic substances and organic molecules containing not more than two carbon atoms. In some instances, such as metal-organic compounds, data are given for substances in which each organic radical contains one or two carbon atoms.
No values are given in these tables for metal alloys or other solid solutions, fused salts, or for substances of undefined chemical composition.

Spectrochemical analysis: Optical spectrometry, x-ray fluorescence spectrometry, and electron probe microanalysis techniques July 1964 to June 1965, ed. B. F. Scribner, *NBS Tech. Note 272 (Oct. 21, 1965), 50 cents.*
A summary is given of the activities of the Spectrochemical Analysis Section for the period from July, 1964 through June, 1965. Activities in optical spectrometry included studies of excitation by arcs and sparks in controlled atmospheres and by the laser probe, the measurement of arc temperatures, and atomic absorption spectrometry. In x-ray spectrometry, methods have been developed for the analysis of copper alloys in solution, as well as silverbase, and gold-base dental alloys. An electron probe microanalyzer has been installed, and a description is given of the modifications that have been made to the instrument, the plans for future investigations, and some applications. Chemical and physical enrichment methods have been developed for the analysis of high-purity tin, zinc, and platinum. Homogeneity tests and analyses have been performed in

the development of standard reference materials. Other activities included analyses of samples to assist other NBS groups and government agencies, and literature surveys. Listings are given of 20 publications and 14 talks by members of the Section within the year.

Boiling heat transfer for oxygen, nitrogen, hydrogen, and helium, E. G. Brentari, P. J. Giarratano, and R. V. Smith, *NBS Tech. Note 317 (Sept. 20, 1965), 60 cents.*
This study has been conducted to provide an orderly examination of the information relative to boiling heat transfer for four cryogenic fluids. The general approach has been to examine experimental data with respect to the predictive correlations which would appear to have probable success and which would be likely to be used by design engineers. These correlations were graphically and statistically compared. The results are discussed, and when it appears a best or acceptable recommendation can be made, computation aids for designers are included. These aids are in the form of graphical presentations for preliminary studies and equations for computer studies. The authors have also indicated the apparent limits for the use of these correlations, when possible. The effect of many variables which would often be significant are not included in the predictive correlations. The influence of these variables is discussed in a separate section on boiling variables.

Surface tensions of normal and parahydrogen, R. J. Corruccini, *NBS Tech. Note 322, (Aug. 11, 1965), 20 cents.*
The published data on the surface tensions of normal hydrogen from three investigations are apparently in disagreement by about 10 percent. In this note it is shown that these data are actually in agreement within about 1 percent if properly computed. The resulting concordant data are represented by functions and by a table suitable for linear interpolation.

Refractive index and dispersion of liquid hydrogen, R. J. Corruccini, *NBS Tech. 323 (Sept. 24, 1965), 25 cents.*
The published experimental values of the refractive index of liquid hydrogen have been correlated by calculating and comparing the values of the Lorentz-Lorenz ratio as a function of wavelength. Because of the scatter found by this analysis, it is proposed that more accurate values can be calculated from available data of other kinds, namely, the dielectric constants determined by Stewart and the optical dispersion determined for the gas at STP. Formulas for this calculation are given.

Buffer solutions of tris (hydroxymethyl) aminomethane for *p*H control in 50 weight percent methanol from 10° to 40° C, M. Woodhead, M. Paabo, R. A. Robinson, and R. G. Bates, *Anal. Chem.* **37,** *1291 (1965).*
Buffer solutions composed of tris (hydroxymethyl) aminomethane and its hydrochloride have proved useful for *p*H control in aqueous solutions of *p*H 7 to 9. The acidity functions p_s ($a_H\gamma_{Cl}$) and pa^*_H for this buffer system in the solvent 50 wt percent methanol from 10 to 40° C have been tabulated. These values can serve as reference data for the study of *pK* values and other acid-base properties in this solvent.

Random-walk model of chain-polymer adsorption at a surface, R. J. Rubin, *J. Chem. Phys.* **43,** *No. 7, 2392–2407 (Oct. 1, 1965).*
A random-walk lattice model of adsorption of an isolated polymer chain at a solution surface is investigated. One-dimensional characteristics of the monomer-unit distribution are determined analytically in the limit of long polymer chains, neglecting the self-excluded volume. The mean number of monomer units adsorbed in the surface layer $\nu(\theta, N)$ is determined, assuming that one end of the polymer chain lies in the surface layer. The parameter N is the number of monomer units in the chain, and θ is the adsorption energy of each monomer unit in the surface layer measured in units of kT. In addition, the mean distance of the free end of the chain from the surface $z(\theta, N)$ is determined. The lattice models considered include the simple-cubic, hexagonal-closepacked, face-centered-cubic, and body-centered-cubic lattices. In the limit in which $N \to \infty$, both $\nu(\theta, N)$ and $z(\theta, N)$ exhibit a very interesting discontinuity at a lattice-dependent adsorption energy θ_c. For example for $\theta > \theta_c$, $\nu(\theta, N)$ (which is also proportional to the average adsorption energy of a polymer chain) is proportional to N. For $\theta < \theta_c$, $\nu(\theta, N)$ is proportional to a constant of order unity; and for $\theta = \theta_c$, $\nu(\theta, N)$ is proportional to $N^{1/2}$. It is shown that the probability distribution of the end of the chain decreases exponentially with increasing distance from the surface layer for $\theta > \theta_c$. In addition, the mean number of monomer units in the kth layer from the surface is determined for $N \gg 1$ and $\theta > \theta_c$ and is found to decrease exponentially with increasing k. In effect, for $\theta > \theta_c$ the polymer chain exists in an adsorbed state. An improvement in the model, which includes short-range correlation between successive steps in the random-walk description, is also considered.

Theoretical electromotive forces for cells containing a single solid or molten oxide, W. J. Hamer, *J. Electroanal. Chem.* **10,** *140–150 (1965).*
An electromotive series of metallic oxides, based on the free energy of formation of the oxides, is presented for temperatures ranging from 25° C to 3000° K. A total of 137 oxides is considered and a comparison with the aqueous series is made at 25° C. The usefulness of the series is outlined.

An anomalous decrease of the elastic moduli at very low temperatures in some 300 series stainless steels, R. P. Reed and R. P. Mikesell, *(Proc. 1964 Cryogenic Engineering Conf., Univ. Pennsylvania, Phila., Pa., Aug. 18–24, 1964), Book, Advances in Cryogenic Engineering 10, Paper A–5, 46–49 (Plenum Press Inc., New York, N.Y., 1965).*
Many AISI 300 series steels are used for a variety of applications at cryogenic temperatures. For some applications an accurate knowledge of Young's Modulus and the shear modulus is very useful. For this reason the elastic moduli of a number of materials were measured isothermally at low temperatures in conjunction with other mechanical property tests by Warren and Reed. Some of the 300 series stainless steels exhibited an anomalous decrease between 76° K and 20° K. This anomaly was further documented by additional shear modulus measurements of AISI 302, 303 and 310 steels in both the annealed and cold-drawn conditions. For these tests a torsion apparatus was used to measure the shear modulus and a special strain gage extensometer was used to measure the Young's modulus. The decrease in moduli has been attributed to a paramagnetic to antiferromagnetic transition which occurs in 18Cr-8Ni alloys in the temperature range 37–42° K. This paper presents a brief summary of the experimental techniques and the experimental results of the above program.

Four methods of determining temperature sensitivity of strain gages at elevated temperatures, C. H. Melton and R. L. Bloss, *ISA J.* **12,** *No. 10, 69–74 (Oct. 1965).*
Tests were made to compare four methods of determining the temperature sensitivity of bonded resistance strain gages at temperatures up to 1000° F (540° C). The results of these tests indicate that the methods give comparable results when the gage is stable and the resistance is a nearly linear function of temperature. When these conditions do not exist, the choice of method might well be determined by the conditions under which the gages are to be used.

International comparison of dielectric measurements, H. E. Bussey, J. E. Gray, E. C. Bamberger, E. Rushton, G. Russell, B. W. Petley, and D. Morris, *IEEE Trans. Instr. Meas.* **IM–13,** *No. 4, 305–311 (Dec. 1964).*
Three materials, namely fused silica, glass, and alumina, were selected for comparison based on known or expected homogeneity, isotropy, and stability. Measurements were made by the three international laboratories, both in the radio frequency range using capacitor type holders either with or without an air gap, and at microwave frequencies using either cavity resonance methods or transmission line impedance methods. The results show agreement among the three laboratories of better than one percent for the real part of the permittivity. Also, the dispersion from 9 GHz to 1 MHz is reasonable. The agreement on loss tangent is less satisfactory and is being investigated. A second round of measurements is in progress with the expectation that closer agreement will result.

Nucleate and film pool boiling design correlations for O_2, N_2, and He, E. G. Brentari and R. V. Smith, *(Proc. 1964 Cryogenic Engineering Conf., Univ. Pennsylvania, Phila., Pa., Aug. 18–24,*

1964), Book, Advances in Cryogenic Engineering 10, Paper T–1, 325–341 (Plenum Press Inc., New York, N.Y., 1965).
Pool boiling heat transfer flux correlations are compared with experimental cryogenic data. The heat transfer correlations of Kutateladze and of Breen and Westwater are presented for the nucleate regime over a pressure range from atmospheric to 0.6 critical pressure and for the film region over a heater diameter range from 1.0 to 0.001 cm, respectively. Points of maximum nucleate pool boiling and of minimum film pool boiling are also indicated.

Solid-vapor equilibrium in the system hydrogen-methane, M. J. Hiza and R. N. Herring, *(Proc. 1964 Cryogenic Engineering Conf., Univ. Pennsylvania, Phila., Pa., 182–191 (Plenum Press Inc., New York, N.Y., 1965).*
Gas phase compositions in the system hydrogen-methane have been measured at eleven integral temperatures, generally at 5° intervals, from 35.00° to 87.00° K between 2 and 150 atmospheres. A flow system was used in which the heavy component in the solid phase is evaporated into a pure light component gas stream. The equilibrium gas was continuously analyzed with a hydrogen flame ionization detector. The data obtained are presented in both graphical and tabular form. Enhancement factors, calculated from the isothermal data, are cross-plotted as isobars and compared with the enhancement factors calculated from other experimental solid-vapor data for this system.

DC dielectric-conductance (reciprocal resistance) and conductivity (reciprocal resistivity) measurements, A. H. Schott, *Book, Testing of Polymers 1, ch. 6, 213–236 (Interscience Publ. Inc., N.Y., 1965).*
Methods of making d.c. conductance (reciprocal resistance) measurements on polymer materials are discussed, giving precautions required and the range of conductarces which can be measured. A new term "d.c. dielectric conductance" is introduced. Insulation conductance, volume and surface conductance, volume and surface conductivity are redefined. Types of contact electrodes which can be used on polymer materials are discussed.

Infrared measurements on allene and allene-d_4, A. G. Maki and R. A. Toth, *J. Mol. Spectr.* **17,** *No. 1, 136–155 (July 1, 1965).*
Several vibration-rotation absorption bands of allene (C_3H_4) and allene-d_4 (C_3D_4) have been measured with high resolution. From measurements of a parallel and a perpendicular band of C_3H_4 the following constants were obtained: $B_0 = 0.2963_2 \pm 0.00004$ cm^{-1}, $D_J = 11._6 \pm 1.6 \times 10^{-8}$ cm^{-1} and $D_{JK} = 4._6 \pm 1.2 \times 10^{-6}$ cm^{-1}. The best measurements on C_3D_4 were for a parallel band at 2790.25 cm^{-1} for which the values $B_0 = 0.2321_4 \pm 0.00005$ cm^{-1} and $D_J = 4.1 \pm 1.3 \times 10^{-8}$ cm^{-1} were obtained. By combining infrared and Raman measurements of ν_d a value of $A_0 = 4.81 \pm 0.02$ cm^{-1} was obtained. The resulting bond parameters are r_0(C−C) = 1.308$_4$ ± 0.0006 Å, r_0 (C−H) = 1.08$_7$ ± 0.005 Å, and < HCH = 118.1 ± 0.4°. Several perturbations in the C_3H_4 spectra are described.

Interaction between configurations with several open shells, U. Fano, *Phys. Rev.* **140,** *No. 1A, A67–A75 (Oct. 4, 1965).*
Antisymmetrized product wave functions are written for atomic configurations with an arbitrary number of partially or entirely filled shells. Interaction matrix elements between such wave functions are calculated and a numerical evaluation is given for the autoionization of an inner excitation level of neon. A suitable notation keeps the analytical complexities within reasonable bounds.

Nuclear resonance study of hyperfine fields in nickel-rich nickle-cobalt alloys, R. L. Streever and G. A. Uriano, *Phys. Rev.* **139,** *No. 1A, A135–A141 (July 5, 1965).*
The nuclear magnetic resonance line shapes of ^{59}Co and ^{61}Ni have been studied in Ni-Co alloy powders, using the free precission method, by plotting the amplitude of the spin-echo signal across the inhomogeneously broadened lines. The ^{59}Co nuclear resonance has been studied in the concentration range from 1 to 41 atomic percent cobalt and the ^{61}Ni from 1 to 15 atomic percent. Both ^{61}Ni and ^{59}Co resonance frequencies increase (although not linearly) with increasing cobalt concentration. The higher concentration ^{59}Co studies were made at 77° K, while the low concentration ^{59}Co studies and ^{61}Ni studies were made at 4° K. At lower cobalt concentrations we have been able to observe structure associated with anisotropic as well as isotropic contributions to the hyperfine field. The effects at low concentrations can be understood if we assume that the isotropic shift associated with one cobalt in the nearest neighbor shell is small. The anisotropic effects can be understood if we assume that for the ^{59}Co case the effective excess dipolar moment associated with one cobalt nearest neighbor is 3.1 μ_B and for the ^{61}Ni case 3.3 μ_B. At higher concentrations a second line is observed ~ 10MHz above the frequency appropriate to dilute ^{59}Co in nickel, which is believed due to cobalt atoms with two cobalt neighbors in the nearest neighbor shell. A similar line is observed in the ^{61}Ni case ~ 5MHz above the pure nickel frequency. A discussion of the relation between hyperfine fields and local atomic moments is also made and it is concluded that the conduction electron polarization is a major contribution to the hyperfine fields in these alloys.

Book, Some aspects of non-equilibrium thermodynamics in the presence of a radiation field, R. N. Thomas (University of Colorado Press, Boulder, Colorado, 1965).
The Aspects focused upon are those of localness and nonlocalness in connection with the spectroscopic diagnostics of the state of a gaseous ensemble where the important radiation field is that produced by the ensemble itself.

Approach to simple exponential decay in vibrational relaxation, T. Carrington, *J. Chem. Phys.* **43,** *No. 2, 473–479 (July 15, 1965).*
When harmonic oscillators are dilutely dispersed in an inert heat bath, populations of the various vibrational levels in an initial non-equilibrium distribution relax toward thermal equilibrium with a time dependence that is a sum of terms like exp ($\lambda_m t$), where $\lambda_m = -m[1 - \exp(-h\nu/kT)]zP_{01}$. z is an arbitrary collision frequency and P_{01} is the probability of a transition from level 1 to 0. $1/\lambda_1$ ordinarily corresponds to the experimental relaxation time τ since this term will dominate at long times. This work investigates cases in which the coefficient of this term, depending on the initial vibrational distribution and the heat bath temperature, may vanish or be so small that the final simple exponential decay corresponding to λ_1 is never reached under experimental conditions.
For example, when the initial distribution has its first n moments equal to the corresponding moments of the equilibrium distribution, then the first n coefficients in the sum of exponentials will be zero. Furthermore, there will be one or more values of the heat bath temperature, independent of the initial distribution, for which the normally dominant exponential decay will be missing in the expression for the time dependence of population in any particular level. Some of these results can be extended qualitatively to anharmonic oscillators.

Experimental atomic scattering factors for magnesium oxide, G. Burley, *J. Phys. Chem. Solids* **26,** *1605–1613 (Apr. 8, 1965).*
The atomic scattering factors for magnesium and oxygen in magnesium oxide have been determined experimentally. Both atoms exist as divalent ions in this structure. At room temperature the scattering factor curve for the oxygen agrees well with that calculated for the 0^{-2} anion, but that for the magnesium ion deviates considerably from the Hartree-Fock self-consistent field derived value. The experimental values are lower to sin θ/λ value of about 0.50Å^{-1} and then merge with the theoretical result. At temperatures above 25 °C the difference between the theoretical and experimental results for magnesium gradually decreases, until at about 600 °C the two curves become identical.

Major revisions made in new dry cell standard, W. J. Hamer, *Mag. Std.* **36,** *No. 10, 306–308 (Oct. 1965).*
The eighth edition of the American Standards Association Specification on Dry Cells and Batteries included a number of new features. The new specification includes nomenclature, sizes, test procedures, and performance data on alkaline manganese dioxide, zinc-silver oxide, and sealed nickel-cadmium cells which had not been included in previous specifications. New tests, designed to evaluate these types of cells, are discussed. The new specification also includes data on cells for battery-operated watches, safety flashers, and electronic photoflash equipment. These are mentioned in this general article.

Members of the new Committee with the organization or company they represent are included for general interest.

The crystal structure of barium tetraborate, $BaO \cdot 2B_2O_3$, S. Block and A. Perloff, *Acta Cryst.* **19,** *Pt. 3, 297–300 (Sept. 1965).* $BaO \cdot 2B_2O_3$ crystallizes in the monoclinic system, $P2_1/c$. The cell data are $a = 10.56$, $b = 8.20$, $c = 13.01$ Å, $\beta = 104°57'$, and $Z = 8$.
The structure was established using Patterson projections and three-dimensional electron density syntheses utilizing the heavy atoms initially to establish some phases. The structure was refined by three-dimensional least squares to a final $R = 10.4\%$.
The borate network can be described as a three-dimensional linkage of alternating six-membered single rings containing two tetrahedral borons and one triangular boron, and double rings containing two tetrahedral borons, one of them being common to both rings, and three triangular borons. Each single ring is directly linked only to double rings and each double ring directly links only to single rings. The barium atoms fit into channels of this network.

Acoustical thermometer, H. H. Plumb and G. Cataland, *Science* **150,** *No. 3693, 155–161 (Oct. 8, 1965).*
A limited discussion of the absolute thermodynamic temperature scale, and its realization is introductory. Because conventional low temperature absolute thermometry possesses certain inherent difficulties, a different approach has been undertaken at the National Bureau of Standards. Isotherms of the speed of sound in helium gas as a function of pressure are discussed as a means for determining values of absolute temperature. The NBS Acoustical Thermometer which is employed in determining the speed-pressure isotherms is described. A new scale NBS P 2–20 (1965) has resulted and in its regions of overlap (2–5 °K: and 12–20 °K) with other existing temperature scales, a comparison between scales has been made.

An international comparison of inductive voltage divider calibrations at 400 to 1000 Hz, W. C. Sze, A. F. Dunn, and T. L. Zapf, *IEEE Trans. Instr. Meas.* **IM-14,** *No. 3, 124–131 (Sept. 1965).*
The establishment and maintenance of the highest possible order of accuracy for the measurements of voltage ratio and phase angle are responsibilities of the national laboratories. This paper reports the results of an international comparison of a seven-decade inductive voltage divider by the United States National Bureau of Standards and the National Research Council of Canada. The calibration techniques used in each laboratory are discussed in detail, and the results of calibration at 400 and 1000 Hz are compared. The accuracies of measurements are within 0.1 ppm of input for voltage ratio and 1 (setting of dials)$^{1/2}$ microradians for phase angle.

Laboratory measurement of the rate of the reaction $N_2^+ + O \rightarrow NO^+ + N$ **at thermal energy,** E. E. Ferguson, F. C. Fehsenfeld, P. D. Goldan, A. L. Schmeltekopf, and H. I. Schiff, *Planet. Space Sci.* **13,** *823–827 (1965).*
The rate coefficient for the reaction $N_2^+ + O \rightarrow NO^+ + N$ at ~ 300 °K has been measured to be $k_1 = 1.5(\pm 0.8) \times 10^{-10}$ cm^3 sec^{-1}. No previous laboratory measurements of this reaction rate at thermal energies have been reported. This reaction clearly plays an important role in the E and F_1 regions of the ionosphere, accounting for significant N_2^+ loss, far outweighing the N_2^+ loss rate with *molecular* oxygen.

New approach to the theory of fluctuations in a plasma, J. Weinstock, *Phys. Rev.* **139,** *No. 2A, A388–A393 (July 19, 1965).*
A rigorous, but simple, method is presented for calculating auto-correlation functions (fluctuations) of non-equilibrium plasmas—including inhomogeneous and non-stationary plasmas—in external fields. This method is based upon the derivation of an exact and remarkably simple formal relation between auto-correlation functions and the usual one-particle distribution function $f_1(\mathbf{R}, \mathbf{v}, t)$. This relation explicitly reduces the problem of calculating fluctuation spectra to the problem of solving the usual kinetic equations for $f_1(\mathbf{R}, \mathbf{v}, t)$. Consequently, the central quantity of fluctuation theory is one and the same with the central quantity of kinetic theory, and the two theories are completely and explicitly united. To first order it is shown that one need only solve the linearized Vlasov equation, for $f_1(\mathbf{R}, \mathbf{v}, t)$, and when this solution is substituted into our formal relation, we obtain a general formula for auto-correlation functions which is valid for non-stationary systems and includes the effects of the transverse motion of the plasma in addition to the longitudinal motion. For stationary systems this formula approaches the numerous calculations of previous authors in the limits where the transverse terms vanish. As a result of the transverse terms, the spectrum of scattered light can have resonant peaks at frequencies which correspond to transverse modes of oscillation as well as to the well-known longitudinal modes.

Other NBS Publications

J. Res. NBS 70C (Engr. and Instr.), No. 1 (Jan.–Mar. 1966), 75 cents.

Coulometric calibration of microvolumetric apparatus. G. Marinenko and J. K. Taylor. (See above abstracts.)

Effect of temperature and notch geometry on the tensile behavior of a titanium alloy. W. D. Jenkins and W. A. Willard.

Measurement standards for low and medium peak pulse voltages. A. R. Ondrejka and P. A. Hudson. (See above abstracts.)

Temperature coefficient of rf permeability measurement using an impedance bridge as an equality indicating device. A. L. Rasmussen.

A test apparatus for the study of forced air-mixing devices. T. K. Faison, J. C. Davis, and P. R. Achenbach.

Oxidation of polycyclic, aromatic hydrocarbons. A review of the literature, R. S. Tipson, NBS Mono. 87 (Sept. 17, 1965), 40 cents.

Spot diagrams for the prediction of lens performance from design data, O. N. Stavroudis and L. E. Sutton, NBS Mono. 93 (Sept. 7, 1965), 75 cents.

Specifications, tolerances, and other technical requirements for commercial weighing and measuring devices, NBS Handb. 44–3rd edition (Oct. 12, 1965), $2.00. Supercedes NBS Handb. 44–2nd edition.

Calibration and test services of the National Bureau of Standards, NBS Misc. Publ. 250, 1965 edition (Oct. 28, 1965), $1.00 Supersedes 1963 edition.

Automotive lifts, CS142–65 (Sept. 1, 1965), 10 cents. Supersedes CS142–62.

Acrylonitrile-butadiene-styrene (ABS) plastic drain, waste, and vent pipe and fittings, CS270–65 (Apr. 1, 1965). 15 cents.

Polyvinyl chloride (PVC) plastic drain, waste, and vent pipe and fittings, CS272–65 (Apr. 1, 1965). 15 cents.

Standard stock sizes of machined tool steel bars (flast and squares), SPR267–65 (Aug. 15, 1965). 10 cents.

The normal phase variations of the 18 kc/s signals from NBA observed at College, Alaska, J. H. Crary and A. C. Murphy, NBS Tech. Note 206–4 (Sept. 30, 1965), 25 cents.

The normal phase variations of the 16 kc/s signals from GBR observed at College, Alaska, J. H. Crary and A. C. Murphy, NBS Tech. Note 206–5 (Sept. 30, 1965), 30 cents.

HAYSTAQ. A mechanized system for searching chemical information, E. C. Marden, NBS Tech. Note 264 (Sept. 27, 1965), 50 cents.

Tabulation of published data on Soviet electron devices through June 1965, C. P. Marsden, NBS Tech. Note 265 (Oct. 1, 1965), 50 cents. Supersedes NBS Tech. Note 186.

Selected values of chemical thermodynamic properties. Part 1. Tables for the first twenty-three elements in the standard order of arrangement, D. D. Wagman, W. H. Evans, I. Halow, V. B. Parker, S. M. Bailey, and R. H. Schumm, NBS Tech. Note 270–1 (Oct. 1, 1965), 65 cents. Supersedes NBS Circ. 500.

Spectrochemical analysis: Optical spectrometry, x-ray fluorescence spectrometry, and electron probe microanalysis techniques July 1964 to June 1965, ed. B. F. Scribner, NBS Tech. Note 272 (Oct. 21, 1965), 50 cents.

Boiling heat transfer for oxygen, nitrogen, hydrogen, and helium, E. G. Brentari, P. J. Giarratano, and R. V. Smith, NBS Tech. Note 317 (Sept. 20, 1965), 60 cents.

Numerical values of the path integrals for low and very low frequencies, L. A. Berry and M. E. Chrisman, NBS Tech. Note 319 (Sept. 2, 1965), 55 cents.

Spark planning damage in copper, J. J. Gniewek, A. F. Clark, and J. C. Moulder, NBS Tech. Note 321 (Sept. 6, 1965), 15 cents.

Surface tensions of normal and parahydrogen, R. J. Corruccini, NBS Tech. Note 322 (Aug. 11, 1965), 20 cents.

Refractive index and dispersion of liquid hydrogen, R. J. Corruccini, NBS Tech. Note 323 (Sept. 24, 1965), 25 cents.

Interference predictions for the instrument landing system, G. D. Gierhart and M. E. Johnson, NBS Tech. Note 324 (Sept. 1965), 30 cents.

Electrode potentials in fused systems. IX. Liquid junction potentials in the AgCl-AgBr system, K. H. Stern, J. Electrochem. Soc. **112,** No. 10, 1049–1050 (Oct. 1965).

Isotopic mixing in nitrogen chemisorbed on W, J. T. Yates, Jr., and T. E. Madey, J. Chem. Phys. **43,** No. 3, 1055–1059 (Aug. 1, 1965).

Matrix isolation study of the reaction of Cl atoms with CO. The infrared spectrum of the free radical ClCO, M. E. Jacox and D. E. Milligan, J. Chem. Phys. **43,** No. 3, 866–870 (Aug. 1, 1965).

Some electrochemical aspects of germanium dissolution. Valence states and electrode potential, W. E. Reid, Jr., Phys. Chem. **69,** No. 9, 3168–3171 (Sept. 1965).

A pulsed refrigeration system for cryogenic magnet application, T. R. Strobridge and D. B. Mann (Proc. 1964 Cryogenic Engineering Conf., Univ. Pennsylvania, Phila., Pa., Aug. 18–24, 1964), Book, Advances in Cryogenic Engineering 10, Paper N–3, 54–61 (Plenum Press, Inc., New York, N. Y., 1965).

Avoiding errors from stray radiation in measuring the spectral emittance of diffusely reflecting specimens, H. E. Clark, Appl. Opt. Letter to Editor **4,** No. 10, 1356–1357 (Oct. 1965).

Calibration of Bell-type provers by bottling and strapping, C. T. Collett (Proc. 24th Annual Appalachian Gas Measurement Short Course, 1964), West Virginia Univ. Tech. Bull. **73,** 59–65 (1965).

Calibration of microphones, vibration pickups, and earphones, R. K. Cook, S. Edelman, and W. Koidan, J. Audio Engr. Soc. **13,** No. 4, 290–296 (Oct. 1965).

Considerations when using turbine-type flow-meters in cryogenic service, W. J. Alspach and T. M. Flynn (Proc. 1964 Cryogenic Engineering Conf., Univ. Pennsylvania, Phila., Pa., Aug. 18–24, 1964), Book, Advances in Cryogenic Engineering 10, Paper F–3, 246–252 (Plenum Press, Inc., New York, N.Y., 1965).

Production of alumina windows, H. Johnson and R. D. Deslattes, Rev. Sci. Instr. **36,** No. 9, 1381–1382 (Sept. 1965).

Transfer line surge, W. G. Steward (Proc. 1964 Cryogenic Engineering Conf., Univ. Pennsylvania, Phila., Pa., Aug. 18–24, 1964), Book, Advances in Cryogenic Engineering 10, Paper I–3, 313–322 (Plenum Press, Inc., New York, N.Y., 1965).

The international system of units, A. G. McNish, Mater. Res. Stds. 5, No. 10, 528–532 (Oct. 1965).

Dispersion characteristics of the 1.15 μ He-Ne laser line, H. S. Boyne, M. M. Birky, and W. G. Schweitzer, Jr., Appl. Phys. Letters 7, No. 3, 62–65 (Aug. 1, 1965).

Inelastic scattering of electrons by helium, G. E. Chamberlain and H. G. M. Heideman, Phys. Rev. Letters **15,** No. 8, 337–338 (Aug. 1965).

Nuclear resonance spin-echo study of Eu^{153} in EuO, G. A. Uriano and R. L. Streever, Physics Letters **17,** No. 3, 205–206 (July 15, 1965).

Nuclear resonance study of gallium-substituted yttrium iron garnet, R. L. Streever and G. A. Uriano, Phys. Rev. **139,** No. 1A, A305–A313 (July 5, 1965).

Results of an absolute determination of the acceleration of gravity, J. E. Faller, J. Geophys. Res. **70,** No. 16, 4035–4038 (Aug. 15, 1965).

Thermal conductivity and thermoelectric power of rutile (TiO_2), W. R. Thurber and A. J. H. Mante, Phys. Rev. **139,** No. 5A, A1655–A1665 (Aug. 30, 1965).

Nature of the electromagnetic field reflected from a coastline, J. R. Wait, Electronics Letters **1,** 65 (May 1965).

Adhesive bonding of various materials to hard tooth tissues. II. Bonding to dentin promoted by a surface-active comonomer, R. L. Bowen, J. Dental Res. **44,** No. 5, 895–902 (Sept.–Oct. 1965).

Adhesive bonding of various materials to hard tooth tissues. III. Bonding to dentin improved by pretreatment and the use of surface-active comonomer, R. L. Bowen, J. Dental Res. **44,** No. 5, 903–905 (Sept.–Oct. 1965).

Adhesive bonding of various materials to hard tooth tissues. IV. Bonding to dentin, enamel, and fluorapatite improved by the use of a surface-active comonomer, R. L. Bowen, J. Dental Res. **44,** No. 5, 906–911 (Sept.–Oct. 1965).

Phase equilibria in the system aluminum oxide-tungsten oxide, J. L. Waring, J. Am. Ceram. Soc. **48,** No. 9, 493–494 (Sept. 1965).

Relative signs of nuclear spin couplings in $^1H^{11}B^{19}F_2$, E. B. Whipple, T. H. Brown, T. C. Farrar, and T. D. Coyle, J. Chem. Phys. **43,** No. 5, 1841–1842 (Sept. 1, 1965).

The system WO_3–B_2O_3, E. M. Levin, J. Am. Ceram. Soc. **48,** No. 9, 491–492 (Sept. 1965).

Vibrational fundamentals of CF_2N_2 from the ultraviolet absorption spectrum, J. D. Simmons, I. R. Bartky, and A. M. Bass, J. Mol. Spectr. **17,** No. 1, 48–49 (July 1965).

A precision noise-comparator, M. G. Arthur, C. M. Allred, and M. K. Cannon, IEEE Trans. Instr. Meas. **IM–13,** No. 4, 301–305 (Dec. 1964).

A variable characteristic impedance coaxial line, J. E. Cruz and R. L. Brooke, IEEE Trans. Micro. Theory Tech. **MTT–13,** No. 4, 477–478 (July 1965).

Impact of new technology on the forest industries, R. W. Smith, Jr., Proc. 2nd Annual Forest Industries Marketing Conference, June 16–17, 1965, pp. 119–130 (University of Oregon Press, Eugene, Oreg., June 16, 1965).

Study of methods for estimationg loudness, E. L. R. Corliss and G. E. Winzer, J. Acoust. Soc. Am. **38,** No. 3, 424–428 (Sept. 1965).

Error bounds for asymptotic expansions of special functions in the complex plane, F. W. J. Olver, Proc. Symp. on Error in Digital Computation, U.S. Army Research Center, Madison, Wis., April 26–28, 1965, Vol. **2,** pp. 55–75 (John Wiley & Sons, Inc., New York, N.Y., 1965).

Precise voltage-ratio measurement, T. L. Zapf, Electro-Technol. **76,** No. 4, 95–102 (Oct. 1965).

An image source technique for calculating reflection of gamma rays or neutrons, C. Eisenhauer, Health Phys. **11,** 1145–1154 (1965).

Angular scattering law for the moon at 6-meter wavelength, W. K. Klemperer, J. Geophys. Res. Letters **70,** No. 15, 3798–3800 (Aug. 1, 1965).

Dissociation of H_2^+ by electron impact, G. H. Dunn, B. Van Zyl, and R. H. Zare, Phys. Rev. Letters **15,** No. 15, 610 (Oct. 11, 1965).

Effects of tropospheric refraction in earth-space links, K. A. Norton, Book, Progress in Radio Science 1960–1963—Radio and Troposphere, ed. F. du Castel, II, 186–210 (Elsevier Publ. Co., Amsterdam, The Netherlands, 1965).

Fermi resonance in condensed CF_4 and CCl_4, S. Abramowitz and J. J. Comeford, Spectrochim. Acta 21, 1479–1486 (1965).

Field desorption of thorium from a field-evaporated tungsten surface, R. D. Young, J. Appl. Phys. **36,** *No. 9,* 2656–2657 (Sept. 1965).

Long-period very low frequency emission pulsations, W. B. Carson, J. A. Koch, J. H. Pope, and R. M. Gallet, J. Geophys. Res. **70,** No. 17, 4293–4303 (Sept. 1, 1965).

Meson and baryon resonances in relativistic SU(6), H. Harari, D. Horn, M. Kugler, H. J. Lipkin, and S. Meshkov, Phys. Rev. **140,** No. 2B, B431–B433 (Oct. 25, 1965).

Positive ion-neutral reactions in the ionosphere, E. E. Ferguson, F. C. Fehsenfeld, P. D. Goldan, and A. L. Schmeltekopf, J. Geophys. Res. **70,** No. 17, 4324–4329 (Sept. 1, 1965).

Potential-energy curves for CO and CO^+, P. H. Krupenie and S. Weissman, J. Chem. Phys. **43,** No. 5, 1529–1534 (Sept. 1, 1965).

Rotating shutter for time-resolved spectroscopy in the microsecond range, I. R. Bartky and A. M. Bass, Appl. Opt. **4,** No. 10, 1354–1356 (Oct. 1965).

Solar-flare frequency and observing-time patterns, C. S. Warwick, Astrophys. J. **142,** No. 2, 767–772 (Aug. 15, 1965).

Solution polishing of oriented single crystals, R. D. Deslattes, B. G. Simson, and A. T. Horton, Rev. Sci. Instr. **36,** No. 7, 943–944 (July 1965).

Spectrum of doubly ionized lanthanum (La III), J. Sugar and V. Kaufman, J. Opt. Soc. Am. **55,** No. 10, 1283–1285 (Oct. 1965).

Speed of sound in fluid parahydrogen, B. A. Younglove, J. Acoust. Soc. Am. **38,** No. 3, 433–438 (Sept. 1965).

Stress-strain relationships in yarns subjected to rapid impact loading. Part XI: Strain distributions resulting from rifle bullet impact, J. C. Smith, C. A. Fenstermaker, and P. J. Shouse, Textile Res. J. **35,** No. 8, 743–757 (Oct. 21, 1965).

$SU(6)_W$ photoproduction and meson-baryon scattering amplitudes, J. C. Carter, J. J. Coyne, S. Meshkov, D. Horn, M. Kugler, and H. J. Lipkin, Phys. Rev. Letters **15,** No. 8, 373–377 (Aug. 23, 1965).

Theory of relaxation in a group of weakly coupled systems, R. L. Peterson, Phys. Rev. **139,** No. 4A, A1151–A1155 (Aug. 1965).

An analysis of the effects of ground reflection in line-of-sight phase systems, M. C. Thompson, Jr., IEEE Trans. Ant. Prop. **AP–13,** No. 4, 564–567 (July 1965).

Conjugate observations of solar proton events: delayed ionospheric changes during twilight, H. J. A. Chivers, and J. K. Hargreaves, Planet Space Sci. **13,** 583–592 (1965).

Cosmic-noise survey at 65 degrees (N) declination in the 5–50 Mc/s band, R. Parthasarathy and G. M. Lerfald, Monthly Notices Roy. Astron. Soc. **129,** No. 6, 395–409 (1965).

Dynamic spectral characteristics of micropulsation pearls, J. H. Pope, J. Geophys. Res. **70,** No. 15, 3595–3603 (Aug. 1, 1965).

On radiation of electromagnetic and electroacoustic waves in a plasma, J. R. Wait, Appl. Sci. Res. **11,** Sec. B, 423–432 (June 11, 1965).

On the determination of the electron density within discrete auroral forms in the *E* region, R. D. Hunsucker, J. Geophys. Res. **70,** No. 15, 3791–3792 (Aug. 1, 1965).

Some additional features of radar returns from the equatorial electrojet, B. B. Balsley, J. Geophys. Res. **70,** No. 13, 3175–3182 (July 1, 1965).

**Publications for which a price is indicated are available by purchase from the Superintendent of Documents, U.S. Government Printing Office, Washington, D.C., 20402 (foreign postage, one-fourth additional). Reprints from outside journals and the NBS Journal of Research may often be obtained directly from the authors.*

JANAF THERMOCHEMICAL TABLES

The long-awaited *JANAF Thermochemical Tables* are now available from the U.S. Department of Commerce through the Clearinghouse. The data are given as a function of temperature for elements and compounds—both common and exotic, liquid, solid, and gaseous. With the publication of the Tables, all laboratories as well as the entire aerospace industry now have one single source of carefully evaluated data on the thermodynamic properties of compounds which are used in many areas of technology as well as in propellants.

The book contains 811 tables of thermodynamic properties in the solid, liquid, and/or ideal gaseous state of 24 elements (Al, B, Be, Br, C, Cl, F, Fe, H, Hg, I, K, Li, Mg, N, Na, O, P, Pb, S, Si, Ti, W, and Zr) and their simple compounds tabulated at even 100° intervals to 6000 °K. The Tables give such data as heat of formation, heat capacity and entropy, heat of sublimation or heat of vaporization, melting points, plus electronic levels and vibrational energy levels. They cover such uncommon compounds as titanium oxide fluoride and phosphoryl difluoride chloride. For instance, for boron there are 98 tables, 94 of which are for compounds ranging from boron monobromide (BBr) to dilead decaborate ($B_{10}O_{17}Pb_2$).

The JANAF (Joint Army-Navy-Air Force, ARPA & NASA) Tables were compiled over a 6-year period in a project sponsored by the Advanced Research Projects Agency. Dow Chemical compiled them and a JANAF Thermochemical Panel of scientists from Government and industry collaborated to critically review them prior to their publication and distribution. According to the Panel: "This approach was designed to insure that the Tables be of the highest possible quality."

The new Tables fill serious gaps in the data heretofore available. In the mid 1950's, when elements other than the conventional carbon, hydrogen, oxygen, nitrogen, chlorine, and fluorine came into consideration as rocket propellant ingredients, physical chemists faced formidable problems when they had to conduct rigorous theoretical performance calculations for these new propellants. The first major problem was calculational techniques; the second was the lack of accurate thermodynamic data.

Computers substantially resolved the calculational technique problem. By the end of 1959, when the large high-speed computers became available to rapidly perform the almost overwhelming number of calculations required for the application of the method of minimization of free energy, the calculations became as accurate as the thermodynamic data upon which they were based.

"However, serious gaps were present in the available data," says ARPA. "For propellant ingredients, only the standard heat-of-formation is required to conduct a performance calculation. However, this must be known to a high degree of accuracy. For combustion products, the enthalpy and entropy must be known, as a function of temperature, in addition to the standard heat-of-formation."

To resolve the problem of a lack of accurate thermodynamic data, a substantial experimental thermodynamic research program was therefore launched under ARPA's sponsorship and technical direction, the new Tables being the end result of the massive effort.

But the production of the Tables will not bring the 6-year project to an end. The Tables will be updated and revised periodically, with Tables for additional elements and compounds being brought to the attention of science and industry as the Clearinghouse receives them from the originating group.

Order *PB 168 370N, JANAF THERMOCHEMICAL TABLES* from Clearinghouse, U.S. Department of Commerce, Springfield, Va., 22151, 945 pages, price $10.00. (Dow Chemical Company, Midland, Mich., sponsored by ARPA and technically assisted by the Joint Army-Navy-Air Force-ARPA-NASA Thermochemical Working Group, Aug. 1965.)

U.S. GOVERNMENT PRINTING OFFICE: 1966 OL—799-883

UNIVERSITY MICROFILMS INC
SERIALS SECTION
313 NORTH FIRST ST
ANN ARBOR MICH

UNITED STATES
GOVERNMENT PRINTING OFFICE
DIVISION OF PUBLIC DOCUMENTS
WASHINGTON, D.C. 20402

OFFICIAL BUSINESS

POSTAGE AND FEES PAID
U.S. GOVERNMENT PRINTING OFFICE

JOURNAL OF RESEARCH of the National Bureau of Standards
A. Physics and Chemistry

Vol. 70A, No. 2 March–April 1966

Contents

Page

Mechanism of the depolymerization of polytetrafluoroethylene with pyrolytic and radiolytic initiation. Roland E. Florin, Midgett S. Parker, and Leo A. Wall. 115

Effect of some halogenated hydrocarbons on the flame speed of methane. Carl Halpern. 133

Rupture-disk ampoule for anhydrous addition of hydrogen fluoride. Augustus R. Glasgow, Jr. 143

Further studies in the annealing of a borosilicate glass. Sam Spinner and Albert Napolitano. 147

Infrared spectra of the hydrated borates. C. E. Weir. 153

Interpretation of the solution absorption spectra of the $(PuO_2)^{++}$ and $(NpO_2)^{+}$ ions. J. C. Eisenstein and M. H. L. Pryce. 165

Vapor pressure and heat of sublimation of rhenium. E. R. Plante and R. Szwarc. 175

Steady-state response of silicon radiation detectors of the diffused *p-n* junction type to x rays. II: Photodiode mode of operation. Karl Scharf and Julian H. Sparrow. 181

Absolute isotopic abundance ratios and the atomic weight of a reference sample of chromium. William R. Shields, Thomas J. Murphy, Edward J. Catanzaro, and Ernest L. Garner. 193

Publications of the National Bureau of Standards. 199

Library of Congress Catalog Card Number: 62–37059

For sale by the Superintendent of Documents, U.S. Government Printing Office, Washington, D.C., 20402. Price $1.00 (single copy). Subscription price: $5 a year; $1.00 additional for foreign mailing.

UNITED STATES GOVERNMENT PRINTING OFFICE, WASHINGTON : 1966